

<https://doi.org/10.15388/vu.thesis.581>

<https://orcid.org/0000-0003-3102-8930>

VILNIUS UNIVERSITY
CENTER FOR PHYSICAL SCIENCES AND TECHNOLOGY

Gleb Gorokhov

Composite-based elements for microwave and terahertz applications

DOCTORAL DISSERTATION

Technological sciences,
Materials Engineering (T 008)

VILNIUS, 2024

This dissertation work was carried out at Vilnius University from 2018 to 2024.

Academic supervisor – Dr. Jan Macutkevicius (Vilnius University, Technological sciences, Materials Engineering, T 008)

Academic consultant – Prof. Polina Kuzhir (University of Eastern Finland).

This doctoral dissertation will be defended in a public meeting of the Dissertation Defense Panel:

Chairwoman – Doc. Dr. Renata Butkutė (Center for Physical Science and Technology, Technological sciences, Materials Engineering, T 008)

Members:

Dr. Ignas Grigelionis (Center for Physical Science and Technology, Technological sciences, Materials engineering, T 008)

Prof. Dr. Irmantas Kašalynas (Center for Physical Science and Technology, Technological sciences, Materials engineering, T 008)

Prof. Dr. Andrzej Molak (University of Silesia in Katowice, Poland, Technological sciences, Materials engineering, T 008)

Doc. Dr. Tomas Šalkus (Vilnius University, Technological sciences, Materials Engineering, T 008)

The dissertation shall be defended at a public meeting of the Dissertation Defense Panel at 14:00 on January 10th 2024 at National Center for physical science and technology, A100 room.

Address: Sauletekio av. 3, Vilnius, Lithuania.

The text of this dissertation can be accessed at the libraries of Vilnius university and Center for Physical Science and Technology, as well as on the website of Vilnius University:

<https://www.vu.lt/naujienos/ivykiu-kalendorius>

<https://doi.org/10.15388/vu.thesis.581>

<https://orcid.org/0000-0003-3102-8930>

VILNIAUS UNIVERSITETAS
FIZINIŲ IR TECHNOLOGIJOS MOKSLŲ CENTRAS

Gleb Gorokhov

Kompozitų pagrindu elementai mikrobangų ir teraherciniams taikymams

DAKTARO DISERTACIJA

Technologiniai mokslai,
Medžiagų inžinerija (T 008)

VILNIUS, 2024

Disertacija rengta 2018–2024 metais Vilniaus universitete

Mokslinis vadovas – Dr. Jan Macutkevič (Vilniaus universitetas, technologiniai mokslai, medžiagų inžinerija, T 008).

Mokslinis konsultantė – Prof. Polina Kuzhir (University of Eastern Finland).

Gynimo taryba:

Pirmininkė – Doc. Dr. Renata Butkutė (Fizinių ir technologijos mokslų centras, technologiniai mokslai, medžiagų inžinerija, T 008)

Nariai:

Dr. Ignas Grigelionis (Fizinių ir technologijos mokslų centras, technologiniai mokslai, medžiagų inžinerija, T 008)

Prof. Dr. Irmantas Kašalynas (Fizinių ir technologijos mokslų centras, technologiniai mokslai, medžiagų inžinerija, T 008)

Prof. Dr. Andrzej Molak (Silezijos universitetas, Lenkija, technologijos mokslai, medžiagų inžinerija, T 008)

Doc. Dr. Tomas Šalkus (Vilniaus universitetas, technologijos mokslai, medžiagų inžinerija, T 008)

Disertacija ginama viešame Gynimo tarybos posėdyje 2024 m. sausio mėn. 10 d. 14 val. Nacionalinio fizinių ir technologijų mokslų centro A100 auditorijoje.

Adresas: Sauletekio al. 3, Vilnius, Lietuva.

Disertaciją galima peržiūrėti Vilniaus universiteto ir Fizinių ir technologijos mokslų centro bibliotekose, ir VU interneto svetainėje adresu:

<https://www.vu.lt/naujienos/ivykiu-kalendoriu>

ACKNOWLEDGEMENTS

The investigations resulted in this thesis would not be possible without will and dedication of *each and every co-author* I had the honor to work with. However, I have to personally mention the impact of my supervisor, Dr. Jan Macutkevic. His expertise, kindness and unquenchable patience inspired me to not giving up on my way and complete this work.

Then I have to express my gratitude to the people who inspired me in very beginning of my scientific career: Prof. Sergey Maksimenko, Dr. Dzmitry Bychanok and Prof. Polina Kuzhir. Their dedication to the science will always be an example for me.

I am also grateful to the brilliant individuals who provided me with valuable consultations and kind attitude throughout this long journey (without a particular order): Alesia Paddubskaya, Nadzeya Valynets, Prof. Evgeni Ivanov, Prof. Rumiana Kotsilkova, Prof. Patrizia Lamberti, Prof. Alexander Okotrub, Prof. Jūras Banys, Prof. Philippe Lambin, Dr. Darya Meisak and Dr. Marina Yakovleva.

Special thanks must be given to my reviewers, Prof. Irmantas Kašalynas and Dr. Tomas Šalkus for well-formulated questions which helped me enhance the overall quality of this work. I also have to mention the impact of Dr. Šarūnas Svirskas to my statements substantiation.

Next, I would like to express my gratitude to all the hardworking laborers whose daily efforts provide me with the opportunity to live and continue my research activity. Acquiring the knowledge, it is important to remember those for whom education remains inaccessible. I hope that one day, my work will be beneficial to them as well.

Finally, I am eternally grateful to my mother, who not only gave me life, but put all her love and effort to raise me as a decent person. She taught me to take every opportunity to learn something new, and I took it as a lifework. And, since the knowledge is nothing without being shared, I am grateful to *you, the reader*. I hope you find this work useful or, at least, rather interesting.

Gleb Gorokhov
Vilnius
December 20, 2023

TABLE OF CONTENTS

Notation	11
Introduction	13
Aim and tasks	18
Scientific novelty	18
Author's contribution	19
Statements presented for defense	20
List of author's publications	21
1 Literature review	29
1.1 Interaction of radiation with dielectric medium	29
1.2 The electromagnetic response concept	31
1.2.1 Complex impedance as a representation of the electromagnetic response	31
1.2.2 Electromagnetic response representation with scat- tering parameters	32
1.3 Electromagnetic shielding effectiveness	33
1.4 Effective medium theory	33
1.4.1 Maxwell Garnett theory	34
1.4.2 Bruggeman effective medium theory	35
1.4.3 Landau-Lifshitz/Looyenga theory	37
2 Experimental techniques	39
2.1 Materials	39
2.1.1 Synthesis of thermoplastic polymer composites with nanocarbon inclusions	39
2.1.2 Preparation of segregated CNT/GNP/polyurethane media for SLS 3D printing	40
2.1.3 Synthesis of MWCNT vertically-aligned arrays	42
2.1.4 Preparation of periodical structures based on MWCNT arrays	43
2.2 Modeling	45
2.2.1 Maxwell Garnett effective medium theory applica- tion for carbon-based nanocomposites	45
2.2.2 Regular porous structures based on tri-periodic minimal surface equations	47
2.2.3 Electromagnetic response of structures with wavelength- comparable dimensions	53

2.3	Measurements of the electromagnetic properties of the material	58
2.3.1	Measurements in microwave range	58
2.3.2	Measurements in terahertz range	59
3	Terahertz spectroscopy of insulated filler particles in a composite material above percolation threshold	63
3.1	Characterization of nanocarbon composites microstructure	64
3.2	Experimental investigation of nanocarbon composites dielectric properties	67
3.2.1	Maxwell Garnett approximation of GNP-based composites permittivity	69
3.2.2	Imaginary Permittivity Peak in Percolated Hybrid Composites	71
3.3	Summary	74
4	Tri-periodic porous structures for electromagnetic shielding applications	75
4.1	Creation of tri-periodic structures for electromagnetic measurements	75
4.2	Electromagnetic properties of tri-periodic structures . . .	77
4.3	Summary	80
5	Terahertz optical elements based on vertically aligned arrays of multi-walled carbon nanotubes	81
5.1	Pyramid-based structure resonant absorbance	81
5.2	1D and 2D-periodic structures electromagnetic response .	82
5.3	Summary	85
	Conclusions	87
	Bibliography	91
	Publications by the Author	112
	THz Spectroscopy as a Versatile Tool for Filler Distribution Diagnostics in Polymer Nanocomposites	113
	On the Synergistic Effect of Multi-Walled Carbon Nanotubes and Graphene Nanoplatelets to Enhance the Functional Properties of SLS 3D-Printed Elastomeric Structures . . .	129
	Terahertz Optics of Materials with Spatially Harmonically Distributed Refractive Index	149
	Creation of metasurface from vertically aligned carbon nanotubes as versatile platform for ultra-light THz components	161

Laser Patterning of Aligned Carbon Nanotubes Arrays: Morphology, Surface Structure, and Interaction with Terahertz Radiation	171
Santrauka lietuvių kalba	183
S.1 Literatūros apžvalga	188
S.2 Eksperimentinės technikos	188
S.2.1 Medžiagų gamyba	188
S.2.2 Modeliavimas	192
S.3 Terahercinė spektroskopija izoliuotų užpildo dalelių kompozite esant koncentracijoms didesniems negu perkoliacijos slenkstis	198
S.4 Trimatės periodinės porėtos struktūros elektromagnetinio slopinimo taikymams.	202
S.5 Teraherciniai optiniai elementai vertikaliai orientuotų DANV masyvų pagrindu.	206
Išvados	209
Literatūra	211
Trumpos žinios apie disertantą	212

NOTATION

AR	Aspect ratio
CNT	Carbon nanotube
CVD	Chemical vapor deposition
GNP	Graphene nanoplatelet
FDM	Fused deposition modeling
MWCNT	Multi-walled carbon nanotube
VNA	Vector network analyzer
PLA	Polylactic acid
SLS	Selective laser sintering
SNA	Scalar network analyzer
SWCNT	Single-walled carbon nanotube
TPMS	Tri-periodical minimal surface
TPU	Thermoplastic polyurethane

INTRODUCTION

The current work is devoted to the experimental investigation of functional materials for application in gigahertz and terahertz frequency ranges including the preparation and characterization of nanocomposite materials, the design of structures with predictable and controllable electromagnetic properties. Speaking about functional materials we usually refer to the group of artificial or engineered materials, which are designed for the specific target or in "target-motivated" approach [1, 2]. Their properties are engineered or tailored in order to meet the conditions of a practical application which can not be met by "conventional" or natural materials.

The concept of functional material is wider than such of composite, because the properties of first may depend on the structural parameters of a single phase, while as the last is by definition a mixture of at least two distinct phases, which combination determines the material's properties. Functional materials include but not limit to composites [3], metamaterials [4–8] and structures with an engineered surface morphology [9–12] or chemical/volume structure [13]. However, it is impossible to speak about functional materials ignoring the composites which are surround us. For example, the most widely-distributed and well-known composite is steel concrete which consists of steel rods with extreme mechanical strength to stretch deformation and the concrete with outstanding compression strength. The most of composites are matrix-type. They consist of a matrix (spatially-consistent phase) and fillers, which are distributed in the matrix. However, there are non-matrix composites, in which it is impossible to distinguish phases as matrix and filler.

Composites based on micro- and nanoscale carbon structures (single [14–16] and multi-walled nanotubes [17–20], graphene flakes [21–24], carbon dots [25–27], nanohorns [28–31], etc.) are of great interest for electromagnetic (EM) applications [32–37]. The simplest way to drastically change the mechanical [38–41], thermal [42, 43] and electromagnetic [44–48] properties of a dielectric material (such as a polymer, ceramic or glass) is to impregnate it with a certain amount of microscopic/nanoscale particles possessing the properties required by the application.

The carbon nanotubes discovered by Iijima et al, [49] in 1991, possess

the highest aspect ratio among all known nanocarbon fillers. The higher the nanomaterial's aspect ratio is, the easier to form a continuous conductive network through a composite, i.e., reach the electric percolation threshold [48, 50] at the smallest possible concentration [33, 51–53]. Therefore the nanotubes are perfect filler [18, 24, 54–57] and even the substrate [58] for producing lightweight composites for electromagnetic applications. Their unique properties arise from slowed-down surface wave (i.e. plasmon-polariton) propagation along CNT axis [59, 60], as well as so-called "finite length" effects (i.e. localized plasmon resonance) inherent for micron-length single-walled nanotube at THz and far-infrared frequencies [61–63].

CNTs characteristics allow creating compact durable and/or flexible [20, 64, 65] electromagnetic components and nano-devices, such as antennas [66–68], interconnects [69, 70], polarizers [71–73], sensors [14], detectors (see [74] and Refs therein) and emitters of sub-mm waves radiation (see [75] for review). The properties of nanotubes may be tailored to meet the application requirements by the nanotube surface modification [17, 76].

Another nanocarbon structure for the functional materials engineering is graphene, discovered by Geim and Novoselov in 2004 [77]. In composite technology the graphene is usually represented as graphene nanoplatelets [78, 79], i.e. small (up to microns) flakes consist of several graphene layers. Their percolation threshold is usually lays in the range of 3.5–10% [80–85]. That is several orders higher than the 0.002 % percolation threshold reported for composites based on single-walled nanotubes [22, 33, 53]. However, for certain applications the difference between nanotubes and graphene nanoplatelets may be compensated due to the cost-efficiency and/or specific properties of the latter.

Creation of hybrid (i.e. containing multiple types of fillers) composites allows not only to save the expensive nanoparticles by low-cost substitution, but even enhance the composite's properties due to the synergistic effect [86–88] and hybrid percolation network creation [89–93]. Recently, hybrid composites containing graphene nanoplatelets and carbon nanotubes have attracted great interest due to the possible synergistic effects in their mechanical, thermal [94, 95] and electric properties [16, 21, 56, 96, 97].

Speaking about the percolation phenomenon one has to remember:

the inner structure of a composite material is more complex than just a uniform distribution of filler particles inside the matrix. The phases arrangement, mechanical, thermal and electrical properties (including the percolation threshold) of a composite are strongly dependent on the production process [53, 98]. Certain preparation styles lead to the appearance of a segregated conductive networks [43, 55, 99–101]. Moreover, even the initially random uniform distribution of filler particles inside the composite may be affected at the stage of the material’s application. For instance, the flow processes during the melt-extrusion of polymer composite containing carbon nanotubes may result in they orientation along the flow direction [71, 102, 103].

Considering the above, the composite materials are perfectly tailorable building elements for artificial structures with controllable electromagnetic performance dependent on their geometry, i.e. metamaterials [104–109]. The nanoparticles may be operated in different ways, not only to be uniformly distributed in matrix. Certain experimental techniques allow to create micro- and nanoscale structures based on several phases, i.e. segregated networks, core-shell structures [110–113], vertically-aligned arrays [114, 115], nanorods and nanowires [116, 117] etc.

One of the important tasks widely solved with help of functional materials is the broadband electromagnetic shielding. Despite conventional materials (usually metals) may be perfect EM shields, composite materials allow to combine the outstanding shielding effectiveness with great EM absorption performance, high elasticity, low density and much more. However, for the electromagnetic shielding applications the performance of simple composite materials may be outrun by microscopic structures [118]. At the same time, composites are proven to be perfect materials for complex structures and metamaterials building [119, 120]. Engineering the spatial [121] and planar layered structures [122–125], thin films [84, 126–128], lightweight foams [129] and aerogels [129–131] allows to reach outstanding shielding performance [132, 133].

Various methods of additive manufacturing (usually referred as 3D-printing) which are used for metamaterials development involve composite materials. Therefore it is extremely important to produce composites not only possessing the required electromagnetic properties, but also applicable for certain technical processes. Polymer composites with

nanocarbon fillers are widely applied in such 3D-printing techniques as the most widely distributed around the world fused deposition modeling (FDM) [134–139], or less distributed but more precise techniques of selective laser sintering (SLS), digital light processing (DLP) and numerous other techniques [103, 140, 141].

Electromagnetic shields are important but not only elements of microwave and terahertz optics which are possible to create using functional materials. Tasks of THz antennas [142], sources [143] and other phase-shifting [144, 145], frequency- or polarization-selective elements [146–148] are widely solved by means of metamaterial engineering [149, 150]. Depending on the applied approach, including but not limited to such as numerous kinds of lithography, various methods of 3D printing, etc. it is possible to create materials with required EM, mechanical and other properties required by particular application.

Another prospective approach to create the passive optical elements for microwave and terahertz range investigated in current work is also based on the carbon nanotubes as a functional material. Vertically-aligned arrays of MWCNTs obtained by chemical vapor deposition are lightweight and possess anisotropic conductivity. Such combination of properties is very promising for vast range of electromagnetic applications. When individual CNT's characteristic parameters are not compatible with the wavelength taking into account slowing down effect, the MWCNT array, film or composite may be considered as a macroscopic homogenized structure, which electromagnetic response is governed by averaged conductivity, rather than "fundamental" electromagnetics specific to individual CNTs. In such a case one typically has porous conductive structure with broadband absorption [151], which properties are dependent on the CNT array/film density, conductivity and geometry of individual tubes forming the array, inter-tubes contact resistance, etc.

In order to effectively reach the electromagnetic properties required by a particular application the metamaterial paradigm [10, 152–154] can be applied to the CNT array. The combination of its intrinsic properties with particular patterning (e.g. grating) is able to provide the interference-based absorbers [108] in particular frequency range.

The current work is organized as follows: The first chapter contains the theoretical background for the whole work. In the second chapter the experimental methods and model approaches are explained. The third

chapter is devoted to the non-destructive control of filler distribution in hybrid nanocarbon composites performed by means of terahertz spectroscopy. In the fourth chapter the engineering of porous structures with high EM absorption in terahertz frequency range is explained. In the fifth chapter the novel method of functional materials engineering is introduced.

Aim and tasks

The current work is aimed at the creation, characterization and modeling of functional materials for microwave and terahertz applications.

In order to achieve the aim of the work, the following tasks were formulated:

- To widen the characterization of filler distribution in polymer composite materials below and above the percolation threshold by means of terahertz spectroscopy.
- To apply SLS 3D-printing technique for the creation of low-density lightweight porous materials with high absorption of gigahertz and terahertz radiation.
- To propose the novel versatile platform for scalable production of ultra-lightweight non-metal electromagnetic components based on laser patterning and polymer impregnation of vertically aligned arrays of MWCNTs.

Scientific novelty

1. Terahertz spectroscopy was applied as a non-invasive method of the filler distribution control in polymer composites both below and above the percolation threshold.
2. Porous regular structures made of TPU/nanocarbon segregated media by means of selective laser sintering show the significant absorptive properties in microwave and THz ranges.
3. A novel technique of material engineering based on the combination of laser profiling followed by polymer impregnation of vertically aligned MWCNT arrays was introduced.

Author's contribution

The theoretical and experimental investigation of electromagnetic properties (i.e. the frequency dependencies of complex permittivity and conductivity) of composite materials and the electromagnetic response (i.e. frequency dependencies of reflectance, transmittance and absorbance) of structured materials presented in the thesis was performed by the author personally under the supervision of Dr. Jan Macutkevic and with vital help of Dr. Dzmitry Bychanok.

The materials preparation was also performed at the experimental facilities of Institute of Mechanics, Bulgarian Academy of Sciences, Sofia, Bulgaria (Chapter 3) State Key Laboratory of Polymer Materials Engineering, Polymer Research Institute, Sichuan University, Chengdu, China and Institute of Polymers, Composites and Biomaterials, National Research Council, Portici, Italy (Chapter 4); Nikolaev Institute of Inorganic Chemistry, Novosibirsk, Russia (Chapter 5).

Measurements were performed at *National Center for Physical Sciences and Technology, Vilnius University*; the Nanoelectromagnetics laboratory of Institute for Nuclear Problems of Belarusian State University, Minsk, Belarus; Moscow Pedagogical State University, Moscow, Russia; Moscow Institute of Physics and Technology, Dolgoprudny, Russia.

The investigations in published articles were fully [A1, A2] or partially (microwave and terahertz response measurements and interpretation in [A3], samples preparation for terahertz response measurements in [A4]; development of the structures under investigation, terahertz response measurements and interpretation [A5]) conducted by the author and prepared to publications with the great discussion support of J. Macutkevic, D. Bychanok, P. Kuzhir, A. Paddubskaya and other co-authors.

Statements presented for defense

1. The imaginary part of a composite material's permittivity exhibited the maximum in terahertz frequency range caused by the contribution of insulated nanocarbon inclusions in composites both below and above the percolation threshold
2. The regular porous media created using selective laser sintering of TPU/MWCNT/GNP composition possess high absorption in the frequency range of 12 GHz–1 THz caused by their multi-level porosity
3. The metasurfaces created by novel technique including the laser engraving and polymer impregnation of vertically aligned carbon nanotubes possess frequency-selective and polarization-dependent properties caused by the interaction between the engraved array and polymer coating

PAPERS INCLUDED IN THESIS

- [A1] **G. Gorokhov**, D. Bychanok, I. Gayduchenko, Y. Rogov, E. Zhukova, S. Zhukov, L. Kadyrov, G. Fedorov, E. Ivanov, R. Kotsilkova, J. Macutkevic, and P. Kuzhir, “THz spectroscopy as a versatile tool for filler distribution diagnostics in polymer nanocomposites,” *Polymers*, vol. 12, no. 12, p. 3037, Dec. 18, 2020.
- [A2] **G. Gorokhov**, D. Bychanok, P. Kuzhir, D. Gorodetskiy, A. Kurennya, O. Sedelnikova, L. Bulusheva, and A. Okotrub, “Creation of metasurface from vertically aligned carbon nanotubes as versatile platform for ultra-light THz components,” *Nanotechnology*, vol. 31, no. 25, p. 255 703, Apr. 3, 2020.
- [A3] G. Rollo, A. Ronca, P. Cerruti, X. P. Gan, G. Fei, H. Xia, **G. Gorokhov**, D. Bychanok, P. Kuzhir, M. Lavorgna, and L. Ambrosio, “On the synergistic effect of multi-walled carbon nanotubes and graphene nanoplatelets to enhance the functional properties of SLS 3D-printed elastomeric structures,” *Polymers*, vol. 12, no. 8, p. 1841, Aug. 17, 2020.
- [A4] D. Bychanok, **G. Gorokhov**, A. Plyushch, A. Ronca, M. Lavorgna, H. Xia, P. Lamberti, and P. Kuzhir, “Terahertz optics of materials with spatially harmonically distributed refractive index,” *Materials*, vol. 13, no. 22, p. 5208, Nov. 18, 2020.
- [A5] O. Sedelnikova, D. Gorodetskiy, A. Kurennya, K. Baskakova, E. Shlyakhova, A. Makarova, **G. Gorokhov**, D. Bychanok, P. Kuzhir, S. Maksimenko, L. Bulusheva, and A. Okotrub, “Laser patterning of aligned carbon nanotubes arrays: Morphology, surface structure, and interaction with terahertz radiation,” *Materials*, vol. 14, no. 12, p. 3275, Jun. 14, 2021.

OTHER PUBLICATIONS

- [O1] D. Bychanok, A. Liubimau, K. Piasotski, **G. Gorokhov**, D. Meisak, I. Bochkov, and P. Kuzhir, “Effective carbon nanotube/phenol formaldehyde resin based double-layer absorbers of microwave radiation: Design and modeling,” *Physica Status Solidi (B)*, vol. 255, no. 1, p. 1 700 224, Jan. 2018.
- [O2] **G. Gorokhov**, D. Bychanok, D. Meisak, I. Shlyk, A. Liubimau, P. Angelova, C. Menseidov, E. Ivanov, R. Kotsilkova, M. Casa, P. Ciambelli, and P. Kuzhir, “Carbon nanotubes vs graphene nanoplatelets for 3D-printable composites,” *IOP Conference Series: Materials Science and Engineering*, vol. 503, p. 012 010, Mar. 25, 2019.
- [O3] M. Shuba, D. Yuko, **G. Gorokhov**, D. Meisak, D. Bychanok, P. Kuzhir, S. Maksimenko, P. Angelova, E. Ivanov, and R. Kotsilkova, “Frequency and density dependencies of the electromagnetic parameters of carbon nanotube and graphene nanoplatelet based composites in the microwave and terahertz ranges,” *Materials Research Express*, vol. 6, no. 9, p. 095 050, Jul. 3, 2019, Publisher: IOP Publishing.
- [O4] **G. Gorokhov**, M. Katsemba, A. Liubimau, A. Lobko, and A. Melnikau, “Specifics of 3D-printed electronics,” in *Engineering of Scintillation Materials and Radiation Technologies*, M. Korzhik and A. Gektin, Eds., vol. 227, Series Title: Springer Proceedings in Physics, Cham: Springer International Publishing, 2019, pp. 315–326.

LIST OF CONFERENCE PRESENTATIONS

- [C1] **G. Gorokhov**, D. Bychanok, D. Meisak, I. Shlyk, A. Liubimau, P. Angelova, E. Ivanov, R. Kotsilkova, M. Casa, and P. Kuzhir, “Electromagnetic properties of carbon-based polymer materials for 3D-printing applications,” in *Fundamental and Applied NanoElectroMagnetics II: THz circuits, materials, devices, FANEM-2018*, Minsk, Belarus, Jun. 5, 2018, p. 40.
- [C2] **Gleb Gorokhov**, Dzmitry Bychanok, Darya Meisak, Ivan Shlyk, Aliaksandr Liubimau, Polya Angelova, Evgeni Ivanov, Rumiana Kotsilkova, Marcello Casa, Paolo Ciambelli, and Polina Kuzhir, “Carbon nanotubes vs graphene nanoplatelets for 3D-printable composites,” in *International Conference of Functional Materials and Nanotechnologies FM&NT-2018 book of abstracts*, Riga, Latvia, Oct. 2, 2018, p. 109.
- [C3] Darya Meisak, Dzmitry Bychanok, Lizaveta Shashkova, **Gleb Gorokhov**, Jan Macutkevic, Evgeni Ivanov, Rumiana Kotsilkova, and Polina Kuzhir, “Influence of aluminosilicate hollow microspheres on the electromagnetic properties of MWCNT / PLA composites,” in *International Conference of Functional Materials and Nanotechnologies FM&NT-2018 book of abstracts*, Riga, Latvia, Oct. 2, 2018, p. 198.
- [C4] **Gleb Gorokhov**, Jan Macutkevic, Juras Banys, Dzmitry Bychanok, Polina Kuzhir, Thomas Ballweg, Karl Mandel, Vanessa Fierro, and Alain Celzard, “Water spheres array for electromagnetic shielding applications,” in *43-ioji Lietuvos nacionalinė fizikos konferencija. Programa ir pranešimų tezės*, Kaunas, Lithuania: KTU leidykla "Technologija", Oct. 3, 2019, p. 195.
- [C5] **G. Gorokhov**, D. Bychanok, P. Kuzhir, J. Macutkevic, J. Banys, D. Gorodetskiy, A. Kurennya, O. Sedelnikova, L. Bulusheva, and A. Okotrub, “Method of laser structuring of multiwall nanotube arrays for terahertz applications,” in *Functional Materials and Nanotechnologies Abstract book*, Virtual Vilnius, Lithuania, Oct. 23, 2020, p. 84.

- [C6] **Gleb Gorokhov**, Alexander Zharov, Jan Macutkevic, Thomas Ballweg, Vanessa Fierro, Dzmitry Bychanok, Polina Kuzhir, and Alain Celzard, “Microwave properties of hollow carbon spheres with different electrical conductivities,” in *INTERACTION OF RADIATION WITH SOLIDS Proceedings of the 14th International Conference Dedicated to the 100th anniversary of the Belarusian State University*, Minsk, Belarus: Belarusian State University, Sep. 21, 2021, pp. 247–249.
- [C7] D. Meisak, J. Macutkevic, D. Bychanok, **G. Gorokhov**, and P. Kuzhir, “Electromagnetic properties of $\text{Fe}_2\text{O}_3\text{H}_2\text{O}$ -based polymer materials,” in “*Fundamental and Applied NanoElectroMagnetics II: THz circuits, materials, devices, FANEM-2018*”, Minsk, Belarus, Jun. 5, 2018, p. 48.
- [C8] **G. Gorokhov**, D. Bychanok, D. Meisak, I. Shlyk, A. Liubimau, P. Angelova, E. Ivanov, R. Kotsilkova, M. Casa, P. Ciambelli, and P. Kuzhir, “Carbon nanocomposites for 3D-printing applications,” in *Modern nanotechnologies and nanophotonics for science and industry*, Suzdal, Russia: Vladimir State university, Nov. 8, 2018, p. 34.
- [C9] D. Meisak, D. Bychanok, **G. Gorokhov**, J. Macutkevic, J. Banys, and P. Kuzhir, “Electromagnetic properties of polymer MWCNT-based composites with aluminosilicate hollow microspheres,” in *Modern nanotechnologies and nanophotonics for science and industry*, Suzdal, Russia: Vladimir State university, Nov. 8, 2018, p. 31.
- [C10] **G. V. Gorokhov**, D. S. Bychanok, P. P. Kuzhir, J. Macutkevic, H. Xia, and M. Lavorgna, “Electromagnetic properties of porous nanocarbon structures created by means of SLS 3D printing,” presented at the Graphene. Molecule and 2D-crystal, Novosibirsk, Russia, Aug. 5, 2019.

Scientific projects

The investigations included in the current work were conducted in frames of the following scientific projects:

- Horizon 2020 RISE project 734164 Graphene 3D;
- The Academy of Finland (Flagship Programme, Photonics Research and Innovation (PREIN), number 320166, and project number 334370);
- National Key R&D Program of China (2017YFE01115000);
- Horizon 2020 RISE project 823728 DiSeTCom;

1. LITERATURE REVIEW

1.1. Interaction of radiation with dielectric medium

In order to give the proper description to the electromagnetic radiation interaction with medium it is necessary to start with the Maxwell equations, which are introducing the electromagnetic field [155] (hereafter the SI units will be used):

$$\nabla \cdot \vec{D} = \rho, \quad (1.1)$$

$$\nabla \cdot \vec{B} = 0, \quad (1.2)$$

$$\nabla \times \vec{E} = -\frac{\partial \vec{B}}{\partial t}, \quad (1.3)$$

$$\nabla \times \vec{H} = \vec{j} + \frac{\partial \vec{D}}{\partial t}, \quad (1.4)$$

where ρ is the density of electric charge, \vec{j} is the current density, \vec{E} and \vec{H} — the electric and magnetic fields, \vec{D} is the electric displacement vector, \vec{B} is the magnetic induction.

The EM field propagation inside the media is introduced by the material equations which are required to consider the

$$\vec{j} = \sigma \vec{E}, \quad (1.5)$$

$$\vec{D} = \varepsilon \varepsilon_0 \vec{E}, \quad (1.6)$$

$$\vec{B} = \mu \mu_0 \vec{H}. \quad (1.7)$$

Here, σ is the conductivity, ε_0 and μ_0 are the vacuum permittivity and permeability, respectively. In the case of isotropic and homogeneous media the mentioned values are scalar. The complex value of ε and μ are the relative permittivity and permeability of medium. The real part of permittivity, ε' , corresponds to the energy storage capacity of a material, and the imaginary part (or sometimes, the loss factor), ε'' , is a measure of all dissipation effects in a material (see Sections 1.2.2.1 and 1.3.1 in [156] for further reference).

In the absence of charges ($\rho = 0$), ($\vec{j} = 0$) the Equations 1.1–1.4 are reduced to the following:

$$\nabla \cdot \vec{D} = 0, \quad (1.8)$$

$$\nabla \cdot \vec{B} = 0, \quad (1.9)$$

$$\nabla \times \vec{E} + \frac{\partial \vec{B}}{\partial t} = 0, \quad (1.10)$$

$$\nabla \times \vec{H} - \frac{\partial \vec{D}}{\partial t} = 0, \quad (1.11)$$

Combining the Equations 1.10 and 1.11 with an account of $\nabla \cdot \vec{D} = 0$, $\nabla \cdot \vec{B} = 0$ one may obtain the following wave equations for each axis:

$$\nabla^2 u - \frac{1}{v^2} \frac{\partial^2 u}{\partial t^2} = 0, \quad (1.12)$$

where:

$$v = \frac{c}{\sqrt{\varepsilon\mu}} \quad (1.13)$$

is the speed of light inside the medium. The solution of Equation 1.12 may be obtained in a form of a plane wave propagating along X axis specified by the following expression:

$$u = e^{ik \cdot x - i\omega t}, \quad (1.14)$$

where the angular frequency ω and the wave vector k are connected by the following relation:

$$k = \frac{\omega}{v} = \sqrt{\varepsilon\mu} \frac{\omega}{c}. \quad (1.15)$$

The analytical models applied in this work are based on the plane wave. The representation of wave vector k varies depending on the specific case such as the rectangular or coaxial waveguides which are used for electromagnetic measurements in microwave range.

1.2. The electromagnetic response concept

Let us understand the *electromagnetic response* as the way of interaction between the physical object (i.e. the sample under investigation) and electromagnetic radiation. The aim of electromagnetic response measurements may be either obtaining the data needed for the calculation of material's intrinsic *electromagnetic properties* (i.e. dielectric permittivity and conductivity, magnetic permeability) or investigation of the electromagnetic response itself (also referred as extrinsic parameters of the medium) [156]. The latter usually means the investigation of shielding effectiveness, reflection or absorption loss and other properties of a particular structure. However, initially all information obtained from the measurements is corresponding to the particular specimen with its spatial dimensions. Therefore, the establishing of intrinsic electromagnetic properties requires further calculations.

1.2.1. Complex impedance as a representation of the electromagnetic response

The piece of medium interacting with the EM field may be represented as a circuit, which includes such elements as resistors, capacitors and coils, i.e. possessing the resistance, capacitance and inductance. The possible representations of such systems are depicted in the Figure 1.1.

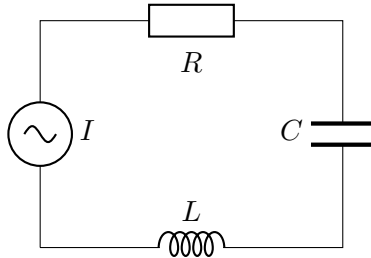


Figure 1.1: a sample of RLC circuit.

The full resistance of the depicted circuit (i.e. the *complex impedance*) may be written as:

$$|Z| = \sqrt{R^2 + (\omega L - 1/\omega C)^2}. \quad (1.16)$$

The impedance value $Z = Z' + iZ''$ may be divided into $Z' = R$, or active resistance and $Z'' = \omega L - 1/\omega C$ or reactive resistance. The active resistance is corresponding to Joule heat, while the reactive causes the phase shift between the current and voltage:

$$\operatorname{tg} \varphi = \frac{\omega L - 1/\omega C}{R}. \quad (1.17)$$

Such consideration is applied not only for low-frequency impedance spectroscopy, which is of great importance for characterization of percolation processes in composite materials, but even at microwave frequencies. Such electromagnetic response characteristics as the reflection loss, etc. are easily derived from the impedance representation.

1.2.2. Electromagnetic response representation with scattering parameters

In the high-frequency measuring apparatus the source or the drain of electromagnetic wave is called a *port*. Depending on the device construction, the port may be a EM wave source, detector or play both roles simultaneously. According to the data collected by ports, the device may be called scalar (measuring only the wave amplitude) or vector (registering both the amplitude and the phase) network analyzer, referred as SNA and VNA respectively. The most of SNA or VNA devices contain 2 ports because usual measurement techniques require at least two ports [157]. However, it will be noticed further that in the case of vector signal measurement the one port combining emitter and detector is enough for dielectric permittivity measurements.

There are several different representations of EM response. The most common approach is the use of so-called scattering parameters or *S-parameters*. It is conventional to refer the scattering parameters by combination of ports numbers as S_{ab} where a and b are the detecting and emitting ports numbers, respectively. If the port 1 is active (i.e. a source of EM wave) and the port 2 is a passive detector, the relative amplitude of reflected and transmitted signals will be referred as S_{11} and S_{21} , respectively.

The reflection, transmission and absorption coefficients related to the reflected, transmitted or absorbed power relative to the initial 1power

value are derived from the scattering parameters in the following way:

$$R = S_{11}^2, \quad (1.18)$$

$$T = S_{21}^2, \quad (1.19)$$

$$R + T + A = 1. \quad (1.20)$$

Here the scattering parameters are given in arbitrary units. Such representation is very intuitive, however less applied in engineering community.

1.3. Electromagnetic shielding effectiveness

Another widely used representation of electromagnetic response is the *EMI shielding effectiveness* usually given in decibels [158, 159]:

$$\text{EMI SE(dB)} = \text{SE}_R + \text{SE}_A, \quad (1.21)$$

$$\text{SE}_A(\text{dB}) = -10 \log \frac{S_{21}^2}{1 - S_{11}^2}, \quad (1.22)$$

$$\text{SE}_R(\text{dB}) = -10 \log(1 - S_{11}^2). \quad (1.23)$$

Here, the EMI SE is the total shielding effectiveness, SE_R and SE_A are its reflective and absorptive components. Such representation is required by the tasks of electromagnetic compatibility.

1.4. Effective medium theory

Considering the interaction of EM wave with a heterogeneous material containing inclusions which characteristic dimensions and distances between them are orders less than the incident radiation wavelength, the structural parameters of material may be, to a certain degree, neglected. The material is represented as a quasi-homogeneous *effective medium* possessing its own *effective* macroscopic parameters. There are several effective medium approaches such as widely used Maxwell Garnett, Landau-Lifshitz/Looyenga, Bruggeman and more [160], which applicability depends on the properties of heterogeneous medium.

The most popular effective medium approaches, such as Maxwell Garnett and Bruggeman theories, are based on the representation of inclusions as ellipsoids with particular polarization [161, 162].

1.4.1. Maxwell Garnett theory

The effective medium theory introduced by James Clerk Maxwell Garnett near 1904 [163] widely used for composite materials of matrix type [83] (i.e. one of the phases is consistent and the volume fraction of the latter phases is not exceed 15 vol. % [160]). Let us consider the composite consist of a matrix and single filler with $f_1 < 0.15$ volume fraction of spherical particles. The permittivities of filler and matrix are ϵ_1 and ϵ_2 respectively. Any given region of a composite containing several filler particles (Figure 1.2a) will possess the effective dielectric permittivity ϵ_{eff} .

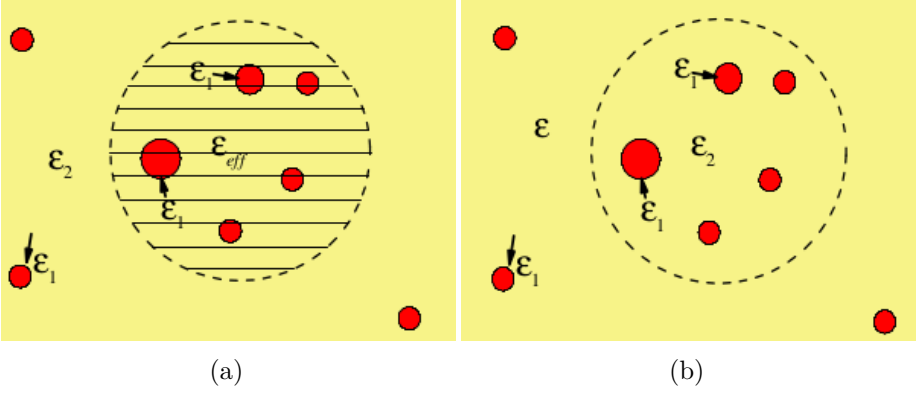


Figure 1.2: Illustration for Maxwell Garnett effective medium model.

In such case the spherical region depicted in Figure 1.2a may be considered as a sphere placed in the medium with ϵ in uniform electric field $\langle \vec{E} \rangle$ (Figure 1.2b). Therefore the spherical region will possess the following polarization.

$$\vec{P} = 3\epsilon_0 \frac{\epsilon_{eff} - \epsilon}{\epsilon_{eff} + 2\epsilon} \langle \vec{E} \rangle. \quad (1.24)$$

From the other hand, the polarization of the spherical region consists of all inclusions polarizations:

$$\vec{P} = \frac{1}{V} \sum_k 3\epsilon_0 \frac{\epsilon_1 - \epsilon}{\epsilon_1 + 2\epsilon} \langle \vec{E} \rangle \Delta V_k, \quad (1.25)$$

or:

$$\vec{P} = 3\epsilon_0 f_1 \frac{\epsilon_1 - \epsilon}{\epsilon_1 + 2\epsilon} \langle \vec{E} \rangle, \quad (1.26)$$

where:

$$f_1 = \frac{1}{V} \sum_k \Delta V_k \quad (1.27)$$

is the volume fraction of inclusions and k . Combining the Equations 1.24 and 1.27 one may obtain the Maxwell Garnett equation for the effective dielectric permittivity:

$$\frac{\varepsilon_{eff} - \varepsilon}{\varepsilon_{eff} + 2\varepsilon} = f_1 \frac{\varepsilon_1 - \varepsilon}{\varepsilon_1 + 2\varepsilon}; \quad (1.28)$$

In the case of $f_1 \rightarrow 0$ the previous equation transforms into

$$\varepsilon_{eff} = \varepsilon + 3 \cdot f_1 \frac{\varepsilon(\varepsilon_1 - \varepsilon)}{\varepsilon_1 + 2\varepsilon}; \quad (1.29)$$

The Equations 1.28–1.29 are introduced for the spherical inclusions. In the case of elliptic filler particles with semiaxes $a \neq b = c$, i.e. spheroidal particles the Equation 1.28 may be generalized as:

$$\frac{\varepsilon_{eff} - \varepsilon}{N(\varepsilon_{eff} - \varepsilon) + \varepsilon} = f_1 \frac{\varepsilon - \varepsilon_1}{\varepsilon + N(\varepsilon_1 - 2\varepsilon)}; \quad (1.30)$$

where N_{\parallel} and N_{\perp} are the depolarization factors along and normal to the spheroid rotation axis, respectively:

$$N_{\parallel} = \frac{1}{1 - (a/b)^2} \cdot \left(1 - \frac{a}{b} \cdot \frac{\arcsin(\sqrt{1 - (a/b)^2})}{\sqrt{1 - (a/b)^2}} \right) \quad (1.31)$$

$$N_{\parallel} + 2N_{\perp} = 1 \quad (1.32)$$

The a/b ratio is called an *aspect ratio*. Depending on that parameter and another properties of filler particles (i.e. material anisotropy) the depolarization factors may be formulated in different ways, however, the approximation will be applicable as long as the volume fractions of filler particles are relatively low. The more detailed view of the depolarization factors for prolate and oblate spheroids are given in the Section 2.2.1.

1.4.2. Bruggeman effective medium theory

The theory, developed by D.A.G. Bruggeman near 1935 [164], or the effective medium theory, EMT is applicable in the case when the volume

fractions of phases are close and it is impossible to consider any phase of a composite as matrix. In the formalism of volume fractions that means f_1 and f_2 are close. In the Figure 1.3a the medium containing two sorts of overlapping spheres with the dielectric permittivities ε_1 and ε_2 is shown.

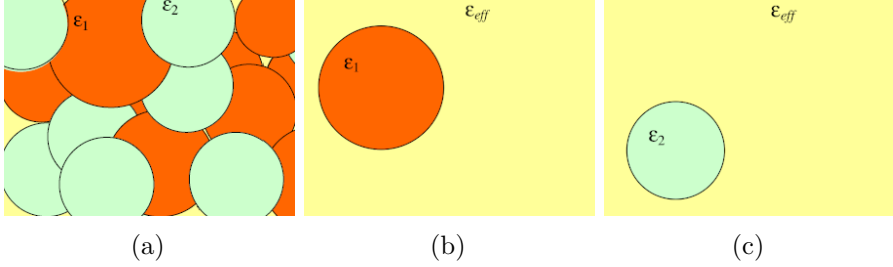


Figure 1.3: Illustration for Bruggeman effective medium model.

Similarly to the Maxwell Garnett model, each inclusion is considered as placed in an effective medium with dielectric permittivity ε_{eff} (Figures 1.3b,c). In such an assumption the electric field inside each sphere with ε_i may be written as:

$$\vec{E}_i = \frac{3\varepsilon_{eff}}{2\varepsilon_{eff} + \varepsilon_i} \langle \vec{E} \rangle. \quad (1.33)$$

The average field along the whole medium may be written as:

$$\langle \vec{E} \rangle = \sum_i f_i \vec{E}_i, \quad (1.34)$$

or, in the case of two components (i.e. $f_1 + f_2 = 1$):

$$\langle \vec{E} \rangle = f_1 \vec{E}_1 + f_2 \vec{E}_2 = \frac{3\varepsilon_{eff}}{2\varepsilon_{eff} + \varepsilon_1} \langle \vec{E} \rangle + \frac{3\varepsilon_{eff}}{2\varepsilon_{eff} + \varepsilon_2} \langle \vec{E} \rangle \quad (1.35)$$

or:

$$f_1 \frac{3\varepsilon_{eff}}{2\varepsilon_{eff} + \varepsilon_1} + f_2 \frac{3\varepsilon_{eff}}{2\varepsilon_{eff} + \varepsilon_2} = 1. \quad (1.36)$$

which is a Bruggeman equation for spherical particles, which also may be written likewise to Maxwell Garnett approach (Equation 1.29):

$$f_1 \frac{\varepsilon_1 - \varepsilon_{eff}}{2\varepsilon_{eff} + \varepsilon_1} + f_2 \frac{\varepsilon_2 - \varepsilon_{eff}}{2\varepsilon_{eff} + \varepsilon_2} = 1. \quad (1.37)$$

The generalization for ellipsoidal particles done in the same manner as the Equation 1.30:

$$f_1 \frac{\varepsilon_1 - \varepsilon_{eff}}{\varepsilon_{eff} + N(\varepsilon_1 - \varepsilon_{eff})} + f_2 \frac{\varepsilon_2 - \varepsilon_{eff}}{\varepsilon_{eff} + N(\varepsilon_2 - \varepsilon_{eff})} = 1, \quad (1.38)$$

allows to consider the anisotropic non-matrix composite systems. Considering the similarity between Maxwell Garnett and Bruggeman approaches it is possible to consider the first as a special case of the last.

However, there is significant difference in the physical systems to which the mentioned models are applicable. While the usual objects of Maxwell Garnett approach application are the composites with polymer matrix, the Bruggeman theory is more applicable for ceramic composites containing several phases of comparable contents, which dielectric or thermal parameters are dependent on the ceramics stoichiometry [165–167].

1.4.3. Landau-Lifshitz/Looyenga theory

The previously explained approaches are based on the particles polarizability. However, for certain class of composite systems, which phases possess the close permittivity values, another approach was introduced by Landau and Lifshitz [168] and, independently, Looyenga [169]. Today it is commonly referred as *LLL-theory*. The effective dielectric permittivity value according to LLL-theory is:

$$\varepsilon_{eff}^{1/3} = \sum_i^N f_i \varepsilon_{eff}^{1/3}. \quad (1.39)$$

The introduced approach allows to evaluate the ε_{eff} without exact knowledge about the geometry of system components. At the same time, it is limited to the case when the dielectric permittivity at any given point $\varepsilon(\vec{r})$ is close to the average permittivity $\langle \varepsilon \rangle$. Such limitations are met in low-density porous materials. Therefore, LLL theory allows to investigate the properties of stochastic foams [170], aerogels and granular materials, etc. [171] and even for absorbed moisture control in composite materials [172].

2. EXPERIMENTAL TECHNIQUES

2.1. Materials

2.1.1. Synthesis of thermoplastic polymer composites with nanocarbon inclusions

Among the wide range of methods used for the thermoplastic nanocomposites preparation [53] the melt-mixing is attractive due to its simplicity, repeatability and scalability. According to its name, the principle of melt-mixing is based on the nanoscale filler introduction into the polymer during its melting and mixing inside the extruder (Figure 2.1). The extruder has several regions with different thermal conditions and screws geometry intended to mix and convey the polymer pellets; melt and steer the polymer and filler particles; pump the mixture to the extrusion nozzle. Varying the nozzle configuration and using additional machines (roll mill, calibrated drawholes, etc.) it is possible to obtain different types of final product: pellets, films, filaments and so on.

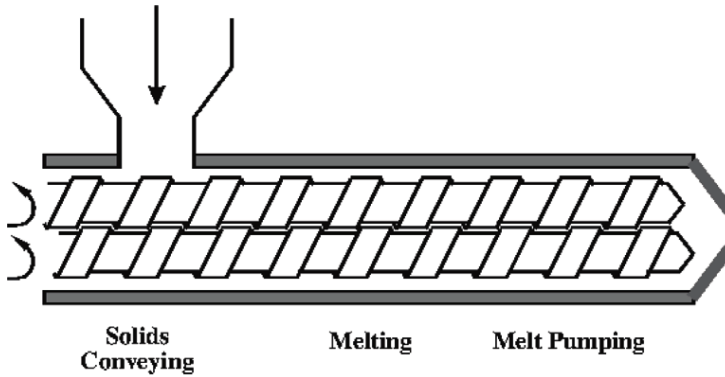


Figure 2.1: The scheme of twin-screw extruder [173].

The polymer matrix used in this study was IngeoTM Biopolymer PLA-3D850 (Nature Works, Minnetonka, MN, USA). The nanofillers used were: commercially available industrial graphene nanoplates, TNIGNP (supplied by TimeNano, Chengdu, China), with 90 wt. % purity; number of layers < 30; thickness < 30 nm; diameter/median size 5–7 μm ; aspect ratio: $\sim 230/165$; and volume resistivity < 0.15 Ohm-cm. Industrial grade

OH-functionalized carbon nanotubes (multi-walled carbon nanotubes; MWCNTs; TimeNano, produced by CVD method) with 95 wt. % purity; 2.48 % OH⁻ content; outer diameter = 10–30 nm, 10–30 µm length; aspect ratio: ~1000; and 100 S/m electric conductivity. A high amount of GNP impurities has an insufficient impact on the PLA composite processing due to the slip effect between GNPs in the PLA matrix during the shear flow [174]. Impurities mostly consist of amorphous carbon; thus their impacts on the electromagnetic properties may be neglected.

Twin-screw extruder (COLLIN Teach-Line ZK25T) was used to prepare nanocomposites at temperatures of 170–180 °C and screw speed 40 rpm in two runs. The mono- and bi-filler nanocomposite hybrids were processed using the melt extrusion method, which includes the preparation of master batches, and further dilution. It was previously shown that both GNP and MWCNT addition significantly suppress the thermal degradation and the aging of polymer nanocomposites (accelerated by humidity uptake, UV light, etc.), compared to the neat PLA, due to the nucleation and the barrier effects of nanofillers [42].

The composites containing a single filler (MWCNT or GNP) with 1.5 wt. %, 3 wt. % and 6 wt. % filler contents, and the hybrid composites (containing PLA, MWCNT and GNP simultaneously) with 3 wt. % and 6 wt. % of total filler content (combining GNP and MWCNT in different proportions) were prepared. Thin films of nanocomposites were obtained by hot pressing at 180 °C and pressure of 1 bar. Before pressing the test samples, composite pellets were dried in a vacuum oven at 80 °C for 4 hours in order to minimize the humidity uptake. The applied temperature range was significantly lower than the PLA thermal degradation onset (230 °C). The physicochemical characteristics of the PLA-based carbon nanocomposites under investigation are given in Table 2.1. Composites' crystallinity was 30 %.

2.1.2. Preparation of segregated CNT/GNP/polyurethane media for SLS 3D printing

Nanocomposite powder preparation

The method of SLS-compatible composite powder preparation directly determines the dispersion of nanofillers in the polymer matrix, and this affects the structural and functional properties of the SLS-printed

Table 2.1: Physicochemical characteristics of synthesized polymer composites after hot pressing [42, 102].

Parameter	Value
Glass transition temperature T_g , °C	65
Cold crystallization temperature T_{cc} , °C	87–92
Melting temperature T_m , °C	175
Melt crystallization temperature T_g , °C	105
Crystallinity, %	30

structures. Two types of composites were prepared on the basis of TPU powder (Mophene3D T90A, Nanjing, China): one composite contained 1 wt. % of MWCNTs (NANOCYL 7000, Nanocyl, Sambreville, Belgium), another contained the mentioned nanotubes and graphene (The Sixth Element Materials, Changzhou, China) with a ratio of 70/30 by weight.

Both fillers were pre-dispersed by a wet ball milling process according to the technology introduced in [175]. The fillers were put into the milling jars with iron balls and milled for 1 h at a speed of 300 rpm. Then dispersed fillers were mixed with anhydrous ethanol and ultrasonicated at 40 W for 1 h in order to obtain a stable nanoparticles dispersion. The TPU powder was then added to the nanofillers suspensions, in such an amount to obtain a final filler content of 1 wt. %, and subjected to mechanical stirring for 2 h. The resulting mixture was filtered with a Buchner funnel under reduced pressure and dried in a vacuum oven at 70 °C for 24 h. Afterwards, the TPU/MWCNT-GNP powders were sieved to remove particles with a size above 150 μm , and silica powder was added to further improve the powder flowability. For a comparative experiment, the control sample TPU/MWCNTs composite powder (Mophene3D CT90A, Nanjing, China) was used as received.

Selective laser sintering of nanocomposite powders

Nanocomposites were obtained in the form of powder applicable for the selective laser sintering (SLS) 3D printing technology. Such method is less distributed than FDM printing, but allows better detalization of printed objects. The principle of SLS printer functioning is based on layer-by-layer sintering of powder material by computer-controlled laser [103, 141, 176].

The CAD models of specimens were generated using the Rhinoceros CAD software (Robert McNeel & Associates, WA, USA.), and exported in the STL format for uploading into the SLS machine. The SLS process was performed on a lab-scale SLS equipment (Sharebot-SnowWhite, Lecco, Italy [177]). Mentioned 3D printer is able to work with only ~ 300 g of powder, which is convenient for experimental applications. Due to the obvious difference in viscosity, thermal conductivity and other parameters between the pure TPU and nanocomposites the sintering conditions had to be optimized. In order to process the nanocomposite powder, the laser was set at 40 % of the maximum energy. The final set of processing parameters for TPU/MWCNTs and TPU/(MWCNTs-GE) is introduced in the Table 2.2.

Table 2.2: Sintering parameters adopted to process the nanocomposite powders (TPU/MWCNT and TPU/MWCNT-GE [43]).

Processing parameter	Value
Laser power, (W)	14
Laser scan spacing, (μm)	200
Laser scan speed, (pps)	175
Part bed temperature, ($^{\circ}\text{C}$)	85
Outline laser power, (W)	5.6
Layer thickness, (μm)	100

The manufactured structures were allowed to cool inside the machine process chamber for approximately 1 h and then they were removed from the part bed. Excess of powder surrounding the structure and non-sintered powder from the interstices were removed by compressed air.

2.1.3. Synthesis of MWCNT vertically-aligned arrays

The standard experimental technique, namely aerosol-assisted catalytic chemical vapor deposition (CCVD) [114, 115, 178, 179], was used for vertically aligned MWCNT arrays growth. The polished silicon wafers of 100 symmetry were used as a substrate. The mentioned type of symmetry allows the rectangular substrates to be easily cut.

A set of substrates was placed into the tubular oven of a chemical reactor (Figure 2.2) constantly flowed with argon at 18 l/h flow ratio and heated at 800 $^{\circ}\text{C}$. The outlet of a tubular oven remained open in

order to keep the atmospheric pressure inside the reactor. The synthesis was carried out using 2 % ferrocene ($\text{Fe}(\text{C}_5\text{H}_5)_2$) solution in toluene ($\text{C}_6\text{H}_5\text{CH}_3$). As a result, with the use of 2.5 ml of the reaction mixture an aligned MWCNT array of $\sim 250 \mu\text{m}$ height was obtained.

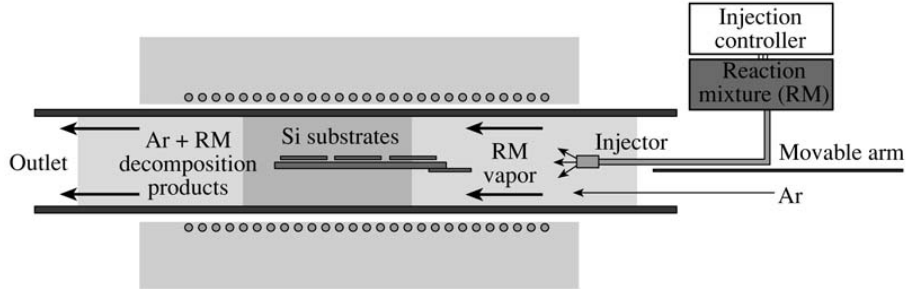


Figure 2.2: Scheme of chemical reactor for aerosol-assisted CCVD synthesis of vertically-aligned MWCNT arrays [114].

To examine the morphology of MWCNTs, the pristine sample was investigated by transmission electron microscopy (TEM) using a JEOL 2010 microscope. TEM image of obtained MWCNTs is shown at Fig. 2.3. Average diameter of nanotubes is $\sim 6 \text{ nm}$.

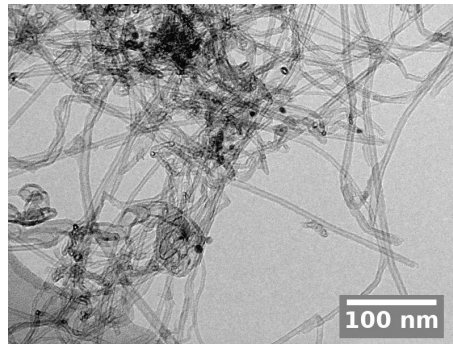


Figure 2.3: TEM image of carbon nanotubes obtained by CCVD method.

2.1.4. Preparation of periodical structures based on MWCNT arrays

The vertically oriented MWCNT arrays created by means of CVD method (see the Section 2.1.3 for reference) were transformed to the periodic arrays of pyramids by means of laser engraving machine with numerical

control. The industrial laser engraver (Winseal, China) with 20 Wt CO₂ laser and 20 mm/s scanning speed was used. The grating period was 250 μm .

To study the structure of the engraved sample and to prove the preservation of nanotubes after the laser treatment, the obtained sample was investigated by scanning electron microscopy (SEM) using a JEOL JSM 6700F microscope. The SEM images of engraved pyramids are presented in Fig. 2.4. It is worth noting that the initial structure of vertically-oriented MWCNT array remained untouched after the engraving operation.

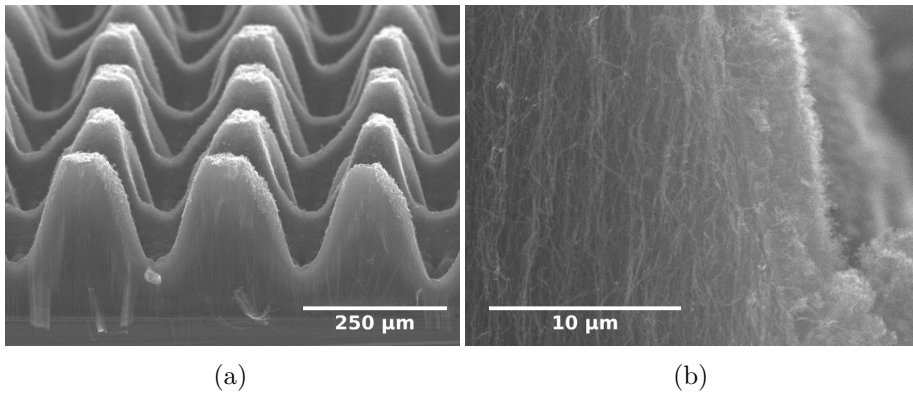


Figure 2.4: (a) Periodic array of CNT-based pyramids; (b) the CNT array structure was not harmed during the laser engraving.

After the engraving array of pyramids was covered with epoxy resin in order to protect its fragile structure. The viscous epoxy resin (Crystal 76) with curing agent added was drop-casted on the engraved structure and then spread over the engraved surface under the vacuum. The general view of structures after covering with the epoxy resin is presented in Fig. 2.5.

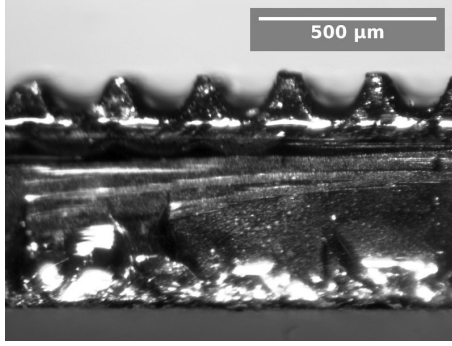


Figure 2.5: Optical microscopy image of engraved MWCNT arrays covered with epoxy resin. Total height of pyramids after all manipulations was $232.9 \pm 11.9 \mu\text{m}$ with $54.9 \pm 6.9 \mu\text{m}$ uncut layer at the bottom. Maximal thickness of epoxy resin in the area between pyramids was $77.0 \pm 4.5 \mu\text{m}$.

2.2. Modeling

2.2.1. Maxwell Garnett effective medium theory application for carbon-based nanocomposites

One of the well-known approaches to describe the electromagnetic properties of a micro- or nanocomposite material is to apply the effective medium theory. In the case when the filler concentration is lower than the percolation threshold, i.e., filler particles are not interacting, the Maxwell Garnett (MG) effective medium theory is applied [83, 160]. This approach assumes the filler particles as ellipsoids with semiaxes a, b, c , and the following polarizability:

$$\alpha_i(\nu, \sigma) = \frac{4\pi abc}{3} \frac{\varepsilon_m \left(1 - \frac{i\sigma}{2\pi\nu\varepsilon_0} - \varepsilon_m\right)}{\varepsilon_m + N_i \left(1 - \frac{i\sigma}{2\pi\nu\varepsilon_0} - \varepsilon_m\right)}, \quad (2.1)$$

where σ is the ellipsoid conductivity; $\varepsilon_0 = 8.85 \cdot 10^{-12}$ F/m is the vacuum permittivity; N_i is the depolarization factor in direction $i = a, b, c$ which is given as:

$$N_i = \frac{1}{abc} \int_0^\infty \frac{ds}{(s + i^2) \sqrt{(s + a^2)(s + b^2)(s + c^2)}}. \quad (2.2)$$

Considering the above, the effective dielectric permittivity of composite material based on dielectric matrix with permittivity ε_m including uni-

formly distributed and randomly oriented equal ellipsoids with volume concentration n is:

$$\varepsilon_{eff} = \varepsilon_m + \frac{1/3 \sum_{i=a,b,c} n\alpha_i/V}{1 - 1/3 \sum_{i=a,b,c} \frac{N_i n\alpha_i/V}{\varepsilon_m}}, \quad (2.3)$$

where ε_m is the dielectric matrix permittivity; n is the volume concentration of filler.

It is possible to show (see the example in Figure 2.6) that the imaginary part of polarizability calculated by Equation (2.1) exhibits a maximum at the critical frequency (Equation (2.4)). Therefore, the imaginary part of permittivity will experience the similar peak.

$$\nu_c = \frac{N_i\sigma}{2\pi\varepsilon_0(\varepsilon_m - N_i\varepsilon_m + N_i)}. \quad (2.4)$$

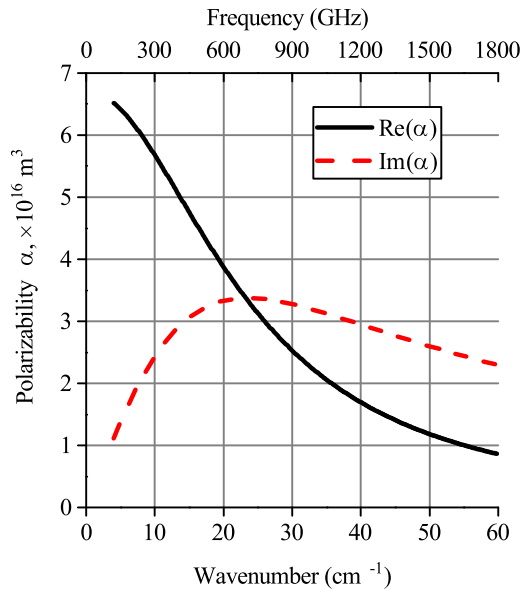


Figure 2.6: Frequency dispersion of the longitudinal polarizability calculated for oblate ellipsoid with $a = b = 5 \mu\text{m}$, $c = 25 \text{ nm}$ (i.e., $\text{AR} = 200$), $\sigma = 10000 \text{ S/m}$ and $\varepsilon_m = 2.5 - 0.1i$.

The dependence shown in Figure 2.6 is given with an assumption that $\sigma = \sigma_{DC} = \text{const}$. However, it is known that the conductivity depends on frequency by the Drude's law. A certain frequency-dependent impact may

be also given by non-uniform field distribution inside the filler particles due to the skin effect and/or the field scattering on the particles [83].

Considering the composites with conductive nanoscale inclusions, which dimensions are orders smaller than both the skin depth and the radiation wavelength, the latter two effects are negligible, whereas the impact of Drude conductivity needs a more detailed description. According to the Drude's law the filler's conductivity is written as:

$$\sigma_f(\nu) = \frac{\sigma_{DC}}{1 - i2\pi\nu\tau_f} \quad (2.5)$$

where i is the imaginary unit, σ_{DC} is the conductivity of filler at direct current and τ_f is the relaxation time of filler's material, which dependence on DC conductivity is similar to the Equation 2.4:

$$\frac{1}{\tau_f} = \frac{\sigma_f}{2\pi\varepsilon_0}. \quad (2.6)$$

The nanocarbon fillers considered in this thesis possess huge DC conductivity, therefore the order of $1/\tau_f$ value will be of tens to hundreds THz [180]. Thus, for the case of current investigation the term $2\pi\nu\tau_f$ is negligible and the σ in Equation 2.3 may be considered as frequency-independent.

2.2.2. Regular porous structures based on tri-periodic minimal surface equations

Tri-periodic porous geometry

Regular periodic structures of high porosity are of great interest for different applications such as electromagnetic absorbers and shields, lightweight passive elements of microwave circuits or THz optics and so on. An effective approach to model the 3D porous structure is to create a spatial region restricted by one of triply periodic minimal surfaces (TPMS). In the scope of current investigation the 3 porous geometries were discussed: Diamond (Equation 2.7), Gyroid (Equation 2.8) and

Schwarz (Equation 2.9) (further mentioned as D, G and S respectively).

$$\begin{aligned} \textbf{Diamond:} \quad & \sin x \sin y \sin z + \sin x \cos y \cos z + \\ & + \cos x \sin y \cos z + \cos x \cos y \sin z > C \end{aligned} \quad (2.7)$$

$$\textbf{Gyroid:} \quad \sin x \cos y + \sin y \cos z + \sin z \cos x > C \quad (2.8)$$

$$\textbf{Schwarz:} \quad \cos x + \cos y + \cos z > C \quad (2.9)$$

where C is the offset factor related to the structure porosity. The correlation between porosity P and C is linear $P = a \cdot C + b$, where a and b values dependent on the TPMS type given in Table 2.3. Hereafter we will refer the structure of a particular geometry and porosity as AX, where A is D, G, or S, and X is porosity in percents. For example, G60 means a body of gyroidal geometry with 60 % porosity.

Table 2.3: Proportional coefficients of porosity P linear dependence on the offset factor C for different TPMS [55].

TPMS geometry type	a	b
Diamond	41.2	50.8
Gyroid	31.1	51.1
Schwarz	27.1	51.7

The images of D, G and S unit cells are given in Figure 2.7. It can be seen that the Schwarz unit cell looks "more bulk" than other geometries under investigation. Indeed, if the density fluctuations along z axis will be calculated, the Schwarz geometry will give the most pronounced fluctuation at the single unit cell (see Figure 2.8). As long, as TPMS geometries are given by trigonometric functions, the density fluctuations will be expected to follow harmonic laws [181], which means the material density, permittivity and other parameters of bulk materials will be harmonically distributed inside the TPMS. However, it may be more or less pronounced. While the values of Schwarz geometry density¹ varies from ~ 0.1 to ~ 0.75 , Diamond and Gyroid possess the lower density fluctuations (Figure 2.8a). Moreover, in the case of 50 % porosity the density fluctuations vanishes for D and G geometries (Figure 2.8b).

¹here we assume the density as a relative volume of the space occupied with material

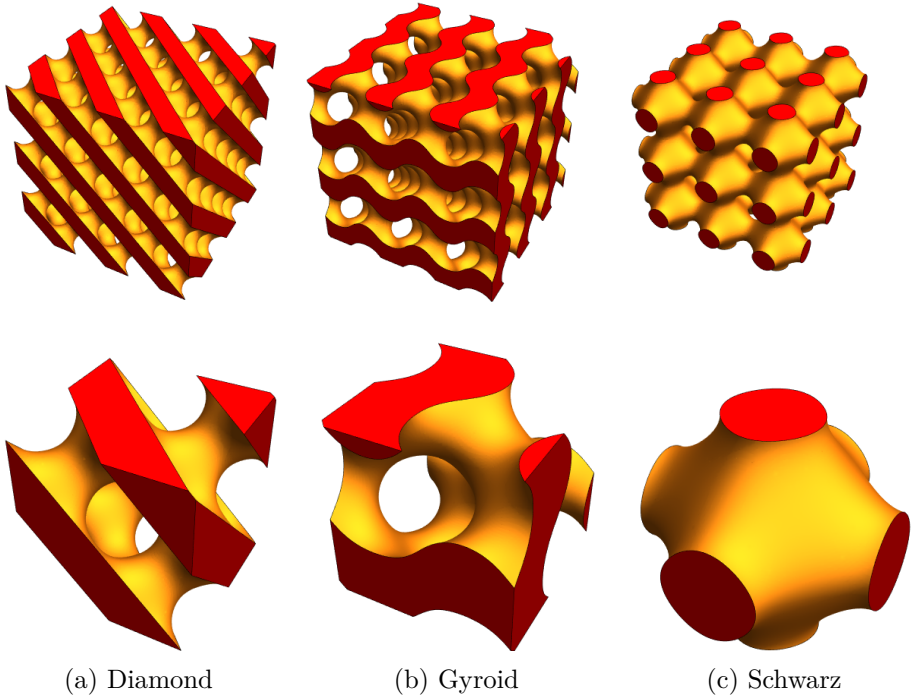


Figure 2.7: TPMS-based 3D-periodic porous structures with 60 % porosity.

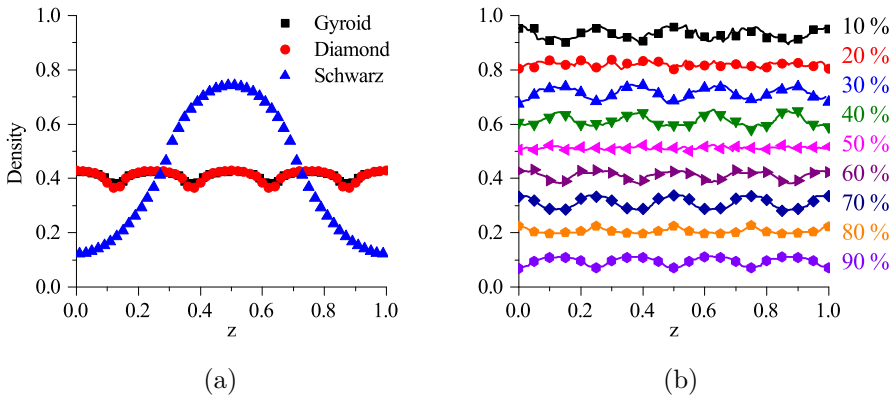


Figure 2.8: a) Density fluctuations at single unit cell for D, G, and S geometries with 60 % porosity, b) Density fluctuations for a single unit cell of G geometry at different porosities.

Electromagnetic response of structures with spatially distributed electromagnetic parameters

Once applied, the effective medium is not limited to be homogeneous and/or isotropic. It means the media parameters may vary along the coordinates according to a certain law. Here the robust and effective approach to calculate the electromagnetic response of structure which dielectric permittivity is varied along z -axis is discussed.

Let us consider the tri-periodic porous structures introduced previously as an effective media. In that case, the values of electromagnetic parameters will fluctuate together with the structure's density. For example, the variation of foam's refractive index along z -axis will be described with the following law:

$$\begin{cases} z < 0; & n = n_0, \\ z \in [0, z_0]; & n = n_{bulk}(1 - S(z)) + n_0S(z), \\ z > z_0; & n = n_0 \end{cases} \quad (2.10)$$

where n_0 and n_{bulk} are the refractive indices of free space and bulk material, S is a relative surface area of a structure cross-section normal to z -axis.

Relative surface $S(z)$ is, obviously, the 2D-representation of porosity. Let us consider the TPMS-based structure possessing the porosity that linearly increases along z -axis (see Figure 2.9a). As the reflection loss at the interface of two phases is proportional to the ratio between their refractive indices, such structure will demonstrate pronounced anti-reflective properties [182]. In the Figure 2.9b one can see the $n(z)$ dependence for gyroids with constant and spatially-variable porosity (i.e. parameter S in the Equation 2.10 has been changed to $S(z) \in [0.95, 0.25]$).

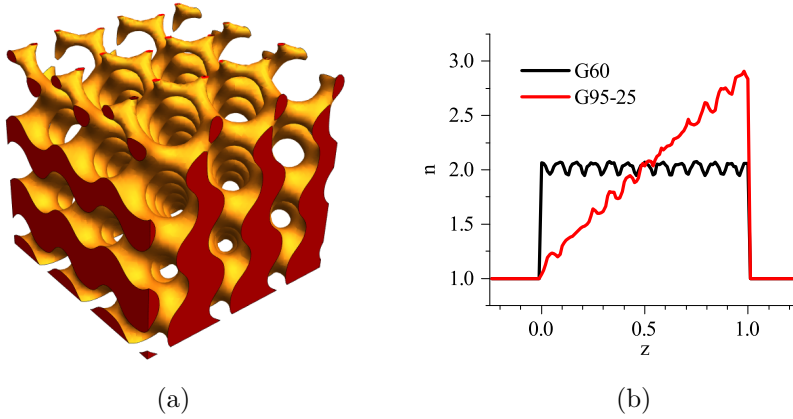


Figure 2.9: (a) G95-25 — a gyroid-based body with porosity varied from 95 % at the top to 25 % at the bottom edge (average porosity is 60 %). (b) Dependence of effective refraction index value on z coordinate for G60 and G95-25 structures.

It worth noting that not all TPMS keep their continuity at high porosities, which makes impossible the practical implementation of S80, D95 and other highly porous structures. Gyroid turns out to be the only applicable TPMS-based geometry for 95 % porosity objects creation (see the Figure 2.10).

If the unit cell of periodic structure is much less than the wavelength of initial radiation, the following procedure can be used for calculation EM response of material under investigation. The amplitudes of reflected (S_{11}) and transmitted (S_{21}) signals through the finite sample are calculated by the matrix method [183, 184] designed for the modeling of wave propagation in a multi-layered medium was used. Such method was effectively adopted for calculation of S-parameters in the microwave and terahertz frequency ranges [105, 106].

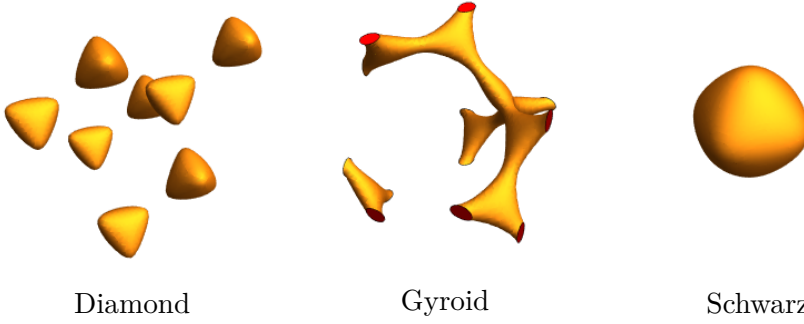


Figure 2.10: TPMS-based 3D-periodic porous structures with 95 % porosity. It can be seen that only G95 unit cell remains connected to other unit cells, i.e. is able to form a continuous structure of multiple cells.

Let us consider a normal scattering of a plane wave propagating along z -axis through a flat slab of bulk material with thickness τ and refractive index distribution $n(z)$. First, we need to divide the whole slab into N layers so that the thickness of each layer is much less than the material's inhomogeneity (i.e. than pore dimension TPMS unit cell, etc.) For example, the dependence shown in Figure 2.9b is calculated with ~ 33 layers per unit cell.

For large N the refractive index may be assumed to be constant within each layer at position z_t and equal $n(z_t)$. The plane wave scattering on each τ_t -thick layer may be described using a characteristic matrix and for a multi-layered structure, the characteristic matrix of the whole system is the product of all single layer matrices. In such case the S_{11} and S_{21} coefficients of the N -layered system in the free space can be calculated as:

$$S_{11} = \frac{n_{air} - C/B}{n_{air} + C/B}, \quad (2.11)$$

$$S_{21} = \frac{2n_{air}}{n_{air} + C/B}, \quad (2.12)$$

where

$$\begin{bmatrix} B \\ C \end{bmatrix} = \left\{ \prod_{t=1}^N \begin{bmatrix} \cos(k_t \tau_t) & i \sin(k_t \tau_t) k_0/k_1 \\ i \sin(k_t \tau_t) k_1/k_0 & \cos(k_t \tau_t) \end{bmatrix} \right\} \begin{bmatrix} 1 \\ n_{air} \end{bmatrix}. \quad (2.13)$$

Here τ_t is the thickness of the layer t , $k_t = \frac{2\pi n(z)}{\lambda}$ and $k_0 = \frac{2\pi n_{air}}{\lambda}$ are

the wavenumbers in the layers with refractive indices $n(z)$ and n_{air} (i.e. investigated material and free space), λ is the wavelength.

2.2.3. Electromagnetic response of structures with wavelength-comparable dimensions

Unlike the situation with polymer composites at subsection 2.2.1, the electromagnetic response of structures, which characteristic dimensions are comparable with wavelength requires a different model.

Let us consider a periodic structure made of conductive material covered with dielectric polymer represented at Fig. 2.11). The electromagnetic response of such structure will be dependent on both conductive and dielectric parts.

Periodic structure contribution

Let us consider the reflection of a plane wave at normal angle of incidence from the infinite array of conductive square pyramids with height h and base width l (see Fig. 2.11).

There are several approaches to calculate the amplitude of the signal reflected by such a structure. In the low frequency region the wavelength is much higher than the characteristic lateral size of pyramids that allows to implement the long-wave approximation and homogenization [105, 106] in the way it was done in the Section 2.2.2. When the wavelength is substantially smaller with respect to the characteristic lateral size of pyramids, the electromagnetic response obeys the principles of linear optics [183]. However, when the wavelength and characteristic dimensions of system are comparable, the Huygens–Fresnel principle should be applied for waves scattering calculations.

Let us consider the wave with amplitude E_0 , which is propagated normally to pyramids bases (along the X axis, Figure 2.11 a) and reflected back. According to the Huygens–Fresnel principle, each point of a wavefront acts as a source of secondary waves, which interfering with each other determine total wavefront. In order to recreate the wavefront of pyramidal array let us consider one edge of a single pyramid (for example edge 1 in Fig. 2.11b). The scattering conditions from all points of the edge are the same except of the path difference, which is equal to $\Delta_x = 2x$ for normal backscattering. Here, only the tangential

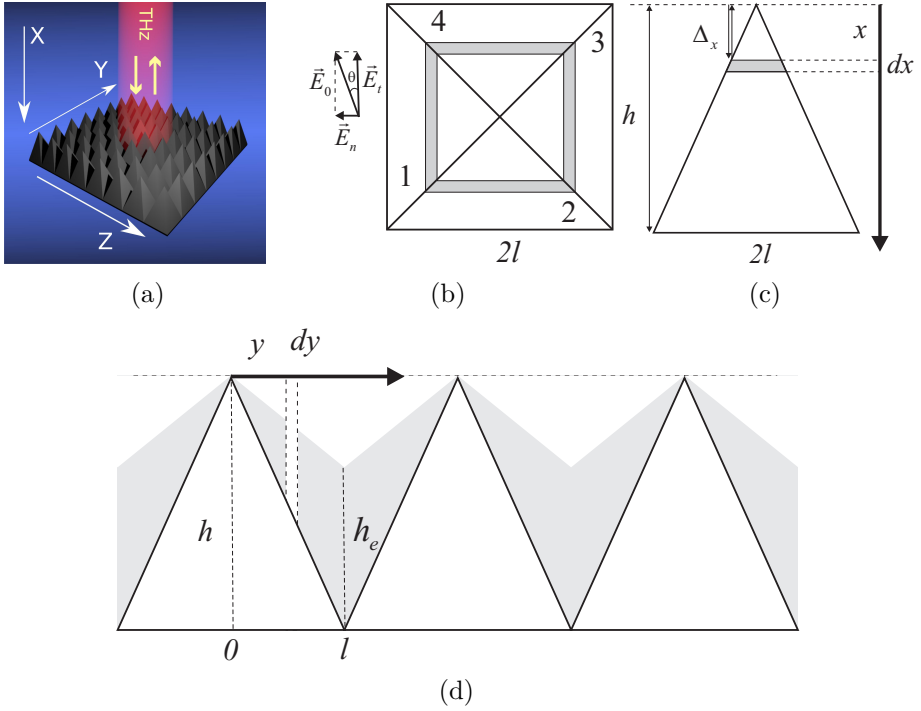


Figure 2.11: Backscattering of plane wave from pyramidal array. (a) Pyramidal array reflecting the terahertz radiation, (b) top view, (c) side view, (d) schematic image of pyramidal array covered with dielectric polymer.

component $E_0 \cos \Theta$ should be considered because the contribution of normal component (E_n in Fig. 2.11b) from equivalent places of edges 1 and 3 are in antiphase.

The contribution of dx -thick layer of edge 1 placed on distance x from the top of pyramid to the total reflected amplitude is:

$$\begin{aligned}
 dE_{t1} &= \frac{E_0 \cos \Theta \exp(i\omega t - ik\Delta_x)}{S_{edge}} dS = \\
 &= \frac{E_0 \cos \Theta \exp(i\omega t - ik2x)}{h^2} 2x dx,
 \end{aligned} \tag{2.14}$$

where k is the wave vector and h is the height of pyramid.

The total contribution of the edge 1 is:

$$\begin{aligned}
 E_{t1} &= \frac{E_0 \cos \Theta \exp(i\omega t)}{h^2} \int_0^h 2x \exp(-ik2x) dx = \\
 &= \frac{E_0 \cos \Theta \exp(i\omega t)}{2k^2 h^2} [\exp[-i2kh](1 + 2ikh) - 1].
 \end{aligned} \tag{2.15}$$

The contribution of the edge 3 is the same as Eq. (2.15). Contributions of the edges 2 and 4 may be obtained from Eq. (2.15) by substitution of $\cos \Theta$ for $\sin \Theta$.

Summarizing the impact of all four edges, it is possible to obtain the scattering parameter S_{11}^p (ratio between reflected and incident radiation amplitudes) for the surface paved with pyramids:

$$S_{11}^p(\nu, h) = \frac{(1 + 2ikh) \exp[-i2kh] - 1}{2k^2 h^2}. \tag{2.16}$$

In Fig. 2.12 the S_{11}^p frequency dependence is presented for various h . Here, the pyramids consist of perfect electric conductor i.e. the flat surface of such material has $|S_{11}|=1$.

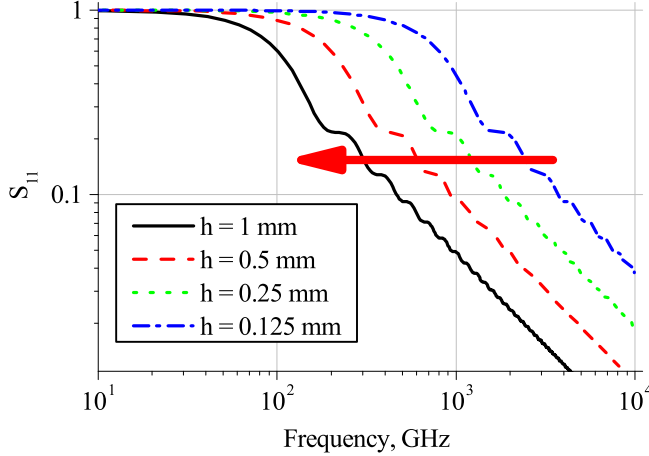


Figure 2.12: The frequency dependence of S_{11} on pyramid height $h = 0.125, 0.25, 0.5, 1.0$ mm.

The increase of pyramid height h shifts the S_{11}^p spectrum to the low frequency region. Fig. 2.12 clearly depicts the transition between long-wave approximation through the Huygens–Fresnel theory to the geometric optics region. At low frequencies the wavelength is much higher than

the pyramid height h , thus the structure interacts with radiation as a perfect reflector. When the wavelength is comparable with h , the amplitude of back-reflected signal decreased with relatively small oscillations caused by interference. Finally, at high frequencies, the S_{11}^p value is significantly damped and the reflection becomes negligible.

Dielectric layer contribution

A widely known example of matching layer is the antireflective coating of optical lens, which damping the reflection using waves reflected from coating's surfaces in antiphase. The dielectric layer covering the pyramids of investigated structure may be considered in the same manner increasing not only the mechanical, but antireflective properties.

For the pyramids array covered with dielectric layer the amplitude of back-reflected signal is also dependent on the dielectric permittivity ε and thickness τ of the latter. To calculate dielectric layer contribution it is necessary to take into account the interference between waves reflecting from top and bottom surfaces of dielectric layer covering the pyramids. The electric field E_I in the region above dielectric layer (in free space) and electric field E_{II} inside the layer may be determined as:

$$\begin{aligned} E_I &= C_1 \exp[-ik_1x] + C_2 \exp[ik_1x], \\ E_{II} &= C_3 \exp[-ik_2x] + C_3\alpha \exp[ik_2x], \end{aligned} \quad (2.17)$$

where C_1, C_2, C_3 are unknown coefficients, $k_1 = \frac{2\pi\nu}{c}$ and $k_2 = \frac{2\pi\nu\sqrt{\varepsilon}}{c}$ are wavenumbers in the free space and in the dielectric layer respectively, ν is the frequency, c is the speed of light. The amplitudes of initial and reflected waves were taken to be C_3 and αC_3 respectively. A term ($|\alpha| \leq 1$) implies imperfection of CNT array as conductor. Therefore, α may be considered as amplitude of the signal reflected by a plane surface of conductive material with semi-infinite depth (in considered case, the CNT array) into a medium (polymer) with the dielectric constant ε . Eq. (2.17) should satisfy the following boundary conditions:

$$\begin{cases} E_I(-\tau) = E_{II}(-\tau), \\ \frac{\partial E_I}{\partial x}|_{-\tau} = \frac{\partial E_{II}}{\partial x}|_{-\tau}. \end{cases} \quad (2.18)$$

Solving Eq. (2.17) with that boundary conditions allows to obtain the am-

plitude of reflected signal from the plane-parallel layer of dielectric with non-perfect back reflector:

$$S_{11}^d(\nu, \tau, \varepsilon, \beta) = \frac{C_2}{C_1} = \frac{e^{2i\tau k_1} (e^{2i\tau k_2} k_1 - e^{2i\tau k_2} k_2 + k_1 \alpha + k_2 \alpha)}{e^{2i\tau k_2} k_1 + e^{2i\tau k_2} k_2 + k_1 \alpha - k_2 \alpha}. \quad (2.19)$$

Eq. (2.19) describes the contribution of dielectric layer to the reflection coefficient of epoxy covered pyramidal CNT array. The parameter $\alpha = \frac{\sqrt{(\varepsilon)-(1-\beta)/(1+\beta)}}{\sqrt{(\varepsilon)+(1-\beta)/(1+\beta)}}$ is related to the amplitude of signal $|\beta| \leq 1$ reflected by plane back reflector made of the same materials as pyramids. In the case when $\beta = -1$, Eq. (2.19) coincides with the amplitude of reflected signal from dielectric layer located on the perfect conductor [185] excepting the phase factor $\exp[2i\tau k_1]$. The normal reflection of THz wave from the investigated plane-parallel MWCNT array was fitted with $\beta = -0.9$. Fig. 2.13 shows the frequency dependence of S_{11} for the dielectric layer of $\tau = 0.1, 0.2, 0.3$ mm thickness.

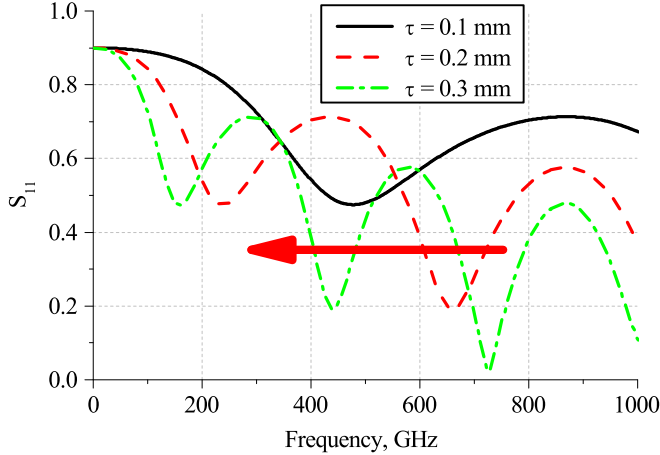


Figure 2.13: Frequency dispersion of S_{11} (scattering parameter responsive for reflectance) at different dielectric layer thickness $\tau = 0.1, 0.2, 0.3$ mm. ($\beta = -0.9, \varepsilon = 3 - 0.4i$)

The typical value for epoxy resin permittivity in THz frequency region $\varepsilon = 3 - 0.4i$ was used. Fig. 2.13 depicts the typical interference oscillations, which are absent for non-covered pyramids. It is important to notice that when the dielectric layer thickness increases, these oscillations shift to the low-frequency region.

Combination of dielectric layer and structure contribution

The real pyramidal array was impregnated with epoxy resin to overcome the pristine pyramids brittleness. The electromagnetic response of such structure is defined by both contributions from dielectric layer and from pyramidal back reflector. Due to surface tension forces, the epoxy resin unevenly covers the CNT pyramids array. As a first approximation, we considered the case when the thickness of the epoxy increases linearly with approaching the base of the pyramid (Fig. 2.11d)). In this case the amplitude of reflected signal from the unit cell may be calculated as:

$$S_{11} = \frac{2}{l^2} \int_0^l S_{11}^d(\nu, \frac{h_e}{l}x, \varepsilon, \beta) \times \exp[-i2k_1x(\frac{h}{l} - \frac{h_e}{l})]xdx, \quad (2.20)$$

where l is the half length of pyramids base, h_e is the height of epoxy layer near the pyramids base. The first multiplier in Eq.(2.20) related to the dielectric layer contribution, the second - to the phase shift caused by the structure.

2.3. Measurements of the electromagnetic properties of the material

2.3.1. Measurements in microwave range

Among the plenty of electromagnetic response measurements methods two techniques were applied. The first one based on coaxial airline is intended to give broadband result. However, due to the geometry of the coaxial cell the method applicability is limited to the uniform isotropic MUTs. In the case of anisotropic materials, polarization-dependent measurements and external field application, etc. the rectangular waveguide is applicable.

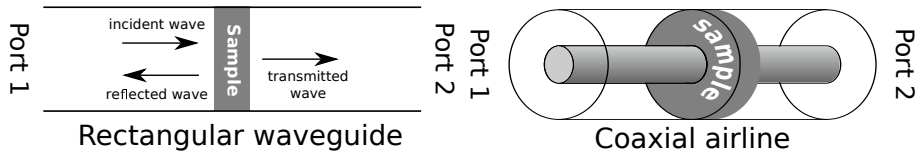


Figure 2.14: The MUT fixture in fully-covered rectangular waveguide (left) and coaxial airline (right).

In the rectangular waveguide the electric field \vec{E} is directed towards the shorter side of waveguide cross-section.

The electromagnetic response was registered as ratios between the amplitude of reflected (transmitted) and incident radiation (S-parameters). The conductivity and complex dielectric permittivity were recalculated from S-parameters by standard methods [157, 186] solving the following equations:

$$S_{11}(\nu, \tau, \varepsilon', \varepsilon'') = \frac{(-1 + e^{2i\tau k_1})(k_0^2 - k_1^2)}{e^{2i\tau k_1}(k_0 + k_1)^2 - (k_0 - k_1)^2}, \quad (2.21)$$

$$S_{21}(\nu, \tau, \varepsilon', \varepsilon'') = \frac{4k_0 k_1 e^{i\tau(k_0 + k_1)}}{e^{2i\tau k_1}(k_0 + k_1)^2 - (k_0 - k_1)^2}, \quad (2.22)$$

where ν is the operating frequency, τ is sample thickness, k_0 and k_1 are the wavenumbers in the free space and inside the sample with the dielectric permittivity $\varepsilon = \varepsilon' - i\varepsilon''$.

In the case of TE₁₀ mode transmitted in the rectangular waveguide, the wavenumbers are written as:

$$k_0 = \frac{\pi\nu}{c} \sqrt{4 - \frac{c^2}{\nu^2 a^2}}; k_1 = \frac{\pi\nu}{c} \sqrt{4\varepsilon(\nu) - \frac{c^2}{\nu^2 a^2}}; \quad (2.23)$$

where a and c are the waveguide width and the speed of light respectively. In the free space the Equation 2.23 is transforming into:

$$k_0 = \frac{2\pi\nu}{c}; k_1 = \frac{\pi\nu}{c} \sqrt{4\varepsilon(\nu)}; \quad (2.24)$$

which is used for free space and coaxial airline measurements.

2.3.2. Measurements in terahertz range

Time-domain terahertz spectroscopy is a non-destructive diagnostic method widely applied for the characterization of polymer-based nanocomposites' [187–189] and thin films' [15, 190, 191] electromagnetic properties in the ~ 0.1 –3 THz frequency range without any predefined assumptions.

Being in between microwave and optical infra-red frequency regions, terahertz radiation easily transmits through most dielectric materials, while the metals and certain dielectrics, such as water, are non-transparent at the mentioned frequencies. Since the inhomogeneities' dimensions are orders less than the wavelength, spectral parameters of nanocomposites may be investigated in the framework of effective medium theory [192, 193].

The THz measurements were carried out using a commercial THz time domain spectrometer "TSPEC" by EKSPLA (Vilnius, Lithuania) in 0.1–1.0 THz frequency range. The optical layout of the spectrometer is represented in Figure 2.15. The photoconductor antennas attached to lens made of high resistance silicon are used as *THz emitter* and *detector*. The antennas are pumped by the radiation of 40 mW *femtosecond laser* with 1050 ± 40 nm wavelength, 50–150 fs pulse duration and ~ 80 MHz pulse repetition rate is divided by the *pellicle beam-splitter* BS1 in 55:45 ratio. The *mirrors* M1 and M2 direct the laser beam into the emitter through the *fast optical delay line* formed by hollow retro-reflector HLR1 oscillating at 10 Hz and *trihedral prism* PR1. The laser beam focusing on the emitting antenna's gap is done with help of *lens* L1. Pumping of detector's photoconductive antenna is performed through the *slow delay line* formed by *stationary prism* PR3 and *moving prism* PR4, *mirror* M3 and focused by *lens* L2.

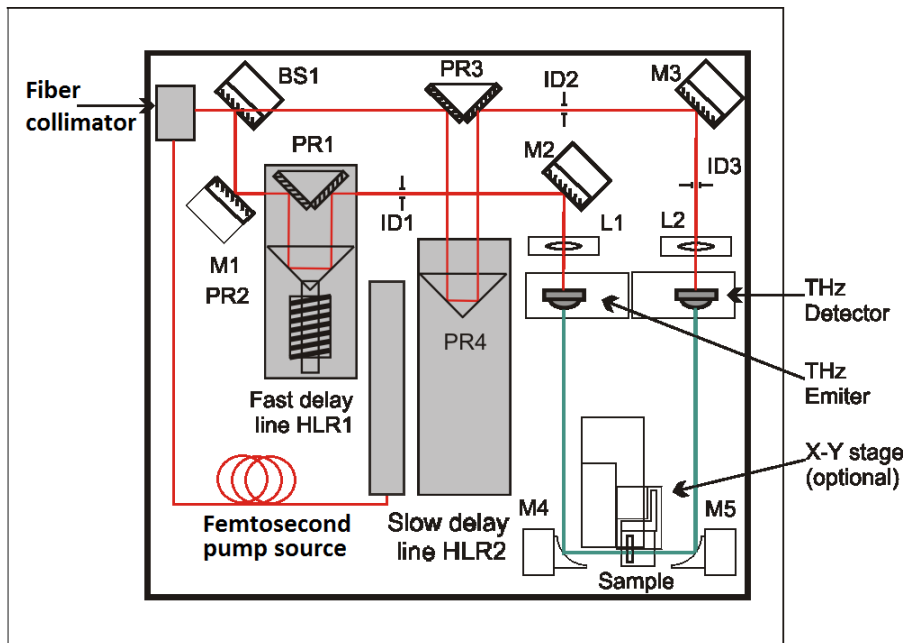


Figure 2.15: Optical layout of EKSPLA "TSPEC" terahertz time-domain spectrometer in transmission geometry. The radiation of laser pumping source and the terahertz radiation are shown in the red and green colors, respectively.

Having a single THz detector, the device requires the interchangeable optical setups for reflectance and transmittance measurements (Figure 2.16). In the transmission setup the sub-picoseconds pulses of terahertz radiation are focused to the sample by *parabolic reflectors* M4 and M5. The reflection setup includes the *beam-splitter* BS2 in addition to two parabolic mirrors focusing the terahertz beam on the reflective sample. Therefore, the signal to noise ratio is sufficiently higher for the reflective setup.

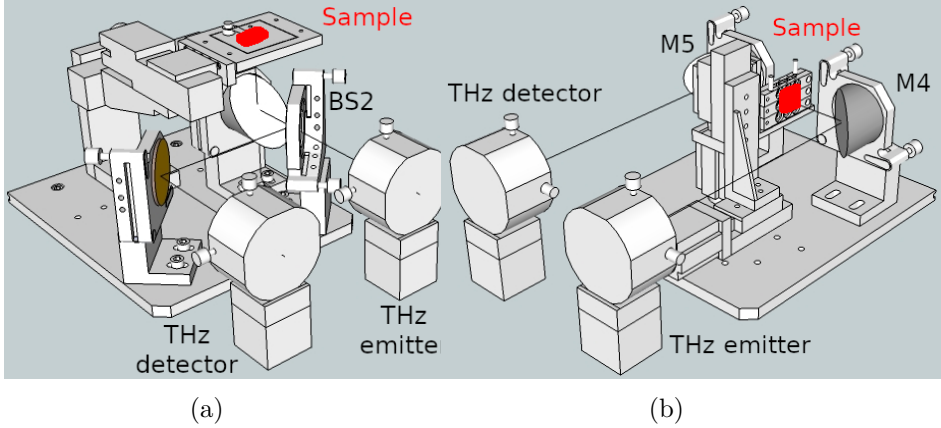


Figure 2.16: Interchangeable fixtures of "TSPEC" terahertz time-domain spectrometer for reflection (a) and transmission (b) coefficients measurements.

According to its functioning principle, the THz spectrometer registers the waveform of THz electrical field in time domain. In order to switch between time and frequency domains the Fourier transform is used. The reflection (transmission) coefficient is evaluated as a ratio between powers of electromagnetic radiation reflected (transmitted) by the sample and the reference. In transmission setup the data obtained at free space is used as a reference, while as the reflection setup requires a close-to-perfect metallic mirror for calibration. In order to increase signal-to-noise ratio each measurement is averaged over 1024 frames.

The radiation given by the terahertz source of the spectrometer is linearly polarized, thus it is possible to investigate samples with polarization-dependent electromagnetic response. At the same time, it should be mentioned that the response of terahertz detector included in the spectrometer is also polarization-dependent (i.e. is capable to

register only the radiation with linear polarization). That design feature may create an uncertainty during the investigation of media/devices in which the rotation of polarization plane is expected. However, such cases are out of current work scope.

3. TERAHERTZ SPECTROSCOPY OF INSULATED FILLER PARTICLES IN A COMPOSITE MATERIAL ABOVE PERCOLATION THRESHOLD

The current chapter is devoted to the insulated (i.e. excluded from the percolation network) particles impact to the electromagnetic properties of composites created by melt-mixing method widely used for composite engineering [174, 194]. Despite its simplicity and scalability, melt-mixing is not the "best" method of composite production in terms of percolation threshold and filler distribution effectiveness [53] (meaning the ratio between the amount of filler involved in percolation network and its total amount). The widely used low-frequency impedance spectroscopy allows to define percolation threshold, however, not to characterize filler distribution. The power of scanning and transmission electronic microscopy allows to visualize single inclusions in the composite, but not to inspect the common character of their distribution. However, the information on filler distribution is of great importance for modern nanocomposite materials industry. Here the information about insulated inclusions in composite material is obtained by means of terahertz spectroscopy.

The diagnostics of insulated filler particles allows to control the efficiency of filler distribution during the composite synthesis. Besides the morphology of fillers, the percolation threshold value strongly depends on the composite preparation technology, the filler dispersion in the dielectric phase (matrix) and the filler–matrix interfacial interactions. In previous studies on the herein investigated nanocomposites, the electrical percolation thresholds of 0.5 % for MWCNT/PLA, 6 % for GNP/PLA and 3 % for the bi-filler composite GNP/MWCNT/PLA were reported [194].

Since the inhomogeneities of materials considered in the current work are orders smaller than the radiation wavelength, spectral parameters of samples under investigation may be considered in the framework of effective medium theory [192, 193].

The dielectric properties of composites above the percolation threshold are mainly governed by electrical transport and Maxwell–Wagner relaxation. However, at higher frequencies, the contributions of big percolating clusters to the Maxwell–Wagner relaxation and the electrical

conductivity become less pronounced, so that in the terahertz frequency range it is possible to separate the contributions of individual nanoparticles' polarizations from the total dielectric permittivity [24]. The most commonly used non-destructive method of composite system characterization is low-frequency impedance spectroscopy, which allows one to easily establish percolation thresholds. However, the dispersion of nanoparticles may be investigated by other direct methods, such as transmission and scanning electron microscopy, near-infrared fluorescence microscopy [195], and indirect methods (noise spectroscopy [196], magnetic susceptibility measurements [197], etc. [34, 198, 199]).

The typical way of how the insulated conductive particles distributed in matrix will impact the electromagnetic properties of the composite is described in Chapter 2. The Maxwell Garnett approach is typically used for the systems under the percolation threshold. However, the approach itself does not contain any restrictions for the matrix conductivity. Therefore it is possible to represent the percolated composite as a conductive matrix plus insulated filler particles. The investigation performed in the current chapter shows that such representation gives a good explanation to the experimentally visible effects.

3.1. Characterization of nanocarbon composites microstructure

According to the low-frequency measurements described in Section 1.2.1, the typical values of percolation threshold for MWCNT-based composite materials produced by melt extrusion method lies between 1.5 and 3 wt. %, while GNP-based composite experiences percolation between 3 and 6 wt. % [56]. Therefore, the set of samples under investigation contains both pre- and post-percolated composites.

The quality of nanoparticles and their distribution in the polymer matrix were examined by means of a Raman spectrometer combined with the confocal microscope (Nanofinder High End, Tokyo Instruments, Belarus-Japan). Raman spectra were obtained using 100X objective with $NA = 0.95$ and the spot size on the sample surface was $0.75 \mu\text{m}$. The excitation source was a 473 nm laser.

It is known that the typical Raman spectra of carbon nanomaterials, including MWCNTs, GNP, graphene, etc., are dominated by three characteristic peaks centered at $\sim 1360 \text{ cm}^{-1}$, $\sim 1580\text{--}1600 \text{ cm}^{-1}$ and $\sim 2600\text{--}2700 \text{ cm}^{-1}$ (usually referred to as D, G and 2D modes, respec-

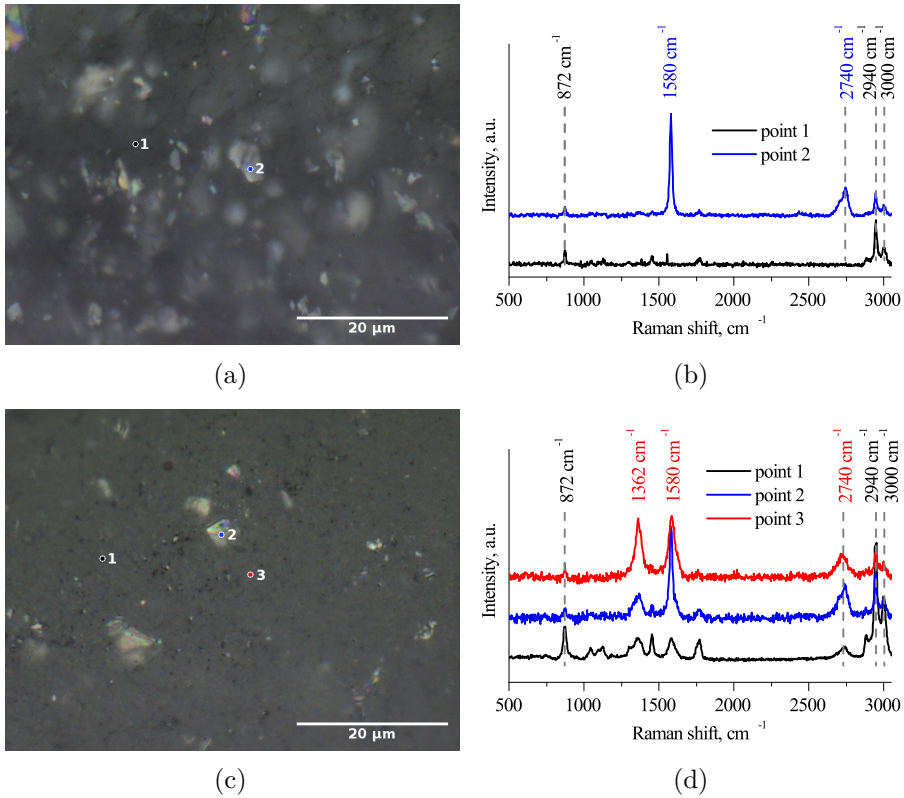


Figure 3.1: Optical microscopy image (a) and Raman spectra (b) of PLA composite containing 1.5 % GNP. Due to the neat PLA transparency, it is possible to see GNPs under the surface of a composite. Optical microscopy image (c) and Raman spectra (d) of PLA composite containing the mixture of 3 % GNP and 3 % MWCNT. Raman spectrum collected at point 2 combines the characteristic peaks of PLA, GNPs, and MWCNTs.

tively) [200–202]. On the other hand, the strongest features of pure PLA are located in the vicinity of 3000 cm^{-1} . Comparing the Raman spectra collected from different points on the surface of the composite containing 1.5 % GNP allows one to figure out GNP particles, points 1 and 2 in Figure 3.1b, correspond to the filler-free area and GNP, respectively. The contrast difference between GNP particles and pure polymer Figure 3.1a indicates the particle distribution in the polymer matrix. It is worth noting that pure PLA is optically transparent; hence, it is possible to observe GNP particles under the sample surface.

However, the addition of a small MWCNT amount makes the PLA matrix non-transparent. As a result, in the bi-filler composites, GNP particles can be identified by optical microscope (Figure 3.1c) only on the sample surface. As can be seen from the Raman spectra (Figure 3.1d), in the bi-filler composites nanotubes are uniformly distributed in the polymer matrix. However, at different points in the sample, the proportions of MWCNTs and PLA impacted the Raman spectrum differently (see points 1 and 3 in Figure 3.1d). Raman spectroscopy allows distinguishing even a small number of MWCNTs which are present on the surfaces of GNP particles (the observed D mode indicates CNTs at point 2).

Bright-field transmission electron microscopy (TEM) analysis was performed using a FEI TECNAI G12 Spirit-Twin (LaB6 source) instrument equipped with an FEI Eagle-4k CCD camera operating with an acceleration voltage of 120 kV. The analysis was performed on sections obtained at room temperature by using a Leica EM UC6/FC6 ultramicrotome. The sections were placed on 400 mesh copper grids. According to the transmission electron microscopy (TEM) of obtained composites, the method applied allows obtaining a mostly uniform distribution of both filler particle types. Figure 3.2a–c proves that GNPs kept their dimensions after the melt extrusion. The TEM images of MWCNTs in mono- (Figure 3.2d,e) and bi-filler (Figure 3.2f) composites show that in both cases, the nanotubes are well-distributed. Due to the significantly higher aspect ratio, they tend to form percolation networks, even at the smallest investigated concentration (compare the number of percolating clusters in Figure 3.2d,e). However, independently of concentrations and the percolation existence, all prepared composites contain a certain number of insulated filler particles. Summarizing the above, both nanocarbon fillers possess good dispersion in the PLA matrix.

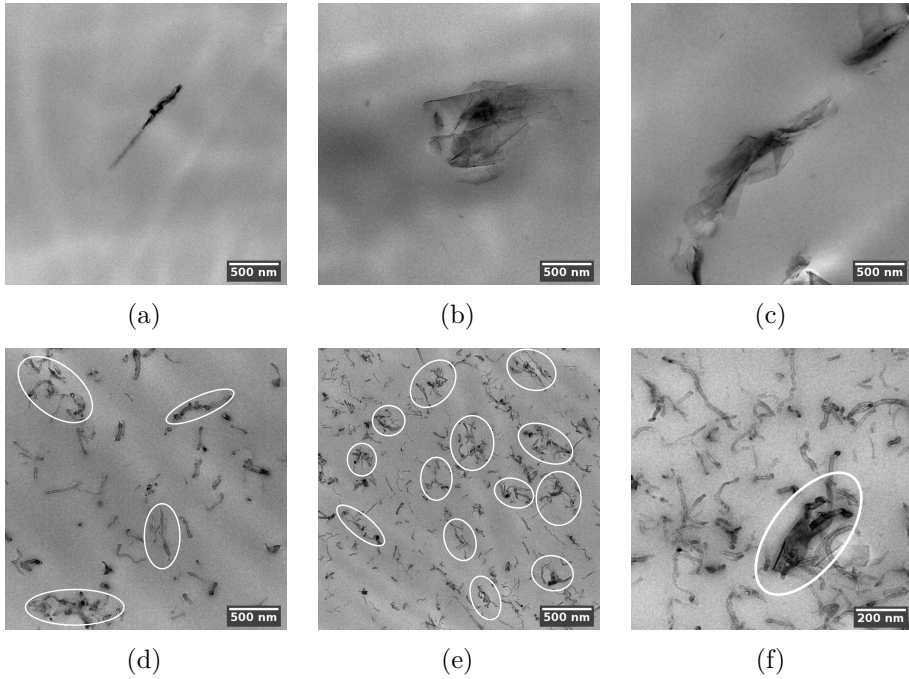


Figure 3.2: TEM images of insulated filler particles in PLA composites with 1.5 (a), 3 (b), and 6 wt. % (c) GNP; insulated particles and percolating clusters (enclosed in ovals) in composites containing 1.5 (d) and 3 wt. % (e) MWCNT; the mixture of 3 % GNP and 3 % MWCNT (f). A graphene nanoplatelet involved in percolation contact with nanotubes is enclosed in an oval.

3.2. Experimental investigation of nanocarbon composites dielectric properties

In order to perform the THz measurements of transmission coefficient, the thicknesses of samples were reduced to 200–300 μm by precise hand polishing with a diamond paste which was removed with isopropanol and water. During the processing, composites were kept near room temperature to prevent heat-induced variation of their structure.

In order to register the imaginary permittivity maximum the terahertz–subterahertz spectra ($5\text{--}60\text{ cm}^{-1}$) of the films were measured by means of commercially available pulsed time-domain spectrometer (TDS) TERA K15 (Menlo Systems).

The amplitude and phase of transmission coefficient were used to determine the real and imaginary parts of the dielectric permittivity of

the investigated samples and their conductivity.

Experimental values of complex permittivity are shown in Figures 3.3 and 3.4. The imaginary part of permittivity (further referred to as ε'') demonstrates a peak for most of the investigated samples containing GNP filler. On the contrary, the MWCNT-based monofiller composites and the bi-filler composites with 1.5 % of GNPs and 4.5 % of MWCNTs demonstrated a monotonous decrease with frequency growth, which is typical for percolated systems. Finally, the non-percolated composite containing 1.5 wt. % MWCNTs did not demonstrate the ε'' peak in the investigated frequency range.

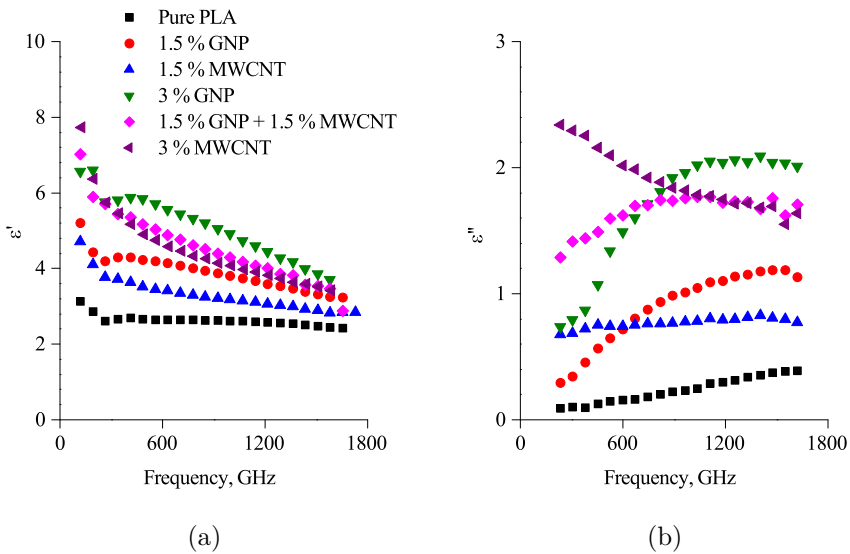


Figure 3.3: Complex permittivity of composites containing 3 wt. % nanocarbon fillers. MWCNT concentrations are above the percolation threshold.

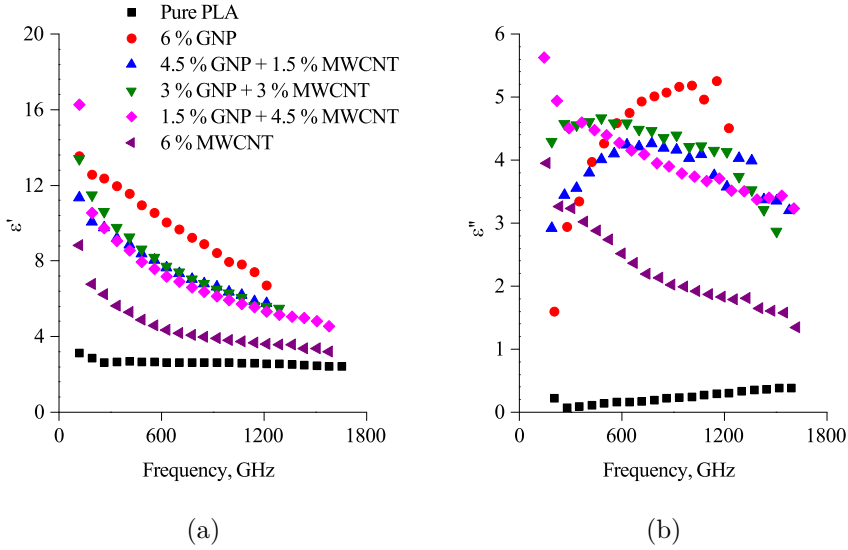


Figure 3.4: Complex permittivity of composites containing 6 wt. % nanocarbon fillers. MWCNT concentrations are above the percolation threshold.

3.2.1. Maxwell Garnett approximation of GNP-based composites permittivity

Typical values for the percolation threshold for GNPs in polymer composites are usually not lower than 3.5 % and strongly depend on the GNP aspect ratio, the polymer type and the quality of particles' distribution [81, 84]. Hereafter let us consider the composite under investigation as uniform distribution of randomly oriented ellipsoidal particles according to the principle described in Section 2.2.1.

Therefore the GNP particles were assumed as uniform ellipsoids with $a = b \gg c$ semiaxes and their density was considered equal to graphite (2.2 g/cm^3). The typical aspect ratio (AR) for graphene nanoplatelets lies in the range of 100–1000. An acceptable fitting of dielectric permittivity of composites containing 1.5 and 3 % GNP (Figure 3.5) was acquired with $\sigma = 20,000 \text{ S/m}$ and $\text{AR} \sim 200$, which is in good agreement with the aspect ratio of used GNP particles given in Section 2.1.1. While the approximation parameters for composites with 1.5 and 3 % GNP concentration are similar, the sample containing 6 % filler requires another set of parameters to be used for approximation. While the conductivity

of ellipsoids remains unchanged, the aspect ratio has to be increased up to nearly 300.

The fact that the Maxwell Garnett approximation is still applicable for 6 % GNP may indicate that in spite of the concentration being higher than previously reported percolation thresholds for GNPs [56], the impact of insulated filler particles still prevails in the investigated frequency region. In the next subsection, we will try to explain the low-frequency shift of ϵ'' maximum.

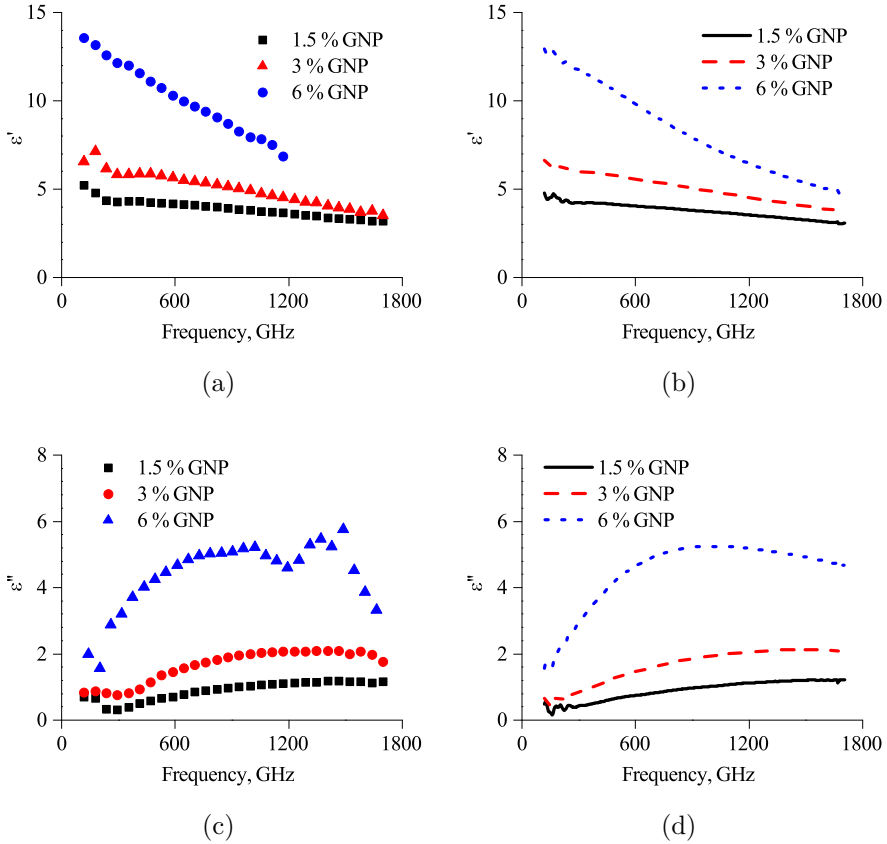


Figure 3.5: Experimental complex permittivity values of composites containing 1.5, 3 and 6 wt. % GNP (a, c) and Maxwell Garnett approximation (b, d) of the experiment with the following fitting parameters: $\sigma = 20000$ S/m, and $AR \sim 197, 208$ and 291 , respectively;

3.2.2. Imaginary Permittivity Peak in Percolated Hybrid Composites

In the previous section, it was shown that the composites with GNP concentrations below the percolation threshold demonstrate the imaginary permittivity maximum predicted in Section 2.2.1. However, the experimental data for composites containing two different fillers show a similar behavior, even with the existence of percolation (Figure 3.3 and 3.4). In a perfect case, every particle of both fillers is expected to be involved in a heterogeneous percolation network, making the Maxwell Garnett approach inapplicable. However, the real composite system always contains a certain amount of filler particles excluded from the percolation network formation. At low frequencies, the response of such insulated particles is hidden by the percolation network impact, but as in the terahertz region, it is possible to distinguish their impact due to electromagnetic coupling.

In Figure 3.6a the complex permittivities of composites containing 1.5 % GNP, 1.5 % MWCNT and their combination are depicted. It is worth noting that both composites used for hybrid composite preparation possess concentrations below the percolation threshold.

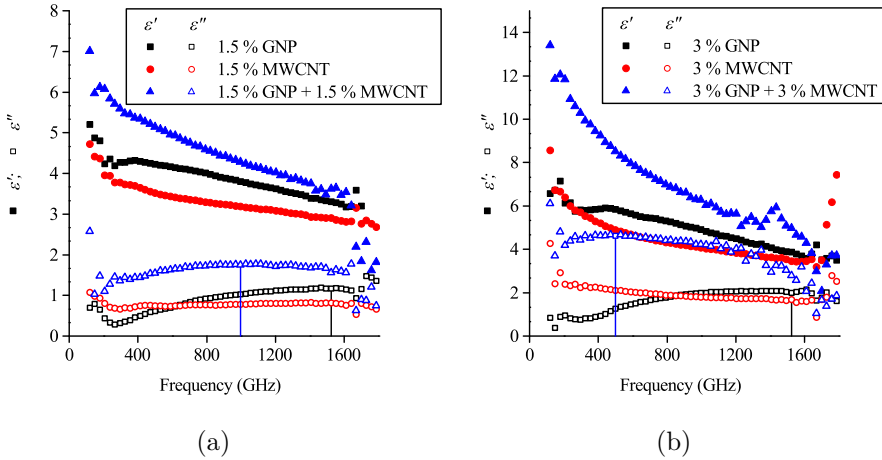


Figure 3.6: Complex permittivities of composites containing (a) 1.5 % GNP, 1.5 % MWCNT and their mixture; (b) 3 % GNP, 3 % MWCNT and their mixture. Peak values of ϵ'' for GNP and GNP + MWCNT composites are indicated by vertical lines.

It can be seen that despite the imaginary part of MWCNT-based composite, the permittivity has no peculiarities, such as peaks in the investigated range; the imaginary part of the GNP-MWCNT bi-filler composite's permittivity shifts towards lower frequencies in comparison with peak inherent for the GNP-based filler.

A similar situation was observed for a mixture of 3% MWCNT and 3 wt. % GNP composites (Figure 3.6b), a set of mixtures with 6 wt. % nanocarbon (Figure 3.4) in which the nanotube content is above the percolation threshold. In both cases, it is possible to conceive the dispersion of bi-filler composite's ε as a superposition of MWCNT (monotonous decrease of both real and imaginary parts of permittivity) and GNP (peak of ε'') curves. Considering Equations (2.1)–(2.3), the ε'' shift can be explained by the growth of the average aspect ratio and/or the conductivity decrease (see Figure 2 in [24]). Due to the higher aspect ratio (~ 1000), non-percolated nanotubes will give a ε'' peak at lower frequencies in comparison with GNPs. That means the GNPs and MWCNTs may be both involved in the percolation network and excluded from it.

Looking into the Maxwell Garnett approach it is possible, to certain extent, not limit to the dielectric nature of the matrix, substituting the ε_m in Equation (2.3) with the permittivity of a perfect percolated composite (every particle of which is involved in percolation network). Then, the effective permittivity of the mixed-filler composite may be introduced as following:

$$\varepsilon_{effmix} = \varepsilon_{MWCNT} + \Delta\varepsilon_{cp} + \Delta\varepsilon_{np} \quad (3.1)$$

where the ε_{MWCNT} term is the permittivity of MWCNT-based composite, $\Delta\varepsilon_{cp}$ is a "synergistic" impact of cross-MWCNT-GNP percolation and $\Delta\varepsilon_{np}$ is an impact on the dielectric permittivity made by non-percolated GNP particles. The expression for $\Delta\varepsilon_{np}$ is similar to the second term on the right side of Equation (2.3).

Results of rough $\Delta\varepsilon_{cp}$ evaluation (considering $\Delta\varepsilon_{np} = \varepsilon_{GNP} - \varepsilon_{PLA}$) for mixed-filler composites containing 1.5 % MWCNT + 1.5 % GNP and 3 % MWCNT + 3 % GNP are presented in the Figure 3.7.

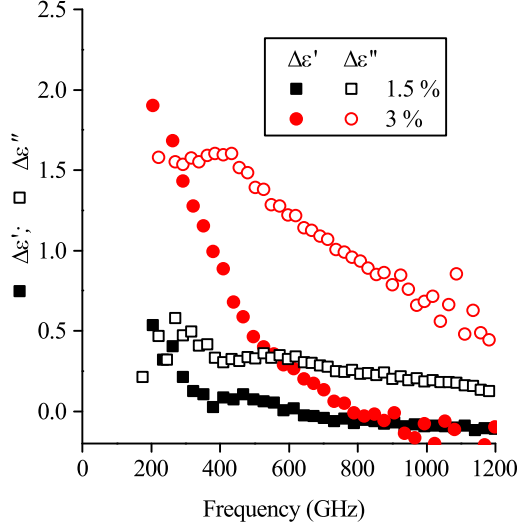


Figure 3.7: Impacts ($\Delta\epsilon_{cp}$) of cross-filler percolation to the dielectric permittivity of composites containing 1.5 % MWCNT + 1.5 % GNP and 3% MWCNT + 3% GNP (referred to as 1.5 % and 3 %, respectively). Both real and imaginary parts behave typically for a percolated composite.

It can be seen that the $\Delta\epsilon_{cp}$ frequency dispersion is typical for composites whose filler particles are mostly involved in the percolation network. However, the non-percolated nanotubes' impact value remains hidden in the total ϵ_{MWCNT} . The ϵ'' shift characteristic to the bi-filler composite (Figure 3.6) may be considered as indirect proof that a certain number of MWCNTs are excluded from the percolation network.

3.3. Summary

The impact of nanofiller particles excluded from the percolation network was demonstrated by means of transmission time-domain terahertz spectroscopy. The theoretically predicted peak of imaginary permittivity was observed on PLA-based nanocomposites filled with GNP, MWCNT and their mixtures both below and above the percolation threshold. Terahertz spectroscopy was demonstrated as a sensitive tool for the estimation of filler distribution character. For instance, the agreement between the experimental value of complex permittivity obtained for mono-filler GNP-based composites and Maxwell Garnett effective medium theory approximation indicates the mostly uniform distribution of insulated graphene nanoplatelets inside the polymer matrix.

The strong variation of the imaginary part of the permittivity dispersion followed by the relatively weak impact to its real part was experimentally shown for the set of bi-filler composites containing 6 wt. % of nanocarbon fillers in total. The variation of GNP fraction in the ternary composite resulted in a change of imaginary permittivity peak frequency, and the real part of permittivity remained mostly unchanged, giving the possibility of electromagnetic property tuning. A simple variation of fillers proportion during the production of the composites by co-extrusion method allows one to precisely control the position of the ϵ'' peak.

Finally, the combination of different nanocarbon fillers allows precise modification of the EM properties of a composite filled with relatively cheap GNPs by addition of CNTs, thereby obtaining a material with high THz performance.

4. TRI-PERIODIC POROUS STRUCTURES FOR ELECTROMAGNETIC SHIELDING APPLICATIONS

The problem of electromagnetic shielding has its extreme importance due to the intensification of wireless technologies development and electromagnetic pollution. Modern applications establish the tasks, which may not be effectively solved with continuous metal screen or metallic Faraday cages due to their weight and/or high reflectivity. In order to create lightweight EM shields it is necessary to pay an attention to the porous media. High absorbance may be achieved applying the structures with pre-defined electromagnetic properties distribution [107, 137, 182].

There are several approaches to create conductive porous media. Carbonization of the sacrificial tannin or TPU foams [203, 204] or even steamed buns [205] by means of annealing in inert gas atmosphere allows to create lightweight porous absorbers with outstanding shielding effectiveness. However, the mechanical properties of such structures are less attractive.

4.1. Creation of tri-periodic structures for electromagnetic measurements

For the electromagnetic properties investigation the samples of TPMS geometries was printed with pure TPU and TPU/MWCNT, TPU/MWCNT-GNP composites (see the Section 2.1.2). Structures were printed with two different porosities: 20 and 60 %. The scale of 3 unit cells per 1 cm was chosen in order to make the inhomogeneities smaller than the typical wavelength at investigated frequency range (i.e. to be able to apply the long-wave approximation).

Figure 4.1 shows an optical image of a G60 structures printed of pure TPU and 16×8 mm sample of TPU/MWCNT-GNP composite. The 1 cm³ cube of G60 contains 3×3×3 unit cells. Samples made of both nanocarbon-based composites have shown the pronounced elasticity and mechanical strength in more than enough amount for repeatable measurements of electromagnetic properties.

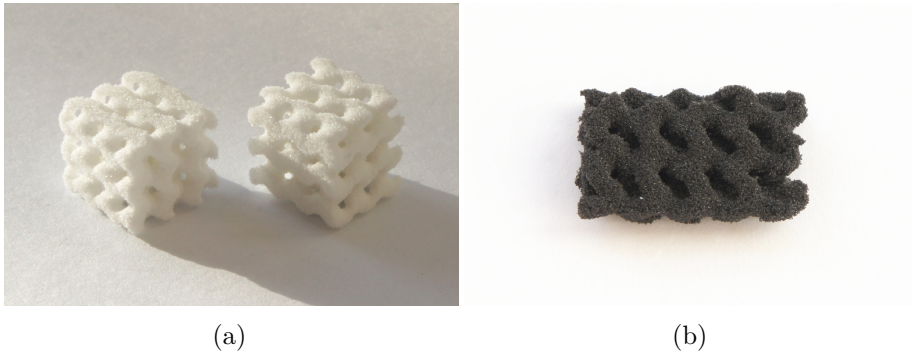


Figure 4.1: Optical image of G60 structure printed of pure TPU (a) and TPU/MWCNT composite (b).

The data obtained by means of electron microscopy points out that both TPU/MWCNT and TPU/MWCNT-GNP composites forms as a segregated medium after printing (see Figure 4.2b, c and e, f respectively).

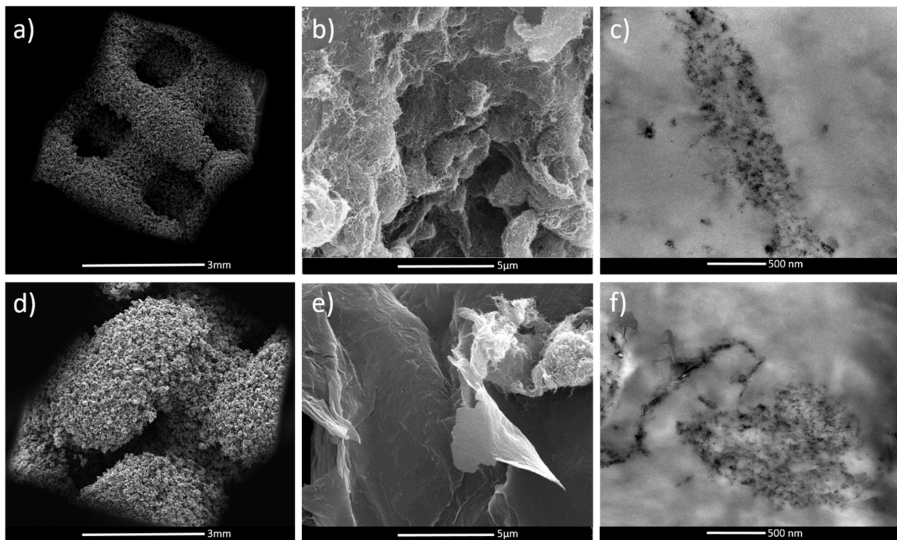


Figure 4.2: SEM of D60 (a) and G60 (d) structures printed with TPU/MWCNT. SEM (b) and TEM (c) images of TPU/MWCNT composite, SEM (e) and TEM (f) images of TPU/MWCNT-GNP after G60 structure printing [43].

Scanning electronic microscopy demonstrates that pre-sintering distribution of carbon nanoparticles on the surface of TPU powder particles is, to a certain degree, remained after the sintering process, which leads

to a continuous conductive network forming through whole sintered body. By means of transmission electronic microscope it is possible to assume the percolation network thread thickness in the range of 200~500 nm. However, at the submicron scale the composite may be considered as a porous medium, therefore, printed TPMS structure will possess both millimeter scale and submicron scale (i.e. multilevel) porosity.

4.2. Electromagnetic properties of tri-periodic structures

The broadband characterization of electromagnetic properties was performed in low-frequency, microwave and terahertz ranges. The impedance spectroscopy was used to ensure the percolation network existence. The conductivity of G20 and G60 porous structures made of TPU/MWCNT and TPU/(MWCNT-GNP) powders was investigated in a 100 kHz – 1 MHz frequency range. Measurements were conducted by a HP4284A LCR-meter (Zurich Instruments, Cambridge, MA, USA). Specimens of approximate $\sim 5 \times 5 \times 3$ mm³ dimensions were placed between two parallel electrodes and measured as quasi-bulk samples. The LCR-meter measures the values of capacity and loss tangent, which allows calculating the conductivity.

The microwave electromagnetic response of G20 and G60 porous structures containing MWCNTs and MWCNTs-GNP was investigated in Ku-band (12–18 GHz) using a Micran R4M (Micran, Tomsk, Russia) vector analyzer and rectangular waveguide transmission line with cross-sectional dimensions of 16×8 mm². Plain-parallel samples of 10.6 mm thickness were placed into the waveguide and their complex S-parameters were measured. The complex permittivity values were calculated from the experimental data solving Equations 2.21 and 2.22.

In the terahertz range the electromagnetic response was measured by means of T-Spec time-domain spectrometer. Two millimeters thick plane-parallel slices of porous structure (7×5 cm²) were placed between emitter and detector normally to the incident EM wave. The measurements were done in both transmission and reflection modes. The absorption coefficient, A , was calculated as $A = 1 - T - R$, where T and R are the transmission and reflection coefficients, respectively.

The broadband spectra of effective conductivity is shown in Figure 4.3. All percolated materials possess a similar frequency dependence of conductivity, consisting of two regions: the DC-like frequency-

independent region is observable at lower frequencies, while at higher frequencies, the $\sigma \sim \omega^\alpha$ dependence exists. For both TPU/MWCNT and TPU/MWCNT-GNP structures the DC-like plateau of the broadband conductivity dependence is an evidence of percolation expected from microscopy results.

The absorption coefficient was measured in microwave and terahertz frequency ranges for the system of 10 mm layer of gyroidal structure placed on metal plate. Such a setup allows to maximize the EM field energy absorption. As can be seen in Figure 4.4a, the absorption spectra are typical for interference in layered structures. That means both G20 and G60 behave as quasi-bulk materials with effective permittivity. The absorption maxima of G60 samples lay at 15 and 16 GHz for TPU/MWCNT and TPU/MWCNT-GNP, respectively, while less porous G20 structures possess the absorption minima at mentioned frequencies, meeting their maxima at frequencies lower than 12 GHz or higher than 18 GHz. Such behavior proves the expected difference in the effective permittivity of structures with different porosities.

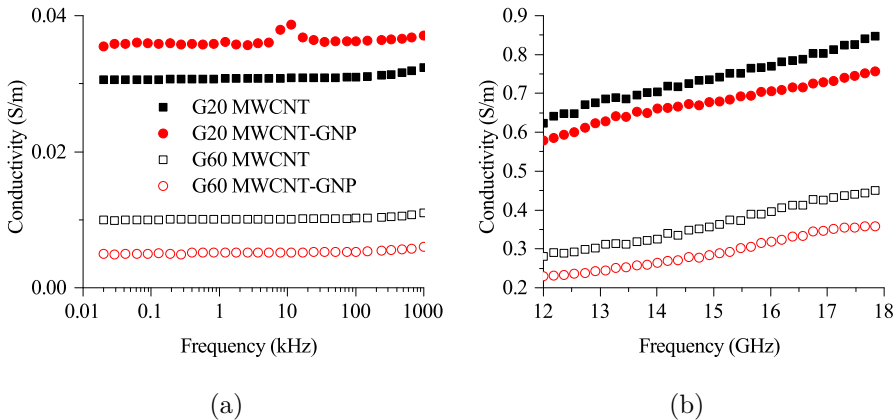


Figure 4.3: The effective value of porous structures broadband conductivity at 0.02 kHz–1 MHz (a) and 12–18 GHz (b).

The different situation is observed in the terahertz frequency region, where freestanding (i.e. without back-reflector) samples of all investigated composites demonstrate perfect broadband absorption starting from 0.3 THz, while the sample thickness was only 2 mm (Figure 4.4b). Such an effect may be explained by microscopic porosity of sintered composites.

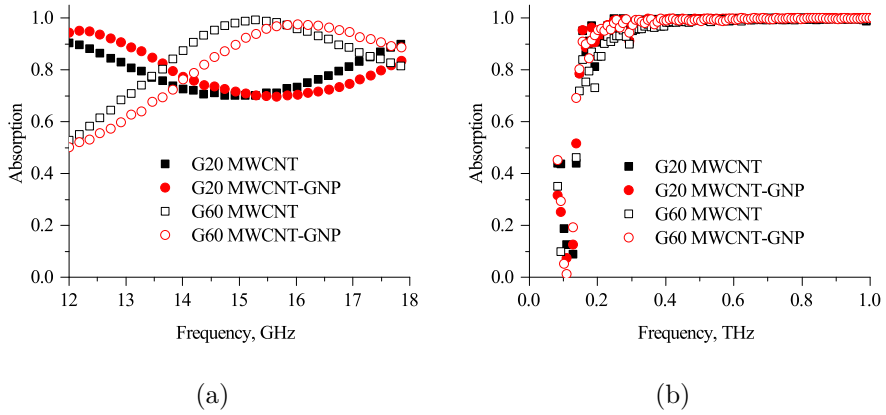


Figure 4.4: (a) Absorption coefficient of 10 mm layer of porous structures with metal back reflector in 12–18 GHz frequency range. (b) Absorption coefficient of 2 mm freestanding layer of porous structures at 0.1–1 THz.

4.3. Summary

- Selective laser sintering 3D printing technique is suitable for preparation of lightweight structures with multilevel porosity. Samples prepared by mentioned technique demonstrated excellent electromagnetic performance alongside with thermal, piezoelectric, etc. described in [43, 55]
- TPU powder with nanocarbon forms a segregated conductive network. Combination of MWCNT and GNP fillers slightly decreases its conductivity (resulting in the decrease of porous structure effective conductivity). However, the mixture of MWCNTs and GNP improves the thermal stability and minimizes coalescence issues existing for systems filled with only GNP particles [43].
- As long, as the characteristic dimensions of porous structures is shorter than the wavelength, the structural pattern does not significantly affect the electromagnetic properties of structure. However, among the investigated TPMS the gyroidal geometry possess the lowest spatial fluctuation of density. Moreover, gyroid is the only option to achieve the highest porosities, because other investigated TPMS are unable to maintain the continuity.
- The modeling shows that gyroid-based system with porosity varied along z -axis must behave as a perfect broadband absorber similar to pyramidal structures described before [182].

5. TERAHERTZ OPTICAL ELEMENTS BASED ON VERTICALLY ALIGNED ARRAYS OF MULTI-WALLED CARBON NANOTUBES

In memory of A. G. Kurenya (1985–2021), without whose kindheartedness, expertise, and strong devotion this research would not be possible.

Elements of microwave and terahertz optics based on regular structures (split-rings [5], Fresnel lens, gratings or grids [10, 60, 206–208]), nanorods [7, 116] and more complex spatial structures [137] recently attracted additional interest since the development of high-speed wireless networking and terahertz optical systems. However, the most of technologies used for such structures preparation are expensive and complex. Therefore any innovations in material engineering methods may be helpful in widening the applications of terahertz optics and spreading its benefits.

The current chapter is introducing the results obtained with help of the novel technology combining the laser-assisted profiling of vertically-aligned arrays of multi-walled nanotubes followed by the polymer impregnation of the profiled nanocarbon material. The agreement between the experimental results presented in current chapter and the model introduced in Section 2.2.3 proves that the electromagnetic response of resulting structure in terahertz frequency range is dependent on both polymer and engraved array parameters. Moreover, the introduced model allows to predict the properties of passive optical elements prepared using the developed technology.

5.1. Pyramid-based structure resonant absorbance

The amplitude of signal normally reflected from periodic arrays of pyramids with $232.9 \pm 11.9 \mu\text{m}$ with $54.9 \pm 6.9 \mu\text{m}$ uncut layer at the bottom (see Figure 2.4) covered with epoxy resin layer of maximum $77.0 \pm 4.5 \mu\text{m}$ (Figure 2.5) was measured in 0.1–1 THz frequency range by means of EXPLA TSpec time-domain terahertz spectrometer.

The comparison between experimentally measured amplitude of the signal reflected by the array of pyramids covered with epoxy resin (Fig. 2.5) and fitted values obtained by Eq. (2.20) is presented in Fig. 5.1.

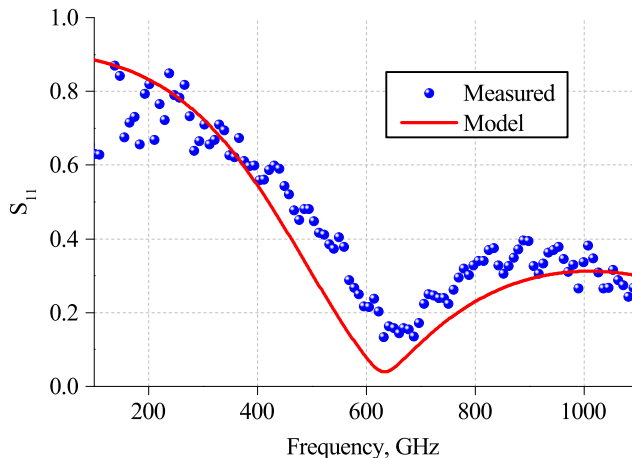


Figure 5.1: Amplitude of back-reflected signal S_{11} from periodic pyramidal CNT-array (pyramids of $232.9 \pm 11.9 \mu\text{m}$ height and $54.9 \pm 6.9 \mu\text{m}$ uncut bottom layer covered by $<77 \mu\text{m}$ layer of epoxy resin). The symbols correspond to the experimental data, solid line — to the modeling results.

The experimental observations are in good agreement with modeling results. Mean absolute percentage error value was 6.4 %. The difference between experiment and modeling results may be related to the nonlinear dependence of epoxy layer thickness in the region near the pyramids base. The model curve in Fig. 5.1 was obtained with the following set of parameters: $\beta = -0.9$, $\varepsilon = 3 - 0.4i$, $h_e = 0.09 \text{ mm}$, $h = 0.25 \text{ mm}$. The results showed that the produced metasurface acts as reflection selective surface with maximal absorption near $\nu_0 = 700 \text{ GHz}$. Below ν_0 the amplitude of signal reflected from CNT array is 0.8, while above ν_0 the S_{11} amplitude is near 0.4.

5.2. 1D and 2D-periodic structures electromagnetic response

The terahertz radiation used in the time-domain spectrometer has linear polarization, which make possible the investigation of engraved structures with expected polarization-dependent electromagnetic response. For that

purpose the set of engraved strips and columns (further referred as 1D and 2D gratings) was created using the method introduced in the Section 2.1.4. The engraving conditions included: scanning speed of 17 mm/s, laser power of 15 W, grating period of $\sim 250 \mu\text{m}$, and engraved element height of $\sim 170 \mu\text{m}$ (see the Figure 5.2). The engraved strips were covered with epoxy resin (Crystal 76) under vacuum conditions. The resin mixed with hardener was applied to the MWCNT array with a pipette until the sample was completely soaked with resin. The excess resin was allowed to drip down from the inclined samples under evacuation.

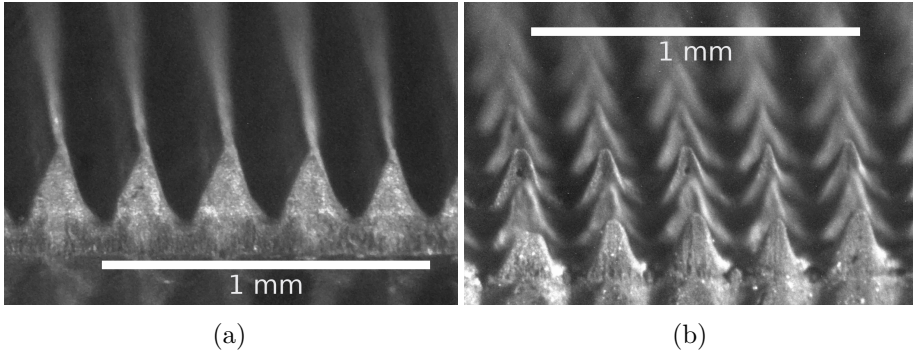


Figure 5.2: Optical images of engraved 1D (a) and 2D (b) gratings with $250 \mu\text{m}$ period and $\sim 300 \mu\text{m}$ total height before the epoxy resin covering.

During the measurements 2D gratings were placed normally to the radiation (similar to the previous experiment, see the Figure 2.11(a)), while the gratings of 1D structures were oriented parallel and orthogonal to the electromagnetic field vector \vec{E} . The reflection coefficients $R = S_{11}^2$ of investigated structures and pristine $\sim 300 \mu\text{m}$ MWCNTs array covered with $70\sim 90 \mu\text{m}$ layer of epoxy resin are shown in Figure 5.3. 1D TE curve corresponds to the grating orientation parallel to \vec{E} while 1D TM means the 90° angle between gratings and electric field.

The pristine MWCNT array covered with epoxy possess the reflection coefficient value in the range of 30 % to 80 % in the frequency range of 0.3–1 THz (Figure 5.3). Such electromagnetic response is a result of the combination of a flat MWCNT array absorption and an interference of waves reflected from the interfaces between free space, epoxy resin and MWCNT array.

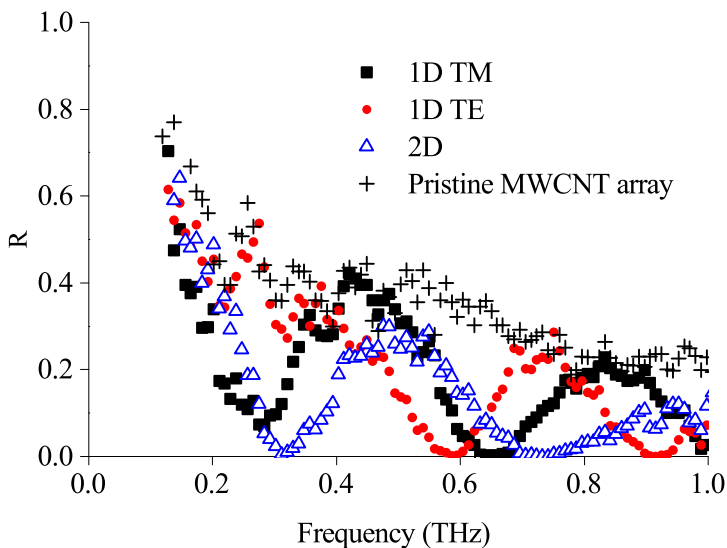


Figure 5.3: Reflection coefficients of pristine MWCNT array, 1D and 2D gratings with 250 μm period.

Considering the patterned samples, the portion of reflected radiation decreased to about 1–5 % near 1 THz. This indicates better absorption performance of patterned samples in comparison to pristine MWCNT array covered with similar amount of resin. For both 1D and 2D gratings the pronounced reflection coefficient oscillations nonexistent for the pristine coated array were observed. Such oscillations arose due to the interference between waves reflected from not only the polymer cover, but the strips and pyramids of MWCNT arrays. Moreover, the response of 1D sample depends on the spatial orientation of gratings relative to the incident wave polarization.

It is noteworthy that the reflection coefficient spectrum of the 1D pattern in TM orientation is close to such of 2D pattern. This suggests that the polarization-dependent properties can be assigned to the geometrical properties of gratings. Therefore, patterned arrays of CNTs can promote the design of advanced THz devices, which can distinguish polar biomolecules more accurately.

5.3. Summary

The concept of frequency selective reflector based on pyramidal metasurfaces and polarization-dependent reflector were implemented and investigated. The impact of pyramids height and dielectric covering layer to the electromagnetic response of investigated structures was theoretically described in a wide frequency range. The possibility to control the reflective behavior of the 2D metasurfaces was theoretically substantiated. The polarization-dependent electromagnetic response of 1D grating implemented with help of the introduced technique was demonstrated.

The 1D and 2D metasurfaces were produced by the laser engraving of vertically aligned MWCNT array followed by the dielectric layer covering. THz reflectivity measurements proved the existence of theoretically predicted local reflection minima. The reflection minimum position may be tuned by change of dielectric cover thickness, while the height of pyramids defines the damping rate of reflected signal.

The presented design of metasurfaces with frequency- and polarization-selective absorption of the electromagnetic radiation in the sub-millimeter frequency range is one of the numerous examples of THz components (such as frequency selective surfaces, filters, lenses, attenuators, etc.) that is possible to be implemented using perfect absorption ability and electromagnetic response peculiarities of 3D-patterned CNT arrays.

CONCLUSIONS

This thesis is focused on the methods of composite materials engineering. The introduced work is divided into 3 interrelated tasks: investigation of composite material structure by means of terahertz spectroscopy; creation of regular porous structures by means of 3D printing; introduction of novel material engineering method based on laser profiling of vertically-aligned MWCNT arrays followed with polymer impregnation.

The following results were obtained during the performed work:

First, the impact of nanofiller particles excluded from the percolation network was demonstrated by means of transmission time-domain terahertz spectroscopy. The theoretically predicted peak of imaginary permittivity was observed on PLA-based nanocomposites filled with GNP, MWCNT and their mixtures both below and above the percolation threshold. Terahertz spectroscopy was demonstrated as a sensitive tool for the estimation of filler distribution character. For instance, the agreement between the experimental value of complex permittivity obtained for mono-filler GNP-based composites and Maxwell Garnett effective medium theory approximation indicates the mostly uniform distribution of insulated graphene nanoplatelets inside the polymer matrix.

The strong variation of the imaginary part of the permittivity dispersion followed by the relatively weak impact to its real part was experimentally shown for the set of hybrid composites containing 6 wt. % of nanocarbon fillers in total. The variation of GNP fraction in the ternary composite resulted in a change of imaginary permittivity peak frequency, and the real part of permittivity remained mostly unchanged, giving the possibility of electromagnetic property tuning. A simple variation of fillers proportion during the production of the composites by co-extrusion method allows one to precisely control the position of the ϵ'' peak.

The combination of different nanocarbon fillers allows precise modification of the EM properties of a composite filled with relatively cheap GNPs by addition of CNTs, thereby obtaining a material with high THz performance.

Second, the absorptive structures with regular porosity were obtained by means of SLS 3D printing with nanocarbon-containing TPU powder. Their electromagnetic performance was investigated in mi-

crowave and terahertz frequency regions. The specific inner structure of material under investigation, namely, the segregated medium, was involved in the electromagnetic response of final printed structure. It was shown, that both TPU/MWCNT and TPU/MWCNT-GNP composites are applicable for absorptive structures building.

The porous structures were built on tri-periodic minimum surfaces geometry. It was shown that among 3 compared TPMS the gyroid-based structure possess the mostly constant density, while the Schwartz geometry gives the pronounced density fluctuation. However, each of considered geometries may find its application. For instance, the gyroid-based system with porosity varied along z -axis shows the best absorbing properties.

Finally, concepts of frequency selective and polarization-dependent reflectors based on pyramidal metasurfaces and gratings were implemented and investigated. The impact of pyramids height and dielectric covering layer to the electromagnetic response of investigated structures was theoretically described in a wide frequency range. The possibility to control the reflective behavior of the metasurfaces was theoretically substantiated.

The metasurfaces were produced by the laser engraving of vertically aligned MWCNT array followed by the dielectric layer covering. In accordance with the theoretical prediction, the experimental reflection spectrum exhibited the local minima in the THz range. Its position is determined by the thickness of the dielectric cover, while the height of pyramids defines the dumping rate of the reflected signal.

The presented design of metasurfaces which effectively absorb the electromagnetic radiation in the submillimeter frequency range is a proof of concept for the introduced MWCNT arrays patterning method. Frequency selective surfaces, filters, lenses, attenuators, etc. are possible to be implemented using the perfect absorption ability and electromagnetic response peculiarities of MWCNT arrays with a specified pattern and polymer impregnation.

The results of current work may be attributed to the technology readiness level 3 (i.e. a proof of concept) [209]. The imaginary permittivity maximum investigation including the measurements and effective medium model application allows the non-destructive detection of insulated filler particles in polymer composites below and above the percolation thresh-

old. The experimental observations of regular structures electromagnetic response supported by analytical modeling provide a solid laboratory-proved background for scalable cost-efficient technological protocol of ultra-lightweight components of microwave and THz optics.

BIBLIOGRAPHY

- [1] A. K. Mallik *et al.*, “Fabrication of polysaccharide-based materials using ionic liquids and scope for biomedical use,” in *Functional Polysaccharides for Biomedical Applications*, Elsevier, 2019, pp. 131–171.
- [2] N. Ali *et al.*, “Fabrication strategies for functionalized nanomaterials,” in *Nanomaterials: Synthesis, Characterization, Hazards and Safety*, Elsevier, 2021, pp. 55–95.
- [3] K. K. Chawla, *Composite Materials: Science and Engineering*. Cham: Springer International Publishing, 2019.
- [4] C. Caloz, *Electromagnetic metamaterials: transmission line theory and microwave applications: the engineering approach*, in collab. with T. Itoh. Hoboken, N.J: John Wiley & Sons, 2006, 352 pp.
- [5] H. O. Moser *et al.*, “Terahertz response of a microfabricated rod-split-ring-resonator electromagnetic metamaterial,” *Physical review letters*, vol. 94, no. 6, p. 063 901, 2005.
- [6] W. Cai and V. Shalaev, *Optical Metamaterials*. New York, NY: Springer New York, 2010.
- [7] C. R. Simovski *et al.*, “Wire Metamaterials: Physics and Applications,” *Advanced Materials*, vol. 24, no. 31, pp. 4229–4248, Aug. 2012.
- [8] C. L. Holloway *et al.*, “An overview of the theory and applications of metasurfaces: The two-dimensional equivalents of metamaterials,” *IEEE Antennas and Propagation Magazine*, vol. 54, no. 2, pp. 10–35, Apr. 2012.
- [9] H. Lin *et al.*, “Design and fabrication of moth-eye subwavelength structure with a waist on silicon for broadband and wide-angle anti-reflection property,” *Coatings*, vol. 8, no. 10, p. 360, Oct. 9, 2018.
- [10] V. Popov *et al.*, “Designing Metagratings via Local Periodic Approximation: From Microwaves to Infrared,” *Physical Review Applied*, vol. 11, no. 4, Apr. 2019.

- [11] J. Bonse, “Quo vadis LIPSS?—recent and future trends on laser-induced periodic surface structures,” *Nanomaterials*, vol. 10, no. 10, p. 1950, Sep. 30, 2020.
- [12] K. Khorkov *et al.*, “Wettability surface control on stainless steel by LIPSS formation,” *Journal of Physics: Conference Series*, vol. 1822, no. 1, p. 012 010, Feb. 1, 2021.
- [13] A. Thomas, “Functional materials: From hard to soft porous frameworks,” *Angewandte Chemie International Edition*, vol. 49, no. 45, pp. 8328–8344, Nov. 2, 2010.
- [14] P. Dharap *et al.*, “Nanotube film based on single-wall carbon nanotubes for strain sensing,” *Nanotechnology*, vol. 15, no. 3, pp. 379–382, Mar. 2004.
- [15] S. Kumar *et al.*, “Terahertz Spectroscopy of Single-Walled Carbon Nanotubes in a Polymer Film: Observation of Low-Frequency Phonons,” *The Journal of Physical Chemistry C*, vol. 114, no. 29, pp. 12 446–12 450, Jul. 2010.
- [16] S. Paszkiewicz *et al.*, “Synergetic effect of single-walled carbon nanotubes (SWCNT) and graphene nanoplatelets (GNP) in electrically conductive PTT-block-PTMO hybrid nanocomposites prepared by in situ polymerization,” *Composites Science and Technology*, vol. 118, pp. 72–77, Oct. 2015.
- [17] F. H. Gojny *et al.*, “Surface modified multi-walled carbon nanotubes in CNT/epoxy-composites,” *Chemical Physics Letters*, vol. 370, no. 5-6, pp. 820–824, Mar. 2003.
- [18] A. V. Okotrub *et al.*, “Transmission of terahertz radiation by anisotropic MWCNT/polystyrene composite films,” *Physica Status Solidi (B)*, vol. 248, no. 11, pp. 2568–2571, Nov. 2011.
- [19] M. V. Shuba *et al.*, “Role of finite-size effects in the microwave and subterahertz electromagnetic response of a multiwall carbon-nanotube-based composite: Theory and interpretation of experiments,” *Physical Review B*, vol. 88, no. 4, p. 045 436, 2013.
- [20] Y. Kato *et al.*, “Stretchable electromagnetic-interference shielding materials made of a long single-walled carbon-nanotube-elastomer composite,” *RSC advances*, vol. 7, no. 18, pp. 10 841–10 847, 2017.

- [21] S.-E. Lee, O. Choi, and H. T. Hahn, "Microwave properties of graphite nanoplatelet/epoxy composites," *Journal of Applied Physics*, vol. 104, no. 3, p. 033705, Aug. 2008.
- [22] X. Sun *et al.*, "Developing Polymer Composite Materials: Carbon Nanotubes or Graphene?" *Advanced Materials*, vol. 25, no. 37, pp. 5153–5176, Oct. 2013.
- [23] A. Kumar and P. S. Alegaonkar, "Impressive Transmission Mode Electromagnetic Interference Shielding Parameters of Graphene-like Nanocarbon/Polyurethane Nanocomposites for Short Range Tracking Countermeasures," *ACS Applied Materials & Interfaces*, vol. 7, no. 27, pp. 14833–14842, Jul. 2015.
- [24] D. Bychanok *et al.*, "Terahertz absorption in graphite nanoplatelets/polylactic acid composites," *Journal of Physics D: Applied Physics*, vol. 51, no. 14, p. 145307, Apr. 2018.
- [25] Z. Kang and S.-T. Lee, "Carbon dots: Advances in nanocarbon applications," *Nanoscale*, vol. 11, no. 41, pp. 19214–19224, 2019.
- [26] C. Xia *et al.*, "Evolution and synthesis of carbon dots: From carbon dots to carbonized polymer dots," *Advanced Science*, vol. 6, no. 23, p. 1901316, Dec. 2019.
- [27] D. Xu, Q. Lin, and H.-T. Chang, "Recent advances and sensing applications of carbon dots," *Small Methods*, vol. 4, no. 4, p. 1900387, Apr. 2020.
- [28] S. Zhu and G. Xu, "Single-walled carbon nanohorns and their applications," *Nanoscale*, vol. 2, no. 12, p. 2538, 2010.
- [29] N. Karousis *et al.*, "Structure, properties, functionalization, and applications of carbon nanohorns," *Chemical Reviews*, vol. 116, no. 8, pp. 4850–4883, Apr. 27, 2016.
- [30] K. I. Baskakova *et al.*, "Modification of structure and conductivity of nanohorns by toluene addition in carbon arc," *Fullerenes, Nanotubes and Carbon Nanostructures*, vol. 28, no. 4, pp. 342–347, Apr. 2, 2020.
- [31] S. Stolyarova *et al.*, "Bromination of carbon nanohorns to improve sodium-ion storage performance," *Applied Surface Science*, vol. 580, p. 152238, Apr. 2022.

- [32] F. Qin and C. Brosseau, "A review and analysis of microwave absorption in polymer composites filled with carbonaceous particles," *Journal of Applied Physics*, vol. 111, no. 6, p. 061301, Mar. 2012.
- [33] L. Liu, A. Das, and C. M. Megaridis, "Terahertz shielding of carbon nanomaterials and their composites – A review and applications," *Carbon*, vol. 69, pp. 1–16, Apr. 2014.
- [34] H. Deng *et al.*, "Progress on the morphological control of conductive network in conductive polymer composites and the use as electroactive multifunctional materials," *Progress in Polymer Science*, vol. 39, no. 4, pp. 627–655, Apr. 2014.
- [35] P. Kuzhir *et al.*, "Microwave probing of nanocarbon based epoxy resin composite films: Toward electromagnetic shielding," *Thin Solid Films*, vol. 519, no. 12, pp. 4114–4118, Apr. 2011.
- [36] A. D. Ugale *et al.*, "Nano-carbon: Preparation, assessment, and applications for NH₃ gas sensor and electromagnetic interference shielding," *RSC Advances*, vol. 6, no. 99, pp. 97266–97275, 2016.
- [37] O. V. Sedelnikova *et al.*, "Percolative Composites with Carbon Nanohorns: Low-Frequency and Ultra-High Frequency Response," *Materials*, vol. 12, no. 11, p. 1848, Jun. 2019.
- [38] P. Verma, P. Saini, and V. Choudhary, "Designing of carbon nanotube/polymer composites using melt recirculation approach: Effect of aspect ratio on mechanical, electrical and EMI shielding response," *Materials & Design*, vol. 88, pp. 269–277, Dec. 2015.
- [39] R. Kotsilkova *et al.*, "Mechanical and electromagnetic properties of 3D printed hot pressed nanocarbon/poly(lactic) acid thin films," *Journal of Applied Physics*, vol. 121, no. 6, p. 064105, Feb. 2017.
- [40] Y.-J. Wan *et al.*, "Anticorrosive, Ultralight, and Flexible Carbon-Wrapped Metallic Nanowire Hybrid Sponges for Highly Efficient Electromagnetic Interference Shielding," *Small*, vol. 14, no. 27, p. 1800534, Jul. 2018.

- [41] P. Song *et al.*, “Honeycomb structural rGO-MXene/epoxy nanocomposites for superior electromagnetic interference shielding performance,” *Sustainable Materials and Technologies*, vol. 24, e00153, Jul. 2020.
- [42] R. Kotsilkova *et al.*, “Exploring thermal annealing and graphene-carbon nanotube additives to enhance crystallinity, thermal, electrical and tensile properties of aged poly(lactic) acid-based filament for 3D printing,” *Composites Science and Technology*, vol. 181, p. 107712, Sep. 2019.
- [43] G. Rollo *et al.*, “On the synergistic effect of multi-walled carbon nanotubes and graphene nanoplatelets to enhance the functional properties of SLS 3D-printed elastomeric structures,” *Polymers*, vol. 12, no. 8, p. 1841, Aug. 17, 2020.
- [44] P. Kuzhir *et al.*, “Epoxy composites filled with high surface area-carbon fillers: Optimization of electromagnetic shielding, electrical, mechanical, and thermal properties,” *Journal of Applied Physics*, vol. 114, no. 16, p. 164304, Oct. 2013.
- [45] A. Joshi *et al.*, “Processing of graphene nanoribbon based hybrid composite for electromagnetic shielding,” *Composites Part B: Engineering*, vol. 69, pp. 472–477, Feb. 2015.
- [46] I. Minin *et al.*, “Investigations of some new focusing properties of cuboidaided photonic jet,” in *ACTUAL PROBLEMS OF RADIOPHYSICS: Proceedings of the VI International Conference "APR-2015" October, 5–10, 2015, Tomsk, Russia*, Red Square Scientific, Ltd., 2016.
- [47] E. Drakakis *et al.*, “A study of the electromagnetic shielding mechanisms in the GHz frequency range of graphene based composite layers,” *Applied Surface Science*, vol. 398, pp. 15–18, Mar. 2017.
- [48] R. Taherian, A. Kausar, and M. M. Ghorbani, *Electrical conductivity in polymer-based composites: experiments, modelling and applications*. 2019, OCLC: 1065207691.
- [49] S. Iijima, “Helical microtubules of graphitic carbon,” *Nature*, vol. 354, no. 6348, pp. 56–58, Nov. 1991.

- [50] D. Stauffer, *Introduction To Percolation Theory*, 2nd ed. Taylor & Francis, Apr. 21, 2014.
- [51] J. Sandler *et al.*, “Ultra-low electrical percolation threshold in carbon-nanotube-epoxy composites,” *Polymer*, vol. 44, no. 19, pp. 5893–5899, Sep. 2003.
- [52] D. Nuzhnyy *et al.*, “Broad-band conductivity and dielectric spectroscopy of composites of multiwalled carbon nanotubes and poly (ethylene terephthalate) around their low percolation threshold,” *Nanotechnology*, vol. 24, no. 5, p. 055 707, Feb. 2013.
- [53] A. V. Eletsii *et al.*, “Electrical characteristics of carbon nanotube-doped composites,” *Physics-Uspexhi*, vol. 58, no. 3, pp. 209–251, 2015.
- [54] G. Spinelli *et al.*, “Rheological and electrical behaviour of nanocarbon/poly(lactic)acid for 3D printing applications,” *Composites Part B: Engineering*, 2018.
- [55] A. Ronca *et al.*, “Selective Laser Sintering Fabricated Thermoplastic Polyurethane/Graphene Cellular Structures with Tailorable Properties and High Strain Sensitivity,” *Applied Sciences*, vol. 9, no. 5, p. 864, Feb. 2019.
- [56] M. Shuba *et al.*, “Frequency and density dependencies of the electromagnetic parameters of carbon nanotube and graphene nanoplatelet based composites in the microwave and terahertz ranges,” *Materials Research Express*, vol. 6, no. 9, p. 095 050, Jul. 3, 2019, Publisher: IOP Publishing.
- [57] **G. Gorokhov** *et al.*, “Carbon nanotubes vs graphene nanoplatelets for 3D-printable composites,” *IOP Conference Series: Materials Science and Engineering*, vol. 503, p. 012 010, Mar. 25, 2019.
- [58] J. Chen and G. Lu, “Controlled decoration of carbon nanotubes with nanoparticles,” *Nanotechnology*, vol. 17, no. 12, pp. 2891–2894, Jun. 2006.
- [59] G. Y. Slepyan *et al.*, “Electrodynamics of carbon nanotubes: Dynamic conductivity, impedance boundary conditions, and surface wave propagation,” *Physical Review B*, vol. 60, no. 24, p. 17 136, 1999.

- [60] J. F. O Hara, R. D. Averitt, and A. J. Taylor, “Terahertz surface plasmon polariton coupling on metallic gratings,” *Optics express*, vol. 12, no. 25, pp. 6397–6402, 2004.
- [61] Y. Lan *et al.*, “Simulation of carbon nanotube THz antenna arrays,” *International Journal of Infrared and Millimeter Waves*, vol. 27, no. 6, pp. 871–877, Feb. 2007.
- [62] G. Y. Slepyan *et al.*, “Terahertz conductivity peak in composite materials containing carbon nanotubes: Theory and interpretation of experiment,” *Physical Review B*, vol. 81, no. 20, May 2010.
- [63] M. V. Shuba *et al.*, “Experimental evidence of localized plasmon resonance in composite materials containing single-wall carbon nanotubes,” *Physical Review B*, vol. 85, no. 16, p. 165 435, 2012.
- [64] S. Walia *et al.*, “Flexible metasurfaces and metamaterials: A review of materials and fabrication processes at micro- and nano-scales,” *Applied Physics Reviews*, vol. 2, no. 1, p. 011 303, Mar. 2015.
- [65] A. Ferraro *et al.*, “Flexible terahertz wire grid polarizer with high extinction ratio and low loss,” *Optics Letters*, vol. 41, no. 9, p. 2009, May 1, 2016.
- [66] G. Hanson, “Fundamental transmitting properties of carbon nanotube antennas,” *IEEE Transactions on Antennas and Propagation*, vol. 53, no. 11, pp. 3426–3435, Nov. 2005.
- [67] G. Y. Slepyan *et al.*, “Theory of optical scattering by achiral carbon nanotubes and their potential as optical nanoantennas,” *Physical Review B*, vol. 73, no. 19, p. 195 416, 2006.
- [68] P. Burke, L. S., and Y. Z., “Quantitative theory of nanowire and nanotube antenna performance,” *IEEE Transactions On Nanotechnology*, vol. 5, no. 4, pp. 314–334, Jul. 2006.
- [69] H. Li *et al.*, “Circuit Modeling and Performance Analysis of Multi-Walled Carbon Nanotube Interconnects,” *IEEE Transactions on Electron Devices*, vol. 55, no. 6, pp. 1328–1337, Jun. 2008.
- [70] A. Maffucci, G. Miano, and F. Villone, “A New Circuit Model for Carbon Nanotube Interconnects With Diameter-Dependent Parameters,” *IEEE Transactions on Nanotechnology*, vol. 8, no. 3, pp. 345–354, May 2009.

- [71] D. S. Bychanok *et al.*, “Anisotropic electromagnetic properties of polymer composites containing oriented multiwall carbon nanotubes in respect to terahertz polarizer applications,” *Journal of Applied Physics*, vol. 114, no. 11, p. 114304, Sep. 2013.
- [72] A. Zubair *et al.*, “Carbon nanotube fiber terahertz polarizer,” *Applied Physics Letters*, vol. 108, no. 14, p. 141107, Apr. 4, 2016.
- [73] O. V. Sedelnikova *et al.*, “Iron-filled multi-walled carbon nanotubes for terahertz applications: Effects of interfacial polarization, screening and anisotropy,” *Nanotechnology*, vol. 29, no. 17, p. 174003, Apr. 2018.
- [74] V. Ryzhii *et al.*, “Two-dimensional plasmons in lateral carbon nanotube network structures and their effect on the terahertz radiation detection,” *Journal of Applied Physics*, vol. 120, no. 4, p. 044501, Jul. 2016.
- [75] R. R. Hartmann, J. Kono, and M. E. Portnoi, “Terahertz science and technology of carbon nanomaterials,” *Nanotechnology*, vol. 25, no. 32, p. 322001, Aug. 2014.
- [76] O. Sedelnikova *et al.*, “Laser patterning of aligned carbon nanotubes arrays: Morphology, surface structure, and interaction with terahertz radiation,” *Materials*, vol. 14, no. 12, p. 3275, Jun. 14, 2021.
- [77] K. S. Novoselov *et al.*, “Electric field effect in atomically thin carbon films,” *Science*, vol. 306, no. 5696, pp. 666–669, 2004.
- [78] A. K. Geim and K. S. Novoselov, “The rise of graphene,” in *Nanoscience and Technology*, Co-Published with Macmillan Publishers Ltd, UK, Aug. 2009, pp. 11–19.
- [79] G. De Bellis *et al.*, “Electromagnetic properties of composites containing graphite nanoplatelets at radio frequency,” *Carbon*, vol. 49, no. 13, pp. 4291–4300, Nov. 2011.
- [80] X. Jiang and L. T. Drzal, “Reduction in percolation threshold of injection molded high-density polyethylene/exfoliated graphene nanoplatelets composites by solid state ball milling and solid state shear pulverization,” *Journal of Applied Polymer Science*, vol. 124, no. 1, pp. 525–535, Apr. 2012.

- [81] O. A. Al-Hartomy *et al.*, “Dielectric and Microwave Properties of Graphene Nanoplatelets /Carbon Black Filled Natural Rubber Composites,” *International Journal of Materials and Chemistry*, vol. 2, no. 3, pp. 116–122, Aug. 2012.
- [82] O. A. Al-Hartomy *et al.*, “Dielectric and Microwave Properties of Natural Rubber Based Nanocomposites Containing Graphene,” *Materials Sciences and Applications*, vol. 03, no. 07, pp. 453–459, 2012.
- [83] M. S. Sarto *et al.*, “Synthesis, Modeling, and Experimental Characterization of Graphite Nanoplatelet-Based Composites for EMC Applications,” *IEEE Transactions on Electromagnetic Compatibility*, vol. 54, no. 1, pp. 17–27, Feb. 2012.
- [84] P. Kopyt *et al.*, “Electric Properties of Graphene-Based Conductive Layers from DC Up To Terahertz Range,” *IEEE Transactions on Terahertz Science and Technology*, vol. 6, no. 3, pp. 480–490, May 2016.
- [85] Z. Wang, J. Luo, and G. Zhao, “Dielectric and microwave attenuation properties of graphene nanoplatelet/epoxy composites,” *AIP Advances*, vol. 4, no. 1, p. 017139, Jan. 2014.
- [86] S. Kumar *et al.*, “Dynamic synergy of graphitic nanoplatelets and multi-walled carbon nanotubes in polyetherimide nanocomposites,” *Nanotechnology*, vol. 21, no. 10, p. 105702, Mar. 2010.
- [87] Y. Gao *et al.*, “Synergistic effects of filler size on thermal annealing-induced percolation in polylactic acid (PLA)/graphite nanoplatelet (GNP) nanocomposites,” *Nanocomposites*, vol. 3, no. 2, pp. 67–75, Apr. 2017.
- [88] H. Zhang *et al.*, “Synergistic effect of carbon nanotube and graphene nanoplates on the mechanical, electrical and electromagnetic interference shielding properties of polymer composites and polymer composite foams,” *Chemical Engineering Journal*, vol. 353, pp. 381–393, Dec. 2018.
- [89] B. Sareni *et al.*, “Effective dielectric constant of random composite materials,” *Journal of Applied Physics*, vol. 81, no. 5, pp. 2375–2383, Mar. 1997.

- [90] J. Sumfleth, X. C. Adroher, and K. Schulte, "Synergistic effects in network formation and electrical properties of hybrid epoxy nanocomposites containing multi-wall carbon nanotubes and carbon black," *Journal of Materials Science*, vol. 44, no. 12, pp. 3241–3247, Jun. 2009.
- [91] P. Bertasius *et al.*, "Fine Tuning of Electrical Transport and Dielectric Properties of Epoxy/Carbon Nanotubes Composites via Magnesium Oxide Additives," *Polymers*, vol. 11, no. 12, p. 2044, Dec. 2019.
- [92] P. Bertasius *et al.*, "Synergy effects in dielectric and thermal properties of layered ethylene vinyl acetate composites with carbon and Fe_3O_4 nanoparticles," *Journal of Applied Polymer Science*, vol. 137, no. 24, p. 48 814, Jun. 2020.
- [93] D. Meisak *et al.*, "Dielectric Relaxation in the Hybrid Epoxy/MWCNT/MnFe₂O₄ Composites," *Polymers*, vol. 12, no. 3, p. 697, Mar. 2020.
- [94] G. Spinelli *et al.*, "Nanocarbon/Poly(Lactic) Acid for 3D Printing: Effect of Fillers Content on Electromagnetic and Thermal Properties," *Materials*, vol. 12, no. 15, p. 2369, Jul. 2019.
- [95] E. Ivanov *et al.*, "PLA/Graphene/MWCNT Composites with Improved Electrical and Thermal Properties Suitable for FDM 3D Printing Applications," *Applied Sciences*, vol. 9, no. 6, p. 1209, Mar. 2019.
- [96] L. Yue *et al.*, "Epoxy composites with carbon nanotubes and graphene nanoplatelets – Dispersion and synergy effects," *Carbon*, vol. 78, pp. 268–278, Nov. 2014.
- [97] A. Gbaguidi, S. Namilae, and D. Kim, "Synergy effect in hybrid nanocomposites based on carbon nanotubes and graphene nanoplatelets," *Nanotechnology*, vol. 31, no. 25, p. 255 704, Apr. 2020.
- [98] O. Sedelnikova *et al.*, "Effect of fabrication method on the structure and electromagnetic response of carbon nanotube/polystyrene composites in low-frequency and Ka bands," *Composites Science and Technology*, vol. 102, pp. 59–64, Oct. 2014.

- [99] Z. Li *et al.*, “Selective laser sintering 3D printing: A way to construct 3D electrically conductive segregated network in polymer matrix,” *Macromolecular Materials and Engineering*, vol. 302, no. 11, p. 1700211, Nov. 2017.
- [100] W.-C. Yu *et al.*, “Selective electromagnetic interference shielding performance and superior mechanical strength of conductive polymer composites with oriented segregated conductive networks,” *Chemical Engineering Journal*, vol. 373, pp. 556–564, Oct. 2019.
- [101] Y. Zhan *et al.*, “Fabrication of a flexible electromagnetic interference shielding Fe_3O_4 @reduced graphene oxide/natural rubber composite with segregated network,” *Chemical Engineering Journal*, vol. 344, pp. 184–193, Jul. 2018.
- [102] G. Spinelli *et al.*, “Effects of Filament Extrusion, 3D Printing and Hot-Pressing on Electrical and Tensile Properties of Poly(Lactic) Acid Composites Filled with Carbon Nanotubes and Graphene,” *Nanomaterials*, vol. 10, no. 1, p. 35, Dec. 2019.
- [103] I. Blanco, “The use of composite materials in 3D printing,” *Journal of Composites Science*, vol. 4, no. 2, p. 42, Apr. 22, 2020.
- [104] Y.-J. Chen *et al.*, “Porous composites coated with hybrid nano carbon materials perform excellent electromagnetic interference shielding,” *Composites Part B: Engineering*, vol. 70, pp. 231–237, Mar. 2015.
- [105] D. Bychanok *et al.*, “Hollow carbon spheres in microwaves: Bio inspired absorbing coating,” *Applied Physics Letters*, vol. 108, no. 1, p. 013701, Jan. 2016.
- [106] D. S. Bychanok *et al.*, “Microwave radiation absorbers based on corrugated composites with carbon fibers,” *Technical Physics*, vol. 61, no. 12, pp. 1880–1884, Dec. 2016.
- [107] D. Bychanok *et al.*, “Fully carbon metasurface: Absorbing coating in microwaves,” *Journal of Applied Physics*, vol. 121, no. 16, p. 165103, Apr. 28, 2017.
- [108] A. Paddubskaya *et al.*, “Tunable Perfect THz Absorber Based on a Stretchable Ultrathin Carbon-Polymer Bilayer,” *Materials*, vol. 12, no. 1, p. 143, Jan. 2019.

- [109] G. Gorokhov *et al.*, “Creation of metasurface from vertically aligned carbon nanotubes as versatile platform for ultra-light THz components,” *Nanotechnology*, vol. 31, no. 25, p. 255 703, Apr. 3, 2020.
- [110] D. Ding *et al.*, “Rational design of core-shell co@c microspheres for high-performance microwave absorption,” *Carbon*, vol. 111, pp. 722–732, Jan. 2017.
- [111] K. Wang *et al.*, “Iron oxide@graphitic carbon core-shell nanoparticles embedded in ordered mesoporous n-doped carbon matrix as an efficient cathode catalyst for PEMFC,” *Applied Catalysis B: Environmental*, vol. 264, p. 118 468, May 2020.
- [112] M. Fadeev *et al.*, “Iron oxide @ gold nanoparticles: Synthesis, properties and potential use as anode materials for lithium-ion batteries,” *Colloids and Surfaces A: Physicochemical and Engineering Aspects*, vol. 603, p. 125 178, Oct. 2020.
- [113] M. Zdorovets *et al.*, “Phase transformations and changes in the dielectric properties of nanostructured perovskite-like LBZ composites as a result of thermal annealing,” *Ceramics International*, vol. 46, no. 10, pp. 14 460–14 468, Jul. 2020.
- [114] A. V. Okotrub *et al.*, “Arrays of carbon nanotubes aligned perpendicular to the substrate surface: Anisotropy of structure and properties,” *Nanotechnologies in Russia*, vol. 3, no. 3-4, pp. 191–200, 2008.
- [115] C. Castro *et al.*, “Dynamics of catalyst particle formation and multi-walled carbon nanotube growth in aerosol-assisted catalytic chemical vapor deposition,” *Carbon*, vol. 48, no. 13, pp. 3807–3816, Nov. 2010.
- [116] G. A. Wurtz *et al.*, “Designed ultrafast optical nonlinearity in a plasmonic nanorod metamaterial enhanced by nonlocality,” *Nature Nanotechnology*, vol. 6, no. 2, pp. 107–111, Feb. 2011.
- [117] D. Zagorskiy *et al.*, “Formation of nanowires of various types in the process of galvanic deposition of iron group metals into the pores of a track membrane,” *Membranes*, vol. 12, no. 2, p. 195, Feb. 8, 2022.

- [118] P. P. Kuzhir *et al.*, “Electromagnetic shielding efficiency in Ka-band: Carbon foam versus epoxy/carbon nanotube composites,” *Journal of Nanophotonics*, vol. 6, no. 1, p. 061 715, Dec. 2012.
- [119] A. Szczurek *et al.*, “Carbon periodic cellular architectures,” *Carbon*, vol. 88, pp. 70–85, Jul. 2015.
- [120] L. Egiziano *et al.*, “Morphological, rheological and electrical study of PLA reinforced with carbon-based fillers for 3D printing applications,” Ischia, Italy, 2018, p. 020 152.
- [121] Y. Song *et al.*, “Three-dimensional ordered mesoporous carbon spheres modified with ultrafine zinc oxide nanoparticles for enhanced microwave absorption properties,” *Nano-Micro Letters*, vol. 13, no. 1, p. 76, Feb. 2021.
- [122] R. D. Seager *et al.*, “Fabric antennas integrated with metamaterials,” in *IEEE European Microwave Conference in 2008*, 2008.
- [123] D. Micheli *et al.*, “Synthesis and electromagnetic characterization of frequency selective radar absorbing materials using carbon nanopowders,” *Carbon*, vol. 77, pp. 756–774, Oct. 2014.
- [124] S. Ogawa and M. Kimata, “Metal-insulator-metal-based plasmonic metamaterial absorbers at visible and infrared wavelengths: A review,” *Materials*, vol. 11, no. 3, p. 458, Mar. 20, 2018.
- [125] A. Y. I. Ashyap *et al.*, “Metamaterial inspired fabric antenna for wearable applications,” *International Journal of RF and Microwave Computer-Aided Engineering*, vol. 29, no. 3, e21640, Mar. 2019.
- [126] L. Wang, R. Zhou, and H. Xin, “Microwave (8–50 GHz) Characterization of Multiwalled Carbon Nanotube Papers Using Rectangular Waveguides,” *IEEE Transactions on Microwave Theory and Techniques*, vol. 56, no. 2, pp. 499–506, 2008.
- [127] B. Gorshunov *et al.*, “Terahertz spectroscopy of charge transport in films of pristine and doped single-wall carbon nanotubes,” *Carbon*, vol. 126, pp. 544–551, Jan. 2018.
- [128] P. Karlsen *et al.*, “Sign inversion in the terahertz photoconductivity of single-walled carbon nanotube films,” *Physical Review B*, vol. 98, no. 24, p. 241 404, 2018.

- [129] Y. Zhang *et al.*, “Broadband and tunable high-performance microwave absorption of an ultralight and highly compressible graphene foam,” *Advanced Materials*, vol. 27, no. 12, pp. 2049–2053, Mar. 2015.
- [130] J. Zou *et al.*, “Ultralight multiwalled carbon nanotube aerogel,” *ACS Nano*, vol. 4, no. 12, pp. 7293–7302, Dec. 28, 2010.
- [131] C. Hao *et al.*, “Superior microwave absorption properties of ultralight reduced graphene oxide/black phosphorus aerogel,” *Nanotechnology*, vol. 29, no. 23, p. 235 604, Jun. 8, 2018.
- [132] M. V. Shuba *et al.*, “Radiofrequency field absorption by carbon nanotubes embedded in a conductive host,” *Journal of Applied Physics*, vol. 108, no. 11, p. 114 302, Dec. 2010.
- [133] M. V. Shuba *et al.*, “Observation of the microwave near-field enhancement effect in suspensions comprising single-walled carbon nanotubes,” *Materials Research Express*, vol. 4, no. 7, p. 075 033, Jul. 2017.
- [134] K. Gnanasekaran *et al.*, “3D printing of CNT- and graphene-based conductive polymer nanocomposites by fused deposition modeling,” *Applied Materials Today*, vol. 9, pp. 21–28, Dec. 2017.
- [135] M. Angjellari *et al.*, “Beyond the concepts of nanocomposite and 3D printing: PVA and nanodiamonds for layer-by-layer additive manufacturing,” *Materials & Design*, vol. 119, pp. 12–21, Apr. 2017.
- [136] J. Ren and J. Yin, “3D-printed low-cost dielectric-resonator-based ultra-broadband microwave absorber using carbon-loaded acrylonitrile butadiene styrene polymer,” *Materials*, vol. 11, no. 7, p. 1249, Jul. 20, 2018.
- [137] R. Contractor, G. D’Aguanno, and C. Menyuk, “Ultra-broadband, polarization-independent, wide-angle absorption in impedance-matched metamaterials with anti-reflective moth-eye surfaces,” *Optics Express*, vol. 26, no. 18, p. 24 031, Sep. 3, 2018.
- [138] Y. Arbaoui *et al.*, “Full 3-D printed microwave termination: A simple and low-cost solution,” *IEEE Transactions on Microwave Theory and Techniques*, vol. 64, no. 1, pp. 271–278, Jan. 2016.

- [139] X. Lleshi *et al.*, “Design and full characterization of a 3-d-printed hyperbolic pyramidal wideband microwave absorber,” *IEEE Antennas and Wireless Propagation Letters*, vol. 20, no. 1, pp. 28–32, Jan. 2021.
- [140] A. Capasso *et al.*, “Ink-jet printing of graphene for flexible electronics: An environmentally-friendly approach,” *Solid State Communications*, vol. 224, pp. 53–63, Dec. 2015.
- [141] U. Kalsoom, P. N. Nesterenko, and B. Paull, “Recent developments in 3D printable composite materials,” *RSC Advances*, vol. 6, no. 65, pp. 60 355–60 371, 2016.
- [142] M. Mirzaee, S. Noghianian, and I. Chang, “Low-profile bowtie antenna with 3D printed substrate,” *Microwave and Optical Technology Letters*, vol. 59, no. 3, pp. 706–710, Mar. 2017.
- [143] M. A. Yakovleva and K. G. Batrakov, “Two layer graphene heterostructures for waves slowing down: Operator approach to waveguide problem,” *Journal of the Belarusian State University. Physics*, no. 1, pp. 73–82, Jan. 31, 2020.
- [144] H.-T. Chen *et al.*, “A metamaterial solid-state terahertz phase modulator,” *Nature Photonics*, vol. 3, no. 3, pp. 148–151, 2009.
- [145] H.-T. Chen *et al.*, “Manipulation of terahertz radiation using metamaterials,” *Laser & Photonics Reviews*, vol. 5, no. 4, pp. 513–533, Jul. 1, 2011.
- [146] L. Deng *et al.*, “Manipulating of different-polarized reflected waves with graphene-based plasmonic metasurfaces in terahertz regime,” *Scientific Reports*, vol. 7, no. 1, p. 10 558, Dec. 2017.
- [147] W. Lai *et al.*, “Ultrathin, highly flexible and optically transparent terahertz polarizer based on transparent conducting oxide,” *Journal of Physics D: Applied Physics*, vol. 53, no. 12, p. 125 109, Mar. 18, 2020.
- [148] Y. Malevich *et al.*, “Video-speed graphene modulator arrays for terahertz imaging applications,” *ACS Photonics*, vol. 7, no. 9, pp. 2374–2380, Sep. 16, 2020.
- [149] N. I. Zheludev, “A roadmap for metamaterials,” *Optics and Photonics News*, vol. 22, no. 3, p. 30, Mar. 1, 2011.

- [150] R. Wang *et al.*, “Graphene based functional devices: A short review,” *Frontiers of Physics*, vol. 14, no. 1, p. 13 603, Feb. 2019.
- [151] M. V. Shuba *et al.*, “Carbon nanotube sponges as tunable materials for electromagnetic applications,” *Nanotechnology*, vol. 29, no. 37, p. 375 202, Sep. 2018.
- [152] S. K. Patel *et al.*, “Graphene based tunable grating structure,” *Materials Research Express*, vol. 6, no. 2, p. 025 602, Nov. 2018.
- [153] S. K. Patel *et al.*, “Graphene-based tunable reflector superstructure grating,” *Applied Physics A*, vol. 125, no. 8, Aug. 2019.
- [154] R. Jadeja *et al.*, “Numerical investigation of graphene-based efficient and broadband metasurface for terahertz solar absorber,” *Journal of Materials Science*, vol. 55, no. 8, pp. 3462–3469, Mar. 2020.
- [155] J. D. Jackson, *Classical electrodynamics*, 3rd ed. New York: Wiley, 1999, 808 pp.
- [156] L. Chen, Ed., *Microwave electronics: measurement and materials characterisation*. Chichester: John Wiley, 2004.
- [157] J. Baker-Jarvis, R. G. Geyer, and P. D. Domich, “A nonlinear least-squares solution with causality constraints applied to transmission line permittivity and permeability determination,” *IEEE Transactions on Instrumentation and Measurement*, vol. 41, no. 5, pp. 646–652, Oct. 1992.
- [158] R. Schulz, V. Plantz, and D. Brush, “Shielding theory and practice,” *IEEE Transactions on Electromagnetic Compatibility*, vol. 30, no. 3, pp. 187–201, Aug. 1988.
- [159] N. Joseph, J. Varghese, and M. T. Sebastian, “Self assembled polyaniline nanofibers with enhanced electromagnetic shielding properties,” *RSC Advances*, vol. 5, no. 26, pp. 20 459–20 466, 2015.
- [160] J. E. Spanier and I. P. Herman, “Use of hybrid phenomenological and statistical effective-medium theories of dielectric functions to model the infrared reflectance of porous SiC films,” *Physical Review B*, vol. 61, no. 15, pp. 10 437–10 450, Apr. 2000.

- [161] A. H. Sihvola and I. V. Lindell, “Polarizability modeling of heterogeneous media,” *Progress in Electromagnetics Research (PIER 6), Dielectric Properties of Heterogeneous Materials*, Priou, A.(ed.), Elsevier, Amsterdam, 1992.
- [162] A. Efimova *et al.*, *Infra-red spectroscopy of reduced dimension solid-state systems*. Moscow: Lan’, 2016, 248 pp.
- [163] J.C. Maxwell Garnett, “XII. colours in metal glasses and in metallic films,” *Philosophical Transactions of the Royal Society of London. Series A, Containing Papers of a Mathematical or Physical Character*, vol. 203, no. 359, pp. 385–420, Jan. 1904.
- [164] D. A. G. Bruggeman, “Berechnung verschiedener physikalischer Konstanten von heterogenen Substanzen. I. Dielektrizitätskonstanten und Leitfähigkeiten der Mischkörper aus isotropen Substanzen,” *Annalen der Physik*, vol. 416, no. 7, pp. 636–664, 1935.
- [165] L. Jylhä and A. Sihvola, “Equation for the effective permittivity of particle-filled composites for material design applications,” *Journal of Physics D: Applied Physics*, vol. 40, no. 16, pp. 4966–4973, Aug. 21, 2007.
- [166] J. P. Angle *et al.*, “Comparison of two-phase thermal conductivity models with experiments on dilute ceramic composites,” *Journal of the American Ceramic Society*, vol. 96, no. 9, D. Smith, Ed., pp. 2935–2942, Sep. 2013.
- [167] A. Sakanas *et al.*, “Broadband dielectric spectroscopy of BaTiO₃-Ni_{0.5}Zn_{0.5}Fe₂O₄ composite ceramics,” *Journal of Alloys and Compounds*, vol. 602, pp. 241–247, Jul. 2014.
- [168] L. D. Landau and E. M. Lifshitz, *Course of theoretical physics*. Elsevier, 2013.
- [169] H. Looyenga, “Dielectric constants of heterogeneous mixtures,” *Physica*, vol. 31, no. 3, pp. 401–406, Mar. 1965.
- [170] H. C. Liu *et al.*, “Additive-manufactured stochastic polyimide foams for low relative permittivity, lightweight electronic architectures,” *ACS Applied Materials & Interfaces*, vol. 13, no. 23, pp. 27364–27371, Jun. 16, 2021.

- [171] W. Theiß, “The use of effective medium theories in optical spectroscopy,” in *Advances in Solid State Physics 33*, R. Helbig, Ed., vol. 33, Series Title: Advances in Solid State Physics, Berlin, Heidelberg: Springer Berlin Heidelberg, 1993, pp. 149–176.
- [172] L. R. Grace, “The effect of moisture contamination on the relative permittivity of polymeric composite radar-protecting structures at x-band,” *Composite Structures*, vol. 128, pp. 305–312, Sep. 2015.
- [173] “Figure 4. twin screw extruder (researchgate.net).,” ResearchGate. (2022), [Online]. Available: https://www.researchgate.net/figure/Twin-screw-extruder-Researchgatenet_fig3_337688729 (visited on 03/22/2022).
- [174] P. A. R. Munoz *et al.*, “Novel improvement in processing of polymer nanocomposite based on 2D materials as fillers,” *Express Polymer Letters*, vol. 12, no. 10, pp. 930–945, 2018.
- [175] X. Gan *et al.*, “Simultaneous realization of conductive segregation network microstructure and minimal surface porous macrostructure by SLS 3D printing,” *Materials & Design*, vol. 178, p. 107 874, Sep. 2019.
- [176] X. Wang *et al.*, “3D printing of polymer matrix composites: A review and prospective,” *Composites Part B: Engineering*, vol. 110, pp. 442–458, Feb. 2017.
- [177] “Sharebot SnowWhite 2 SLS 3D printer overview.” (2022), [Online]. Available: <https://www.sharebot.it/en/snowwhite-2/> (visited on 05/12/2022).
- [178] A. P. Singh *et al.*, “Probing the engineered sandwich network of vertically aligned carbon nanotube-reduced graphene oxide composites for high performance electromagnetic interference shielding applications,” *Carbon*, vol. 85, pp. 79–88, Apr. 2015.
- [179] L. Qiu *et al.*, “Remarkably enhanced thermal transport based on a flexible horizontally-aligned carbon nanotube array film,” *Scientific Reports*, vol. 6, no. 1, p. 21 014, Aug. 2016.

- [180] J. Jorudas *et al.*, “Characterization of graphene drude conductivity by terahertz and infrared spectroscopy methods,” in *2021 46th International Conference on Infrared, Millimeter and Terahertz Waves (IRMMW-THz)*, Chengdu, China: IEEE, Aug. 29, 2021, pp. 1–2.
- [181] D. Bychanok *et al.*, “Terahertz optics of materials with spatially harmonically distributed refractive index,” *Materials*, vol. 13, no. 22, p. 5208, Nov. 18, 2020.
- [182] D. Meisak *et al.*, “Robust design of compact microwave absorbers and waveguide matched loads based on DC-conductive 3D-printable filament,” *Journal of Physics D: Applied Physics*, vol. 53, no. 30, p. 305 301, Jul. 22, 2020.
- [183] M. Born and E. Wolf, *Principles of optics: electromagnetic theory of propagation, interference and diffraction of light*, 7th expanded ed. Cambridge ; New York: Cambridge University Press, 1999.
- [184] H. A. Macleod, *Thin-film optical filters* (Series in optics and optoelectronics), 4th ed. Boca Raton, FL: CRC Press/Taylor & Francis, 2010, 782 pp., OCLC: ocn176924832.
- [185] D. Bychanok *et al.*, “Exploring carbon nanotubes/BaTiO₃/Fe₃O₄ nanocomposites as microwave absorbers,” *Progress In Electromagnetics Research C*, 2016.
- [186] D. Bychanok *et al.*, “Window tinting films for microwave absorption and terahertz applications,” *Journal of Applied Physics*, vol. 131, no. 2, p. 025 110, Jan. 14, 2022.
- [187] Y. Ji *et al.*, “Dispersion and Alignment of Carbon Nanotubes in Liquid Crystalline Polymers and Elastomers,” *Advanced Materials*, vol. 22, no. 31, pp. 3436–3440, Apr. 2010.
- [188] O. Peters *et al.*, “Determination of the Carbon Nanotube Concentration and Homogeneity in Resin Films by THz Spectroscopy and Imaging,” *Journal of Infrared, Millimeter, and Terahertz Waves*, vol. 33, no. 12, pp. 1221–1226, Dec. 2012.
- [189] R. Casini *et al.*, “Dispersion of carbon nanotubes in melt compounded polypropylene based composites investigated by THz spectroscopy,” *Optics Express*, vol. 23, no. 14, p. 18 181, Jul. 2015.

- [190] R. Rungsawang *et al.*, “Terahertz spectroscopy of carbon nanotubes embedded in a deformable rubber,” *Journal of Applied Physics*, vol. 103, no. 12, p. 123 503, Jun. 2008.
- [191] X.-C. Zhang and J. Xu, *Introduction to THz wave photonics*. New York: Springer, 2010, OCLC: ocn428029012.
- [192] C. Wong *et al.*, “A precise numerical prediction of effective dielectric constant for polymer-ceramic composite based on effective-medium theory,” *IEEE Transactions on Components and Packaging Technologies*, vol. 23, no. 4, pp. 680–683, Dec. 2000.
- [193] H. Nishimura, N. Minami, and R. Shimano, “Dielectric properties of single-walled carbon nanotubes in the terahertz frequency range,” *Applied Physics Letters*, vol. 91, no. 1, p. 011 108, Jul. 2007.
- [194] R. Kotsilkova *et al.*, “Effects of sonochemical modification of carbon nanotubes on electrical and electromagnetic shielding properties of epoxy composites,” *Composites Science and Technology*, vol. 106, pp. 85–92, Jan. 2015.
- [195] D. A. Tsybouski, S. M. Bachilo, and R. B. Weisman, “Versatile Visualization of Individual Single-Walled Carbon Nanotubes with Near-Infrared Fluorescence Microscopy,” *Nano Letters*, vol. 5, no. 5, pp. 975–979, May 2005.
- [196] C. Barone, S. Pagano, and H. C. Neitzert, “Transport and noise spectroscopy of MWCNT/HDPE composites with different nanotube concentrations,” *Journal of Applied Physics*, vol. 110, no. 11, p. 113 716, Dec. 2011.
- [197] T. Makarova *et al.*, “Assessing carbon nanotube arrangement in polystyrene matrix by magnetic susceptibility measurements,” *Carbon*, vol. 96, pp. 1077–1083, Jan. 2016.
- [198] C. Li, E. T. Thostenson, and T.-W. Chou, “Sensors and actuators based on carbon nanotubes and their composites: A review,” *Composites Science and Technology*, vol. 68, no. 6, pp. 1227–1249, May 2008.
- [199] W. Bauhofer and J. Z. Kovacs, “A review and analysis of electrical percolation in carbon nanotube polymer composites,” *Composites Science and Technology*, vol. 69, no. 10, pp. 1486–1498, Aug. 2009.

- [200] A. Sadezky *et al.*, “Raman microspectroscopy of soot and related carbonaceous materials: Spectral analysis and structural information,” *Carbon*, vol. 43, no. 8, pp. 1731–1742, Jul. 2005.
- [201] A. C. Ferrari *et al.*, “Raman Spectrum of Graphene and Graphene Layers,” *Physical Review Letters*, vol. 97, no. 18, Oct. 2006.
- [202] L. Malard *et al.*, “Raman spectroscopy in graphene,” *Physics Reports*, vol. 473, no. 5-6, pp. 51–87, Apr. 2009.
- [203] G. Tondi *et al.*, “Tannin-based carbon foams,” *Carbon*, vol. 47, no. 6, pp. 1480–1492, May 2009.
- [204] M. Letellier *et al.*, “Electromagnetic properties of model vitreous carbon foams,” *Carbon*, vol. 122, pp. 217–227, Oct. 2017.
- [205] F. Qi *et al.*, “Robust Ti3C2Tx MXene/starch derived carbon foam composites for superior EMI shielding and thermal insulation,” *Materials Today Physics*, vol. 21, p. 100512, Nov. 2021.
- [206] I. Yamada *et al.*, “Terahertz wire-grid polarizers with micrometer-pitch Al gratings,” *Optics letters*, vol. 34, no. 3, pp. 274–276, 2009.
- [207] S. Indrišiūnas *et al.*, “Laser-processed diffractive lenses for the frequency range of 4.7 THz,” *Optics Letters*, vol. 44, no. 5, p. 1210, Mar. 1, 2019.
- [208] N. I. Valynets *et al.*, “Fluorinated graphene grating metasurface for terahertz dark state excitation,” *Nanotechnology*, vol. 34, no. 18, p. 185702, Apr. 30, 2023.
- [209] European Commission, *Technology readiness levels (TRL); extract from part 19 - commission decision c(2014)4995*, 2014.

PUBLICATIONS BY THE AUTHOR

1 publikacija / 1st publication

**THz Spectroscopy as a Versatile Tool for Filler Distribution
Diagnostics in Polymer Nanocomposites**

G. Gorokhov, D. Bychanok, I. Gayduchenko, Y. Rogov, E. Zhukova,
S. Zhukov, L. Kadyrov, G. Fedorov, E. Ivanov, R. Kotsilkova,







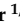


J. Macutkevic, P. Kuzhir,

Polymers **2020** 12 3037

DOI: 10.3390/polym12123037

Article

THz Spectroscopy as a Versatile Tool for Filler Distribution Diagnostics in Polymer Nanocomposites

Gleb Gorokhov ^{1,2,*} , Dzmitry Bychanok ^{1,3} , Igor Gayduchenko ⁴ , Yuriy Rogov ⁵ , Elena Zhukova ⁵, Sergei Zhukov ⁵, Lenar Kadyrov ⁵, Georgy Fedorov ⁵ , Evgeni Ivanov ^{6,7} , Rumiana Kotsilkova ⁶ , Jan Macutkevic ²  and Polina Kuzhir ^{1,8} 

¹ Institute for Nuclear Problems of Belarusian State University, Bobruiskaya Str., 11, 220006 Minsk, Belarus; dzmitrybychanok@ya.ru (D.B.); polina.kuzhir@gmail.com (P.K.)

² Physics Faculty, Vilnius University, Sauletekio 9, LT-10222 Vilnius, Lithuania; jan.macutkevic@gmail.com

³ Radiophysics Department, Tomsk State University, Lenin Avenue 36, 634050 Tomsk, Russia

⁴ Moscow Pedagogical State University, Malaya Pirogovskaya Str., 1/1, 119991 Moscow, Russia; igorandg@gmail.com

⁵ Moscow Institute of Physics and Technology, Institutskiy per., 9, 141701 Dolgoprudny, Russia; rogov.iup@phystech.edu (Y.R.); zhukovaelenka@gmail.com (E.Z.); zhukov@phystech.org (S.Z.); kadyrov@phystech.edu (L.K.); gefedorov@mail.ru (G.F.)

⁶ OLEM, Institute of Mechanics Bulgarian Academy of Sciences, Acad. G. Bonchev Str., Bl. 4, 1113 Sofia, Bulgaria; ivanov_evgeni@yahoo.com (E.I.); kotsilkova@yahoo.com (R.K.)

⁷ Research and Development of Nanomaterials and Nanotechnologies (NanoTech Lab Ltd.), Acad. G. Bonchev Str. Block 4, 1113 Sofia, Bulgaria

⁸ Institute of Photonics, University of Eastern Finland, Yliopistokatu 7, FI-80101 Joensuu, Finland

* Correspondence: glebgorokhov@yandex.ru

Received: 1 November 2020; Accepted: 15 December 2020; Published: 18 December 2020



Abstract: Polymer composites containing nanocarbon fillers are under intensive investigation worldwide due to their remarkable electromagnetic properties distinguished not only by components as such, but the distribution and interaction of the fillers inside the polymer matrix. The theory herein reveals that a particular effect connected with the homogeneity of a composite manifests itself in the terahertz range. Transmission time-domain terahertz spectroscopy was applied to the investigation of nanocomposites obtained by co-extrusion of PLA polymer with additions of graphene nanoplatelets and multi-walled carbon nanotubes. The THz peak of permittivity's imaginary part predicted by the applied model was experimentally shown for GNP-containing composites both below and above the percolation threshold. The physical nature of the peak was explained by the impact on filler particles excluded from the percolation network due to the peculiarities of filler distribution. Terahertz spectroscopy as a versatile instrument of filler distribution diagnostics is discussed.

Keywords: nanocomposites; THz spectroscopy; percolation threshold

1. Introduction

Functional materials based on micro- and nanocarbon structures (single and multi-walled nanotubes, graphene flakes, carbon dots, nanohorns, etc.) are of great interest for electromagnetic (EM) applications alongside composites [1–7] and structures [8–12] on their basis. The simplest way to drastically change the mechanical [13–16] and EM [17–20] properties of a dielectric material (such as a polymer, ceramic or glass) is to fill it with conductive particles of microscopic/nanoscale size. Possessing the highest possible aspect ratio among all nanocarbon fillers, nanotubes are the first candidate to create a conductive network inside a composite, i.e., reach the electric percolation threshold at the smallest possible concentration [2,21–23]. Another widely-used nanocarbon filler, namely,

graphene nanoplatelets, usually have the percolation threshold of 3.5–10% [24–28]. That is several orders higher than the 0.002% percolation threshold possible for composites based on single-walled nanotubes [2,23,29].

Multi-filler composites containing different types of fillers (including non-carbon) tend to form heterogeneous percolation networks [30–32]. This fact allows making composite materials without expensive fillers through the introduction of low-cost ones into the hybrid percolation network [33,34], or even enhancing the electromagnetic properties due to the synergistic effect [35–37]. Recently, bi-filler composites containing graphene nanoplatelets and carbon nanotubes have attracted great interest due to the possible synergistic effects in their mechanical, thermal and electric properties [38–41]. Besides the filler morphology, the percolation threshold value strongly depends on the composite preparation technology, the filler dispersion in the dielectric phase (matrix) and the filler–polymer interfacial interactions. In previous studies on the herein investigated nanocomposites, the electrical percolation thresholds of 0.5% for MWCNT/PLA, 6% for GNP/PLA and 3% for the bi-filler composite GNP/MWCNT/PLA were reported [42]. In the framework of the current research, we speak only about the electric percolation, i.e., the interconnected conductive network formation of filler particles, where the dielectric matrix plays a direct role only in the electron tunneling [43]. However, the characteristics of polymer and/or composite preparation technology may significantly affect the distribution of filler particles.

The dielectric properties of composites above the percolation threshold are mainly governed by electrical transport and Maxwell–Wagner relaxation. However, at higher frequencies, the contributions of big percolating clusters to the Maxwell–Wagner relaxation and the electrical conductivity become less important, so that in the terahertz frequency range it is possible to separate the contributions of individual nanoparticles' polarizations from the total dielectric permittivity [44]. The most commonly used non-destructive method of composite system characterization is low-frequency impedance spectroscopy, which allows one to easily establish percolation thresholds. However, the dispersion of nanoparticles may be investigated by other direct methods, such as transmission and scanning electron microscopy, and indirect methods (noise spectroscopy [45], magnetic susceptibility measurements [46], etc.) [3,47,48].

Time-domain terahertz spectroscopy is a non-destructive diagnostic method widely applied for the characterization of polymer-based nanocomposites' [49–51] and thin films' [52–54] electromagnetic properties in the 100 GHz–3 THz frequency range without any predefined assumptions. Being in between microwave and optical infra-red frequency regions, terahertz radiation easily transmits through most dielectric materials, while the metals and certain dielectrics, such as water, are non-transparent at the mentioned frequencies. Since the inhomogeneities' dimensions are orders less than the wavelength, spectral parameters of nanocomposites may be investigated in the framework of effective medium theory [55,56].

It is worth noting that the percolation threshold is usually considered as a filler concentration at which the percolation network appears. However, due to the imperfections of filler distribution, the actual number of particles involved in the percolation network is lower than the threshold. The current investigation is aimed at distinguishing the impacts of filler particles excluded from the percolation network on the terahertz electromagnetic properties of a composite. Additionally, the possibilities to tune the frequency dispersion of permittivity in THz range by variation of filler contents in composites based on GNP, MWCNT and their mixtures are discussed.

2. Materials

2.1. Composites Fabrication

The polymer matrix used in this study was Ingeo™ Biopolymer PLA-3D850 (Nature Works, Minnetonka, MN, USA). The nanofillers used were: commercially available industrial graphene nanoplates, TNIGNP (supplied by TimeNano, Chengdu, China), with 90 wt.% purity; number of layers < 30; thickness < 30 nm; diameter/median size 5–7 μm; aspect ratio: ~230/165; and volume resistivity < 0.15 Ohm/cm. Industrial grade OH-functionalized carbon nanotubes (multi-walled carbon nanotubes; MWCNTs; TimeNano, produced by CVD method) with 95 wt.% purity; 2.48 % OH⁻ content; size (outer D = 10–30 nm, length = 10–30 μm); aspect ratio: ~1000; and 100 S/m electric conductivity. A high amount of GNP impurities has an insufficient impact on the PLA composite processing due to the slip effect between GNPs in the PLA matrix during the shear flow [57]. Impurities mostly consist of amorphous carbon; thus their impacts on the electromagnetic properties may be neglected.

Twin-screw extruder (COLLIN Teach-Line ZK25T) was used to prepare nanocomposites at temperatures of 170–180 °C and screw speed 40 rpm in two runs. The mono- and bi-filler nanocomposite hybrids were processed using the melt extrusion method, which includes the preparation of master batches, and further dilution. It was previously shown that both GNP and MWCNT addition significantly suppress the thermal degradation and the aging of polymer nanocomposites (accelerated by humidity uptake, UV light, etc.), compared to the neat PLA, due to the nucleation and the barrier effects of nanofillers [58].

The mono-filler composites (PLA/MWCNT and PLA/GNP) with 1.5 wt.%, 3 wt.% and 6 wt.% filler contents, and the bi-filler composites (PLA/MWCNT/GNP) with 3 wt.% and 6 wt.% total filler content (combining GNP and MWCNT in different proportions) were prepared. Thin films of nanocomposites were obtained by hot pressing at 180 °C and pressure of 1 bar. Before pressing the test samples, composite pellets were dried in a vacuum oven at 80 °C for 4 hours in order to minimize the humidity uptake. The applied temperature range was significantly lower than the PLA thermal degradation onset (230 °C). The physicochemical characteristics of the PLA-based carbon nanocomposites under investigation are given in Table 1. Composites' crystallinity was 30%.

Table 1. Physicochemical characteristics of polymer composites after hot pressing [43,58].

Parameter	Value
Glass transition temperature T_g , °C	65
Cold crystallization temperature T_{cc} , °C	87–92
Melting temperature T_m , °C	175
Melt crystallization temperature T_g , °C	105
Crystallinity, %	30

2.2. Sample Characterization

According to the low-frequency measurements described before (see Figure 4 in [40]), the percolation threshold for MWCNTs lies between 1.5 and 3 wt.%, while GNP-based composite experiences percolation between 3 and 6 wt.%. Therefore, the set of samples under investigation contains both pre- and post-percolated composites.

The quality of nanoparticles and their distribution in the polymer matrix were examined by means of a Raman spectrometer combined with the confocal microscope (Nanofinder High End, Tokyo Instruments, Belarus-Japan). Raman spectra were obtained using 100X objective with NA = 0.95 and the spot size on the sample surface was 0.75 μm. The excitation source was a 473 nm laser.

It is known that the typical Raman spectra of carbon nanomaterials, including MWCNTs, GNP, graphene, etc., are dominated by three characteristic peaks centered at ~1360 cm⁻¹, ~1580–1600 cm⁻¹ and ~2600–2700 cm⁻¹ (usually referred to as D, G and 2D modes, respectively) [59–61]. On the other hand, the strongest features of pure PLA are located in the vicinity of 3000 cm⁻¹. Comparing the

Raman spectra collected from different points on the surface of the composite containing 1.5% GNP allows one to figure out GNP particles, points 1 and 2 in Figure 1b, correspond to the filler-free area and GNP, respectively. The contrast difference between GNP particles and pure polymer Figure 1a indicates the particle distribution in the polymer matrix. It is worth noting that pure PLA is optically transparent; hence, it is possible to observe GNP particles under the sample surface. However, the addition of a small MWCNT amount makes the PLA matrix non-transparent. As a result, in the bi-filler composites, GNP particles can be identified by optical microscope (Figure 1c) only on the sample surface. As can be seen from the Raman spectra (Figure 1d), in the bi-filler composites nanotubes are uniformly distributed in the polymer matrix. However, at different points in the sample, the proportions of MWCNTs and PLA impacted the Raman spectrum differently (see points 1 and 3 in Figure 1d). Raman spectroscopy allows distinguishing even a small number of MWCNTs which are present on the surfaces of GNP particles (the observed D mode indicates CNTs at point 2).

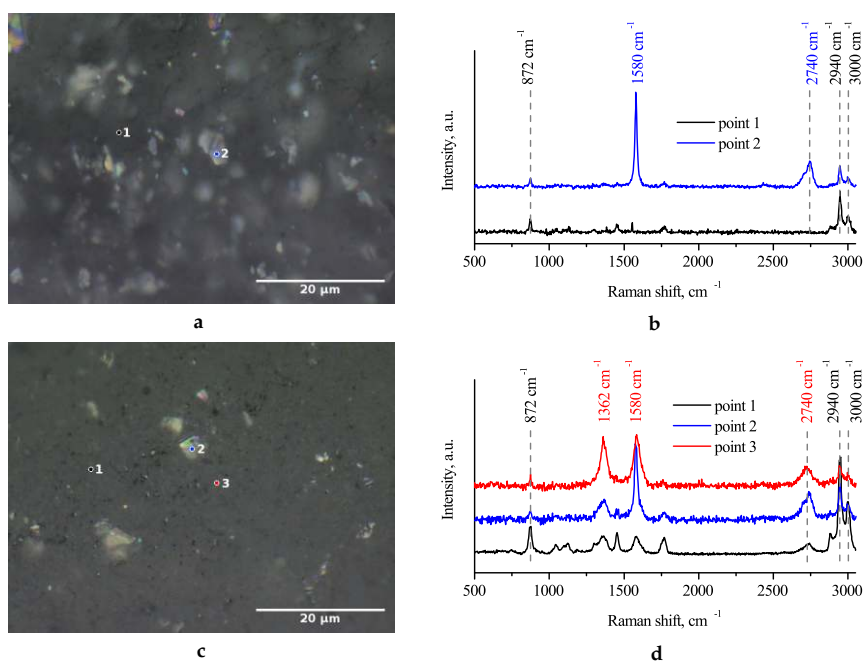


Figure 1. Optical microscopy image (a) and Raman spectra (b) of PLA composite containing 1.5% GNP. Due to the neat PLA transparency, it is possible to see GNPs under the surface of a composite. Optical microscopy image (c) and Raman spectra (d) of PLA composite containing the mixture of 3% GNP and 3% MWCNT. Raman spectrum collected at point 2 combines the characteristic peaks of PLA, GNPs, and MWCNTs.

Bright-field transmission electron microscopy (TEM) analysis was performed using a FEI TECNAI G12 Spirit-Twin (LaB6 source) instrument equipped with an FEI Eagle-4k CCD camera operating with an acceleration voltage of 120 kV. The analysis was performed on sections obtained at room temperature by using a Leica EM UC6/FC6 ultramicrotome. The sections were placed on 400 mesh copper grids. According to the transmission electron microscopy (TEM) of obtained composites, the method applied allows obtaining a mostly uniform distribution of both filler particle types. Figure 2a–c proves that GNPs kept their dimensions after the melt extrusion processing.

The TEM images of MWCNTs in mono- (Figure 2d,e) and bi-filler (Figure 2f) composites show that in both cases, the nanotubes are well-distributed. Due to the significantly higher aspect ratio, they tend to form percolation networks, even at the smallest investigated concentration (compare the number of percolating clusters in Figure 2d,e). However, independently of concentrations and the percolation existence, all prepared composites contain a certain number of insulated filler particles. Summarizing the above, both nanocarbon fillers possess good dispersion in the PLA matrix.

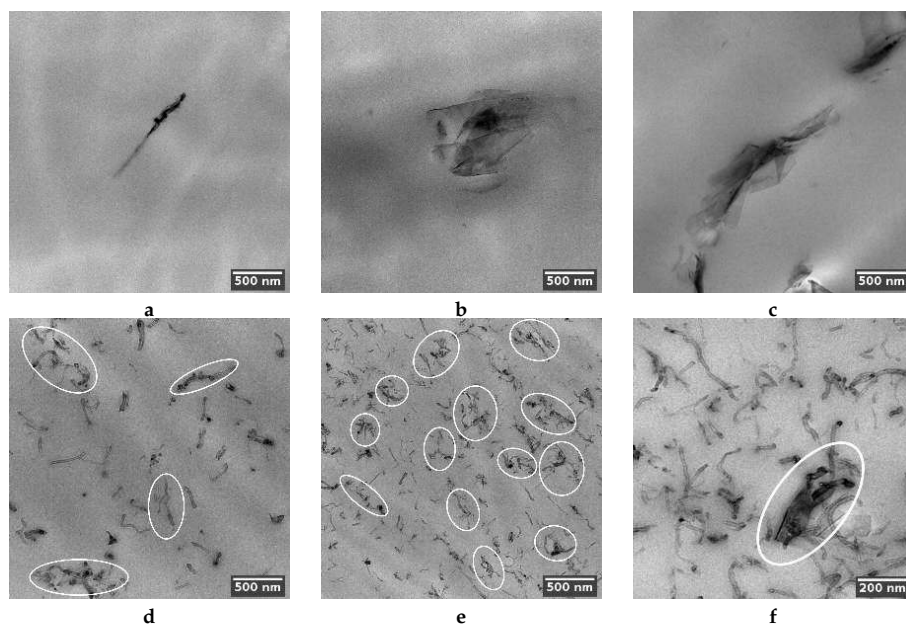


Figure 2. TEM images of insulated filler particles in PLA composites with 1.5 (a), 3 (b), and 6 wt.% (c) GNP; insulated particles and percolating clusters (enclosed in ovals) in composites containing 1.5 (d) and 3 wt.% (e) MWCNT; the mixture of 3% GNP and 3% MWCNT (f). A graphene nanoplatelet involved in percolation contact with nanotubes is enclosed in an oval.

3. Experimental: Time-Domain THz Transmission Measurements

In order to perform the THz measurements, the thicknesses of samples were reduced to 200–300 μm by precise hand polishing with a diamond paste which was removed with isopropanol and water. During the processing, composites were kept near room temperature to prevent heat-induced variation of their structure. All films were studied by transmission microscopy, which requires very thin samples. The terahertz–subterahertz spectra (5–60 cm^{-1}) of the films were measured by means of commercially available pulsed time-domain spectrometer (TDS) TERA K15 (Menlo Systems). In a TDS spectrometer, the sample is exposed to a picosecond pulse that contains frequency components in a wide range up to several terahertz. The position and amplitude of the pulse are detected when the measurement channel is empty and blocked by the sample. The difference in time between the two peaks is a measure of the radiation delay caused by the sample, and a peak's amplitude gives the measure of radiation absorption in the sample. The transition from the time domain to the frequency domain was implemented using the Fourier transformation, and resulted in the spectra of transmission coefficient amplitude and phase. This data were sufficient to determine the real and imaginary parts of the complex conductivity and dielectric permittivity of the investigated sample. The latter, written as $\epsilon = \epsilon' - i\epsilon''$, consists of two parts. The real part of permittivity, ϵ' , corresponds to the energy storage

capacity of a material, and the imaginary part (or sometimes, the loss factor), ϵ'' , is a measure of all dissipation effects in a material (see Sections 1.2.2.1 and 1.3.1 in [62] for further reference).

Experimental values of complex permittivity are shown in Figure 3. The imaginary part of permittivity (further referred to as ϵ'') demonstrates a peak for most of the investigated samples containing GNP filler. On the contrary, the MWCNT-based monofiller composites and the bi-filler composites with 1.5% GNP and 4.5% MWCNT demonstrated a monotonous decrease with frequency growth, which is typical for percolated systems. Finally, the non-percolated composite containing 1.5 wt.% MWCNT did not demonstrate the ϵ'' peak in the investigated frequency range.

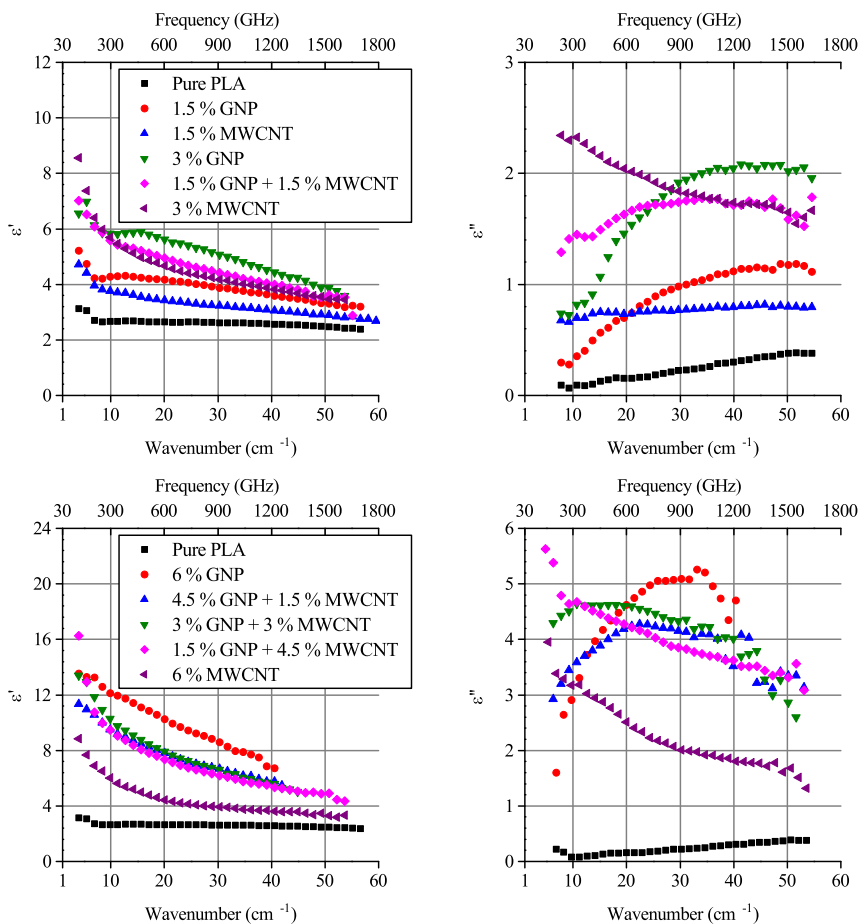


Figure 3. Complex permittivity of composites containing 3 (top) and 6 (bottom) wt.% nanocarbon fillers. MWCNT concentrations are above the percolation threshold.

Another feature of the electromagnetic response is very close values of the real part of permittivity for all three bi-filler composites containing 6 wt.% nanocarbon, accompanied by significant variation in the imaginary part. In Section 5 we will try to clarify the physics origin of these peculiarities inherent for two different kinds of complex permittivity behavior, characteristic for percolated and non-percolated composites, and whether the filler particles' distribution in the polymer could play a significant role.

4. Modeling: MG Effective Medium Theory

One of the well-known approaches to describe the electromagnetic properties of a micro- or nanocomposite material is to apply the effective medium theory. In the case when the filler concentration is lower than the percolation threshold, i.e., filler particles are not interacting, the Maxwell Garnett (MG) effective medium theory is applied [26,63]. This approach assumes the filler particles as ellipsoids with semiaxes a, b, c , and the following polarizability:

$$\alpha_i(v, \sigma) = \frac{4\pi abc}{3} \frac{\epsilon_m \left(1 - \frac{i\sigma}{2\pi v \epsilon_0} - \epsilon_m\right)}{\epsilon_m + N_i \left(1 - \frac{i\sigma}{2\pi v \epsilon_0} - \epsilon_m\right)}, \tag{1}$$

where σ is the ellipsoid conductivity. ϵ_0 is vacuum permittivity; N_i is the depolarization factor in direction $i = a, b, c$ which is given as:

$$N_i = \frac{1}{abc} \int_0^\infty \frac{ds}{(s + i^2) \sqrt{(s + a^2)(s + b^2)(s + c^2)}}. \tag{2}$$

Considering the above, the effective dielectric permittivity is:

$$\epsilon_{eff} = \epsilon_m + \frac{1/3 \sum_{i=a,b,c} n \alpha_i / V}{1 - 1/3 \sum_{i=a,b,c} \frac{N_i n \alpha_i / V}{\epsilon_m}}, \tag{3}$$

where ϵ_m is the dielectric matrix permittivity; n is the volume concentration of filler.

It is possible to show (see the example in Figure 4) that the imaginary part of polarizability calculated by Equation (1) experiences a maximum at the critical frequency (Equation (4)). Therefore, the imaginary part of permittivity will experience the same peak.

$$v_c = \frac{N_i \sigma}{2\pi \epsilon_0 (\epsilon_m - N_i \epsilon_m + N_i)}. \tag{4}$$

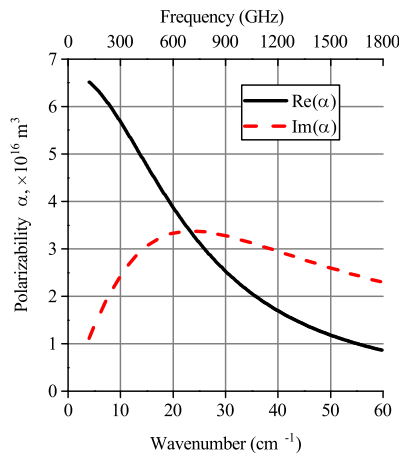


Figure 4. Frequency dispersion of the longitudinal polarizability calculated for oblate ellipsoid with $a = b = 5 \mu\text{m}$, $c = 25 \text{ nm}$ (i.e., $AR = 200$), $\sigma = 10,000 \text{ S/m}$ and $\epsilon_m = 2.5 - 0.1i$.

5. Results and Discussion

5.1. MG Approximation of GNP-Based Composites Permittivity

Typical values for the percolation threshold for GNPs in polymer composites are usually not lower than 3.5% and strongly depend on the GNP aspect ratio, the polymer type and the quality of particles' distribution [25,27]. When the wavelength is orders larger than GNPs lateral dimensions, it is possible to apply the Maxwell Garnett effective medium theory [44]. Let us assume that the GNP particles are uniform ellipsoids with $a = b \gg c$ semiaxes and consider their density equal to graphite (2.2 g/cm^3). The typical aspect ratio (AR) for graphene nanoplatelets lies in the range of 100–1000. An acceptable fitting of dielectric permittivity of composites containing 1.5 and 3% GNP (Figure 5) was acquired with $\sigma = 20,000 \text{ S/m}$ and $\text{AR} \sim 200$, which is in good agreement with the aspect ratio of used GNP particles given in Section 2.1. While the approximation parameters for composites with 1.5 and 3% GNP concentration are similar, the sample containing 6% filler requires another set of parameters to be used for approximation. While the conductivity of ellipsoids remains unchanged, the aspect ratio has to be increased up to nearly 300.

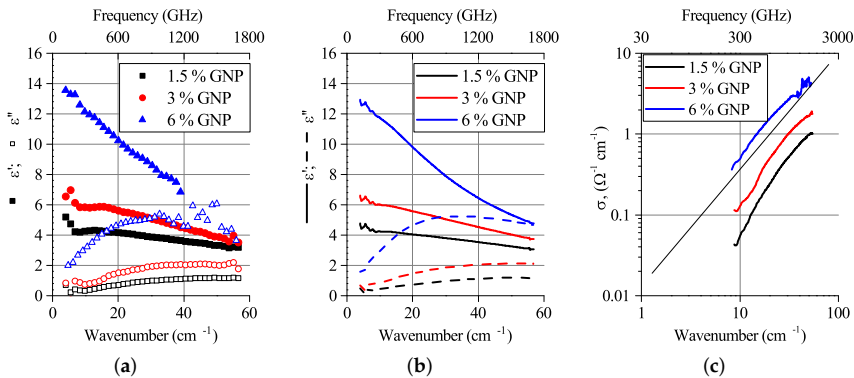


Figure 5. (a) Complex permittivity of composites containing 1.5, 3 and 6 wt.% GNP; (b) Maxwell Garnett approximation of the experiment with the following fitting parameters: $\sigma = 20,000 \text{ S/m}$, and $\text{AR} \sim 197, 208$ and 291 , respectively; (c) conductivity values of GNP-based composites having similar slopes.

The fact that the Maxwell Garnett approximation is still applicable for 6% GNP may indicate that in spite of the concentration being higher than previously reported percolation thresholds for GNPs [40], the impact of insulated filler particles still prevails. In the next subsection, we will try to explain the low-frequency shift of ϵ'' maximum.

5.2. Imaginary Permittivity Peak in Percolated Mixed-Filler Composites

In the previous section, it was shown that the composites with GNP concentrations below the percolation threshold demonstrate the imaginary permittivity maximum predicted in Section 4. However, the experimental data for composites containing a mixture of fillers show a similar behavior, even with the existence of percolation (Figure 3).

In a perfect case, every particle of both fillers is expected to be involved in a heterogeneous percolation network, making the Maxwell Garnett approach inapplicable. However, the real composite system always contains a certain amount of filler particles excluded from the percolation network formation. At low frequencies, the response of such insulated particles is hidden by the percolation network impact, but as in the terahertz region, it is possible to distinguish their impact due to electromagnetic coupling.

In Figure 6a the complex permittivities of composites containing 1.5% GNP, 1.5% MWCNT and their mixture are depicted. Both parts of this mixture have concentrations below the percolation threshold. It can be seen that despite the imaginary part of MWCNT-based composite, the permittivity has no peculiarities, such as peaks in the investigated range; the imaginary part of the GNP-MWCNT bi-filler composite's permittivity shifts towards lower frequencies in comparison with peak inherent for the GNP-based filler.

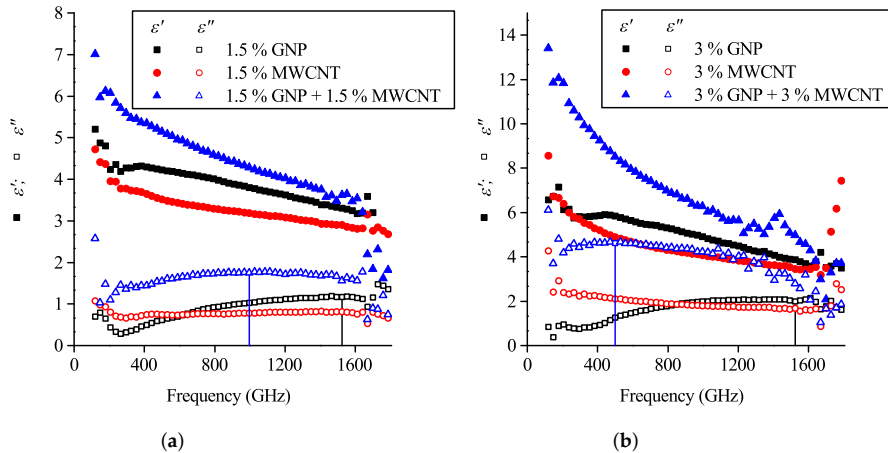


Figure 6. Complex permittivities of composites containing (a) 1.5% GNP, 1.5% MWCNT and their mixture; (b) 3% GNP, 3% MWCNT and their mixture. Peak values of ϵ'' for GNP and GNP + MWCNT composites are indicated by vertical lines.

A similar situation was observed for a mixture of 3% MWCNT and 3 wt.% GNP composites (Figure 6b), a set of mixtures with 6 wt.% nanocarbon (Figure 3) in which the nanotube content is above the percolation threshold. In both cases, it is possible to conceive the dispersion of bi-filler composite's ϵ as a superposition of MWCNT (monotonous decrease of both real and imaginary parts of permittivity) and GNP (peak of ϵ'') curves. Considering Equations (1)–(3), the ϵ'' shift can be explained by the growth of the average aspect ratio and/or the conductivity decrease (see Figure 2 in [44]). Due to the higher aspect ratio (~ 1000), non-percolated nanotubes will give a ϵ'' peak at lower frequencies in comparison with GNPs. That means the GNPs and MWCNTs may be both involved in the percolation network and excluded from it.

As soon as the Maxwell Garnett approach does not require the dielectric nature of the matrix, it is possible to substitute the ϵ_m in Equation (3) with the permittivity of a perfect percolated composite (every particle of which is involved in percolation network). Then, the effective permittivity of the mixed-filler composite may be introduced as following:

$$\epsilon_{effmix} = \epsilon_{MWCNT} + \Delta\epsilon_{cp} + \Delta\epsilon_{np} \quad (5)$$

where the ϵ_{MWCNT} term is the permittivity of MWCNT-based composite, $\Delta\epsilon_{cp}$ is a “synergistic” impact of cross-MWCNT-GNP percolation and $\Delta\epsilon_{np}$ is an impact on the dielectric permittivity made by non-percolated GNP particles. The expression for $\Delta\epsilon_{np}$ is similar to the second term on the right side of Equation (3).

Results of rough $\Delta\epsilon_{cp}$ evaluation (considering $\Delta\epsilon_{np} = \epsilon_{GNP} - \epsilon_{PLA}$) for mixed-filler composites containing 1.5 % MWCNT + 1.5% GNP and 3 % MWCNT + 3 % GNP are presented in the Figure 7.

It can be seen that the $\Delta\epsilon_{cp}$ frequency dispersion is typical for composites whose filler particles are mostly involved in the percolation network. However, the non-percolated nanotubes' impact value remains hidden in the total ϵ_{MWCNT} . The ϵ'' shift characteristic to the bi-filler composite (Figure 6) may be considered as indirect proof that a certain number of MWCNTs are excluded from the percolation network.

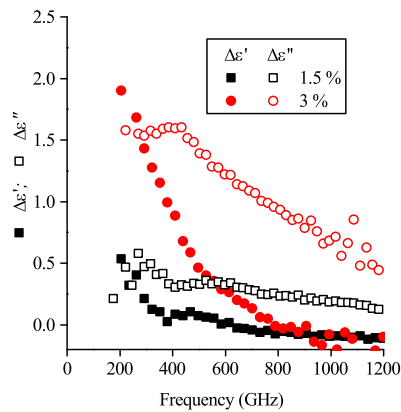


Figure 7. Impacts ($\Delta\epsilon_{cp}$) of cross-filler percolation to the dielectric permittivity of composites containing 1.5% MWCNT + 1.5% GNP and 3% MWCNT + 3% GNP (referred to as 1.5% and 3%, respectively). Both real and imaginary parts behave typically for a percolated composite.

6. Conclusions

The impact of nanofiller particles excluded from the percolation network was demonstrated by means of transmission time-domain terahertz spectroscopy. The theoretically predicted peak of imaginary permittivity was observed on PLA-based nanocomposites filled with GNP, MWCNT and their mixtures both below and above the percolation threshold. Terahertz spectroscopy was demonstrated as a sensitive tool for the estimation of filler distribution character. For instance, the agreement between the experimental value of complex permittivity obtained for mono-filler GNP-based composites and Maxwell Garnett effective medium theory approximation indicates the mostly uniform distribution of insulated graphene nanoplatelets inside the polymer matrix.

The strong variation of the imaginary part of the permittivity dispersion followed by the relatively weak impact to its real part was experimentally shown for the set of bi-filler composites containing 6 wt.% of nanocarbon fillers in total. The variation of GNP fraction in the ternary composite resulted in a change of imaginary permittivity peak frequency, and the real part of permittivity remained mostly unchanged, giving the possibility of electromagnetic property tuning. A simple variation of fillers proportion during the production of the composites by co-extrusion method allows one to precisely control the position of the ϵ'' peak.

Finally, the combination of different nanocarbon fillers allows precise modification of the EM properties of a composite filled with relatively cheap GNPs by addition of CNTs, thereby obtaining a material with high THz performance.

Author Contributions: Conceptualization, G.G., D.B. and P.K.; investigation, G.G., D.B. and I.G.; THz measurements, Y.R., E.Z., S.Z. and L.K.; writing—original draft preparation, G.G.; writing—review and editing, R.K., E.L., J.M., G.F. and P.P.; supervision, P.K.; funding acquisition, G.G. and I.G. All authors have read and agreed to the published version of the manuscript.

Funding: This research is supported by H2020 RISE project 734164 Graphene 3D, BRFFR grant number F19RM-007, “Carbon filler based polymer composites with controllable electromagnetic properties in microwave and THz ranges”; RFBR research project number 1 19-52-04010, “Polymer composites based on carbon fillers with controlled electromagnetic properties in microwave and THz ranges”; the Academy of Finland (Flagship Programme, Photonics Research and Innovation (PREIN), number 320166, and project number 334370). PK is supported by Horizon 2020 IF TURANDOT project 836816.

Acknowledgments: We are thankful to Alesia Paddubskaya (INP BSU) for her help with the Raman spectra analysis and interpretation. Authors R.K. and E.I. are thankful for the support of the BGNSF project DCP-06-COST/11 and H2020-SGS-FET-Graphene Flagship-881603 Graphene Core 3. G.F. acknowledges support of the Russian Foundation for Basic Science within project number 18-29-20116. D.B. is thankful for support by Tomsk State University’s Competitiveness Improvement Program.

Conflicts of Interest: The authors declare no conflict of interest.

Abbreviations

The following abbreviations are used in this manuscript:

MWCNT	Multi-walled carbon nanotube
GNP	Graphene nanoplatelets
PLA	Polylactic acid
TEM	Transmission electronic microscopy
AR	Aspect ratio

References

1. Qin, F.; Brosseau, C. A review and analysis of microwave absorption in polymer composites filled with carbonaceous particles. *J. Appl. Phys.* **2012**, *111*, 0613015. [[CrossRef](#)]
2. Liu, L.; Das, A.; Megaridis, C.M. Terahertz shielding of carbon nanomaterials and their composites—A review and applications. *Carbon* **2014**, *69*, 1–16. [[CrossRef](#)]
3. Deng, H.; Lin, L.; Ji, M.; Zhang, S.; Yang, M.; Fu, Q. Progress on the morphological control of conductive network in conductive polymer composites and the use as electroactive multifunctional materials. *Prog. Polym. Sci.* **2014**, *39*, 627–655. [[CrossRef](#)]
4. Kuzhir, P.; Paddubskaya, A.; Bychanok, D.; Nemilentsau, A.; Shuba, M.; Plusch, A.; Maksimenko, S.; Bellucci, S.; Coderoni, L.; Micciulla, F.; et al. Microwave probing of nanocarbon based epoxy resin composite films: Toward electromagnetic shielding. *Thin Solid Film* **2011**, *519*, 4114–4118. [[CrossRef](#)]
5. Kumar, A.; Alegaonkar, P.S. Impressive Transmission Mode Electromagnetic Interference Shielding Parameters of Graphene-like Nanocarbon/Polyurethane Nanocomposites for Short Range Tracking Countermeasures. *ACS Appl. Mater. Interfaces* **2015**, *7*, 14833–14842. [[CrossRef](#)]
6. Ugale, A.D.; Jagtap, R.V.; Pawar, D.; Datar, S.; Kale, S.N.; Alegaonkar, P.S. Nano-carbon: Preparation, assessment, and applications for NH₃ gas sensor and electromagnetic interference shielding. *RSC Adv.* **2016**, *6*, 97266–97275. [[CrossRef](#)]
7. Sedelnikova, O.V.; Baskakova, K.I.; Gusel’nikov, A.V.; Plyusnin, P.E.; Bulusheva, L.G.; Okotrub, A.V. Percolative Composites with Carbon Nanohorns: Low-Frequency and Ultra-High Frequency Response. *Materials* **2019**, *12*, 1848. [[CrossRef](#)]
8. Chen, Y.J.; Li, Y.; Chu, B.; Kuo, I.T.; Yip, M.; Tai, N. Porous composites coated with hybrid nano carbon materials perform excellent electromagnetic interference shielding. *Compos. Part B Eng.* **2015**, *70*, 231–237. [[CrossRef](#)]
9. Bychanok, D.; Li, S.; Sanchez-Sanchez, A.; Gorokhov, G.; Kuzhir, P.; Ogrin, F.Y.; Pasc, A.; Ballweg, T.; Mandel, K.; Szczurek, A.; et al. Hollow carbon spheres in microwaves: Bio inspired absorbing coating. *Appl. Phys. Lett.* **2016**, *108*, 013701. [[CrossRef](#)]

10. Bychanok, D.S.; Plyushch, A.O.; Gorokhov, G.V.; Bychanok, U.S.; Kuzhir, P.P.; Maksimenko, S.A. Microwave radiation absorbers based on corrugated composites with carbon fibers. *Tecl. Phys.* **2016**, *61*, 1880–1884. [[CrossRef](#)]
11. Paddubskaya, A.; Demidenko, M.; Batrakov, K.; Valušis, G.; Kaplas, T.; Svirko, Y.; Kuzhir, P. Tunable Perfect THz Absorber Based on a Stretchable Ultrathin Carbon-Polymer Bilayer. *Materials* **2019**, *12*, 143. [[CrossRef](#)] [[PubMed](#)]
12. Gorokhov, G.; Bychanok, D.S.; Kuzhir, P.; Gorodetskiy, D.; Kurenaya, A.G.; Sedelnikova, O.V.; Bulusheva, L.G.; Okotrub, A.V. Creation of metasurface from vertically aligned carbon nanotubes as versatile platform for ultra-light THz components. *Nanotechnology* **2020**. [[CrossRef](#)] [[PubMed](#)]
13. Verma, P.; Saini, P.; Choudhary, V. Designing of carbon nanotube/polymer composites using melt recirculation approach: Effect of aspect ratio on mechanical, electrical and EMI shielding response. *Mater. Des.* **2015**, *88*, 269–277. [[CrossRef](#)]
14. Kotsilkova, R.; Ivanov, E.; Todorov, P.; Petrova, I.; Volynets, N.; Paddubskaya, A.; Kuzhir, P.; Uglov, V.; Biró, I.; Kertész, K.; et al. Mechanical and electromagnetic properties of 3D printed hot pressed nanocarbon/poly(lactic) acid thin films. *J. Appl. Phys.* **2017**, *121*, 064105. [[CrossRef](#)]
15. Wan, Y.J.; Zhu, P.L.; Yu, S.H.; Sun, R.; Wong, C.P.; Liao, W.H. Anticorrosive, Ultralight, and Flexible Carbon-Wrapped Metallic Nanowire Hybrid Sponges for Highly Efficient Electromagnetic Interference Shielding. *Small* **2018**, *14*, 1800534. [[CrossRef](#)]
16. Song, P.; Qiu, H.; Wang, L.; Liu, X.; Zhang, Y.; Zhang, J.; Kong, J.; Gu, J. Honeycomb structural rGO-MXene/epoxy nanocomposites for superior electromagnetic interference shielding performance. *Sustain. Mater. Technol.* **2020**, *24*, e00153. [[CrossRef](#)]
17. Kuzhir, P.; Paddubskaya, A.; Plyushch, A.; Volynets, N.; Maksimenko, S.; Macutkevicius, J.; Kranauskaitė, I.; Banys, J.; Ivanov, E.; Kotsilkova, R.; et al. Epoxy composites filled with high surface area-carbon fillers: Optimization of electromagnetic shielding, electrical, mechanical, and thermal properties. *J. Appl. Phys.* **2013**, *114*, 164304. [[CrossRef](#)]
18. Joshi, A.; Bajaj, A.; Singh, R.; Anand, A.; Alegaonkar, P.; Datar, S. Processing of graphene nanoribbon based hybrid composite for electromagnetic shielding. *Compos. Part B Eng.* **2015**, *69*, 472–477. [[CrossRef](#)]
19. Minin, I.; Minin, O.; Suslyayev, V.; Dorofeev, I.; Yakubov, V.; PachecoPena, V.; Beruete, M. Investigations of some new focusing properties of cuboidaided photonic jet. In Proceedings of the Actual Problems of Radiophysics: VI International Conference “APR-2015”, Tomsk, Russia, 5–10 October 2015.
20. Drakakis, E.; Kymakis, E.; Tzagkarakis, G.; Louloudakis, D.; Katharakis, M.; Kenanakis, G.; Suche, M.; Tudose, V.; Koudoumas, E. A study of the electromagnetic shielding mechanisms in the GHz frequency range of graphene based composite layers. *Appl. Surf. Sci.* **2017**, *398*, 15–18. [[CrossRef](#)]
21. Sandler, J.; Kirk, J.; Kinloch, I.; Shaffer, M.; Windle, A. Ultra-low electrical percolation threshold in carbon-nanotube-epoxy composites. *Polymer* **2003**, *44*, 5893–5899. [[CrossRef](#)]
22. Nuzhnyy, D.; Savinov, M.; Bovtun, V.; Kempa, M.; Petzelt, J.; Mayoral, B.; McNally, T. Broad-band conductivity and dielectric spectroscopy of composites of multiwalled carbon nanotubes and poly(ethylene terephthalate) around their low percolation threshold. *Nanotechnology* **2013**, *24*, 055707. [[CrossRef](#)] [[PubMed](#)]
23. Eletsii, A.V.; Knizhnik, A.A.; Potapkin, B.V.; Kenny, J.M. Electrical characteristics of carbon nanotube-doped composites. *Physics-Uspokhi* **2015**, *58*, 209–251. [[CrossRef](#)]
24. Jiang, X.; Drzal, L.T. Reduction in percolation threshold of injection molded high-density polyethylene/exfoliated graphene nanoplatelets composites by solid state ball milling and solid state shear pulverization. *J. Appl. Polym. Sci.* **2012**, *124*, 525–535. [[CrossRef](#)]
25. Al-Hartomy, O.A.; Al-Ghamdi, A.A.; Al-Salamy, F.; Dishovsky, N.; Shtarkova, R.; Iliev, V.; El-Tantawy, F. Dielectric and Microwave Properties of Graphene Nanoplatelets /Carbon Black Filled Natural Rubber Composites. *Int. J. Mater. Chem.* **2012**, *2*, 116–122. [[CrossRef](#)]
26. Sarto, M.S.; D’Aloia, A.G.; Tamburrano, A.; De Bellis, G. Synthesis, Modeling, and Experimental Characterization of Graphite Nanoplatelet-Based Composites for EMC Applications. *IEEE Trans. Electromagn. Compat.* **2012**, *54*, 17–27. [[CrossRef](#)]
27. Kopyt, P.; Salski, B.; Zagrajek, P.; Janczak, D.; Sloma, M.; Jakubowska, M.; Olszewska-Placha, M.; Gwarek, W. Electric Properties of Graphene-Based Conductive Layers from DC Up To Terahertz Range. *IEEE Trans. Terahertz Sci. Technol.* **2016**, *6*, 480–490. [[CrossRef](#)]

28. Wang, Z.; Luo, J.; Zhao, G. Dielectric and microwave attenuation properties of graphene nanoplatelet-epoxy composites. *AIP Adv.* **2014**, *4*, 017139. [[CrossRef](#)]
29. Sun, X.; Sun, H.; Li, H.; Peng, H. Developing Polymer Composite Materials: Carbon Nanotubes or Graphene? *Adv. Mater.* **2013**, *25*, 5153–5176. [[CrossRef](#)]
30. Bertasius, P.; Meisak, D.; Macutkevicius, J.; Kuzhir, P.; Selskis, A.; Volnyanko, E.; Banys, J. Fine Tuning of Electrical Transport and Dielectric Properties of Epoxy/Carbon Nanotubes Composites via Magnesium Oxide Additives. *Polymers* **2019**, *11*, 2044. [[CrossRef](#)]
31. Bertasius, P.; Macutkevicius, J.; Banys, J.; Gaidukovs, S.; Barkane, A.; Vaivodis, R. Synergy effects in dielectric and thermal properties of layered ethylene vinyl acetate composites with carbon and Fe₃O₄ nanoparticles. *J. Appl. Polym. Sci.* **2020**, *137*, 48814. [[CrossRef](#)]
32. Meisak, D.; Macutkevicius, J.; Plyushch, A.; Kuzhir, P.; Selskis, A.; Banys, J. Dielectric Relaxation in the Hybrid Epoxy/MWCNT/MnFe₂O₄ Composites. *Polymers* **2020**, *12*, 697. [[CrossRef](#)] [[PubMed](#)]
33. Sareni, B.; Krähenbühl, L.; Beroual, A.; Brosseau, C. Effective dielectric constant of random composite materials. *J. Appl. Phys.* **1997**, *81*, 2375–2383. [[CrossRef](#)]
34. Sumfleth, J.; Adroher, X.C.; Schulte, K. Synergistic effects in network formation and electrical properties of hybrid epoxy nanocomposites containing multi-wall carbon nanotubes and carbon black. *J. Mater. Sci.* **2009**, *44*, 3241–3247. [[CrossRef](#)]
35. Kumar, S.; Sun, L.L.; Caceres, S.; Li, B.; Wood, W.; Perugini, A.; Maguire, R.G.; Zhong, W.H. Dynamic synergy of graphitic nanoplatelets and multi-walled carbon nanotubes in polyetherimide nanocomposites. *Nanotechnology* **2010**, *21*, 105702. [[CrossRef](#)]
36. Gao, Y.; Picot, O.T.; Zhang, H.; Bilotti, E.; Peijs, T. Synergistic effects of filler size on thermal annealing-induced percolation in polylactic acid (PLA)/graphite nanoplatelet (GNP) nanocomposites. *Nanocomposites* **2017**, *3*, 67–75. [[CrossRef](#)]
37. Zhang, H.; Zhang, G.; Tang, M.; Zhou, L.; Li, J.; Fan, X.; Shi, X.; Qin, J. Synergistic effect of carbon nanotube and graphene nanoplates on the mechanical, electrical and electromagnetic interference shielding properties of polymer composites and polymer composite foams. *Chem. Eng. J.* **2018**, *353*, 381–393. [[CrossRef](#)]
38. Yue, L.; Pircheraghi, G.; Monemian, S.A.; Manas-Zloczower, I. Epoxy composites with carbon nanotubes and graphene nanoplatelets – Dispersion and synergy effects. *Carbon* **2014**, *78*, 268–278. [[CrossRef](#)]
39. Paszkiewicz, S.; Szymczyk, A.; Sui, X.; Wagner, H.; Linares, A.; Ezquerro, T.; Roslaniec, Z. Synergetic effect of single-walled carbon nanotubes (SWCNT) and graphene nanoplatelets (GNP) in electrically conductive PTT-block-PTMO hybrid nanocomposites prepared by in situ polymerization. *Compos. Sci. Technol.* **2015**, *118*, 72–77. [[CrossRef](#)]
40. Shuba, M.; Yuko, D.; Gorokhov, G.; Meisak, D.; Bychanok, D.S.; Kuzhir, P.; Maksimenko, S.A.; Angelova, P.; Ivanov, E.; Kotsilkova, R. Frequency and density dependencies of the electromagnetic parameters of carbon nanotube and graphene nanoplatelet based composites in the microwave and terahertz ranges. *Mater. Res. Express* **2019**, *6*, 095050. [[CrossRef](#)]
41. Gbaguidi, A.; Namilae, S.; Kim, D. Synergy effect in hybrid nanocomposites based on carbon nanotubes and graphene nanoplatelets. *Nanotechnology* **2020**, *31*, 255704. [[CrossRef](#)]
42. Kotsilkova, R.; Ivanov, E.; Bychanok, D.; Paddubskaya, A.; Demidenko, M.; Macutkevicius, J.; Maksimenko, S.; Kuzhir, P. Effects of sonochemical modification of carbon nanotubes on electrical and electromagnetic shielding properties of epoxy composites. *Compos. Sci. Technol.* **2015**, *106*, 85–92. [[CrossRef](#)]
43. Spinelli, G.; Kotsilkova, R.; Ivanov, E.; Petrova-Doycheva, I.; Menseidov, D.; Georgiev, V.; Di Maio, R.; Silvestre, C. Effects of Filament Extrusion, 3D Printing and Hot-Pressing on Electrical and Tensile Properties of Poly(Lactic) Acid Composites Filled with Carbon Nanotubes and Graphene. *Nanomaterials* **2019**, *10*, 35. [[CrossRef](#)] [[PubMed](#)]
44. Bychanok, D.; Angelova, P.; Paddubskaya, A.; Meisak, D.; Shashkova, L.; Demidenko, M.; Plyushch, A.; Ivanov, E.; Krastev, R.; Kotsilkova, R.; et al. Terahertz absorption in graphite nanoplatelets/polylactic acid composites. *J. Phys. D Appl. Phys.* **2018**, *51*, 145307. [[CrossRef](#)]
45. Barone, C.; Pagano, S.; Neitzert, H.C. Transport and noise spectroscopy of MWCNT/HDPE composites with different nanotube concentrations. *J. Appl. Phys.* **2011**, *110*, 113716. [[CrossRef](#)]
46. Makarova, T.; Zakharchuk, I.; Geydt, P.; Lahderanta, E.; Komlev, A.; Zyrianova, A.; Lyubchik, A.; Kanygin, M.; Sedelnikova, O.; Kurenya, A.; et al. Assessing carbon nanotube arrangement in polystyrene matrix by magnetic susceptibility measurements. *Carbon* **2016**, *96*, 1077–1083. [[CrossRef](#)]

47. Li, C.; Thostenson, E.T.; Chou, T.W. Sensors and actuators based on carbon nanotubes and their composites: A review. *Compos. Sci. Technol.* **2008**, *68*, 1227–1249. [[CrossRef](#)]
48. Bauhofer, W.; Kovacs, J.Z. A review and analysis of electrical percolation in carbon nanotube polymer composites. *Compos. Sci. Technol.* **2009**, *69*, 1486–1498. [[CrossRef](#)]
49. Ji, Y.; Huang, Y.Y.; Rungsawang, R.; Terentjev, E.M. Dispersion and Alignment of Carbon Nanotubes in Liquid Crystalline Polymers and Elastomers. *Adv. Mater.* **2010**, *22*, 3436–3440. [[CrossRef](#)]
50. Peters, O.; Busch, S.F.; Fischer, B.M.; Koch, M. Determination of the Carbon Nanotube Concentration and Homogeneity in Resin Films by THz Spectroscopy and Imaging. *J. Infrared, Millimeter, Terahertz Waves* **2012**, *33*, 1221–1226. [[CrossRef](#)]
51. Casini, R.; Papari, G.; Andreone, A.; Marrazzo, D.; Patti, A.; Russo, P. Dispersion of carbon nanotubes in melt compounded polypropylene based composites investigated by THz spectroscopy. *Opt. Express* **2015**, *23*, 18181. [[CrossRef](#)]
52. Rungsawang, R.; Geethamma, V.G.; Parrott, E.P.J.; Ritchie, D.A.; Terentjev, E.M. Terahertz spectroscopy of carbon nanotubes embedded in a deformable rubber. *J. Appl. Phys.* **2008**, *103*, 123503. [[CrossRef](#)]
53. Kumar, S.; Kamaraju, N.; Karthikeyan, B.; Tondusson, M.; Freysz, E.; Sood, A.K. Terahertz Spectroscopy of Single-Walled Carbon Nanotubes in a Polymer Film: Observation of Low-Frequency Phonons. *J. Phys. Chem. C* **2010**, *114*, 12446–12450. [[CrossRef](#)]
54. Zhang, X.C.; Xu, J. *Introduction to THz Wave Photonics*; Springer: New York, NY, USA, 2010.
55. Rao, Y.; Qu, J.; Marinis, T.; Wong, C.P. A precise numerical prediction of effective dielectric constant for polymer-ceramic composite based on effective-medium theory. *IEEE Trans. Components Packag. Technol.* **2000**, *23*, 680–683.
56. Nishimura, H.; Minami, N.; Shimano, R. Dielectric properties of single-walled carbon nanotubes in the terahertz frequency range. *Appl. Phys. Lett.* **2007**, *91*, 011108. [[CrossRef](#)]
57. Munoz, P.A.R.; de Oliveira, C.F.P.; Amurin, L.G.; Rodriguez, C.L.C.; Nagaoka, D.A.; Tavares, M.I.B.; Domingues, S.H.; Andrade, R.J.E.; Fechine, G.J.M. Novel improvement in processing of polymer nanocomposite based on 2D materials as fillers. *Express Polym. Lett.* **2018**, *12*, 930–945. [[CrossRef](#)]
58. Kotsilkova, R.; Petrova-Doycheva, I.; Menseidov, D.; Ivanov, E.; Paddubskaya, A.; Kuzhir, P. Exploring thermal annealing and graphene-carbon nanotube additives to enhance crystallinity, thermal, electrical and tensile properties of aged poly(lactic) acid-based filament for 3D printing. *Compos. Sci. Technol.* **2019**, *181*, 107712. [[CrossRef](#)]
59. Sadezky, A.; Muckenhuber, H.; Grothe, H.; Niessner, R.; Pöschl, U. Raman microspectroscopy of soot and related carbonaceous materials: Spectral analysis and structural information. *Carbon* **2005**, *43*, 1731–1742. [[CrossRef](#)]
60. Ferrari, A.C.; Meyer, J.C.; Scardaci, V.; Casiraghi, C.; Lazzeri, M.; Mauri, F.; Piscanec, S.; Jiang, D.; Novoselov, K.S.; Roth, S.; et al. Raman Spectrum of Graphene and Graphene Layers. *Phys. Rev. Lett.* **2006**, *97*. [[CrossRef](#)]
61. Malard, L.; Pimenta, M.; Dresselhaus, G.; Dresselhaus, M. Raman spectroscopy in graphene. *Phys. Rep.* **2009**, *473*, 51–87. [[CrossRef](#)]
62. Chen, L. (Ed.) *Microwave Electronics: Measurement and Materials Characterisation*; John Wiley: Chichester, UK, 2004.
63. Spanier, J.E.; Herman, I.P. Use of hybrid phenomenological and statistical effective-medium theories of dielectric functions to model the infrared reflectance of porous SiC films. *Phys. Rev. B* **2000**, *61*, 10437–10450. [[CrossRef](#)]

Publisher's Note: MDPI stays neutral with regard to jurisdictional claims in published maps and institutional affiliations.



© 2020 by the authors. Licensee MDPI, Basel, Switzerland. This article is an open access article distributed under the terms and conditions of the Creative Commons Attribution (CC BY) license (<http://creativecommons.org/licenses/by/4.0/>).

2 publikacija / 2nd publication

**On the Synergistic Effect of Multi-Walled Carbon Nanotubes
and Graphene Nanoplatelets to Enhance the Functional
Properties of SLS 3D-Printed Elastomeric Structures**

G. Rollo, A. Ronca, P. Cerruti, X. Gan, G. Fei, H. Xia, **G. Gorokhov**,
D. Bychanok, P. Kuzhir, M. Lavorgna, L. Ambrosio

Polymers **2020** 12 1841

DOI: 10.3390/polym12081841

Article

On the Synergistic Effect of Multi-Walled Carbon Nanotubes and Graphene Nanoplatelets to Enhance the Functional Properties of SLS 3D-Printed Elastomeric Structures

Gennaro Rollo ^{1,2,†}, Alfredo Ronca ^{2,3,†}, Pierfrancesco Cerruti ^{1,2}, Xin Peng Gan ⁴, Guoxia Fei ⁴, Hesheng Xia ^{2,4,*}, Gleb Gorokhov ^{5,6}, Dzmitry Bychanok ^{5,7}, Polina Kuzhir ^{5,8}, Marino Lavorgna ^{2,9,*} and Luigi Ambrosio ¹

¹ Institute of Polymers, Composites and Biomaterials, National Research Council, Via Campi Flegrei, 34-80078 Pozzuoli (NA), Italy; gennaro.rollo@ipcb.cnr.it (G.R.); cerruti@ipcb.cnr.it (P.C.); luigi.ambrosio@cnr.it (L.A.)

² Institute of Polymers, Composites and Biomaterials, National Research Council, Via Previati, 1, 23900 Lecco, Italy; alfredo.ronca@cnr.it

³ Institute of Polymers, Composites and Biomaterials, National Research Council Viale J.F. Kennedy, 54-80125 Naples, Italy

⁴ State Key Laboratory of Polymer Materials Engineering, Polymer Research Institute, Sichuan University, Chengdu 610065, China; xinpenggan@163.com (X.P.G.); feiguoxia1981@163.com (G.F.)

⁵ Institute for Nuclear Problems of Belarusian State University, Bobruiskaya 11, 220006 Minsk, Belarus; glebgorokhov@yandex.ru (G.G.); dzmitrybychanok@ya.ru (D.B.); polina.kuzhir@gmail.com (P.K.)

⁶ Physics Faculty, Vilnius University, Sauletekio 9, LT-10222 Vilnius, Lithuania

⁷ Radiophysics department, Tomsk State University, Lenin Avenue 36, 634050 Tomsk, Russia

⁸ Institute of Photonics, University of Eastern Finland, Yliopistokatu 7, FI-80101 Joensuu, Finland

⁹ Institute of Polymers, Composites and Biomaterials, National Research Council, P. le Enrico Fermi, 1-80055 Portici (NA), Italy

* Correspondence: xiahs@scu.edu.cn (H.X.); marino.lavorgna@cnr.it (M.L.)

† These authors contributed equally to the work.

Received: 30 June 2020; Accepted: 11 August 2020; Published: 17 August 2020



Abstract: Elastomer-based porous structures realized by selective laser sintering (SLS) are emerging as a new class of attractive multifunctional materials. Herein, a thermoplastic polyurethane (TPU) powder for SLS was modified by 1 wt.% multi-walled carbon nanotube (MWCNTs) or a mixture of MWCNTs and graphene (GE) nanoparticles (70/30 wt/wt) in order to investigate on both the synergistic effect provided by the two conductive nanostructured carbonaceous fillers and the correlation between formulation, morphology, and final properties of SLS printed porous structures. In detail, porous structures with a porosity ranging from 20% to 60% were designed using Diamond (D) and Gyroid (G) unit cells. Results showed that the carbonaceous fillers improve the thermal stability of the elastomeric matrix. Furthermore, the TPU/1 wt.% MWCNTs-GE-based porous structures exhibit excellent electrical conductivity and mechanical strength. In particular, all porous structures exhibit a robust negative piezoresistive behavior, as demonstrated from the gauge factor (GF) values that reach values of about -13 at 8% strain. Furthermore, the G20 porous structures (20% of porosity) exhibit microwave absorption coefficients ranging from 0.70 to 0.91 in the 12–18 GHz region and close to 1 at THz frequencies (300 GHz–1 THz). Results show that the simultaneous presence of MWCNTs and GE brings a significant enhancement of specific functional properties of the porous structures, which are proposed as potential actuators with relevant electro-magnetic interference (EMI) shielding properties.

Keywords: selective laser sintering; piezoresistivity; thermoplastic polyurethane (TPU); carbonaceous filler; EMI shielding

1. Introduction

Piezoresistivity is defined as the electrical resistance variation induced by an external mechanical stimulus [1]. Piezoresistive sensors are traditionally fabricated by metallic or inorganic semiconductor materials, but they are typically rigid, heavy, and brittle, and this limits their utilization in many fields [2]. To address these drawbacks, in recent years, porous polymer materials reinforced with conductive nanostructured fillers have been engineered as piezoresistive sensors. The goal is to obtain electrical conductive polymer composites by forming a three-dimensional interconnected conductive network made of conductive fillers. In this respect, metal nanoparticles [3], intrinsically conductive polymers [4] dispersed in polymer matrix [5], or carbonaceous fillers such as carbon black [6], carbon fibers [7], carbon nanotubes [8], graphite [9], and graphene [9] have been widely used. Flexibility, high porosity, ultra-low density, good energy conversion, and storage properties are the properties achieved by these nanocomposites [10]. Such conductive nanocomposites find a wide range of applications as pressure sensors [11] as well as flexible circuits [12], antistatic materials [13], and electromagnetic interference shielding devices [14].

However, constructing 3D interconnected conductive networks using conventional manufacturing such as *in situ* polycondensation [15], templating methods [16], melt processing [17], and solution mixing [18] is a challenging task, because the high shearing force present in these conventional processes breaks the conductive network structure. 3D printing is an innovative manufacturing technology that, based on Computer-Aided Design (CAD) data, can directly turn complex 3D models into real objects [19–21]. Selective laser sintering (SLS) is one of the most significant 3D printing techniques, which is applied in many fields, from biomedicine to aerospace [22]. SLS is a powder-based process in which 3D structures are obtained by the layer-by-layer sintering of thermoplastic polymer powder via a computer controlled scanning laser beam [23]. Differently from other 3D printing techniques, such as fused deposition modelling (FDM), SLS is a shear-free and free-flowing process that, in case the raw polymeric powder is coated with conductive filler, allows the formation of a segregated filler network within the polymer matrix [24].

Thermoplastic polyurethane (TPU) is a soft and flexible elastomer widely used as building material for the SLS process [25]. Recently, TPU composites reinforced with nanoscale fillers drew great attention for their enhanced mechanical, thermal, and electrical properties [26,27]. In fact, combining a TPU matrix with conductive fillers and SLS manufacturing is a simple and effective approach to prepare nanocomposite materials with optimized thermal, anticorrosive, and electromagnetic shielding properties [11,28–30]. Xia et al., recently developed a novel approach to construct a 3D electrically conductive segregated network in TPU/CNTs composite polymer matrix by SLS [24]. Later, they reported the simultaneous realization of conductive segregation network microstructure and minimal surface porous macrostructure by SLS 3D printing of single-walled carbon nanotubes (SWCNTs)-wrapped TPU composite powder. [31] The Schwarz (S-) structure was found to be capable of producing the best piezoresistive properties of the SWCNTs/TPU composite sensor with a gauge factor (GF) much higher than that for Gyroid and Diamond structures.

In a previous research, some of the authors have manufactured TPU/1 wt.% graphene (GE) porous systems, and demonstrated the correlation between geometrical features and electrical properties of the 3D-printed porous structures. All porous structures exhibited a robust negative piezoresistive behavior, with outstanding strain sensitivity. However, the obtained results showed that GE particles obstruct the polymer powder coalescence, thereby resulting in a porous structure that exhibits an imperfect percolative network and poor mechanical properties [27]. The analysis of the literature confirms that elastomer-based porous structures realized by SLS technology with powders modified

with carbonaceous fillers have been exhaustively investigated as innovative materials for piezoresistive sensors. However, in this context, a fully understanding of the formulations–properties correlations which establish when 2D and 1D carbonaceous filler mixtures are used to modify the elastomeric-based SLS particles are still missing.

Alongside with outstanding piezoresistive behavior, the elastomer-based conductive porous structures exhibit interesting properties to be used in the field of Electromagnetic Interference Shielding. In fact, the porosity and electrical conductivity are the most important material parameters responsible for the electro-magnetic (EM) response of materials [32]. Thus, in case of high conductivity and zero porosity, like, e.g., conventional metals of valuable thickness (thicker than skin depth), electro-magnetic interference shielding efficiency (EMI SE) is high and ascribed mainly to the reflection from the topmost metal surface. For thinner than skin depth films with metallic conductivity (e.g., graphene and other carbon nm-films [33–35]), high absorption close to 100% is possible in case of placing it to $\lambda/4$ dielectric plate or back reflector separated from the conductive film by a fine insulating slab (so-called Salisbury screen) [34,36].

In case of porous monoliths, even for a highly conductive backbone, in contrast to bulk metals, it is possible to reach resonant perfect electromagnetic absorption. For that, the void/cell size should be compatible with the wavelength [37].

However, for many applications, it is not necessary resonant, even perfect, absorption. Many applications, especially in the field of EMI shields, require high but not perfect broadband absorption. The simplest way is to use slightly conductive media of proper thickness in order to suppress the reflection due to constructive interference effects. However, such a solution demands a thick and heavy EMI shielding layer (e.g., epoxy filled with multi-walled carbon nanotube (MWCNT) above the percolation threshold must be not less than 10 mm thick and have a targeting frequency of 10 GHz [38,39]), and it again supports resonant absorption.

The advantage of Diamond (D) and Gyroid (G) lattices fabricated by SLS 3D printing from conductive polymer composites is the option to tune their geometrical features (porosity, void size) to target a particular frequency range. Moreover, the conductivity of the lattices skeleton has to be enough to ensure Joule heating (true absorption of electromagnetic waves), and to secure multiple reflection from the void/cell walls enhancing resultant absorption.

In this research, different types of carbonaceous fillers able to improve the electrical properties of the porous structures realized by SLS were investigated. In detail, two kinds of fillers were used to coat the TPU powders: multi-walled carbon nanotubes (MWCNTs) and a combination of MWCNTs and GE (70/30 wt/wt). MWCNTs are a low-cost filler, if compared to single-walled carbon nanotubes (SWCNTs), and SLS 3D printing induces their segregation, improving the conductive percolation network. Moreover, it has been demonstrated that the combined use of MWCNTs and GE allows the realization of nanocomposites with better electrical properties in terms of conductivity and gauge factor if compared to MWCNTs and GE alone. Nanocomposite TPU powders have been processed by SLS to obtain mathematically defined structures with different shapes and porosities. The effect of the filler, porosity, and geometry on the electrical and mechanical properties of the structures was evaluated, and a comparison with our previously reported research was conducted. Moreover, electromagnetic shielding characterization was performed on the porous structures that showed the best electrical properties.

2. Materials and Methods

2.1. Preparation of Nanocomposites Powder

The method of SLS-compatible composite powder preparation directly determines the dispersion of nanofillers in the polymer matrix, and this affects the structural and functional properties of the SLS-printed structures. MWCNTs (NANOCYL 7000, Nanocyl, Sambreville, Belgium) and Graphene (The Sixth Element Materials, Changzhou, China) with a MWCNTs/GE ratio of 70/30 wt/wt. were first

pre-dispersed by a wet ball milling process as previously described [31]. The ball mill jars were fixed on the planetary mill and then milled continuously for 1 h at a speed of 300 rpm due to the action of iron balls in the milling jars. Anhydrous ethanol was then added to the dark dispersion and the solution was sonicated (40 W for 1 h) to obtain a stable MWCNTs-GE dispersion. The TPU powders (Mophene3D T90A, Nanjing, China) were then added to the MWCNTs-GE suspension, in such an amount to obtain a final filler content of 1 wt.%, and subjected to mechanical stirring for 2 h. The resulting mixture was filtered with a Buchner funnel under reduced pressure and dried in a vacuum oven at 70 °C for 24 h. Afterwards, the TPU/MWCNTs-GE powders were sieved to remove particles with a size over 150 µm, and silica powder was added to further improve the powder flowability. For a comparative experiment, the control sample TPU/MWCNTs composite powder (Mophene3D CT90A, Nanjing, China) was used as received.

2.2. Porous Structures Design and Manufacturing by SLS Technology

To design 3D porous structures, a mathematical approach was used starting from triply periodic minimal surfaces equations (TPMS). TPMS are minimal surfaces periodic in three independent directions, extending infinitely and, in the absence of self-intersections, partitioning the space into two labyrinths. The Wolfram Mathematica software was used to generate the 3D structure based on Gyroid (G) and Diamond (D) equations with different porosity. The following trigonometric equations, i.e., Equation (1) for G and Equation (2) for D structures, were used with boundary condition $x, y, z = [-3\pi, 3\pi]$:

$$\cos(x) \cdot \sin(y) + \cos(y) \cdot \sin(z) + \cos(z) \cdot \sin(x) = C \quad (1)$$

$$\sin(x) \cdot \sin(y) \cdot \sin(z) + \sin(x) \cdot \cos(y) \cdot \cos(z) + \cos(x) \cdot \sin(y) \cdot \cos(z) + \cos(x) \cdot \cos(y) \cdot \sin(z) = C \quad (2)$$

where C is the offset parameter and controls the porosity of the structures. Porous structures with three different porosities (20%, 40%, and 60%) were designed to study the correlation between porosity and electrical properties. Hereinafter, Gyroid and Diamond porous structures will be labelled as G_x and D_x , respectively, where G and D represent the geometry and x represents the porosity in %. As an example, G_{20} stands for Gyroid architectures with 20% porosity. The CAD model of the specimen was generated using the Rhinoceros CAD software (Robert McNeel & Associates, WA, USA.), and exported in the STL format for uploading into the SLS machine. The SLS process was performed on a lab-scale SLS equipment (Sharebot-SnowWhite, Lecco, Italy). The optimized sintering process parameters for TPU/MWCNTs and TPU/(MWCNTs-GE) are shown in Table 1. To process the nanocomposite powder, the laser was set at 40% of the maximum energy.

Table 1. Sintering parameters adopted to process the nanocomposite powders (thermoplastic polyurethane (TPU)/multi-walled carbon nanotubes (MWCNTs) and TPU/(MWCNTs-graphene (GE))).

Process Parameters	Value
Laser power (W)	14
Laser scan spacing (µm)	200
Laser scan speed (pps)	40,000
Part bed temperature (°C)	85
Outline laser power (W)	5.6
Layer thickness (µm)	100

The manufactured structures were allowed to cool inside the machine process chamber for approximately 1 h and then they were removed from the part bed. Excess of powder surrounding the structure and non-sintered powder from the interstices were removed by compressed air.

Examples of D and G architectures with 60% porosity, starting from the CAD unit cell, the 3D structure and, finally, a picture of the 3D-printed samples are shown in Figure 1.

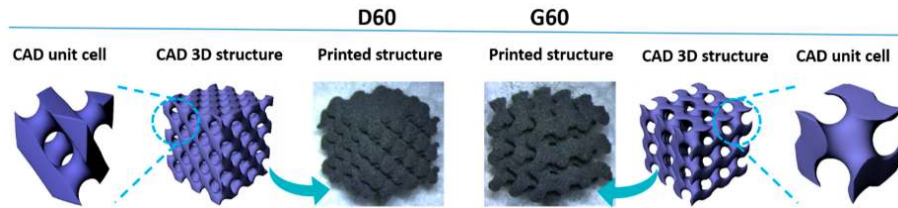


Figure 1. Computer-Aided Design (CAD) unit cell, CAD 3D structure, and printed for D60 and G60 systems.

2.3. Electron Microscopy

Scanning electron microscopy (SEM) observations were performed by a Fei Quanta 200 SEM (Hillsboro, OR, USA) to study the morphology of the porous structures. The samples were fixed on a support and metallized with a gold-palladium alloy to ensure better conductivity and prevent the formation of electrostatic charges. Transmission electron microscopy (TEM) imaging was performed using a Tecnai G2 Spirit TWIN electron microscope (FEI, Hillsboro, OR, USA) operating at 120 kV on thin sections obtained from the bulk samples using a Leica EM UC7 ultracryomicrotome (Leica Microsystems Srl, Milano, Italy) at $-100\text{ }^{\circ}\text{C}$, cut rate between 1 and 8 mm/s, and nominal feed 140 nm

2.4. Thermal Characterization

Thermal properties of SLS-printed samples were measured by thermogravimetric analysis (TGA) using a PerkinElmer Pyris Diamond TG/DTA (Waltham, MA, USA). Approximately 8 mg of sample were first heated to $90\text{ }^{\circ}\text{C}$ at $10\text{ }^{\circ}\text{C}/\text{min}$, kept in isothermal conditions for 10 min, and then heated to $800\text{ }^{\circ}\text{C}$ at a heating rate of $5\text{ }^{\circ}\text{C}/\text{min}$ under nitrogen atmosphere.

2.5. Piezoresistive Measurements

The experimental setup for the evaluation of the mechanical and piezoresistive properties of the 3D-printed porous structures consisted in a mechanical tester (Instron 5564 dynamometer, Torino, Italy) and a multimeter (Agilent 34401A $6\frac{1}{2}$ Digit Multimeter, Santa Clara, CA, USA) controlled by a homemade LabVIEW program. The multimeter was set up with the 2-probe measurement method, able to continuously monitor the change in the electrical resistance of the specimen submitted to loading and unloading cycles. The top and bottom surfaces of the cubic specimens ($10 \times 10 \times 10\text{ mm}^3$) were covered with copper conductive tape as electrode. In detail, the electrical resistance changes were evaluated by submitting the samples at room temperature ($25\text{ }^{\circ}\text{C}$) to cyclic loading/unloading, with 8% deformation and 3 mm/min actuation rate.

2.6. Electromagnetic Shielding

2.6.1. Low-Frequency Range

The low-frequency conductivity of G20 and G60 structures made of TPU/MWCNT and TPU/(MWCNT-GE) powders was investigated in a 100 kHz-1 MHz range in order to ensure the existence of percolation in composites. Measurements were conducted by a HP4284A LCR-meter (Zurich Instruments, Cambridge, MA, USA). Specimens of approximate $\sim 5 \times 5 \times 3\text{ mm}^3$ dimensions were placed between two parallel electrodes and measured as quasi-bulk samples. The LCR-meter measures the values of capacity and loss tangent, which allows calculating the conductivity.

2.6.2. Microwave Range

The electromagnetic response of structures G20 and G60 (cubic samples) containing MWCNTs and MWCNTs-GE was investigated in Ku-band (12–18 GHz) using a Micran R4M (Micran, Tomsk,

Russia) vector analyzer and rectangular waveguide transmission line with cross-sectional dimensions of $16 \times 8 \text{ mm}^2$. Plain-parallel samples of 10.6 mm thickness were placed into the waveguide and their complex S_{21} -parameters (being square root of sample transmission) were measured. The complex permittivity value was calculated from the experimental data by standard methods [40].

2.6.3. THz Range

The electromagnetic response in the terahertz frequencies was measured by the time-domain spectrometer "T-Spec" by EKSPILA (Vilnius, Lithuania). The measurement procedure has been described in detail elsewhere [41]. Two millimeters thick plane-parallel slices of porous structure ($7 \times 5 \text{ cm}^2$) were placed between emitter and detector normally to the incident EM wave. The THz detector output is proportional to the instant electrical field strength of the THz pulse during the ultrashort pumping pulse. The Fourier transform of the waveform of electrical field of THz radiation gives the frequency dependence of complex transmission and reflection coefficients. The measurements were done in both transmission and reflection modes. The absorption coefficient, A , was calculated as $A = 1 - T - R$, where T and R are the transmission and reflection coefficients, respectively.

3. Results and Discussion

3.1. Morphological Characterization of the Porous Structures

SEM and TEM analysis of the porous structures (Figure 2) demonstrated that MWCNTs and GE sheets were segregated between the TPU particle boundaries, forming a percolated conductive network. Figure 2a,d reports the SEM images of TPU/MWCNTs D60 and G60 porous structures at low magnification. It is possible to see the differences in pore structures and thickness of internal trabeculae of D and G geometries as obtained by the SLS process. In particular, it is quite evident that the trabeculae of the G geometry are bigger than the trabeculae of the D geometry (about 30% bigger, as also discussed later in the paper). Indeed, the sintering of the TPU nanocomposite particles results in the formation of a continuous filler path spanning within the polymer matrix [24]. More specifically, SEM images (Figure 2b,e) clearly demonstrate that the surface of the TPU particles are covered with MWCNTs and GE filler particles. TEM pictures (Figure 2c,f) illustrate the formation of the percolated network due to the filler confinement between the sintered TPU particles, with a thread thickness ranging from 200 to 500 nm. It is worth noting that in the sample TPU/(MWCNTs-GE) G40, it is possible to observe that both fillers (MWCNTs and GE) were trapped between the polymer particles, forming a stable percolative network with a low filler concentration (i.e., 1 wt.%).

3.2. Thermal Properties

Thermal characterization of TPU-based samples was performed by TGA analysis. The thermogravimetric curves of TPU-based samples are compared in Figure 3. TPU degradation occurs in two steps as already described in our previous research [27]. Briefly, the first degradation that starts at about 280 °C is attributed to the cleavage of urethane bonds of TPU [42] and shows a maximum rate at 309 °C, accounting for about 30% mass loss. The second weight loss, with a maximum rate at 387 °C, is related to the decomposition of soft segments of TPU leading to a residual char value of 1.2%. The presence of the MWCNTs filler affects both the degradation onset, which occurred at about 300 °C, and the degradation rate maximum, which shifted to 340 °C. For the mixed system TPU/(MWCNTs GE), a dramatically different degradation curve was recorded with respect to the pristine TPU.

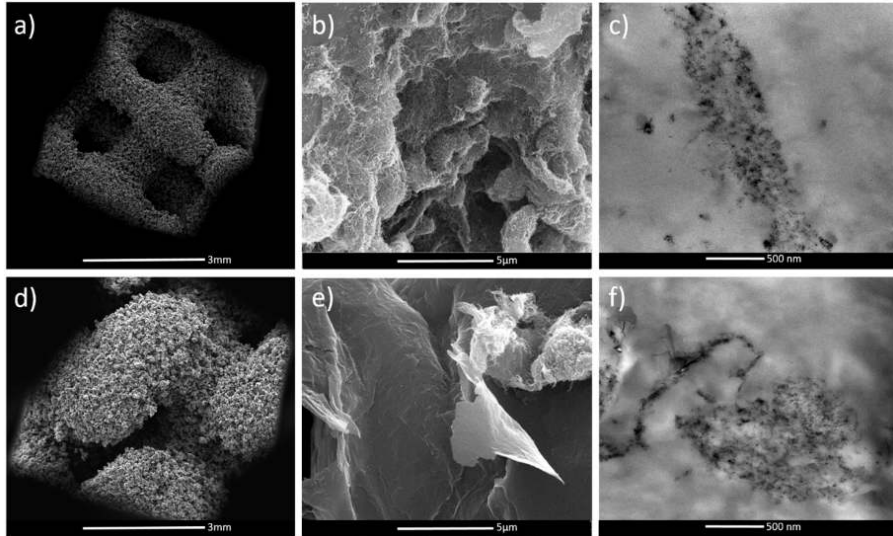


Figure 2. SEM of TPU/MWCNTs D60 and G60 samples at 50× magnification (a,d), SEM (b) and TEM (c) images of TPU/MWCNTs G60, and SEM (e) and TEM (f) images of TPU/(MWCNTs-GE) G60 porous structures.

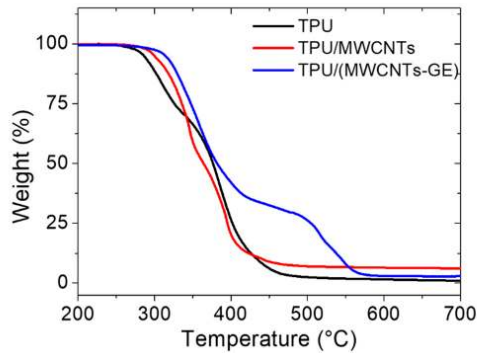


Figure 3. Thermogravimetric analysis (TGA) of TPU (black), TPU/MWCNTs (red), and TPU/(MWCNTs-GE) (blue).

The first degradation step started at around 310 °C, followed by a second degradation step at 488 °C. Therefore, the addition of fillers brings about an improvement of thermal stability of TPU, in particular, there is a synergistic effect of the CNTs and GE in the system with mixed fillers [43].

3.3. Mechanical and Piezoresistive Characterization

Compression tests were performed to study the effects of porosity and geometry on the mechanical behavior of the 3D porous structures. The samples were tested at small strain values (<10%) in order to consider the behavior in the linear elastic region. The values of elastic modulus are reported in Figure 4.

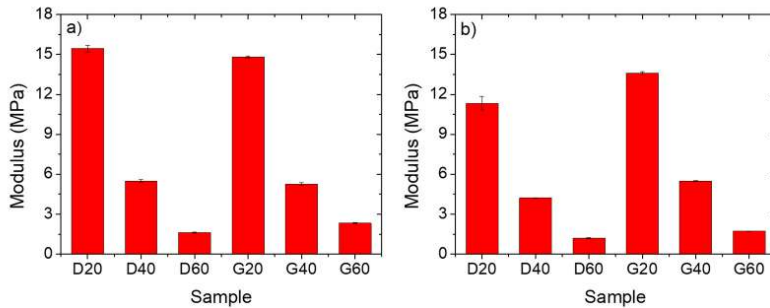


Figure 4. Compression elastic modulus of the selective laser sintering (SLS)-fabricated TPU/MWCNTs (a), and TPU/(MWCNTs-GE) (b) porous structures.

The average thickness of the trabeculae for TPU/MWCNTs and TPU/(MWCNTs-GE) systems with comparable geometry is similar, and this explains the comparable results above all for the systems with G unit cell geometry. As expected, raising the percentage of porosity causes the elastic modulus to strongly decrease, going, for the systems containing MWCNTs, from 15 MPa of the D20 to the 1.5 MPa of the D60. This is easily understandable by thinking that structures with higher porosity are characterized by thinner internal trabeculae, and this in turn strongly affects the mechanical response [31]. Moreover, it can be assessed that the type of filler seems to influence the mechanical response of the samples. In fact, the MWCNTs-based systems show better mechanical properties if compared to the MWCNTs/GE-based ones. This can be ascribed to the presence of GE nanosheets on the TPU particle surface that prevent the coalescence of the particle during the sintering process, thereby reducing the mechanical properties of the porous structure. This was confirmed also by comparing the mechanical properties of the proposed systems with the TPU/GE systems that we reported in a previous paper, where for the D60 system the elastic modulus value was 1.4 MPa [27].

The piezoresistive behavior of the 3D-printed porous structures was studied by submitting the samples to strain-controlled compression cycles with a maximum strain of 8%. Alongside with the mechanical response, the electrical resistance (R) of the structures was measured as a function of the compressive strain. The samples were submitted to 50 compressive cycles and the results of the TPU/MWCNTs systems with 60% of porosity are reported in Figure 5. By comparing the data shown in Figure 5a,b, it is possible to assess the effect of the geometry for the systems with the same formulation. The R values are similar, but the variation of the electrical resistance, ΔR , as consequence of the mechanical compression, is larger for the sample with G geometry. In the cyclic compression process, the mechanical response of the sample was very stable, whereas the electrical response presented some slight instability (which could also be ascribed to the electrical contact between the sample and the electrode) all over the experiment. However, the results confirmed the signal reversibility, with a direct correlation between the strain and the electrical resistance, that decreased by increasing the compression strain.

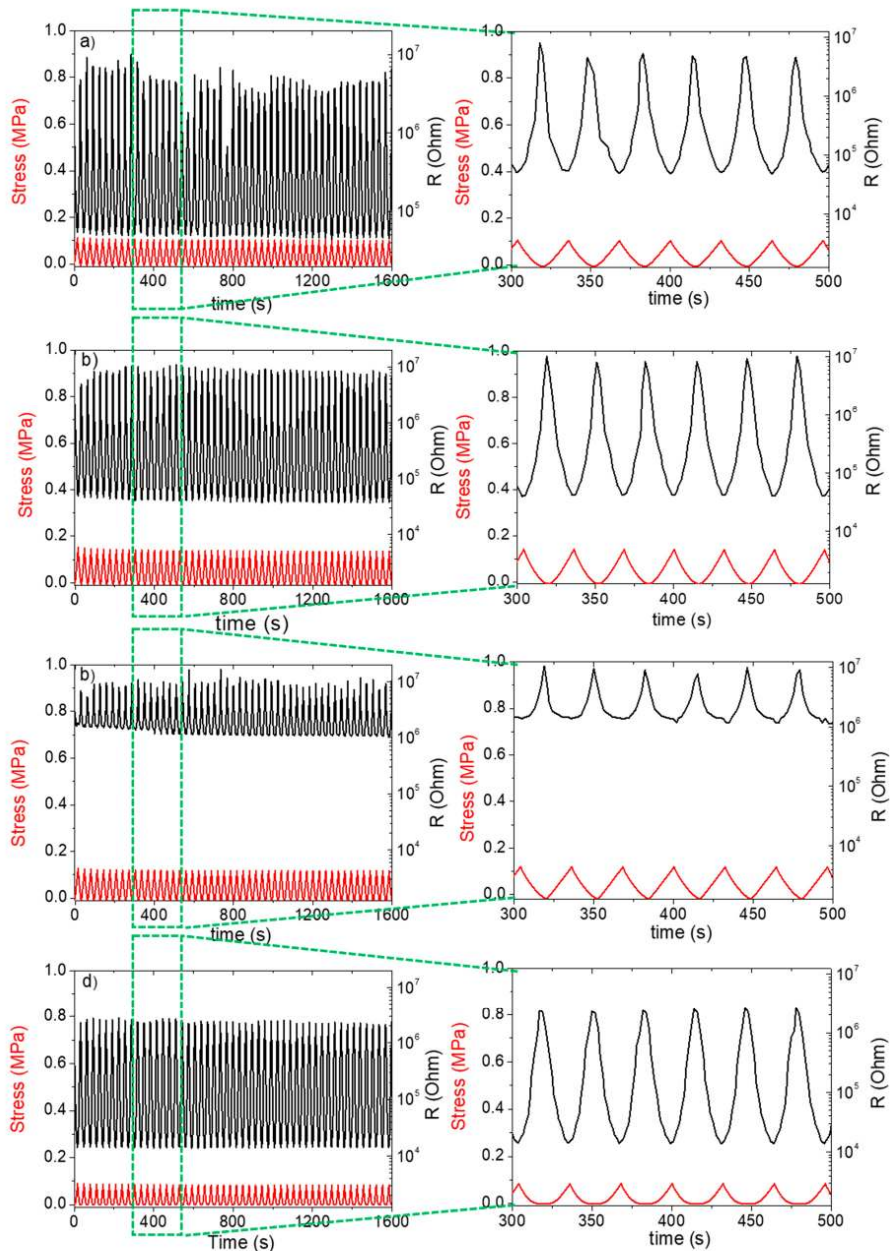


Figure 5. Piezoresistive behavior in terms of variation of compression stress and electrical resistance for the systems of (a) TPU/MWCNTs with D geometry, (b) TPU/MWCNTs, (c) TPU/GE, and (d) TPU/(MWCNTs-GE) with G geometry. All systems have 60% porosity and are submitted to compression loading/unloading cycles of up to 8% strain.

A direct comparison between the effects of different fillers on the piezoresistive behavior of printed samples with the same geometry and porosity is useful to give evidence of a possible synergistic effect. For sake of comparison, in this context, it has been considered important to present also the results related to the systems realized with GE nanoplatelets that were the object of a previous paper [27]. Electrical resistance of the TPU/GE system, after compression at 8% strain (Figure 5c), was higher than that of the MWCNTs system (Figure 5b). This behavior is in agreement with the literature data and the lower conductivity of GE-based composites as compared with the MWCNTs composites [44,45].

Moreover, it was possible to observe a synergistic effect of the fillers in the TPU/(MWCNTs-GE) system (Figure 5d). In fact, the resistance values for the TPU/(MWCNTs-GE) system at 0% and 8% strain were lower than those of the TPU/MWCNTs composite. This can be ascribed to the formation of more conductive pathways [46]. Furthermore, as it was expected, the resistance at 8% strain depends on sample porosity and geometry (see Figure 6) resulting larger for the systems with higher porosity (more details are provided later). Finally, the electrical resistance does not change during loading/unloading cycles as consequence of the satisfying robustness and stability of the porous structures.

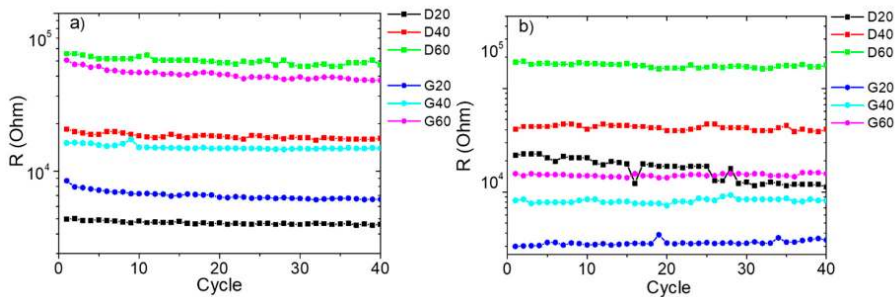


Figure 6. Resistance values at 8% strain for TPU/MWCNTs (a) and TPU/(MWCNTs-GE) (b) porous structures during the compression loading/unloading cycles.

It is worth noting that for the TPU/(MWCNTs-GE) composite, the systems with Gyroid structures showed significantly lower electrical resistance when subjected to compressive strain. This can be ascribed to the different internal structures of D60 and G60 samples. As shown in Figure 7, the cross-section area of G60 present thicker trabeculae if compared with D60 geometries (as also confirmed by SEM images reported in Figure 2). In fact, the average thickness of the G60 structure trabeculae is 1.360 ± 0.001 mm, which is 30% higher compared with the thickness of the D60 structure (equal to 1.040 ± 0.001 mm). This means that in the G60 structure, during compression loadings, the fillers create more effective percolating networks by forming more MWCNTs and GE nanoplatelets contacts.

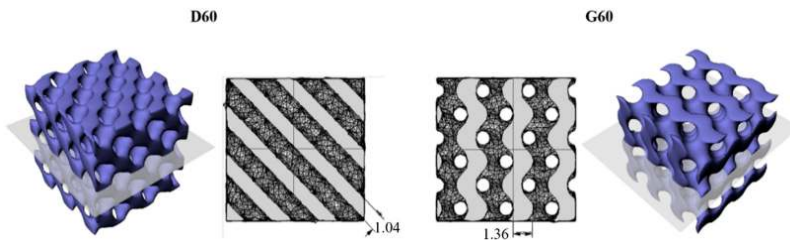


Figure 7. Cross-section areas and thickness of trabeculae for D60 and G60 structures.

To compare our results with those found in literature, it is worth noting that the average $\Delta R/R_0$ value measured for our systems is equal to 99.4% with a compression strain of 8%. Kang et al., measured a $\Delta R/R_0$ equal to 0.8% for a pressure of 5 MPa for systems consisting of single-wall-carbon nanotube/Polyimide, which is one order of magnitude higher compared with the compression stress applied in this research (i.e., about 0.2 MPa as shown in Figures 5 and 6) [47]. Similarly, a value of $\Delta R/R_0 \approx 15\%$, that is still lower as compared to the one shown by the systems investigated in this paper, at similar deformation ($\epsilon \approx 8\text{--}10\%$) was reported by Ku-Herrera et al. for poly (vinyl ester) filled with 0.3 wt.% of multi-wall carbon nanotubes (PVE-MWCNT) [48]. Bao et al., found that PDMS-SWCNT materials could have a resolution of minimum detectable stress in compression of 50 KPa and report a $\Delta R/R_0$ value of 8% for a strain of 50% [49]. Similar results are reported for a system of poly(isoprene)-reduced graphene oxide PI-RGO [50]. The comparisons with the above-mentioned systems allows us to conclude that the approach exploited in this paper, which combines nanocomposite powder and SLS printing technology, reveals that nanocomposite sensors are extremely sensitive to deformation, with a reproducible and stable piezoelectric behavior.

In order to gain a deeper understanding of the effect of geometry, SLS printing technology, printing resolution, and formulations on the electrical resistance of the considered systems, the resistivity of materials was calculated by taking into account the porosity and the measured resistance values at 0% strain. The calculations were performed by relating the measured electrical resistance only to the bulk materials, and considering the porosity as the empty fraction volume of the total volume of samples submitted to the electrical characterization, following the model developed by Montes et al. [51]. They analyzed the problem of the electrical conduction in powdered systems and proposed an equation for computing the effective electrical resistivity of sintered aggregates (Equation (3)).

$$\rho = R \left(\frac{S}{l} \right) \cdot \sqrt{(1 - \theta)^3} \quad (3)$$

where ρ is the resistivity of the porous system, R is the calculated resistance of the porous system, S is the contact surface between electrode and sample (in this case correspond with the surface of the sample), l is the distance between the electrodes (in this case correspond with the side of the sample), and θ is the porosity values.

Figure 8 shows the resistivity values for the TPU/MWCNTs and TPU/(MWCNTs-GE) systems, calculated accordingly with Equation (3).

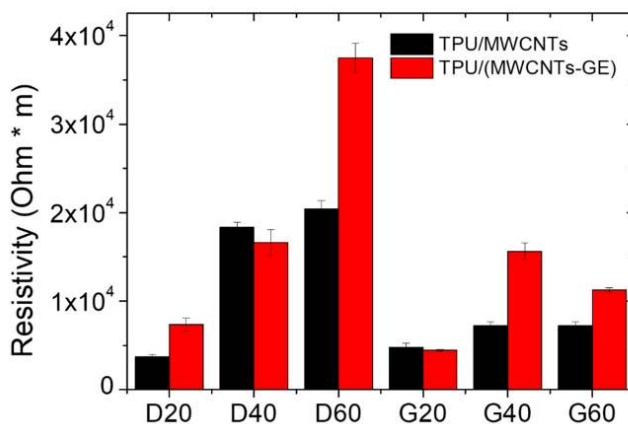


Figure 8. Electrical resistivity calculated by accounting for both the porosity of the systems and the electrical resistance (at 0% of strain).

The values of resistivity, which should be constant being the resistivity an intrinsic property of the materials, confirm that both the SLS printing process and geometry have a significant effect on the electrical resistance of the proposed systems. In fact, for the G samples, the resistivity is somewhat constant and does not depend on the porosity, in the range of approximations, due to the adoption of a very simple model to account for the porosity of samples. On the other side, for the systems with D geometry, the resistivity increases significantly with the porosity, confirming that the SLS printing process affects the formation of the conductive network that becomes worse and worse by increasing the porosity. This can be ascribed to the dimension of the trabeculae, which result smaller for the geometry D and give rise to a percolation network with less effective contact points between the MWCNTs and GE nanoparticles. Thus, the comparison of the electrical resistance values of systems with G geometry is robust and the variation can be related to the porosity, whereas for the D systems, it is worth considering that the geometry and SLS printing resolution affect the electrical resistance along with the porosity.

The compression sensitivity of several porous structures was evaluated by measuring the gauge factor (GF), defined as the ratio between the relative change of the electrical resistance of the composites and their initial resistance, divided by the applied strain. All samples displayed high absolute values of GF, and, in the range of errors, no significant differences can be noticed between TPU/MWCNTs and TPU/(MWCNTs-GE) nanocomposite structures. It has to be pointed out that GF values are higher for a strain below 8%, confirming the valuable feature of the composite structures to detect small deformations. In particular, the G20 TPU/MWCNT structure showed an almost double GF value at 1% deformation, suggesting its possible use in very sensitive strain sensing devices. For all samples, GF tended to a plateau as the maximum strain value was approached, as shown in Figure 9. The presence of the plateau at high compression deformation is to be ascribed to the densification of the conductive pathways, which do not further change with the compression.

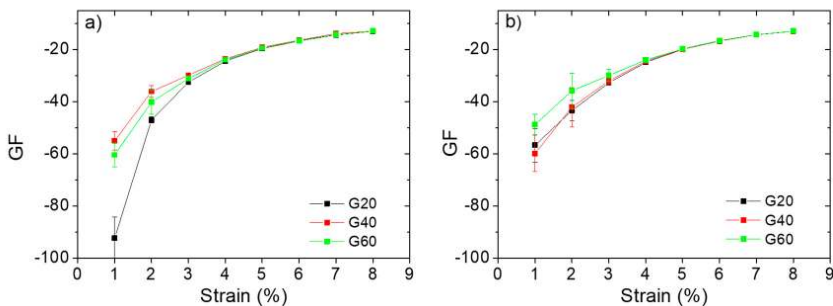


Figure 9. Variation of the gauge factor as a function of compression strain for TPU/MWCNTs (a) and TPU/(MWCNTs-GE) structures (b) with Gyroid unit cells.

3.4. EM Characterization

The broadband conductivity of investigated samples is shown in Figure 10. All percolated materials possess a similar frequency dependence of conductivity, consisting of two regions: the DC-like frequency-independent region is observable at lower frequencies, while at higher frequencies, the $\sigma \sim \omega^{-\alpha}$ dependence exists. For both TPU/MWCNT and TPU/(MWCNT-GE) structures, the presence of the DC-like conductivity at low frequencies is an evidence of percolation.

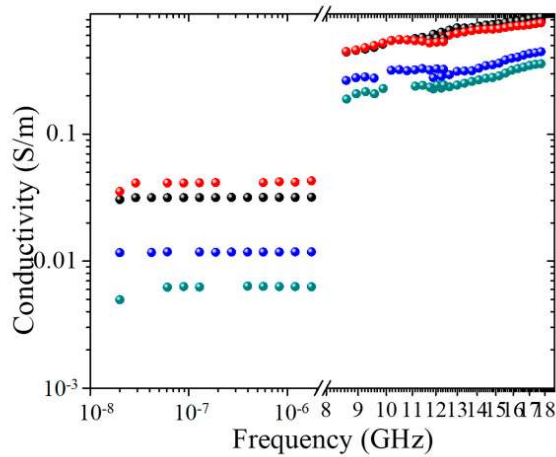


Figure 10. Broadband conductivity of porous structures: DC-like (0.02 kHz–1 kHz) and dielectric (12–18 GHz) conductivity behavior for TPU/MWCNTs G20 (black), TPU/MWCNTs G60 (blue), TPU/(MWCNTs-GE) G20 (red), and TPU/(MWCNTs-GE) G60 (green).

It is also possible to mention that in the DC-like range, for the systems with high porosity, the conductivity of TPU/MWCNT samples is higher than that of the systems based on TPU/MWCNT-GE, whereas only for the systems with low porosity, it seems that the GE nanoplatelets have a positive effect allowing an increment of the conductivity. The discrepancy found by comparing these results with those reported in Figure 5, may be ascribed to the fact that for broadband conductivity measurements were used with smaller samples ($\sim 5 \times 5 \times 3 \text{ mm}^3$) as compared to those used for piezoresistive characterization. That, above all for samples with high porosity (60%), may affect the reproducibility of the results.

The electromagnetic shielding performance of the SLS-printed porous structures was evaluated for the G20 and G60 made of TPU/MWCNTs and TPU/(MWCNTs-GE) systems. The frequency dependence of real and imaginary parts of dielectric permittivity is presented in Figure 11.

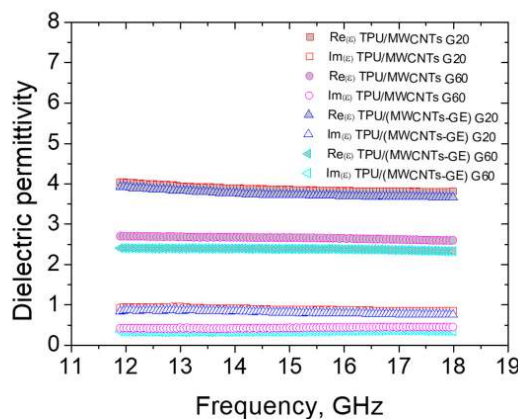


Figure 11. The dielectric permittivity of TPU/(MWCNTs-GE) G20 and G60 samples.

The dielectric permittivity of all samples remains almost constant within 12–18 GHz. A minor decrease of both components of dielectric permittivity (ϵ) is observed for the denser sample G20. The higher values of permittivity of sample G20 vs. G60 (dense vs. lighter) are in good correspondence with the effective medium Maxwell Garnett model for composite containing conductive particles [52]

The observed values of dielectric permittivity are suitable for the effective absorption of electromagnetic waves in both free space and the waveguide combined with the mirror (back reflector) [53]. According to Figure 12a, the microwave absorption coefficient within the Ku-band (12–18 GHz) is in the range of 0.51–0.99 and 0.70–0.91 for 10.6 mm thick samples of G60 and G20 series, respectively, with the peak absorption being close to 100% at 15–16 GHz.

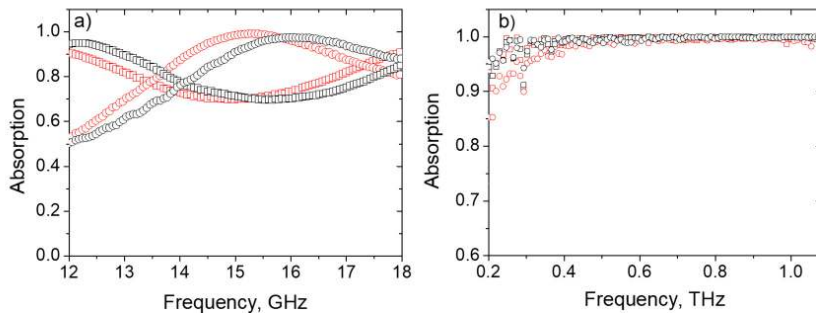


Figure 12. (a) Absorption coefficient of 10.6 mm thick samples with back reflector in the waveguide. (b) Absorption coefficient of 2 mm thick samples in the free space for TPU/MWCNTs G20 (red square), TPU/MWCNTs G60 (red ring), TPU/(MWCNTs-GE) G20 (black square), and TPU/(MWCNTs-GE) G60 (black ring).

The absorption coefficients of all investigated samples were calculated in the frequency range 0.2–1 THz (see Figure 12b) from the data collected for transmission and reflection by THz time-domain spectroscopy.

All samples (G20 and G60 series) are very lossy in the THz range and demonstrate outstanding absorption ability: the absorption coefficient of 2 mm thick samples is close to 100% starting from 300 GHz.

All investigated samples show not only extensive EMI SE, but also very high efficiency as EM waves absorbers in broad frequency range spanning from tens GHz to 1 THz. The reason is that SLS-printed samples made of TPU/MWCNTs and TPU/(MWCNTs-GE) comprise three levels of “porosity”. The inherent pores with the size coming from the lattice parameters is of 0.1 mm order (corresponding to the THz wavelength). Multiple reflection from the sides of these pores followed by Ohmic losses of the structure skeleton are the reasons of high absorption ability of G20–G60 in the THz range.

The second level is the porosity of the systems, easily visible in the SEM images (Figure 2). It corresponds to 50–100 nm pores originated by defects in the sintering of wrapped TPU particles, and because of their small size are “invisible” for both investigated microwave and THz radiation, just making the overall structure slightly lighter.

To summarize, due to nested “Russian doll” porosity structure, it is possible to approach very high absorption in different frequency ranges with one sample. Moreover, this is the way of tailoring EMI SE (absorption) addressing many frequency slots, i.e., just changing the pore size by 3D printing, porosity of the structure skeleton, and geometrical features/carbonaceous filler properties of the segregated network.

4. Conclusions

Porous conductive 3D structures were successfully fabricated by SLS using TPU powder wrapped with MWCNTs and a mixture of MWCNTs and GE nanofillers. The samples had a porosity ranging from 20% to 60% and were realized with the Gyroid and Diamond unit cell. Mechanical, electrical, and electromagnetic properties were investigated and correlated with porosity and internal architecture of printed samples.

SEM and TEM characterization clearly indicated that SLS manufacturing is suitable to create a high pore interconnectivity. Moreover, upon processing, the nanofillers remain segregated between the particle boundaries, forming a conductive network that facilitates the electrical percolation. The presence of GE improves the thermal stability of TPU. Compression tests and electrical conductivity measurements revealed a correlation between geometrical features and elastic modulus as well as a gauge factor. In particular, G structures showed higher elastic modulus in comparison to the D architectures.

Moreover, MWCNTs-based structures displayed satisfying electrical properties, and a synergistic conductivity enhancement was observed for the TPU/(MWCNTs-GE)-based G architectures. This was ascribed to the structure of samples with G geometry, which present bigger trabeculae and thus a better percolating network as compared to the systems with D geometry. All structures showed robust piezoresistivity, with a gauge factor value of -13 at 8% strain for all systems, which remarkably varied from -70 to -20 over strain extents ranging from 1% to 5%, which is the strain range in which the composite can be used as a sensor.

Finally, a high level of EMI SE, caused by absorption of electromagnetic waves in Ku-band (12–18 GHz), was observed for G-type samples having different porosity. The waves from 300 GHz to 1 THz could not pass through 2 mm thick G20 (60) lattice due to perfect absorption. EM response peculiarities have been associated with the multi-level porosity of the samples (starting from their cellular SLS-printed structure and due to the MWCNT/GE segregated percolative network).

Highlights: The results demonstrate that mixing MWCNTs and GE minimizes the coalescence issue, which was observed in literature for GE systems.

The right balance between mechanical and functional properties of the printed structures make these systems suitable as stable piezoresistive sensors.

The systems have relevant EMI shielding properties.

Author Contributions: Conceptualization, M.L., L.A., P.K., and H.X.; methodology and sample preparation, A.R., G.F., and X.P.G.; data analysis, A.R., G.R., G.F., G.G., P.C., and D.B.; writing—original draft preparation, A.R., G.R., D.B., and P.C.; writing—review & editing, M.L., P.C., P.K., L.A., and H.X. All authors have read and agreed to the published version of the manuscript.

Funding: This research was funded by the Marie Skłodowska-Curie Actions (MSCA) Research and Innovation Staff Exchange (RISE) H2020-MSCA-RISE-2016, Project Acronym: Graphene 3D—Grant Number: 734164, the National Key R&D Program of China (2017YFE01115000), and NATO SPS proposal G5697 CERTAIN project. P.K. is supported by Horizon 2020 IF TURANDOT project 836816 and Academy of Finland Flagship Programme, Photonics Research and Innovation (PREIN), decision 320166. D.B. is thankful for the support by the Tomsk State University Competitiveness Improvement Program.

Conflicts of Interest: The authors declare no conflict of interest.

References

1. Yan, Y.; Sencadas, V.; Zhang, J.; Zu, G.; Wei, D.; Jiang, Z. Processing, characterisation and electromechanical behaviour of elastomeric multiwall carbon nanotubes-poly (glycerol sebacate) nanocomposites for piezoresistive sensors applications. *Compos. Sci. Technol.* **2017**, *142*, 163–170. [[CrossRef](#)]
2. Yaseer Omar, M.; Xiang, C.; Gupta, N.; Strbik, O.M.; Cho, K. Syntactic foam core metal matrix sandwich composite: Compressive properties and strain rate effects. *Mater. Sci. Eng. A* **2015**, *643*, 156–168. [[CrossRef](#)]
3. Mahendia, S.; Tomar, A.K.; Kumar, S. Electrical conductivity and dielectric spectroscopic studies of PVA-Ag nanocomposite films. *J. Alloys Compd.* **2010**, *508*, 406–411. [[CrossRef](#)]

4. Hansen, T.S.; West, K.; Hassager, O.; Larsen, N.B. Highly stretchable and conductive polymer material made from poly(3,4-ethylenedioxythiophene) and polyurethane elastomers. *Adv. Funct. Mater.* **2007**, *17*, 3069–3073 [[CrossRef](#)]
5. Liu, H.; Dong, M.; Huang, W.; Gao, J.; Dai, K.; Guo, J.; Zheng, G.; Liu, C.; Shen, C.; Guo, Z. Lightweight conductive graphene/thermoplastic polyurethane foams with ultrahigh compressibility for piezoresistive sensing. *J. Mater. Chem. C* **2017**, *5*, 73–83.
6. Wang, L.; Ding, T.; Wang, P. Thin flexible pressure sensor array based on carbon black/silicone rubber nanocomposite. *IEEE Sens. J.* **2009**, *9*, 1130–1135.
7. Tao, J.; Liu, N.; Ma, W.; Ding, L.; Li, L.; Su, J.; Gao, Y. Solid-state high performance flexible supercapacitors based on polypyrrole-MnO₂-carbon fiber hybrid structure. *Sci. Rep.* **2013**, *3*, 22687–22694.
8. Guan, X.; Zheng, G.; Dai, K.; Liu, C.; Yan, X.; Shen, C.; Guo, Z. Carbon nanotubes-adsorbed electrospun PA66 nanofiber bundles with improved conductivity and robust flexibility. *ACS Appl. Mater. Interfaces* **2016**, *8*, 14150–14159.
9. Gupta, P.; Yadav, S.K.; Agrawal, B.; Goyal, R.N. A novel graphene and conductive polymer modified pyrolytic graphite sensor for determination of propranolol in biological fluids. *Sens. Actuators B Chem.* **2014**, *204*, 791–798.
10. Bai, J.; Zhou, A.; Huang, Z.; Wu, J.; Bai, H.; Li, L. Ultra-light and elastic graphene foams with a hierarchical structure and a high oil absorption capacity. *J. Mater. Chem. A* **2015**, *3*, 22687–22694.
11. Liu, H.; Gao, J.; Huang, W.; Dai, K.; Zheng, G.; Liu, C.; Shen, C.; Yan, X.; Guo, J.; Guo, Z. Electrically conductive strain sensing polyurethane nanocomposites with synergistic carbon nanotubes and graphene bifillers. *Nanoscale* **2016**, *8*, 12977–12989. [[PubMed](#)]
12. Zhang, D.; Chi, B.; Li, B.; Gao, Z.; Du, Y.; Guo, J.; Wei, J. Fabrication of highly conductive graphene flexible circuits by 3D printing. *Synth. Met.* **2016**, *217*, 79–86.
13. Wang, H.; Xie, G.; Fang, M.; Ying, Z.; Tong, Y.; Zeng, Y. Electrical and mechanical properties of antistatic PVC films containing multi-layer graphene. *Compos. Part. B Eng.* **2015**, *79*, 444–450.
14. Chen, Z.; Xu, C.; Ma, C.; Ren, W.; Cheng, H. Lightweight and flexible graphene foam composites for high-performance electromagnetic interference shielding. *Adv. Mater.* **2013**, *25*, 1296–1300.
15. Tang, D.; Ma, G.; Zhang, L.; Chen, G. Graphene-epoxy composite electrode fabricated by in situ polycondensation for enhanced amperometric detection in capillary electrophoresis. *J. Chromatogr. A* **2013**, *1316*, 127–134.
16. Zhan, Y.; Lavorgna, M.; Buonocore, G.; Xia, H. Enhancing electrical conductivity of rubber composites by constructing interconnected network of self-assembled graphene with latex mixing. *J. Mater. Chem.* **2012**, *22*, 10464–10468.
17. Bose, S.; Bhattacharyya, A.R.; Kulkarni, A.R.; Pötschke, P. Electrical, rheological and morphological studies in co-continuous blends of polyamide 6 and acrylonitrile-butadiene-styrene with multiwall carbon nanotubes prepared by melt blending. *Compos. Sci. Technol.* **2009**, *69*, 365–372. [[CrossRef](#)]
18. Araby, S.; Meng, Q.; Zhang, L.; Kang, H.; Majewski, P.; Tang, Y.; Ma, J. Electrically and thermally conductive elastomer/graphene nanocomposites by solution mixing. *Polymer* **2014**, *55*, 201–210.
19. Manapat, J.Z.; Chen, Q.; Ye, P.; Advincula, R.C. 3D printing of polymer nanocomposites via stereolithography. *Macromol. Mater. Eng.* **2017**, *302*, 1600553.
20. Chen, Q.; Mangadla, J.D.; Wallat, J.; De Leon, A.; Pokorski, J.K.; Advincula, R.C. 3D printing biocompatible polyurethane/poly (lactic acid)/graphene oxide nanocomposites: Anisotropic properties. *ACS Appl. Mater. Interfaces* **2017**, *9*, 4015–4023.
21. Lee, J.-Y.; An, J.; Chua, C.K. Fundamentals and applications of 3D printing for novel materials. *Appl. Mater. Today* **2017**, *7*, 120–133.
22. Paggi, R.A.; Beal, V.E.; Salmoria, G.V. Process optimization for PA12/MWCNT nanocomposite manufacturing by selective laser sintering. *Int. J. Adv. Manuf. Technol.* **2013**, *66*, 1977–1985.
23. Shuai, C.; Gao, C.; Feng, P.; Peng, S. Graphene-reinforced mechanical properties of calcium silicate scaffolds by laser sintering. *RSC Adv.* **2014**, *4*, 12782–12788. [[CrossRef](#)]
24. Li, Z.; Wang, Z.; Gan, X.; Fu, D.; Fei, G.; Xia, H. Selective laser sintering 3D printing: A way to construct 3d electrically conductive segregated network in polymer matrix. *Macromol. Mater. Eng.* **2017**, *302*, 1700211.
25. Yuan, S.; Shen, F.; Bai, J.; Chua, C.K.; Wei, J.; Zhou, K. 3D soft auxetic lattice structures fabricated by selective laser sintering: TPU powder evaluation and process optimization. *Mater. Des.* **2017**, *120*, 317–327.

26. Robertson, J.M.; Torbati, A.H.; Rodriguez, E.D.; Mao, Y.; Baker, R.M.; Qi, H.J.; Mather, P.T. Mechanically programmed shape change in laminated elastomeric composites. *Soft Matter* **2015**, *11*, 5754–5764.
27. Ronca, A.; Rollo, G.; Cerruti, P.; Fei, G.; Gan, X.; Buonocore, G.G.; Lavorgna, M.; Xia, H.; Silvestre, C.; Ambrosio, L. Selective laser sintering fabricated thermoplastic polyurethane/graphene cellular structures with tailorable properties and high strain sensitivity. *Appl. Sci.* **2019**, *9*, 864. [[CrossRef](#)]
28. Liu, H.; Li, Y.; Dai, K.; Zheng, G.; Liu, C.; Shen, C.; Yan, X.; Guo, J.; Guo, Z. Electrically conductive thermoplastic elastomer nanocomposites at ultralow graphene loading levels for strain sensor applications *J. Mater. Chem. C* **2016**, *4*, 157–166.
29. Geetha, S.; Satheesh Kumar, K.K.; Rao, C.R.K.; Vijayan, M.; Trivedi, D.C. EMI shielding: Methods and materials—A review. *J. Appl. Polym. Sci.* **2009**, *112*, 2073–2086.
30. Pang, H.; Xu, L.; Yan, D.-X.; Li, Z.-M. Conductive polymer composites with segregated structures *Prog. Polym. Sci.* **2014**, *39*, 1908–1933.
31. Gan, X.; Wang, J.; Wang, Z.; Zheng, Z.; Lavorgna, M.; Ronca, A.; Fei, G.; Xia, H. Simultaneous realization of conductive segregation network microstructure and minimal surface porous macrostructure by SLS 3D printing. *Mater. Des.* **2019**, *178*, 107874. [[CrossRef](#)]
32. Zhan, Y.; Oliviero, M.; Wang, J.; Sorrentino, A.; Buonocore, G.G.; Sorrentino, L.; Lavorgna, M.; Xia, H.; Iannace, S. Enhancing the EMI shielding of natural rubber-based supercritical CO₂ foams by exploiting their porous morphology and CNT segregated networks. *Nanoscale* **2019**, *11*, 1011–1020. [[CrossRef](#)] [[PubMed](#)]
33. Tasolamprou, A.C.; Koulouklidis, A.D.; Daskalaki, C.; Mavidiis, C.P.; Kenanakis, G.; Deligeorgis, G.; Viskadourakis, Z.; Kuzhir, P.; Tzortzakis, S.; Kafesaki, M. Experimental demonstration of ultrafast THz absorption in a graphene-based thin film absorber through negative photoinduced conductivity *ACS Photonics* **2019**, *6*, 720–727. [[CrossRef](#)] [[PubMed](#)]
34. Paddubskaya, A.; Demidenko, M.; Batrakov, K.; Valušis, G.; Kaplas, T.; Svirko, Y.; Kuzhir, P. Tunable perfect THz absorber based on a stretchable ultrathin carbon-polymer bilayer. *Materials* **2019**, *12*, 143. [[CrossRef](#)] [[PubMed](#)]
35. Kuzhir, P.P.; Paddubskaya, A.G.; Volynets, N.I.; Batrakov, K.G.; Kaplas, T.; Lamberti, P.; Kotsilkova, R.; Lambin, P. Main principles of passive devices based on graphene and carbon films in microwave—THz frequency range. *J. Nanophotonics* **2017**, *11*, 32504. [[CrossRef](#)]
36. Batrakov, K.; Kuzhir, P.; Maksimenko, S.; Volynets, N.; Voronovich, S.; Paddubskaya, A.; Valušis, G.; Kaplas, T.; Svirko, Y.; Lambin, P. Enhanced microwave-to-terahertz absorption in graphene. *Appl. Phys. Lett.* **2016**, *108*, 123101. [[CrossRef](#)]
37. Letellier, M.; Macutkevicius, J.; Kuzhir, P.; Banys, J.; Fierro, V.; Celzard, A. Electromagnetic properties of model vitreous carbon foams. *Carbon N. Y.* **2017**, *122*, 217–227. [[CrossRef](#)]
38. Kotsilkova, R.; Ivanov, E.; Bychanok, D.; Paddubskaya, A.; Demidenko, M.; Macutkevicius, J.; Maksimenko, S.; Kuzhir, P. Effects of sonochemical modification of carbon nanotubes on electrical and electromagnetic shielding properties of epoxy composites. *Compos. Sci. Technol.* **2015**, *106*, 85–92. [[CrossRef](#)]
39. Kuzhir, P.; Paddubskaya, A.; Bychanok, D.; Nemilentsau, A.; Shuba, M.; Plusch, A.; Maksimenko, S.; Bellucci, S.; Coderoni, L.; Micciulla, F. Microwave probing of nanocarbon based epoxy resin composite films: Toward electromagnetic shielding. *Thin Solid Films* **2011**, *519*, 4114–4118. [[CrossRef](#)]
40. ASTM. *D5568-95 Standard Test Method for Measuring Relative Complex Permittivity and Relative Magnetic Permeability of Solid Materials at Microwave Frequencies*; ASTM International: West Conshohocken, PA, USA, 2001.
41. Paddubskaya, A.; Valynets, N.; Kuzhir, P.; Batrakov, K.; Maksimenko, S.; Kotsilkova, R.; Velichkova, H.; Petrova, I.; Biró, I.; Kertész, K. Electromagnetic and thermal properties of three-dimensional printed multilayered nano-carbon/poly (lactic) acid structures. *J. Appl. Phys.* **2016**, *119*, 135102. [[CrossRef](#)]
42. Liu, H.; Huang, W.; Yang, X.; Dai, K.; Zheng, G.; Liu, C.; Shen, C.; Yan, X.; Guo, J.; Guo, Z. Organic vapor sensing behaviors of conductive thermoplastic polyurethane–graphene nanocomposites. *J. Mater. Chem. C* **2016**, *4*, 4459–4469. [[CrossRef](#)]
43. Wang, X.; Hu, Y.; Song, L.; Yang, H.; Xing, W.; Lu, H. In situ polymerization of graphene nanosheets and polyurethane with enhanced mechanical and thermal properties. *J. Mater. Chem.* **2011**, *21*, 4222–4227. [[CrossRef](#)]
44. Xie, S.H.; Liu, Y.Y.; Li, J.Y. Comparison of the effective conductivity between composites reinforced by graphene nanosheets and carbon nanotubes. *Appl. Phys. Lett.* **2008**, *92*, 243121. [[CrossRef](#)]

45. Du, J.; Zhao, L.; Zeng, Y.; Zhang, L.; Li, F.; Liu, P.; Liu, C. Comparison of electrical properties between multi-walled carbon nanotube and graphene nanosheet/high density polyethylene composites with a segregated network structure. *Carbon N. Y.* **2011**, *49*, 1094–1100. [[CrossRef](#)]
46. Hodlur, R.M.; Rabinal, M.K. Self assembled graphene layers on polyurethane foam as a highly pressure sensitive conducting composite. *Compos. Sci. Technol.* **2014**, *90*, 160–165. [[CrossRef](#)]
47. Kang, J.H.; Park, C.; Scholl, J.A.; Brazin, A.H.; Holloway, N.M.; High, J.W.; Lowther, S.E.; Harrison, J.S. Piezoresistive characteristics of single wall carbon nanotube/polyimide nanocomposites. *J. Polym. Sci. Part B Polym. Phys.* **2009**, *47*, 994–1003. [[CrossRef](#)]
48. Ku-Herrera, J.J.; Avilés, F. Cyclic tension and compression piezoresistivity of carbon nanotube/vinyl ester composites in the elastic and plastic regimes. *Carbon N. Y.* **2012**, *50*, 2592–2598. [[CrossRef](#)]
49. Lipomi, D.J.; Vosgueritchian, M.; Tee, B.C.K.; Hellstrom, S.L.; Lee, J.A.; Fox, C.H.; Bao, Z. Skin-like pressure and strain sensors based on transparent elastic films of carbon nanotubes. *Nat. Nanotechnol.* **2011**, *6*, 788–792
50. Kumar, S.K.; Castro, M.; Saiter, A.; Delbreilh, L.; Feller, J.F.; Thomas, S.; Grohens, Y. Development of poly (isobutylene-co-isoprene)/reduced graphene oxide nanocomposites for barrier, dielectric and sensing applications. *Mater. Lett.* **2013**, *96*, 109–112. [[CrossRef](#)]
51. Montes, J.M.; Cuevas, F.G.; Cintas, J.; Ternero, F.; Caballero, E.S. Electrical resistivity of powdered porous compacts. In *Electrical and Electronic Properties of Materials*; IntechOpen: London, UK, 2018.
52. Bychanok, D.; Angelova, P.; Paddubskaya, A.; Meisak, D.; Shashkova, L.; Demidenko, M.; Plyushch, A.; Ivanov, E.; Krastev, R.; Kotsilkova, R. Terahertz absorption in graphite nanoplatelets/polylactic acid composites. *J. Phys. D Appl. Phys.* **2018**, *51*, 145307. [[CrossRef](#)]
53. Bychanok, D.; Gorokhov, G.; Meisak, D.; Kuzhir, P.; Maksimenko, S.A.; Wang, Y.; Han, Z.; Gao, X.; Yue, H. Design of carbon nanotube-based broadband radar absorber for ka-band frequency range. *Prog. Electromagn. Res.* **2017**, *53*, 9–16. [[CrossRef](#)]



© 2020 by the authors. Licensee MDPI, Basel, Switzerland. This article is an open access article distributed under the terms and conditions of the Creative Commons Attribution (CC BY) license (<http://creativecommons.org/licenses/by/4.0/>).

3 publikacija / 3rd publication

**Terahertz Optics of Materials with Spatially Harmonically
Distributed Refractive Index**



D.S. Bychanok, **G.V. Gorokhov**, A. Plyushch, A. Ronca, M. Lavorgna,
H. Xia, P. Lamberti and P. Kuzhir

Materials **2020** 13 5208

DOI: 10.3390/ma13225208

Article

Terahertz Optics of Materials with Spatially Harmonically Distributed Refractive Index

Dzmitry Bychanok ^{1,2,*}, Gleb Gorokhov ^{1,3}, Artyom Plyushch ^{1,3}, Alfredo Ronca ⁴,
Marino Lavorgna ⁴, Hesheng Xia ^{4,5}, Patrizia Lamberti ⁶ and Polina Kuzhir ^{1,7}

- ¹ Research Institute for Nuclear Problems Belarusian State University, Bobruiskaya str. 11, 220030 Minsk, Belarus; glebgorokhov@yandex.ru (G.G.); artyom.plyushch@ff.vu.lt (A.P.); polina.kuzhir@gmail.com (P.K.)
 - ² Radioelectronics Department, Faculty of Radiophysics, Tomsk State University, 36 Lenin Prospekt, 634050 Tomsk, Russia
 - ³ Faculty of Physics, Vilnius University, Sauletekio 3, LT-10222 Vilnius, Lithuania
 - ⁴ Institute of Polymer, Composite and Biomaterials, National Research Council, Via G.PreViati, 1/E, 23900 Lecco, Italy; alfredo.ronca@cnr.it (A.R.); mlavorgn@unina.it (M.L.); xiahs@scu.edu.cn (H.X.)
 - ⁵ State Key Laboratory of Polymer Materials Engineering, Polymer Research Institute, Sichuan University, Chengdu 610065, China
 - ⁶ Dept. of Information and Electrical Engineering and Applied Mathematics, University of Salerno, Via Giovanni Paolo II, 132-84084 Fisciano (SA), Italy; plamberti@unisa.it
 - ⁷ Institute of Photonics, University of Eastern Finland, Yliopistokatu 7, FI-80101 Joensuu, Finland
- * Correspondence: dzmitrybychanok@yandex.by

Received: 14 October 2020; Accepted: 12 November 2020; Published: 18 November 2020



Abstract: The electromagnetic properties of structures with spatially periodic distributed graded refractive index were investigated in the terahertz frequency range. The band structure and electromagnetic response of material with harmonically distributed refractive index were calculated and analyzed. The analytical expressions for frequencies of the first and second bandgap are derived. 3D printed gyroid based architectures were proven to be harmonically graded refractive index structures with designed bandgaps in THz frequency ranges. The transmission coefficient of thermoplastic polyurethane-based samples were experimentally measured in the frequency range 100–500 GHz and compared with theoretical results. Due to losses in the real world produced samples, the predicted response is significantly dumped in the terahertz range and only traces of band gaps are experimentally observed. This funding paves the way toward a new generation of 3D printed THz components for gradient-index optics applications.

Keywords: terahertz bandgap; graded index materials; harmonically distributed refractive index

1. Introduction

The dielectric based periodic structures are widely investigated in the visible frequency range [1–3] and often may be considered as graded refractive index materials [4,5], being a practical realization of a gradient-index optics [6–8]. Graded refractive index materials can be found in nature (in particular, butterfly wings where colors appear due to a certain shape of chitin, gyroid) [4,9,10] and may be produced artificially [3,11].

Gyroid was first developed by NASA physicist Alan Schoen [12] as a result of his search for ultra-light and ultra mechanically robust material for space applications. A gyroid is a connected structure endlessly repeating in three dimensions that has the smallest possible surface. Passing through gyroid based butterfly wings, the light is refracted and we see such beautiful overflows and fantastic tones.

The gyroids are multifunctional structures—particularly in [13] they are proposed for designing bone scaffolds. The electromagnetic study of the gyroids structures of certain geometrical parameters will allow designing a new generation of components to manipulate light of different wavelength, including infrared and terahertz.

Nowadays the materials with a bandgap in the terahertz region have attracted a lot of attention of the scientific community [14–16]. The design, manufacturing, and tuning of such materials is a challenging problem for material science. Actually, the minimal surfaces were proposed in [17] as candidates for photonic bandgap materials. Recently, the mechanically tunable microwave properties of gyroid photonic crystal were investigated in [18].

In this communication, we suggest simple and reproducible road toward THz gradient-index optics by 3D printing of gyroid-based architectures as harmonically graded refractive index structures. We demonstrate both theoretically and experimentally the possibility to design the bandgap of 3D printed gyroid based structure in the submillimeter frequency range.

2. One-Dimensional Structures with Periodically Distributed Refractive Index

Let us consider material with harmonically distributed refractive index along z -axis (see Figure 1a):

$$n(z) = n_0 + \Delta n \cos(2\pi z/\lambda), \quad (1)$$

where n_0 is the average value of the refractive index, Δn is the dispersion of refractive index, λ is the distribution period.

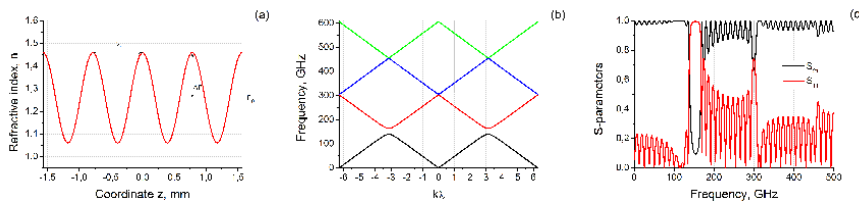


Figure 1. (a) The refractive index distribution along z -axis; (b) The band structure of considered material with parameters $n_0 = 1.26$, $\Delta n = 0.20$ and $\lambda = \pi/4$ mm; (c) relative amplitudes of reflected (S_{11}) and transmitted (S_{21}) signals of piece of material with thickness $\tau = 3\pi \simeq 9.5$ mm.

We start to study the features of propagation of electromagnetic waves along the z -axis in such material with the calculation of dispersion relation and band structure. The transformation of $n(z)$ to $\omega(k)$ may be performed by using plane wave expansion method [19–21] (see details in Appendix A). The calculated band structure of considered material with parameters $n_0 = 1.26$, $\Delta n = 0.20$ and $\lambda = \pi/4$ mm is presented in Figure 1b. One can see that the structure has at least two bandgaps near 150 and 300 GHz. The detailed inspection of Figure 1b shows that exist also very narrow (the width less than 1 GHz) the third bandgap near 450 GHz.

The electromagnetic response (i.e., relative amplitudes of reflected S_{11} and transmitted S_{21} plane waves normally scattered on the sample of finite thickness τ) of material with spatial refractive index distribution may be calculated using matrix method [22,23] (see Appendix B). The results of S-parameters calculations for $\tau = 3\pi$ mm are presented in Figure 1c. The material becomes to be not transparent and electromagnetic waves are reflecting from it near 140–163 GHz. The second and third reflection and transmission peaks also exist at the frequencies near 300 GHz and 450 GHz. The most pronounced is the first peak, the second one has lower amplitude and is more narrow, the amplitude of the third peak (and all next ones) becomes almost comparable with the interference oscillations related to the finite size of a sample τ .

The physical origin of the observable band structure is based on interference of reflected from investigated sample waves. The position of the band gaps is generally determined by the averaged

value of the refractive index and the distance between the maxima of the periodic function n . Partial waves reflected from regions separated by distance λ are added to each other and form a signal reflected from the sample. When the phase difference between them reaches 2π , the first bandgap appears. In this case, the effective wavelength is $2\lambda = \pi/2$ mm, which corresponds to frequencies of about 150 GHz. Waves reflected from neighboring regions, in this case, are in phase and amplify each other. This is the origin of why material becomes opaque for frequencies within the bandgap.

The general feature of presented in Figure 1b,c dispersion relation and electromagnetic response is two pronounced bandgaps near 140–163 GHz and 300 GHz. Important to note that the gaps are equidistant and the second bandgap (also the third and all next ones) is significantly less than the first. This type of band structure is a specific feature of structure with refractive index n distribution by Equation (1) in contrast to, for example, a photonic crystal formed by a one-dimensional array of air slabs penetrating a dielectric background [19].

In the sections below we will examine how the position and width of the lowest two gaps depend on the average value of the refractive index, its dispersion and distribution period.

2.1. Dependence of Gap on n , Δn and λ

2.1.1. Numerical Results

According to numerical calculations the first bandgap in Figure 1 is about 23.8 GHz the second is 5.6 GHz for $n_0 = 1.26$, $\Delta n = 0.20$ and $\lambda = \pi/4$ mm. To estimate how the electromagnetic response depends on parameters in Equation (1) we first of all performed the simplest numerical experiment and calculated the spectra of S_{11} and S_{21} varying n , Δn and λ . In general, the structure of spectra remains the same as the Figure 1c, but the position and width of the bandgaps are changed.

Particularly, by increasing n_0 in two times, the middle frequencies of bandgaps are shifting down twice, and the bandgap width suppresses approximately 4 times. For $n_0 = 2.52$ the first bandgap is about 6.0 GHz and locating near 75 GHz. The second bandgap is about 0.7 GHz and locating near 150 GHz.

The decrease of Δn in two times remains the middle frequency of bandgaps the same and width of the first gap decreases by about two times. For $\Delta n = 0.1$ the first bandgap is about 12 GHz near 150 GHz. The second bandgap is about 1.4 GHz and locating near 300 GHz.

The decrease λ in two times shifts the frequency up twice and the width of both bandgaps is increased by about two times. For $\lambda = \pi/8$ the first bandgap is about 47.7 GHz and locating near 300 GHz. The second bandgap is about 11.3 GHz and locating near 600 GHz.

Analyzing the numerical experiments results, one may conclude that the width of the first gap is $\Delta v_1 \sim \Delta n / (n_0^2 \lambda)$, for the second gap $\Delta v_2 \sim \Delta n^2 / \lambda$. These equations are intuitive relations obtained from numerical experiments based on the matrix method [22,23]. Their exact values will be derived in the next section using the wave expansion method.

2.1.2. Analytical Results

The method of band structure calculation described in Appendix A is valid for arbitrary periodic distribution of refractive index along the z -axis. Throughout the article we use SI units and assumed a $\exp[i\omega t - ikz]$ harmonic time convention. In the case of harmonic distribution Equation (1), the coefficients k_m^e in the Fourier expansion (see Equation (A4)) are forming the series with very fast decreasing terms (in considered in Figure 1 example, they are 0.654, -0.104 , 0.012, -0.0013 for $n = 0, \pm 1, \pm 2, \pm 3$, correspondingly). The general contribution may be considered by using only first terms $n = 0, \pm 1$. In this case, there exists a relatively simple equation for dispersion relation $\omega(k)$. To calculate $\omega(k)$ it is necessary to solve the following equation (see details of derivations in Appendix A):

$$\det \begin{pmatrix} n_0^2 + \frac{1}{2}\Delta n^2 - \frac{c^2}{\omega^2} \left(-\frac{2\pi}{\lambda} + k\right)^2 & n_0\Delta n & \frac{1}{4}\Delta n^2 \\ n_0\Delta n & n^2 + \frac{1}{2}\Delta n^2 - \frac{c^2}{\omega^2}k^2 & n_0\Delta n \\ \frac{1}{4}\Delta n^2 & n_0\Delta n & n^2 + \frac{1}{2}\Delta n^2 - \frac{c^2}{\omega^2} \left(\frac{2\pi}{\lambda} + k\right)^2 \end{pmatrix} = 0, \quad (2)$$

where n , Δn and λ are parameters from Equation (1), $\omega = 2\pi\nu$ is angular frequency, c is the speed of light.

The roots of Equation (2) with $k = \pi/\lambda$ gives frequencies for the first bandgap. In case of the second bandgap (substituting $k = 0$ in Equation (2)) it is possible to simplify significantly the Equation (2) and obtain simple analytical expression for the second gap:

$$\Delta\nu_2 = \nu_3 - \nu_2 = \frac{2c\sqrt{2n_0^2 + \Delta n^2}}{\lambda\sqrt{8n_0^4 - 6\Delta n^2n_0^2 + \Delta n^4}} - \frac{2c}{\lambda\sqrt{4n_0^2 + \Delta n^2}}. \quad (3)$$

Equations (2) and (3) provide very good correspondence with the numerical calculations. Via matrix method and may be applied for quick estimation of the frequencies ν_1 , ν_2 , ν_3 and corresponding bandgaps $\Delta\nu_1$, $\Delta\nu_2$.

The mentioned above band structures of materials with a harmonically distributed refractive index may be useful for terahertz applications. Particularly, the realization of structures with a distributed refractive index may be obtained using 3D-printing technology. In the sections below, we propose to use gyroid-based 3D-printed structures as an example of spatially distributed refractive index material. The specialty in gyroids is their unique form, which provide periodic cosine-like distribution of effective refractive index in this material. Exactly this feature provides a simple way to form a periodic structure with predictable, analytically solvable, and equidistant band structure for a wide range of terahertz applications.

3. Gyroid Structures Production

The gyroid is an infinitely connected triply periodic minimal surface described in the Cartesian coordinate system by equation [24]:

$$\sin(x)\cos(y) + \sin(y)\cos(z) + \sin(z)\cos(x) = 0. \quad (4)$$

To obtain volume structure from surface described by Equation (4) the following inequality should be used:

$$\sin(\alpha x)\cos(\alpha y) + \sin(\alpha y)\cos(\alpha z) + \sin(\alpha z)\cos(\alpha x) > C, \quad (5)$$

where C is parameter related to the average porosity of the structure [25] and α is the scaling factor. Below we will use the scaling factor $\alpha = 2 \text{ mm}^{-1}$. The typical gyroid-based structure with porosity 60% related to $C_1 = 0.27$ is presented in Figure 2a. The cross-sections perpendicular to z -axis are presented in Figure 2b. They are forming periodic patterns of air voids and material areas depending on depth αz .

The presented in Figure 2 structure may be produced by 3D-printing technology, which offers unprecedented opportunities for production complex periodic structures with advanced mechanical, thermal and electromagnetic properties [26–29]. Particularly, here the selective laser sintering (SLS) technology was used. The details of the preparation were discussed in [25]. Particularly the micrometer-sized thermoplastic polyurethane (TPU) particles were sintered using laser beam layer-by-layer within the area satisfying Equation (5). This strategy allows forming from TPU powder the gyroid structure with porosity about 60%. The lateral dimension of 3 period thick printed samples was about $3\pi \simeq 9.5 \text{ mm}$.

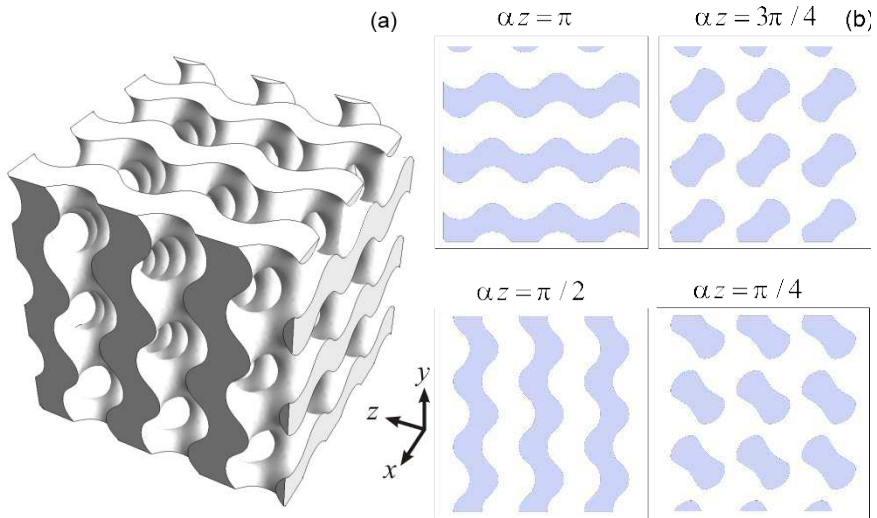


Figure 2. (a) The gyroid-based structure with porosity 60%; (b) The cross-sections of gyroid structure with porosity 60% in the plane perpendicular to z-axis (gray regions are related to material, white—to the air).

4. Scattering of the Electromagnetic Wave

The scattering of electromagnetic waves in millimeter and submillimeter frequency ranges on studied gyroid structures may be considered within the longwave approximation. In practice, this approach is well applicable for the normal scattering of a plane wave on not very thick periodic arrays infinite in directions perpendicular to the initial wave vector [30,31].

To apply this approach and calculate the transmitted and reflected signals along to the initial wave vector direction it is necessary to consider the average density variation within the unit cell of the structure. Let us consider the cross-sections of presented in Figure 2a structure in the plane perpendicular to z-axis (see Figure 2b). The dark areas are related to the regions filled with material, bright ones are air. Depending on position z there is a variation of air and material fractions inside the sample. Averaging the refractive index according to the air and material fractions it is possible to obtain its effective distribution of n_{eff} along the z-axis. The similar averaging procedure was performed in [13] for effective density calculations. In this case $n_{eff}(z)$ may be calculated as [4]:

$$n_{eff} = n_{bulk}(1 - S(z)/4\pi^2) + n_{air}S(z)/4\pi^2, \tag{6}$$

where $S(z)$ is the air surface in cross-section plane perpendicular to z-axis within the unit cell $ax \in [-\pi, \pi], ay \in [-\pi, \pi], n_{bulk}$ is the refractive index of bulk material, the term $4\pi^2$ is the total surface of the unit cell, $n_{air} = 1$.

In the case of gyroid $S(z)$ may be easily numerically calculated by considering one unit cell by Quasi Monte-Carlo method [32]. The results of calculation are presented in Figure 3a.

From this figure, we can see that average porosity of considered structure within the unit cell (see inset of Figure 3a) is varied near 60% [25]. Nevertheless, the penetration inside the sample along z-axis shows that there are areas within the structure which are more or less dense than the average value. The variation of density is relatively small and its maximum deviation is about 5%.

The calculated distribution of refractive index using Equation (6) is presented in Figure 3b, where we used the typical for TPU value of refractive index $n_{bulk} = 1.64 - i0.06$. This distribution will be used below to calculate transmitted and reflected signals along z-axis of three periods thick layer

(see Figure 3c) formed by gyroid infinitely translated along x- and y-axes (total thickness of structure was 3π mm).

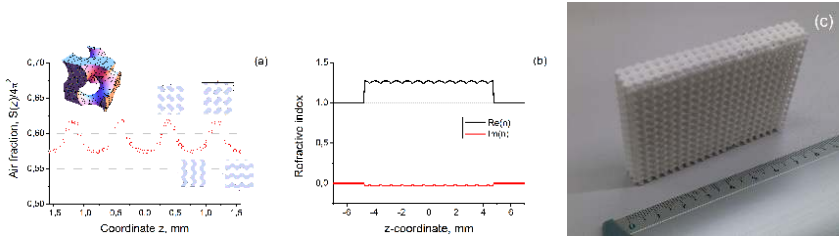


Figure 3. (a) Relative air fraction distribution in gyroid along the z-axis (Inset: single unit cell of the structure and characteristic cross-sections of periodic material); (b) calculated distribution of refractive index about z-axis; (c) printed sample.

5. Terahertz Measurements in Free Space

The time-domain spectrometer “T-Spec” produced by EKSPLA was used for measurements of the electromagnetic response of printed samples in the 100–500 GHz range. A pumping 1050 ± 40 nm wavelength laser with 40 mW averaged output power was used to excite a photoconductor antenna and produced THz radiation pulse with an aperture about 8 mm, normally scattered on the investigated sample. The experiments were performed in transmission geometry. The Fourier transform of the measured waveform transmitted through the sample THz pulse gives the frequency dependence of the complex transmission coefficient of the investigated material. The measurement procedure was in details described in our recent works related to terahertz properties of nanocarbon based structures [33,34]. The results of measurements of the transmitted through the sample signal in the logarithmic scale $S_{21\log} = 20 \lg(S_{21lin})$ are presented in Figure 4 (bold blue line).

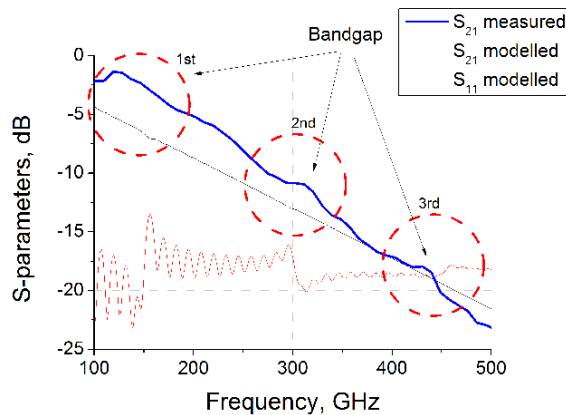


Figure 4. Experimentally measured and numerically calculated S-parameters of 9.5mm-thick gyroid samples in the free space.

The losses in the real TPU have significantly dumped the interference and transmission is essentially decreased with frequency. Nevertheless, Figure 4 shows that traces of the band structure are observed near the frequencies of 150, 300 and 450 GHz. The bend in experimental and theoretical spectra is most probably due to the difference of real refractive index distribution in gyroid (Figure 3) to harmonic Equation (1). At higher frequencies about 500 GHz the wavelength becomes less than 0.5 mm and measured spectra differs significantly from predicted within the longwave approximation results.

6. Conclusions

The obtained results show that structures with a harmonically distributed refractive index might be utilized as materials with controlled bandgap in the terahertz frequency range. In particular case of material with $n_0 = 1.26$, $\Delta n = 0.20$ and $\lambda = \pi/4$ mm the bandgaps are locating near frequencies 150 GHz, 300 and 450 GHz. The analytical model demonstrates that the width of the bandgaps is generally defined by parameter $\Delta n = 0.20$. The bandgaps positions may be shifted to a higher frequency range by decreasing of period λ or by applying structures with higher porosity (i.e., higher air fraction and correspondingly lower n_{eff}).

The gyroid based architectures were proposed as a practical realization of harmonically distributed refractive index structures. The variation of average density within the unit cell provides a cosine-like distribution of refractive index in such structures within the longwave approximation. The presence of three equidistant bandgaps was experimentally proved in 3D printed thermoplastic polyurethane-based gyroid.

It is important to note that without losses the expected spectra of produced sample are very similar to that presented in Figure 1c. In the terahertz region, the losses in the polymer matrix become significant for samples with a thickness of more than several millimeters. For thick samples, the transmission substantially decreases with frequency. This tendency is clearly seen in Figure 4. Due to dumping, the partial waves deeply penetrating the material have reduced impact on the overall electromagnetic response. The interference oscillations are smoothing and the band structure becomes less visible. Actually, in the experiment (Figure 4) we observed only “traces” of the band structure theoretically predicted. Nevertheless, the positions of peaks correspond to the expected frequencies.

The difference between experiment and modeling may be explained by the two reasons. First, the refractive index of TPU is frequency-dependent $n = n(\nu)$ in the considered 100–500 GHz frequency range. The systems with $n(\nu)$ are of great practical interest but require additional investigation. Another reason is the one-dimensionality of the considered model. For a more accurate wave scattering calculation, complex numerical simulations based on the Huygens-Fresnel principle are required.

To reduce the losses' impact it is necessary to decrease the thickness of the sample with the same number of periods. In this case, the band structure will be much more pronounced. Therefore the need to reduce the period λ is clear. However, most printers available today do not allow producing high quality samples in gyroid geometry with a period of less than 0.5 mm. The obtained results prove the concept of THz optics of graded refractive index materials and demonstrate the importance of miniaturization for THz applications. They open the route stimulating the development of new 3D printing technologies with higher resolution and smaller characteristic size. For further applications it is also necessary to develop 3D-printable polymer materials with low losses in the THz range. We hope that the results obtained in this work will be soon implemented on thinner samples and will stimulate the development of terahertz optics of graded refractive index materials.

Author Contributions: Conceptualization, P.K., D.B. and M.L.; methodology, A.P., G.G., P.L.; software, D.B.; validation, H.X., A.R. and M.L.; formal analysis, D.B.; investigation, D.B. and A.P.; resources, G.G.; data curation, G.G.; writing—original draft preparation, D.B.; writing—review and editing, P.K.; visualization, D.B.; supervision, P.K. and P.L.; project administration, P.K.; funding acquisition, P.K. All authors have read and agreed to the published version of the manuscript.

Funding: The work is supported by H2020 RISE 734164 Graphene 3D. P.K. acknowledges the financial support from H2020-MSCA-IF-2018 project 836816 TURANDOT and the Academy of Finland Flagship Programme, Photonics Research and Innovation (PREIN) [Project No 320166]. D.B. is thankful for support by Tomsk State University Competitiveness Improvement Program. This research was also partially supported by the Belarusian Republican Foundation for Fundamental Research(BRFFR) project F18AZ-015 and NATO SPS project G5697 CERTAIN.

Conflicts of Interest: The authors declare no conflict of interest.

Appendix A. Band-Structure Calculation

To calculate the dispersion relations in the considered structures we will generally follow the plane wave expansion method for calculation of photonic crystal band diagrams in detail presented in [19]. For the plane wave propagating along the z-axis in one dimension case the Maxwell equations for electric field E transform to single differential equation:

$$-\frac{1}{\varepsilon(z)} \frac{\partial^2 E}{\partial z^2} = \frac{\omega^2}{c^2} E, \quad (\text{A1})$$

where $\varepsilon(z)$ is the dielectric permittivity, ω is the angular frequency, c is the speed of light.

In case of arbitrary periodic function $\varepsilon(z)$ with period T the strategy to transform them into the dispersion relation $\omega(k)$ is following.

The first step is the application of Fourier series expansions for the electric field E and dielectric permittivity function $\varepsilon(z)$:

$$\frac{1}{\varepsilon(z)} = \sum_{m=-\infty}^{m=+\infty} k_m^\varepsilon \exp(-i\frac{2\pi mz}{T}), \quad (\text{A2})$$

$$E = \sum_{n=-\infty}^{n=+\infty} k_n^E \exp(-i\frac{2\pi nz}{T}) \exp(-ikz), \quad (\text{A3})$$

where coefficients k_m^ε in Equation (A2) are:

$$k_m^\varepsilon = \frac{1}{T} \int_{-T/2}^{T/2} \frac{1}{\varepsilon(z)} \exp(i\frac{2\pi mz}{T}). \quad (\text{A4})$$

After substituting Equations (A2)–(A4) in Equation (A1), multiplying by an orthogonal function $\exp(i\frac{2\pi mz}{T})$ and integrating over a unit cell Equation (A1) transforms to

$$\sum_n \left(\frac{2\pi n}{T} + k\right)^2 k_{m-n}^\varepsilon k_n^E = \frac{\omega^2}{c^2} k_m^E. \quad (\text{A5})$$

Writing Equation (A5) in the matrix form and calculating of eigenvalues of the matrix on the left side trivially gives us the values of ω^2/c^2 and allow to obtain band structure $\omega(k)$.

The direct application of Equations (A1)–(A5) for calculating of band structure of material with $n(z)$ distributed by Equation (1) gives results presented in Figure 1. The intermediate calculations show that in this case the coefficients k_m^ε vanishing extremely fast and for satisfactory reproduction of band structure it is enough to consider only three terms $n = -1; 0; 1$. This is a feature of harmonically distributed refractive index Equation (1), which is "almost" orthogonal to the plane waves used for expansion (A3).

Moreover in case of Equation (1) it is possible to significantly simplify the relations (A1)–(A5). In this case Equation (A1) transforms to (we consider only three terms in sums):

$$-\sum_{n=-1,0,1} k_n^E \left(\frac{2\pi n}{\lambda} + k\right)^2 \exp\left(-i\frac{2\pi nz}{\lambda}\right) + \frac{\omega^2}{c^2} \left(n_0 + \Delta n \cos \frac{2\pi z}{\lambda}\right)^2 \sum_{n=-1,0,1} k_n^E \exp\left(-i\frac{2\pi nz}{\lambda}\right) = 0. \quad (\text{A6})$$

After multiplying Equation (A6) by an orthogonal function $\exp(i\frac{2\pi mz}{T})$, $m = -1; 0; 1$ and integrating over a unit cell (i.e., $\frac{1}{T} \int_{-T/2}^{T/2} \dots dz$) Equation (A6) transforms to

$$\begin{cases} k_{-1}^E \left[n_0^2 + \frac{1}{2} \Delta n^2 - \frac{c^2}{\omega^2} \left(-\frac{2\pi}{\lambda} + k \right)^2 \right] + k_0^E [n_0 \Delta n] + k_1^E \left[\frac{1}{4} \Delta n^2 \right] = 0 \\ k_{-1}^E [n_0 \Delta n] + k_0^E \left[n^2 + \frac{1}{2} \Delta n^2 - \frac{c^2}{\omega^2} k^2 \right] + k_1^E [n_0 \Delta n] = 0, \\ k_{-1}^E \left[\frac{1}{4} \Delta n^2 \right] + k_0^E [n_0 \Delta n] + k_1^E \left[n^2 + \frac{1}{2} \Delta n^2 - \frac{c^2}{\omega^2} \left(\frac{2\pi}{\lambda} + k \right)^2 \right] = 0 \end{cases} \quad (A7)$$

The nontrivial solution of Equation (A7) exists only if determinant is equal to 0:

$$\det \begin{pmatrix} n_0^2 + \frac{1}{2} \Delta n^2 - \frac{c^2}{\omega^2} \left(-\frac{2\pi}{\lambda} + k \right)^2 & n_0 \Delta n & \frac{1}{4} \Delta n^2 \\ n_0 \Delta n & n^2 + \frac{1}{2} \Delta n^2 - \frac{c^2}{\omega^2} k^2 & n_0 \Delta n \\ \frac{1}{4} \Delta n^2 & n_0 \Delta n & n^2 + \frac{1}{2} \Delta n^2 - \frac{c^2}{\omega^2} \left(\frac{2\pi}{\lambda} + k \right)^2 \end{pmatrix} = 0 \quad (A8)$$

The numeric solution of the last equation gives the dispersion relation $\omega(k)$. To calculate frequencies ν_1 and ν_2 , and the lowest (first) bandgap width $\nu_2 - \nu_1$ it is necessary to solve Equation (A8) for $k = \pi/\lambda$. For $k = 0$ Equation (A8) simplifies and gives the analytic relation for the second bandgap width $\nu_3 - \nu_2$:

$$\Delta \nu = \nu_3 - \nu_2 = \frac{2c \sqrt{2n_0^2 + \Delta n^2}}{\lambda \sqrt{8n_0^4 - 6\Delta n^2 n_0^2 + \Delta n^4}} - \frac{2c}{\lambda \sqrt{4n_0^2 + \Delta n^2}}. \quad (A9)$$

Appendix B. Calculation of Scattering Parameters

To calculate amplitudes of reflected (S_{11}) and transmitted (S_{21}) signals through the finite sample we used the matrix method from optics [22,23] designed for the modeling of wave propagation in a multi-layered medium. This method was effectively adopted for calculation of S-parameters in the microwave and terahertz frequency ranges [30,35].

Let us consider a normal scattering of a plane wave propagating along z-axis on the layer of bulk material with thickness τ and refractive index distribution $n(z)$.

First, we need to divide the whole layer into N parts so that the thickness of each layer is much less than the wavelength of initial radiation. For large N refractive index may be assumed to be constant within for each layer at position z_t and equal $n(z_t)$.

The plane wave scattering on each τ_t -thick layer may be described using a characteristic matrix and for a multi-layered structure, the characteristic matrix of the whole system is the product of all single layer matrices. The S_{11} and S_{21} coefficients of the N -layered system in the free space can be calculated as:

$$S_{11} = \frac{n_{air} - C/B}{n_{air} + C/B'} \quad (A10)$$

$$S_{21} = \frac{2n_{air}}{n_{air}B + C'} \quad (A11)$$

where

$$\begin{bmatrix} B \\ C \end{bmatrix} = \left\{ \prod_{t=1}^N \begin{bmatrix} \cos(k_t \tau_t) & i \sin(k_t \tau_t) k_0 / k_t \\ i \sin(k_t \tau_t) k_t / k_0 & \cos(k_t \tau_t) \end{bmatrix} \right\} \begin{bmatrix} 1 \\ n_{air} \end{bmatrix}. \quad (A12)$$

Here τ_t is the thickness of layer t , $k_t = \frac{2\pi n(z)}{\gamma}$ and $k_0 = \frac{2\pi n_{air}}{\gamma}$ are the wave vectors in the layer of refractive index $n(z)$ and in air (refractive index $n_{air} = 1$), respectively, γ being the wavelength.

For the numerical calculations, we used Equation (1) to obtain the refractive index inside the region $|z| < \tau/2$ and $n_{air} = 1$ outside the layer.

References

1. Devarapu, G.C.R.; Foteinopoulou, S. Broadband near-unidirectional absorption enabled by phonon-polariton resonances in SiC micropillar arrays. *Phys. Rev. Appl.* **2017**, *7*, 034001. [[CrossRef](#)]
2. Deparis, O.; Khuzayim, N.; Parker, A.; Vigneron, J.P. Assessment of the antireflection property of moth wings by three-dimensional transfer-matrix optical simulations. *Phys. Rev. E* **2009**, *79*, 041910. [[CrossRef](#)] [[PubMed](#)]
3. Sun, C.H.; Jiang, P.; Jiang, B. Broadband moth-eye antireflection coatings on silicon. *Appl. Phys. Lett.* **2008**, *92*, 061112. [[CrossRef](#)]
4. Stavenga, D.G.; Foletti, S.; Palasantzas, G.; Arikawa, K. Light on the moth-eye corneal nipple array of butterflies. *Proc. R. Soc. B* **2005**, *273*, 661–667. [[CrossRef](#)] [[PubMed](#)]
5. Leem, J.W.; Joo, D.H.; Yu, J.S. Biomimetic parabola-shaped AZO subwavelength grating structures for efficient antireflection of Si-based solar cells. *Sol. Energy Mater. Sol. Cells* **2011**, *95*, 2221–2227. [[CrossRef](#)]
6. Mouroulis, P.; Macdonald, J.; Macdonald, J. *Geometrical Optics and Optical Design*; Oxford University Press: New York, NY, USA, 1997; Volume 39.
7. Moore, D.T. Gradient-index optics: A review. *Appl. Opt.* **1980**, *19*, 1035–1038. [[CrossRef](#)]
8. Smith, D.R.; Mock, J.J.; Starr, A.F.; Schurig, D. Gradient index metamaterials. *Phys. Rev. E* **2005**, *71*, 036609. [[CrossRef](#)]
9. Vukusic, P.; Sambles, J.R. Photonic structures in biology. *Nature* **2003**, *424*, 852. [[CrossRef](#)]
10. Saranathan, V.; Osuji, C.O.; Mochrie, S.G.J.; Noh, H.; Narayanan, S.; Sandy, A.; Dufresne, E.R.; Prum, R.O. Structure, function, and self-assembly of single network gyroid (I4132) photonic crystals in butterfly wing scales. *Proc. Natl. Acad. Sci. USA* **2010**, *107*, 11676–11681. [[CrossRef](#)]
11. Kristensen, A.; Yang, J.K.W.; Bozhevolnyi, S.I.; Link, S.; Nordlander, P.; Halas, N.J.; Mortensen, N.A. Plasmonic colour generation. *Nat. Rev. Mater.* **2017**, *2*, 16088. [[CrossRef](#)]
12. Schoen, A.H. *Infinite Periodic Minimal Surfaces without Self-Intersections*; National Aeronautics and Space Administration: Washington, DC, USA, 1970.
13. Jin, Y.; Kong, H.; Zhou, X.; Li, G.; Du, J. Design and Characterization of Sheet-Based Gyroid Porous Structures with Bioinspired Functional Gradients. *Materials* **2020**, *13*, 3844. [[CrossRef](#)]
14. Rana, F. Graphene terahertz plasmon oscillators. *IEEE Trans. Nanotechnol.* **2008**, *7*, 91–99. [[CrossRef](#)]
15. Gu, P.; Tani, M.; Kono, S.; Sakai, K.; Zhang, X.C. Study of terahertz radiation from InAs and InSb. *J. Appl. Phys.* **2002**, *91*, 5533–5537. [[CrossRef](#)]
16. Ferguson, B.; Zhang, X.C. Materials for terahertz science and technology. *Nat. Mater.* **2002**, *1*, 26. [[CrossRef](#)] [[PubMed](#)]
17. Martin-Moreno, L.; Garcia-Vidal, F.J.; Somoza, A.M. Self-assembled triply periodic minimal surfaces as molds for photonic band gap materials. *Phys. Rev. Lett.* **1999**, *83*, 73. [[CrossRef](#)]
18. Pouya, C.; Overvelde, J.T.B.; Kolle, M.; Aizenberg, J.; Bertoldi, K.; Weaver, J.C.; Vukusic, P. Characterization of a mechanically tunable gyroid photonic crystal inspired by the butterfly parides sesostris. *Adv. Opt. Mater.* **2016**, *4*, 99–105. [[CrossRef](#)]
19. Danner, A.J. *An Introduction to the Plane Wave Expansion Method for Calculating Photonic Crystal Band Diagrams*; University of Illinois: Champaign, IL, USA, 2002.
20. Ho, K.M.; Chan, C.T.; Soukoulis, C.M. Existence of a photonic gap in periodic dielectric structures. *Phys. Rev. Lett.* **1990**, *65*, 3152. [[CrossRef](#)]
21. Villeneuve, P.R.; Piche, M. Photonic band gaps in two-dimensional square and hexagonal lattices. *Phys. Rev. B* **1992**, *46*, 4969. [[CrossRef](#)]
22. Born, M.; Wolf, E. *Principles of Optics: Electromagnetic Theory of Propagation, Interference and Diffraction of Light*; Elsevier: London, UK, 2013.
23. Macleod, H.A. *Thin-Film Optical Filters*; CRC Press: Chicago, IL, USA, 2001.
24. Scherer, M.R.J. *Double-Gyroid-Structured Functional Materials: Synthesis and Applications*; Springer Science & Business Media: New York, NY, USA, 2013.
25. Ronca, A.; Rollo, G.; Cerruti, P.; Fei, G.; Gan, X.; Buonocore, G.G.; Lavorgna, M.; Xia, H.; Silvestre, C.; Ambrosio, L. Selective Laser Sintering Fabricated Thermoplastic Polyurethane/Graphene Cellular Structures with Tailorable Properties and High Strain Sensitivity. *Appl. Sci.* **2019**, *9*, 864. [[CrossRef](#)]

26. Smay, J.E.; Cesarano, J.; Lewis, J.A. Colloidal inks for directed assembly of 3-D periodic structures. *Langmuir* **2002**, *18*, 5429–5437. [[CrossRef](#)]
27. Abueidda, D.W.; Bakir, M.; Al-Rub, R.K.A.; Bergström, J.S.; Sobh, N.A.; Jasiuk, I. Mechanical properties of 3D printed polymeric cellular materials with triply periodic minimal surface architectures. *Mater. Des.* **2017**, *122*, 255–267. [[CrossRef](#)]
28. Szczurek, A.; Ortona, A.; Ferrari, L.; Rezaei, E.; Medjahdi, G.; Fierro, V.; Bychanok, D.; Kuzhir, P.; Celzard, A. Carbon periodic cellular architectures. *Carbon* **2015**, *88*, 70–85. [[CrossRef](#)]
29. Boyle, B.M.; French, T.A.; Pearson, R.M.; McCarthy, B.G.; Miyake, G.M. Structural color for additive manufacturing: 3D-printed photonic crystals from block copolymers. *ACS Nano* **2017**, *11*, 3052–3058. [[CrossRef](#)] [[PubMed](#)]
30. Bychanok, D.; Li, S.; Sanchez-Sanchez, A.; Gorokhov, G.; Kuzhir, P.; Ogrin, F.Y.; Pasc, A.; Ballweg, T.; Mandel, K.; Szczurek, A. Hollow carbon spheres in microwaves: Bio inspired absorbing coating. *Appl. Phys. Lett.* **2016**, *108*, 013701. [[CrossRef](#)]
31. Bychanok, D.; Li, S.; Gorokhov, G.; Piasotski, K.; Meisak, D.; Kuzhir, P.; Burgess, E.A.; Gallagher, C.P.; Ogrin, F.Y.; Hibbins, A.P. Fully carbon metasurface: Absorbing coating in microwaves. *J. Appl. Phys.* **2017**, *121*, 165103. [[CrossRef](#)]
32. Caflisch, R.E. Monte carlo and quasi-monte carlo methods. *Acta Numer.* **1998**, *7*, 1–49. [[CrossRef](#)]
33. Bychanok, D.; Angelova, P.; Paddubskaya, A.; Meisak, D.; Shashkova, L.; Demidenko, M.; Plyushch, A.; Ivanov, E.; Krastev, R.; Kotsilkova, R. Terahertz absorption in graphite nanoplatelets/polylactic acid composites. *J. Phys. D* **2018**, *51*, 145307. [[CrossRef](#)]
34. Batrakov, K.; Kuzhir, P.; Maksimenko, S.; Volynets, N.; Voronovich, S.; Paddubskaya, A.; Valusis, G.; Kaplas, T.; Svirko, Y.; Lambin, P. Enhanced microwave-to-terahertz absorption in graphene. *Appl. Phys. Lett.* **2016**, *108*, 123101. [[CrossRef](#)]
35. Bychanok, D.S.; Plyushch, A.O.; Gorokhov, G.V.; Bychanok, U.S.; Kuzhir, P.P.; Maksimenko, S.A. Microwave radiation absorbers based on corrugated composites with carbon fibers. *Tech. Phys.* **2016**, *61*, 1880–1884. [[CrossRef](#)]

Publisher’s Note: MDPI stays neutral with regard to jurisdictional claims in published maps and institutional affiliations.



© 2020 by the authors. Licensee MDPI, Basel, Switzerland. This article is an open access article distributed under the terms and conditions of the Creative Commons Attribution (CC BY) license (<http://creativecommons.org/licenses/by/4.0/>).

4 publikacija / 4th publication

**Creation of metasurface from vertically aligned carbon
nanotubes as versatile platform for ultra-light THz
components**

G.V. Gorokhov, D.S. Bychanok, P.P. Kuzhir, D.V. Gorodetskiy,
A.G. Kurennya, O.V. Sedelnikova, L.G. Bulusheva and A.V. Okotrub

Nanotechnology **2020** 31 255703

DOI: 10.1088/1361-6528/ab7efa

Creation of metasurface from vertically aligned carbon nanotubes as versatile platform for ultra-light THz components

G.V. Gorokhov^{1,2}, D.S. Bychanok^{1,3}, P.P. Kuzhir^{4,1},
D.V. Gorodetskiy⁵, A.G. Kurennya⁵, O.V. Sedelnikova^{3,5},
L.G. Bulusheva^{3,5} and A.V. Okotrub^{3,5}

¹Institute for Nuclear Problems Belarusian State University, 11 Bobruiskaya str., 220030, Minsk, Belarus

²Physics Faculty, Vilnius University, Sauletekio 9, Vilnius LT-10222, Lithuania

³Tomsk State University, 36 Lenin Ave, Tomsk 634050, Russia

⁴Institute of Photonics, University of Eastern Finland, Yliopistokatu 7, FI-80101 Joensuu, Finland

⁵Nikolaev Institute of Inorganic Chemistry, SB RAS, 3 Acad. Lavrentiev Ave., 630090, Novosibirsk, Russia

E-mail: g1ebgorokhov@yandex.ru

November 2019

Abstract. Here a simple and reproducible method for obtaining terahertz metasurfaces formed from multiwall carbon nanotubes (MWCNTs) is presented. The metasurfaces were obtained from a vertically aligned array of MWCNTs using a laser engraving technique followed by polymer covering. The structures under study demonstrate frequency-selective reflection in terahertz range following the Huygens–Fresnel formalism. For a normal incidence of the electromagnetic wave, the model for numerical calculation of backscattering from the metasurfaces was proposed. Lightweight and compact MWCNT-based metasurfaces are capable to replace conventional pyramidal absorbers and proved to serve as a versatile platform for scalable cost-efficient production of ultra-light electromagnetic components for THz applications.

Keywords: Terahertz absorption, carbon nanotubes, diffraction gratings, periodic structures

Submitted to: *Nanotechnology*

1. Introduction

Carbon nanotubes (CNTs) are well-known as perfect filler [1, 2, 3, 4, 5, 6] and even the substrate [7] for producing lightweight composites for electromagnetic applications. Along with graphene [8] the unique properties of CNTs allow creating compact durable and/or flexible [9] electromagnetic components and nano-devices, such as antennas [10, 11, 12], interconnects [13, 14], polarizers [15, 16], sensors [17], detectors (see [18] and Refs therein) and emitters of sub-mm waves radiation (see [19] for review).

Such a wide applicability of CNTs is due to their unique electromagnetics arising from plasmon-polariton (i.e. slowed-down surface wave) propagation along CNT axis [20], as well as so-called “finite length” effects (i.e. localized plasmon resonance) inherent for micron-length single-walled nanotube at THz and far-infrared frequencies [21, 22]. The valuable skin effect caused by electromagnetic radiation screening in low frequency ranges [23, 24] up to microwaves was predicted and experimentally observed for long multi-walled carbon nanotubes (MWCNTs). The recently demonstrated negative photo-induced conductivity [25] supported the possibility of ultra-fast tuning of CNT’s THz optical density that opens a way for the development of electromagnetic devices. To summarize, percolated composites [4, 6, 26], films [1, 17], meshes and sponges [27] behave like ultra-lightweight quasi-metals, demonstrating conductivity peaks at THz range in case of relatively short single-walled CNTs. In case of long single-walled [28] and multi-walled CNTs, and CNT bundles [29] the conductivity peak shifts towards much lower frequencies (hundreds of MHz and GHz).

However, in many cases, when individual CNT’s characteristic parameters are not compatible with the wavelength taking into account slowing down effect, one may consider CNT array, film or composite as a macroscopic homogenized structure, which electromagnetic response is governed by averaged conductivity, rather than “fundamental” electromagnetics specific to individual CNTs. In such a case one typically has porous conductive structure with broadband absorption [27], which properties are dependent on the CNT array/film density, conductivity and geometry of individual tubes forming the array, inter-tubes contact resistance, etc. In order to effectively reach the electromagnetic properties required by a particular ap-

plication the metamaterial paradigm [30, 31, 32, 33] can be applied to the CNT array combining its intrinsic properties with particular patterning providing the constructive interference [34].

The idea of this communication is to propose the versatile platform for scalable cost-efficient production of ultra-light electromagnetic components based on patterned vertically aligned arrays of MWCNTs. We demonstrate that MWCNT arrays grown via conventional aerosol assisted synthesis may be easily machined using a laser engraving technique in order to obtain complex geometry structures. As a proof of concept, several 3D-metasurfaces made of pyramidal CNT arrays with pyramids height about 0.1 – 0.5 mm (see Fig. 1) has been successfully produced and experimentally examined in 0.1 – 1 THz frequency range. At the same time, the possibility of tuning the electromagnetic response of fabricated metasurfaces was studied theoretically in 0.01 – 10 THz frequency range. The studied 3D CNT-based metasurface covered with a thin layer of insulating polymer is proved to be effective anti-reflection coating and reflection selective surface for THz range, supporting the ideology of scalable protocol of producing 3D metasurfaces composed of CNT-arrays as microwave-to-THz components.

The present paper is organized as follows. Section 2 contains the details of ordered MWCNT arrays preparation, structures engraving and experimental terahertz measurements. The basic principles of investigated structure electromagnetic response modeling are described at Section 3. Herein, the theoretical approach is compared with the experimental and absorption properties of the ordered CNT arrays are discussed. Finally, the Conclusions section summarizes the findings and gives an outlook on potential application of such metasurfaces.

2. Experimental

2.1. Preparation of materials

Vertically aligned MWCNT arrays were grown on silicon substrates using an aerosol-assisted catalytic chemical vapor deposition (CCVD) method described elsewhere [35].

A silicon substrate was placed into the tubular oven constantly flowed with argon and heated at 800 °C. The synthesis was carried out using 2 %

ferrocene ($\text{Fe}(\text{C}_5\text{H}_5)_2$) solution in toluene ($\text{C}_6\text{H}_5\text{CH}_3$). As a result, with the use of 2.5 ml of the reaction mixture an aligned MWCNT array of $\sim 250 \mu\text{m}$ height was obtained. To examine the morphology of MWCNTs, the pristine sample was investigated by transmission electron microscopy (TEM) using a JEOL 2010 microscope. TEM image of obtained MWCNTs is shown at Fig. 1 (a). Average diameter of nanotubes is $\sim 6 \text{ nm}$.

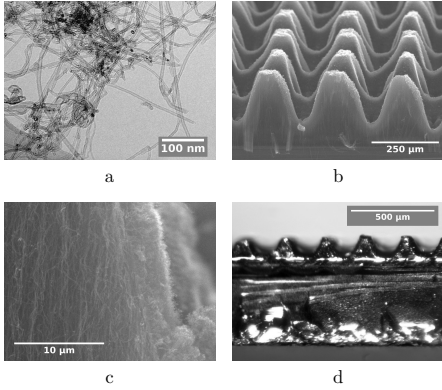


Figure 1. (a) TEM image of MWCNTs obtained by CVD technology; (b, c) SEM images of MWCNT-based pyramids periodic array; (d) Image of the general view of arrays covered with epoxy layer.

The plane-parallel MWCNT arrays were transformed to the arrays of pyramids using laser engraving. The industrial laser engraver (Winseal, China) with 20 Wt CO_2 laser and 20 mm/s scanning speed was used. Grating period was $250 \mu\text{m}$. To study the structure of the engraved sample and to prove the preservation of nanotubes after the laser treatment, the obtained sample was investigated by scanning electron microscopy (SEM) using a JEOL JSM 6700F microscope. The SEM images of engraved pyramids are presented in Fig. 1 (b, c).

After the engraving array of pyramids was covered with epoxy resin in order to protect its fragile structure. The viscous epoxy resin (Crystal 76) was dropped and then spread over the engraved surface under the vacuum. Total height of pyramids after all manipulations measured by means of optic microscopy was $232.9 \pm 11.9 \mu\text{m}$ with $54.9 \pm 6.9 \mu\text{m}$ uncut layer at the bottom. Maximal thickness of epoxy resin between pyramids was $77.0 \pm 4.5 \mu\text{m}$. General view of structures after covering with the epoxy resin is presented in Fig. 1 (d). The impact to electromagnetic response of the investigated system done by polymer cover is discussed in the section 3.

2.2. Terahertz measurements

The THz measurements were carried out using a commercial THz time domain spectrometer "TSPEC" by EKSPLA in 0.1 – 1.0 THz frequency range. The sample was placed normally to the initial electromagnetic wave. According to its functioning principle, the THz spectrometer registers the waveform of THz electrical field with perfect reflector (as a reference) and with sample (as experimental data). For the purpose to increase signal-to-noise ratio each measurement is averaged over 1024 frames. In order to switch between time and frequency domains the Fourier transform is used. The reflection coefficient is evaluated as a ratio between powers of electromagnetic radiation reflected by the sample and the reference.

3. Modeling

3.1. Periodic structure contribution

Let us consider the backscattering of plane wave from the infinite array of conductive square pyramids with height h and base width l (see Fig. 2).

There are several approaches to calculate the amplitude of the signal reflected by such a structure. In the low frequency region the wavelength is much higher than the characteristic lateral size of pyramids that allows to implement the long-wave approximation and homogenization [36, 37]. When the wavelength is substantially smaller with respect to the characteristic lateral size of pyramids, the electromagnetic response obeys the principles of linear optics [38]. However, when the wavelength and characteristic dimensions of system are comparable, the Huygens–Fresnel principle should be applied for waves scattering calculations.

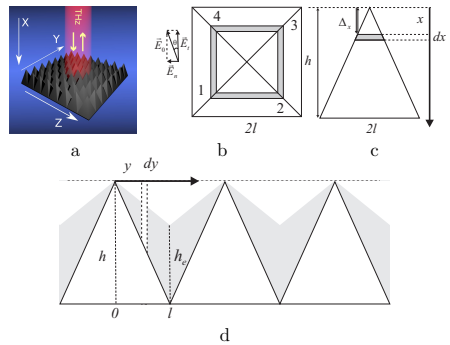


Figure 2. Backscattering of plane wave from pyramidal array. (a) Pyramidal array reflecting the terahertz radiation, (b) top view, (c) side view, (d) schematic image of pyramidal array covered with dielectric polymer.

Let us consider the wave with amplitude E_0 , which is propagated normally to pyramids bases (along the X axis, Figure 2 a) and reflected back. According to the Huygens–Fresnel principle, each point of a wavefront acts as a source of secondary waves, which interfering with each other determine total wavefront. In order to recreate the wavefront of pyramidal array let us consider one edge of a single pyramid (for example edge 1 in Fig. 2 (b)). The scattering conditions from all points of the edge are the same except of the path difference, which is equal to $\Delta_x = 2x$ for normal backscattering. Here, only the tangential component $E_0 \cos \Theta$ should be considered because the contribution of normal component (E_n in Fig. 2 (b)) from equivalent places of edges 1 and 3 are in antiphase.

The contribution of dx -thick layer of edge 1 placed on distance x from the top of pyramid to the total reflected amplitude is:

$$\begin{aligned} dE_{t1} &= \frac{E_0 \cos \Theta \exp(i\omega t - ik\Delta_x)}{S_{edge}} dS = \\ &= \frac{E_0 \cos \Theta \exp(i\omega t - ik2x)}{h^2} 2x dx, \end{aligned} \quad (1)$$

where k is the wave vector, h is the height of pyramid.

The total contribution of the edge 1 is:

$$\begin{aligned} E_{t1} &= \frac{E_0 \cos \Theta \exp(i\omega t)}{h^2} \int_0^h 2x \exp(-ik2x) dx = \\ &= \frac{E_0 \cos \Theta \exp(i\omega t)}{2k^2 h^2} [\exp[-i2kh](1 + 2ikh) - 1]. \end{aligned} \quad (2)$$

The contribution of the edge 3 is the same as Eq. (2). Contributions of the edges 2 and 4 may be obtained from Eq. (2) by substitution of $\cos \Theta$ for $\sin \Theta$.

Summarizing the impact of all four edges, it is possible to obtain the scattering parameter S_{11}^p (ratio between reflected and incident radiation amplitudes) for the surface paved with pyramids:

$$S_{11}^p(\nu, h) = \frac{(1 + 2ikh) \exp[-i2kh] - 1}{2k^2 h^2}. \quad (3)$$

In Fig. 3 the S_{11}^p frequency dependence is presented for various h . Here, the pyramids consist of perfect electric conductor i.e. the flat surface of such material has $|S_{11}|=1$.

The increase of pyramid height h shifts the S_{11}^p spectrum to the low frequency region. Fig. 3 clearly depicts the transition between long-wave approximation through the Huygens–Fresnel theory to the geometric optics region. At low frequencies the wavelength is much higher than the pyramid height h , thus the structure interacts with radiation as a perfect reflector. When the wavelength is comparable with h , the amplitude of back-reflected signal decreased with relatively small oscillations caused by interference. Finally, at high frequencies, the S_{11}^p value is significantly damped and back-reflection becomes negligible.

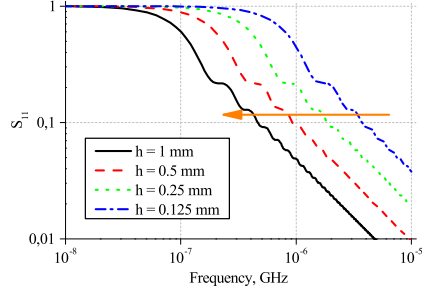


Figure 3. The frequency dependence of S_{11} on pyramid height $h = 0.125, 0.25, 0.5, 1.0$ mm.

3.2. Dielectric Layer contribution

A widely known example of matching layer is the optical lens antireflective coating, which decreases the difference between refractive indices of free space and lens making their interface less reflective. For the pyramids array covered with dielectric layer the amplitude of back-reflected signal is also dependent on the dielectric permittivity ϵ and thickness τ of the latter. To calculate dielectric layer contribution it is necessary to take into account the interference between waves reflecting from top and bottom surfaces of dielectric layer covering the pyramids. The electric field E_I in the region above dielectric layer (in free space) and electric field E_{II} inside the layer may be determined as:

$$\begin{aligned} E_I &= C_1 \exp[-ik_1 x] + C_2 \exp[ik_1 x] \\ E_{II} &= C_3 \exp[-ik_2 x] + C_3 \alpha \exp[ik_2 x], \end{aligned} \quad (4)$$

where C_1, C_2, C_3 are unknown coefficients, $k_1 = \frac{2\pi\nu}{c}$ and $k_2 = \frac{2\pi\nu\sqrt{\epsilon}}{c}$ are wavenumbers in the free space and in the dielectric layer respectively, ν is the frequency, c is the speed of light. The amplitudes of initial and reflected wave were taken to be C_3 and αC_3 respectively. A term ($|\alpha| \leq 1$) implies imperfection of CNT array as conductor. Therefore, α may be considered as amplitude of the signal reflected by a plane surface of conductive material with semi-infinite depth (in considered case, the CNT array) into a medium (polymer) with the dielectric constant ϵ . Eq. (4) should satisfy the following boundary conditions:

$$\begin{aligned} E_I(-\tau) &= E_{II}(-\tau), \\ \frac{\partial E_I}{\partial x} \Big|_{-\tau} &= \frac{\partial E_{II}}{\partial x} \Big|_{-\tau}. \end{aligned} \quad (5)$$

Solving Eq. (4)-(5) allows to obtain the amplitude of reflected signal from the plane-parallel layer of

dielectric with non-perfect back reflector:

$$S_{11}^d(\nu, \tau, \varepsilon, \beta) = \frac{C_2}{C_1} = \frac{e^{2i\tau k_1} (e^{2i\tau k_2} k_1 - e^{2i\tau k_2} k_2 + k_1 \alpha + k_2 \alpha)}{e^{2i\tau k_2} k_1 + e^{2i\tau k_2} k_2 + k_1 \alpha - k_2 \alpha}. \quad (6)$$

Eq. (6) describes the contribution of dielectric layer to the reflection coefficient of epoxy covered pyramidal CNT array. The parameter $\alpha = \frac{\sqrt{(\varepsilon)-(1-\beta)/(1+\beta)}}{\sqrt{(\varepsilon)+(1-\beta)/(1+\beta)}}$ is related to the amplitude of reflected signal $|\beta| \leq 1$ from plane back reflector in the free space. In the case when $\beta = -1$, Eq. (6) coincides with the amplitude of reflected signal from dielectric layer located on the perfect conductor [39] excepting the phase factor $\exp[2i\tau k_1]$. In order to represent the normal reflection of THz wave from plane-parallel MWCNT array $\beta = -0.9$ was used.

Fig. 4 shows the frequency dependence of S_{11} for the dielectric layer of $\tau = 0.1, 0.2, 0.3$ mm thickness.

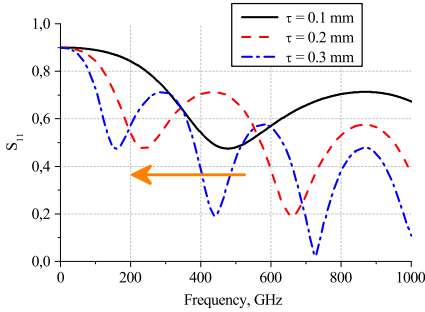


Figure 4. Frequency dispersion of S_{11} scattering parameter at different dielectric layer thickness $\tau = 0.1, 0.2, 0.3$ mm. ($\beta = -0.9, \varepsilon = 3 - 0.4i$)

The typical value for epoxy resin permittivity in THz frequency region $\varepsilon = 3 - 0.4i$ was used. Fig. 4 depicts the typical interference oscillations, which are absent for non-covered pyramids. When the dielectric layer becomes thicker, these oscillations shift to the low-frequency region.

3.3. Combination of dielectric layer and structure contribution

The real pyramidal array was impregnated with epoxy resin to overcome the pristine pyramids brittleness. The electromagnetic response of such structure is defined by both contributions from dielectric layer and from pyramidal back reflector. Due to surface tension forces, the epoxy resin unevenly covers the CNT pyramids array. As a first approximation, we

considered the case when the thickness of the epoxy increases linearly with approaching the base of the pyramid (Fig. 2 (d)). In this case the amplitude of reflected signal from the unit cell may be calculated as:

$$S_{11} = \frac{2}{l^2} \int_0^l S_{11}^d(\nu, \frac{h_e}{l}x, \varepsilon, \beta) \times \exp[-i2k_1x(\frac{h}{l} - \frac{h_e}{l})]x dx, \quad (7)$$

where l is the half length of pyramids base, h_e is the height of epoxy layer near the pyramids base. The first multiplier in Eq.(7) related to the dielectric layer contribution, the second - to the phase shift caused by the structure.

3.4. Comparison between experiment and modeling

The comparison between experimentally measured amplitude of the signal reflected by the array of pyramids covered with epoxy resin (Fig. 1 (d)) and fitted values obtained by Eq. (7) is presented in Fig. 5.

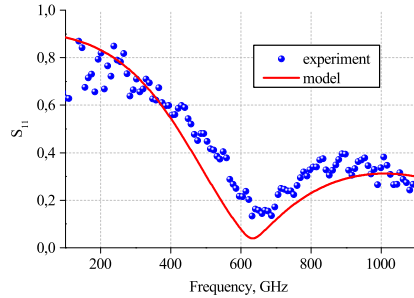


Figure 5. Amplitude of back-reflected signal S_{11} from periodic pyramidal CNT-array covered with epoxy resin layer (symbols correspond to the experimental data, line — to the modeling results).

The experimental data are in good agreement with modeling results. Mean absolute percentage error value was 6.4 %. The difference between experiment and modeling results may be related to the nonlinear dependence of epoxy layer thickness in the region near the pyramids base. The model curve in Fig. 5 was obtained with the following set of parameters: $\beta = -0.9, \varepsilon = 3 - 0.4i, h_e = 0.09$ mm, $h = 0.25$ mm. The results showed that the produced metasurface acts as reflection selective surface with maximal absorption near $\nu_0 = 700$ GHz. Below ν_0 the amplitude of signal reflected from CNT array is 0.8, while above ν_0 the S_{11} amplitude is near 0.4.

Conclusions

The concept of frequency selective reflector based on pyramidal metasurfaces was implemented and investigated. The impact of pyramids height and dielectric covering layer to the electromagnetic response of investigated structures was theoretically described in a wide frequency range. The possibility to control the reflective behavior of the metasurfaces was theoretically substantiated.

The metasurface was produced by the laser engraving of vertically aligned MWCNT array followed by the dielectric layer covering. In accordance with the theoretical prediction, the experimental reflection spectrum exhibited the local minima in the THz range. Its position is determined by the thickness of the dielectric cover, while the height of pyramids defines the dumping rate of the reflected signal.

The presented design of metasurfaces which effectively absorb the electromagnetic radiation in the submillimeter frequency range is one of the numerous examples of THz component (such as frequency selective surfaces, filters, lenses, attenuators, etc.) that is possible to be realized using perfect absorption ability and electromagnetic response peculiarities of 3D-patterned CNT arrays. Targeting to the technology readiness level 3, these experimental observations supported by simple analytical model provide a solid laboratory-proved background for scalable cost-efficient technological protocol of ultra-lightweight THz components.

ACKNOWLEDGEMENTS

The work is supported by RFBR Grant number 19-33-50048, the Academy of Finland Flagship Programme, Photonics Research and Innovation (PREIN), decision 320166, H2020 RISE project 734164 Graphene 3D and Horizon 2020 RISE DiSeTCom project 823728. PK is supported by Horizon 2020 IF TURANDOT project 836816 and Grant of the President of the Republic of Belarus in science, education, health, culture in 2019. GG is supported by World Federation of Scientists project "Science and Technologies". All coauthors are thankful for support by Tomsk State University Competitiveness Improvement Program.

References

- [1] A. V. Okotrub, V. V. Kubarev, M. A. Kanygin, O. V. Sedelnikova, and L. G. Bulusheva. Transmission of terahertz radiation by anisotropic MWCNT/polystyrene composite films. *physica status solidi (b)*, 248(11):2568–2571, November 2011.
- [2] D. Bychanok, P. Angelova, A. Paddubskaya, D. Meisak, L. Shashkova, M. Demidenko, A. Plyushch, E. Ivanov, R. Krastev, R. Kotsilkova, F. Y. Ogrin, and P. Kuzhir. Terahertz absorption in graphite nanoplatelets/poly(lactic acid) composites. *Journal of Physics D: Applied Physics*, 51(14):145307, April 2018.
- [3] G. Spinelli, P. Lamberti, Tucci V., R. Ivanova, S. Tabakova, E. Evgeni Ivanov, R. Kotsilkova, S. Cimmino, R. Rosa Di Maio, and C. Silvestre. Rheological and electrical behaviour of nanocarbon/poly(lactic)acid for 3d printing applications. *Composites Part B: Engineering*, 2018.
- [4] A. Ronca, G. Rollo, P. Cerruti, G. Fei, X. Gan, G. Buonocore, M. Lavorgna, H. Xia, C. Silvestre, and L. Ambrosio. Selective Laser Sintering Fabricated Thermoplastic Polyurethane/Graphene Cellular Structures with Tailorable Properties and High Strain Sensitivity. *Applied Sciences*, 9(5):864, February 2019.
- [5] M. Shuba, D. Yuko, G. Gorokhov, D. Meisak, D. S. Bychanok, P. Kuzhir, S. A. Maksimenko, P. Angelova, E. Ivanov, and R. Kotsilkova. Frequency and density dependencies of the electromagnetic parameters of carbon nanotube and graphene nanoplatelet based composites in the microwave and terahertz ranges. *Materials Research Express*, July 2019.
- [6] G. Gorokhov, D. Bychanok, D. Meisak, I. Shlyk, A. Liubimau, P. Angelova, C. Menseidov, E. Ivanov, R. Kotsilkova, M. Casa, P. Ciambelli, and P. Kuzhir. Carbon nanotubes vs graphene nanoplatelets for 3d-printable composites. *IOP Conference Series: Materials Science and Engineering*, 503:012010, March 2019.
- [7] J. Chen and G. Lu. Controlled decoration of carbon nanotubes with nanoparticles. *Nanotechnology*, 17(12):2891–2894, June 2006.
- [8] A. K. Geim and K. S. Novoselov. The rise of graphene. In *Nanoscience and Technology*, pages 11–19. Co-Published with Macmillan Publishers Ltd, UK, August 2009.
- [9] Y. Kato, M. Horibe, S. Ata, T. Yamada, and K. Hata. Stretchable electromagnetic-interference shielding materials made of a long single-walled carbon-nanotube-elastomer composite. *RSC advances*, 7(18):10841–10847, 2017.
- [10] G.W. Hanson. Fundamental transmitting properties of carbon nanotube antennas. *IEEE Transactions on Antennas and Propagation*, 53(11):3426–3435, November 2005.
- [11] G. Ya Slepyan, M. V. Shuba, S. A. Maksimenko, and A. Lakhtakia. Theory of optical scattering by achiral carbon nanotubes and their potential as optical nanoantennas. *Physical Review B*, 73(19):195416, 2006.
- [12] P.J. Burke, Li S., and Yu Z. Quantitative theory of nanowire and nanotube antenna performance. *IEEE Transactions On Nanotechnology*, 5(4):314–334, July 2006.
- [13] H. Li, W. Yin, K. Banerjee, and J. Mao. Circuit Modeling and Performance Analysis of Multi-Walled Carbon Nanotube Interconnects. *IEEE Transactions on Electron Devices*, 55(6):1328–1337, June 2008.
- [14] A. Maffucci, G. Miano, and F. Villone. A New Circuit Model for Carbon Nanotube Interconnects With Diameter-Dependent Parameters. *IEEE Transactions on Nanotechnology*, 8(3):345–354, May 2009.
- [15] D. S. Bychanok, M. V. Shuba, P. P. Kuzhir, S. A. Maksimenko, V. V. Kubarev, M. A. Kanygin, O. V. Sedelnikova, L. G. Bulusheva, and A. V. Okotrub. Anisotropic electromagnetic properties of polymer composites containing oriented multiwall carbon nanotubes in respect to terahertz polarizer applications. *Journal of Applied Physics*, 114(11):114304, September 2013.
- [16] O. V. Sedelnikova, E. Yu. Korovin, K. V. Dorozhkin, M. A. Kanygin, V. E. Arkhipov, Yu. V. Shubin, V. A. Zhuravlev, V. I. Suslyayev, L. G. Bulusheva, and A. V. Okotrub. Iron-filled multi-walled carbon

- nanotubes for terahertz applications: effects of interfacial polarization, screening and anisotropy. *Nanotechnology*, 29(17):174003, April 2018.
- [17] P. Dharap, Z. Li, S. Nagarajaiah, and E. V. Barrera. Nanotube film based on single-wall carbon nanotubes for strain sensing. *Nanotechnology*, 15(3):379–382, March 2004.
- [18] V. Ryzhii, T. Otsuji, M. Ryzhii, V. G. Leiman, G. Fedorov, G. N. Goltzman, I. A. Gayduchenko, N. Titova, D. Coquillat, D. But, W. Knap, V. Mitin, and M. S. Shur. Two-dimensional plasmons in lateral carbon nanotube network structures and their effect on the terahertz radiation detection. *Journal of Applied Physics*, 120(4):044501, July 2016.
- [19] R. R. Hartmann, J. Kono, and M. E. Portnoi. Terahertz science and technology of carbon nanomaterials. *Nanotechnology*, 25(32):322001, August 2014.
- [20] G. Ya Slepyan, S. A. Maksimenko, Akhlesh Lakhtakia, O. Yevtushenko, and A. V. Gusakov. Electrodynamics of carbon nanotubes: Dynamic conductivity, impedance boundary conditions, and surface wave propagation. *Physical Review B*, 60(24):17136, 1999.
- [21] G. Ya. Slepyan, M. V. Shuba, S. A. Maksimenko, C. Thomsen, and A. Lakhtakia. Terahertz conductivity peak in composite materials containing carbon nanotubes: Theory and interpretation of experiment. *Physical Review B*, 81(20), May 2010.
- [22] M. V. Shuba, A. G. Paddubskaya, A. O. Plyushch, P. P. Kuzhir, G. Ya Slepyan, S. A. Maksimenko, V. K. Ksenevich, P. Buka, D. Seljuta, and I. Kasalynas. Experimental evidence of localized plasmon resonance in composite materials containing single-wall carbon nanotubes. *Physical Review B*, 85(16):165435, 2012.
- [23] Mikhail V. Shuba, Gregory Ya. Slepyan, Sergey A. Maksimenko, and George W. Hanson. Radiofrequency field absorption by carbon nanotubes embedded in a conductive host. *Journal of Applied Physics*, 108(11):114302, December 2010.
- [24] M. V. Shuba, A. V. Melnikov, A. G. Paddubskaya, P. P. Kuzhir, S. A. Maksimenko, A. C. Thomsen. Role of finite-size effects in the microwave and subterahertz electromagnetic response of a multiwall carbon-nanotube-based composite: Theory and interpretation of experiments. *Physical Review B*, 88(4):045436, 2013.
- [25] P. Karlsen, M. V. Shuba, P. P. Kuzhir, A. G. Nasibulin, P. Lamberti, and E. Hendry. Sign inversion in the terahertz photoconductivity of single-walled carbon nanotube films. *Physical Review B*, 98(24):241404, 2018.
- [26] O.V. Sedelnikova, M.A. Kanygin, E.Yu. Korovin, L.G. Bulusheva, V.I. Suslyayev, and A.V. Okotrub. Effect of fabrication method on the structure and electromagnetic response of carbon nanotube/polystyrene composites in low-frequency and Ka bands. *Composites Science and Technology*, 102:59–64, October 2014.
- [27] M. V. Shuba, D. I. Yuko, P. P. Kuzhir, S. A. Maksimenko, M. De Crescenzi, and M. Scarselli. Carbon nanotube sponges as tunable materials for electromagnetic applications. *Nanotechnology*, 29(37):375202, September 2018.
- [28] B.P. Gorshunov, E.S. Zhukova, Ju.S. Starovatykh, M.A. Belyanchikov, A.K. Grebenko, A.V. Bubis, V.I. Tsebro, A.A. Tonkikh, D.V. Rybkovskiy, A.G. Nasibulin, E.I. Kauppinen, and E.D. Obraztsova. Terahertz spectroscopy of charge transport in films of pristine and doped single-wall carbon nanotubes. *Carbon*, 126:544–551, January 2018.
- [29] P. P. Kuzhir, A. G. Paddubskaya, M. V. Shuba, S. A. Maksimenko, A. Celzard, V. Fierro, G. Amaral-Labat, A. Pizzi, G. Valusis, J. Macutkevicius, M. Ivanov, J. Banys, S. Bistarelli, A. Cataldo, M. Mastroianni, F. Micciulla, I. Sacco, E. Stefanutti, and S. Bellucci. Electromagnetic shielding efficiency in Ka-band: carbon foam versus epoxy/carbon nanotube composites. *Journal of Nanophotonics*, 6(1):061715, December 2012.
- [30] S. K. Patel, M. Ladumor, V. Sorathiya, and T. Guo. Graphene based tunable grating structure. *Materials Research Express*, 6(2):025602, November 2018.
- [31] S. K. Patel, M. Ladumor, J. Parmar, and T. Guo. Graphene-based tunable reflector superstructure grating. *Applied Physics A*, 125(8), August 2019.
- [32] V. Popov, M. Yakovleva, F. Boust, J. Pelouard, F. Pardo, and S. N. Burckur. Designing Metagratings via Local Periodic Approximation: From Microwaves to Infrared. *Physical Review Applied*, 11(4), April 2019.
- [33] R. Jadeja, S. Charola, S. K. Patel, J. Parmar, M. Ladumor, T. K. Nguyen, and V. Dhasarathan. Numerical investigation of graphene-based efficient and broadband metasurface for terahertz solar absorber. *Journal of Materials Science*, 55(8):3462–3469, March 2020.
- [34] A. Paddubskaya, M. Demidenko, K. Batrakov, G. Valusis, T. Kaplas, Y. Svirko, and P. Kuzhir. Tunable Perfect THz Absorber Based on a Stretchable Ultrathin Carbon-Polymer Bilayer. *Materials*, 12(1):143, January 2019.
- [35] A. V. Okotrub, L. G. Bulusheva, A. G. Kudashov, V. V. Belavin, and S. V. Komogortsev. Arrays of carbon nanotubes aligned perpendicular to the substrate surface: Anisotropy of structure and properties. *Nanotechnologies in Russia*, 3(3-4):191–200, 2008.
- [36] D. S. Bychanok, A. O. Plyushch, G. V. Gorokhov, U. S. Bychanok, P. P. Kuzhir, and S. A. Maksimenko. Microwave radiation absorbers based on corrugated composites with carbon fibers. *Technical Physics*, 61(12):1880–1884, December 2016.
- [37] D. Bychanok, Sijin Li, A. Sanchez-Sanchez, G. Gorokhov, P. Kuzhir, F. Y. Ogrin, Andreea Pasc, T. Ballweg, K. Mandel, and A. Szcurek. Hollow carbon spheres in microwaves: Bio inspired absorbing coating. *Applied Physics Letters*, 108(1):013701, 2016.
- [38] M. Born and E. Wolf. *Principles of optics: electromagnetic theory of propagation, interference and diffraction of light*. Cambridge University Press, Cambridge ; New York, 7th expanded ed edition, 1999.
- [39] D. Bychanok, G. Gorokhov, D. Meisak, A. Plyushch, P. Kuzhir, A. Sokal, K. Lapko, A. Sanchez-Sanchez, V. Fierro, and A. Celzard. Exploring carbon nanotubes/BaTiO₃/Fe₃O₄ nanocomposites as microwave absorbers. *Progress In Electromagnetics Research C*, 2016.
- [40] P. Kopyt, B. Salski, P. Zagrajek, D. Janczak, M. Sloma, M. Jakubowska, M. Olszewska-Placha, and W. Gwarek. Electric Properties of Graphene-Based Conductive Layers from DC Up To Terahertz Range. *IEEE Transactions on Terahertz Science and Technology*, 6(3):480–490, May 2016.
- [41] Y. Lan, B. Zeng, H. Zhang, B. Chen, and Z. Yang. SIMULATION OF CARBON NANOTUBE THz ANTENNA ARRAYS. *International Journal of Infrared and Millimeter Waves*, 27(6):871–877, February 2007.
- [42] J. F. O Hara, R. D. Averitt, and A. J. Taylor. Terahertz surface plasmon polariton coupling on metallic gratings. *Optics express*, 12(25):6397–6402, 2004.
- [43] A. Szcurek, A. Ortona, L. Ferrari, E. Rezaei, G. Medjahdi, V. Fierro, D. Bychanok, P. Kuzhir, and A. Celzard. Carbon periodic cellular architectures. *Carbon*, 88:70–85, July 2015.
- [44] C. R. Simovski, P. A. Belov, A. V. Atrashchenko, and Y. S. Kivshar. *Wire Metamaterials: Physics and Applications*. *Advanced Materials*, 24(31):4229–4248, August 2012.
- [45] I. Yamada, K. Takano, M. Hangyo, M. Saito, and W. Watanabe. Terahertz wire-grid polarizers with micrometer-pitch Al gratings. *Optics letters*, 34(3):274–276, 2009.

- [46] G. A. Wurtz, R. Pollard, W. Hendren, G. P. Wiederrecht, D. J. Gosztola, V. A. Podolskiy, and A. V. Zayats. Designed ultrafast optical nonlinearity in a plasmonic nanorod metamaterial enhanced by nonlocality. Nature Nanotechnology, 6(2):107–111, February 2011.
- [47] F. Qin and C. Brosseau. A review and analysis of microwave absorption in polymer composites filled with carbonaceous particles. Journal of applied physics, 111(6):4, 2012.
- [48] H. O. Moser, B. D. F. Casse, O. Wilhelm, and B. T. Saw. Terahertz response of a microfabricated rod-split-ring-resonator electromagnetic metamaterial. Physical review letters, 94(6):063901, 2005.
- [49] C. Castro, M. Pinault, S. Coste-Leconte, D. Porterat, Nedjma Bendiab, C. Reynaud, and M. Mayne-LHermitte. Dynamics of catalyst particle formation and multi-walled carbon nanotube growth in aerosol-assisted catalytic chemical vapor deposition. Carbon, 48(13):3807–3816, 2010.
- [50] M. V. Shuba, A. G. Paddubskaya, P. P. Kuzhir, S. A. Maksimenko, G. Valusis, M. Ivanov, J. Banyas, V. Ksenevich, and G. W. Hanson. Observation of the microwave near-field enhancement effect in suspensions comprising single-walled carbon nanotubes. Materials Research Express, 4(7):075033, July 2017.
- [51] D. A. Tsybouski, S. M. Bachilo, and R. B. Weisman. Versatile Visualization of Individual Single-Walled Carbon Nanotubes with Near-Infrared Fluorescence Microscopy. Nano Letters, 5(5):975–979, May 2005.

5 publikacija / 5th publication

**Laser Patterning of Aligned Carbon Nanotubes Arrays:
Morphology, Surface Structure, and Interaction with Terahertz
Radiation**

O.V. Sedelnikova, D.V. Gorodetskiy, A.G. Kurennya, K.I. Baskakova,
E.V. Shlyakhova, A.A. Makarova, **G.V. Gorokhov**, D.S. Bychanok,
P.P. Kuzhir, S.A. Maksimenko, L.G. Bulusheva and A.V. Okotrub

Materials **2021** 14 3275

DOI: 10.3390/ma14123275

Article

Laser Patterning of Aligned Carbon Nanotubes Arrays: Morphology, Surface Structure, and Interaction with Terahertz Radiation

Olga V. Sedelnikova ^{1,*}, Dmitriy V. Gorodetskiy ¹, Alexander G. Kurenya ¹, Kseniya I. Baskakova ¹, Elena V. Shlyakhova ¹, Anna A. Makarova ², Gleb V. Gorokhov ^{3,4}, Dzmityr S. Bychanok ³, Polina P. Kuzhir ^{3,5}, Sergey A. Maksimenko ³, Lyubov G. Bulusheva ¹ and Alexander V. Okotrub ^{1,*}

- ¹ Nikolaev Institute of Inorganic Chemistry SB RAS, 630090 Novosibirsk, Russia; gordim2005@yandex.ru (D.V.G.); kurenyaag@niic.sbras.ru (A.G.K.); baskakova@niic.nsc.ru (K.I.B.); ShlyakhovaEV@niic.sbras.ru (E.V.S.); bul@niic.nsc.ru (L.G.B.)
- ² Physical Chemistry, Institute of Chemistry and Biochemistry, Free University of Berlin, 14195 Berlin, Germany; anna.makarova@fu-berlin.de
- ³ Institute for Nuclear Problems, Belarusian State University, 11 Bobruiskaya str., 220006 Minsk, Belarus; glebgorokhov@yandex.ru (G.V.G.); dzmityrbychanok@yandex.by (D.S.B.); polina.kuzhir@uef.fi (P.P.K.); sergey.maksimenko@gmail.com (S.A.M.)
- ⁴ Physics Faculty, Vilnius University, Sauletekio 9, LT-10222 Vilnius, Lithuania
- ⁵ Institute of Photonics, University of Eastern Finland, Yliopistokatu 7, FI-80101 Joensuu, Finland
- * Correspondence: o.sedelnikova@gmail.com (O.V.S.); spectrum@niic.nsc.ru (A.V.O.)



Citation: Sedelnikova, O.V.; Gorodetskiy, D.V.; Kurenya, A.G.; Baskakova, K.I.; Shlyakhova, E.V.; Makarova, A.A.; Gorokhov, G.V.; Bychanok, D.S.; Kuzhir, P.P.; Maksimenko, S.A.; et al. Laser Patterning of Aligned Carbon Nanotubes Arrays: Morphology, Surface Structure, and Interaction with Terahertz Radiation. *Materials* **2021**, *14*, 3275. <https://doi.org/10.3390/ma14123275>

Academic Editor: Alexander Vul

Received: 30 April 2021

Accepted: 8 June 2021

Published: 14 June 2021

Publisher's Note: MDPI stays neutral with regard to jurisdictional claims in published maps and institutional affiliations.



Copyright: © 2021 by the authors. Licensee MDPI, Basel, Switzerland. This article is an open access article distributed under the terms and conditions of the Creative Commons Attribution (CC BY) license (<https://creativecommons.org/licenses/by/4.0/>).

Abstract: The patterning of arrays of aligned multi-walled carbon nanotubes (MWCNTs) allows creating metastructures for terahertz (THz) applications. Here, the strips and columns from MWCNTs vertically grown on silicon substrates are prepared using CO₂ laser treatment. The tops of the patterned arrays are flat when the laser power is between 15 and 22 W, and craters appear there with increasing power. Laser treatment does not destroy the alignment of MWCNTs while removing their poorly ordered external layers. The products of oxidative destruction of these layers deposit on the surfaces of newly produced arrays. The oxygen groups resulting from the CO₂ laser treatment improve the wettability of nanotube arrays with an epoxy resin. We show that the patterned MWCNT arrays absorb the THz radiation more strongly than the as-synthesized arrays. Moreover, the pattern influences the frequency behavior of the absorbance.

Keywords: CNT arrays; laser patterning; SEM; XPS; NEXAFS; Raman; terahertz elements

1. Introduction

Carbon nanotubes (CNTs) possess exceptionally high terahertz (THz) conductivity and, therefore, can replace the bulk metallic components and nanowires in nanoelectronics [1], communications [2,3], medicine [4], and many others [5,6]. However, the use of individual CNTs is limited in practice because of the sensitive dependence of nanotube properties on the structural configuration, which can be random, despite certain progress in the synthesis of CNTs with specific geometry [7,8]. Today, bulk materials based on CNTs are drawing the attention of researchers. Arrays of CNTs stand out among such materials for several reasons, the main one being their morphology. Arrays, composed of packed side-by-side parallel CNTs of equal length and close diameter, have electrical conductivity closest to individual CNTs due to the minor contribution of the CNT-CNT tunneling effect in charge transport phenomena [9].

The ordering of conducting microelements allows controlling and manipulating the incident THz radiation [10]. Transfer of this ideology to CNTs requires the development of a method for their precise positioning [11]. Only a few techniques allow obtaining patterned growth of aligned CNT areas, such as templating of a substrate to define the patterns of

catalytic layers [12,13] or using lithography [14–16] followed by the conventional chemical vapor deposition (CVD) synthesis of nanotubes. Another technique is the post-growth treatment based on the ablation of an array by a focused laser beam. Applications of femtosecond [17–21] and nanosecond [17,22–27] pulsed and continuous [17,28–31] lasers were considered. Due to the high longitudinal thermal conductivity of nanotubes and significantly suppressed radial heat transfer [32,33], the patterning of arrays with short-pulse lasers does not provide a decisive benefit in the quality of cut edges [17] as it is used for the ablation of dense targets [34]. With the need to scan a large area and reduce the overall cost of material, a high-power continuous laser seems to be the best choice for the patterning technology of CNT arrays.

Although the idea to use focused laser irradiation for the microstructuring of CNT arrays is not new, the quality of engraved elements surfaces and the possible transformation of preserved nanotubes after treatment are understudied. Commonly used characterization methods are scanning electron microscopy (SEM) and Raman spectroscopy. The former method does not reflect changes in the CNT walls, and the latter summarizes the spectra of the nanotubes located within a thickness of 500 nm below the array surface. As a result, the surface state of engraved array areas remains to be hidden.

In this study, we used continuous CO₂ lasers in the 15–38 W range to pattern arrays of aligned CNTs grown using an aerosol-assistant catalytic CVD technique. The methods of SEM, surface-probing X-ray photoelectron spectroscopy (XPS), bulk-probing near-edge X-ray absorption fine structure (NEXAFS) spectroscopy, and micro-Raman spectroscopy were used to study the effect of laser power on the structure and composition of CNTs forming arrays. We determined the laser power that does not lead to significant modifications of the CNTs and prepared arrays of ordered strips and columns of aligned CNTs. The effect of the pattern on the THz response of aligned CNT array was revealed.

2. Materials and Methods

Vertically aligned multi-walled CNTs (MWCNTs) arrays of uniform height ca. 300 μm were grown using a CVD method on silicon wafers with (100) orientation [35]. A reaction mixture composed of 4 wt % of ferrocene and 96 wt % of toluene was injected into a tubular reactor heated at 800 °C. An analysis of the TEM images (a JEOL-2010 microscope, JEOL Ltd., Tokyo, Japan; Figure S1a in Supplementary Materials) of the nanotubes determined the average values of ca. 20 nm for the outer diameter (Figure S1b in Supplementary Materials), ca. 8 nm for the inner diameter (Figure S1c in Supplementary Materials), and about 6 nm for wall thickness. The estimated number of layers in the MWCNTs was 17. High-resolution TEM images showed good-quality internal layers aligned along the nanotube cavity and poorer ordering of the outer layers (Figure S1 d in Supplementary Materials).

The arrays were patterned by a laser engraver (Winseal, Guangzhou, China) equipped with a continuous CO₂ laser with a wavelength of 10.4 μm. The method, described in detail elsewhere [36,37], is based on the oxidation of nanotubes under infrared radiation. Briefly, the laser beam with a diameter of ca. 50 μm was focused on the top surface of an array. Strips of MWCNT arrays were obtained through line-by-line scanning of the MWCNT samples. To create the columns, the samples were rescanned in a cross-direction. The scanning speed was kept at 17 mm/s, and the grating period was about 300 μm. The laser output power was ca. 15, 22, 30, and 38 W. As a result, four patterned samples composed of spaced columns of MWCNTs were obtained, denoted as Sample A, B, C, and D, respectively. During laser treatment, white-light emission from irradiated areas was observed. This effect can be attributed to laser-induced incandescence associated with invasive burnout of individual CNTs [30].

The morphology of the engraved arrays was studied by SEM on a Hitachi S-3400N microscope (Hitachi Ltd., Tokyo, Japan).

Room-temperature Raman scattering spectra were acquired using a LabRAM HR Evolution spectrometer (Horiba, Kyoto, Japan) using a 514 nm excitation of Ar⁺-laser, normalized to an intensity of 1572 cm⁻¹ (G peak).

The elemental compositions of the initial engraved arrays were determined by energy-dispersive X-ray (EDX) spectroscopy on a Hitachi S-3400N scanning microscope (Hitachi Ltd., Tokyo, Japan) and XPS. The chemical state of the carbon was studied by NEXAFS. XPS and NEXAFS spectra were recorded at the synchrotron radiation facility BESSY II, Helmholtz-Zentrum Berlin, using radiation from the Russian-German dipole (RGLB dipole) beamline. Arrays were placed into a chamber maintained at a pressure of 10⁻⁹ mbar. The XPS spectra were measured at a monochromatic radiation of 830 eV. The electrons emitted normally to the sample surface were collected, and the angle between the incident radiation and analyzer was 55°. After subtracting a Shirley background, the C 1s and O 1s XPS spectra were fitted using Gaussian/Lorentzian functions within Casa XPS software (version 2.3.15, Casa Software Ltd, Teignmouth, UK). The NEXAFS spectra near the C K-edge were recorded in the total-electron yield.

To demonstrate the prospects of microstructured MWCNT arrays for THz technologies, we investigated two samples composed of spaced strips and columns by scanning with aligned MWCNTs arrays (denoted as Samples 1 and 2). The engraving conditions included: scanning speed of 17 mm/s, laser power of 15 W, grating period of ca. 250 μm, and engraved element height of ca. 170 μm. The engraved strips were covered with epoxy resin (Crystal 76) under vacuum conditions. The resin mixed with hardener was applied to the MWCNT array with a pipette until the sample was completely soaked with resin. The excess resin was allowed to drip down from the inclined samples under evacuation. The THz mirror reflection coefficient was measured using a TSPEC time-domain spectrometer (EKSPLA, Vilnius, Lithuania) in a 0.1–1.4 THz frequency range.

3. Results and Discussion

3.1. Effect of the Laser Power

We first analyzed the effect of laser power on the array structure. Four samples with similar columnar patterns were engraved with the 15, 22, 30, and 38 W laser beams (denoted as Samples A, B, C, and D, respectively). The optical images showed that all arrays were burned down to the substrates (Figure 1a–d). The increase in laser power enhanced the deviation in the columns from parallelepipeds and changed their top surface. In particular, the tops of the columns of Sample A were flat (Figure 1e). Samples B and C had small holes in the column centers (Figure 1f,g). The columns in Sample D had deep craters with ragged edges (Figure 1h). There were round-shaped carbonaceous material contaminations (shown by green and red arrows in Figure 1e,f,g,h) presented on vertexes of Sample A columns, whereas for Samples B, C, and D, they were found mainly on the silicon substrates. The side surface of columns in Sample A contained shortened nanotubes, whose initial length before engraving was an array height of ~300 μm (Figure 1i). The nanotubes were generally aligned perpendicular to the substrate. The image taken from a crack of one of the columns showed a good ordering of the interior MWCNTs (Figure 1j), the same as the initial array (see Ref. [4]). Moreover, there was a poorly structured surface layer of ~5–10 μm in width. This meant that the interior regions of arrays were unaffected by the 15 W beam. Burning holes in the column centers under processing with higher laser power suggested that even the internal MWCNTs, which were not directly exposed to the beam, were modified during the engraving. Moreover, the morphology of Sample D surface layer changed. Nanotubes were entangled with each other, forming a cotton layer instead of an aligned structure (Figure 1k). The dark nanoparticles distributed on the surface were probably de-encapsulated catalyst nanoparticles.

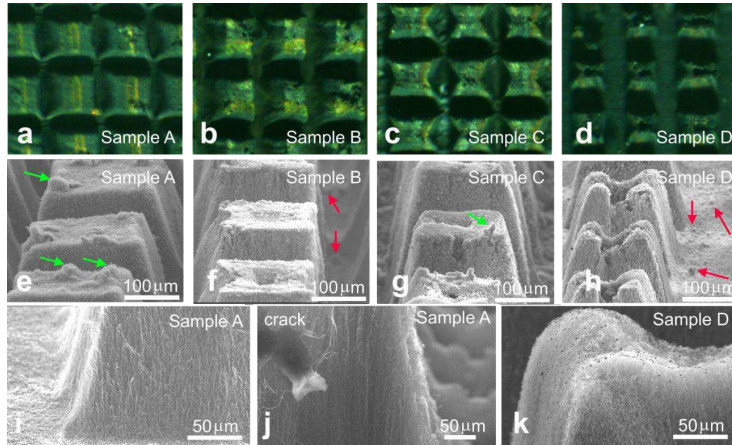


Figure 1. Optical and SEM images of Sample A (a and e,i,j), Sample B (b and f), Sample C (c and g), and Sample D (d and h,k).

The XPS method was used to reveal differences in the chemical states of atoms located on the surface of columns treated by the 15 and 38 W laser beams (Figure 2a). The survey XPS spectra in the range of 0–830 eV (not shown) were recorded to identify the surface elements present in the samples. For the initial array, the major constituent was carbon (~98 at %), with a minor contribution from oxygen (~2 at %). Few peaks fit the XPS C 1s spectra. The dominant component located at 284.5 eV (peak C1) corresponds to the sp^2 -hybridized carbon. For this feature, the full width at half maximum (FWHM) was ca. 1.4 eV (Figure 2a), which significantly exceeds the value for highly oriented pyrolytic graphite (ca. 0.9 eV). During the BESSY II experiments, the samples were attached to the spectrometer holder so that the spectrum of the initial array was collected from its top surface. The probing depth of XPS acquired using radiation of 830 eV was ca. 3 nm [38], indicating rather high disorientation of MWCNTs in the vertex of the untreated array. The weak high-energy shoulder consisted of peaks located at 285.2 eV (peak C2) and 286.4 eV (peak C3). The former component is due to contributions from sp^3 -hybridized carbons [39] or carbon atoms linked with –CO species [40], and the latter is due to different oxidized forms of carbon (C–O–C or C–OH) [40–42].

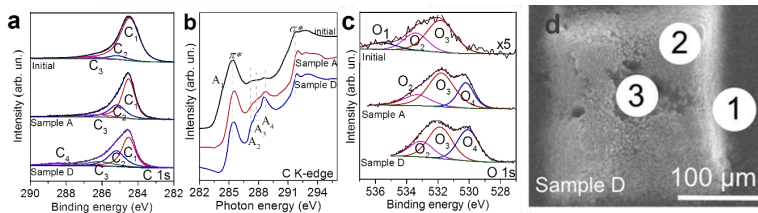


Figure 2. XPS C 1s (a), NEXAFS C K-edge (b), and XPS O 1s (c) spectra of initial and engraved MWCNT arrays. SEM image of a column of Sample D (d). Circles indicate regions used for EDX analysis.

The NEXAFS C K-edge spectrum of the initial array was dominated by two resonances (Figure 2b) assigned to the 1s electron transition to unoccupied π^* and σ^* orbitals of the sp^2 -hybridized carbon structure (positioned at 285.4 and 291.8 eV, respectively). Shoulder A1 on the low-energy side of π^* resonance can be associated with the states of disordered carbon [43]. Weak peaks at ~287.1 eV (A2), 287.9 eV (A3), and 288.6 eV (A4) indicated that few covalent bonds of carbon with heteroatoms were in agreement with the XPS data. According to previous works [40,43,44], peaks A2 and A3 correspond to carbon bonded with hydroxyl and ethers and/or aliphatic groups, peak A4 can be assigned either to the transitions to π^* states of a carboxyl group or σ^* states of C–H bonds from amorphous carbon species.

According to XPS data, the engraved samples obtained at the lowest and highest laser power (Samples A and D, respectively) contained about 14 at % of oxygen and about 4 at % of iron. The emergence of iron occurs due to the transport of encapsulated catalyst nanoparticles from the cavities of nanotubes under high-energy exposure. A similar effect was previously obtained for plasma-treated MWCNTs [45], single-walled CNTs filled with sulfur [46], and MWCNTs under femtosecond laser radiation [18]. The XPS C1s spectra are also governed by sp^2 -hybridized carbons (peak C1) with the FWHM of ca. 0.9 eV (Figure 2a), indicating a rather high quality of MWCNTs. The NEXAFS data confirm this. The π^* resonance at 285.4 eV of Samples A and D was quite narrow without the shoulder, and the σ^* resonance at 291.8 eV was sharpening. (Figure 2b). However, a significant contribution from sp^3 carbon was observed. Firstly, the C1s spectra contained notable peaks at 285.5 eV (peak C2). The ratio of sp^3/sp^2 carbon deduced from the areas of the components C2 and C1 increased from a value of 1/12 for the initial array to two-fifths for Sample A and three-fifths for Sample D. Secondly, the C K-edge spectra of the engraved samples showed a decrease in the π^*/σ^* ratio compared with that of the initial array and prominent resonance at 288.6 eV. The latter should be mainly related to C–H bonds due to a rather low intensity of carboxyl-related peak (peak C4) in the XPS C 1s spectra of the engraved samples. These findings suggest that in addition to well-ordered MWCNTs, Samples A and D consisted of amorphous-like carbonaceous components. The latter could be assigned to round-shaped particles observed in SEM images (Figure 1). In contrast, the initial array contained weakly functionalized nanotubes with disordered external layers in agreement with a recent study [47] and our TEM results (Supplementary Materials). Moreover, both the XPS and NEXAFS spectra indicated the presence of oxygen-containing moieties on the sample surface, namely, peaks C3 at 286.4 eV and C4 at 288.6 eV in the C 1s spectra and peaks A2 at 287.1 eV and A3 at 287.9 eV in the C K-edge spectra.

The consequent increase in the intensities of oxygen-related peaks in the carbon spectra with laser power was a good indicator of surface functionalization of Samples A and D. The XPS O 1s spectra helped determine the location of the moieties (Figure 2c). The spectrum of the initial array was fitted by three peaks positioned at 535.5 eV (peak O1), 533.5 eV (peak O2), and 531.8 eV (peak O3). These bands can be related to the adsorbed water (peak O1), ether (C–O–C), and hydroxyl (–OH) groups (peak O2), or the C=O bonds in the carboxyl group (peak O3). For the engraved samples, the contribution from adsorbed water was absent, during which the iron oxide peak O4 located at 530.2 eV appeared. The O3/O2 ratio decreased under engraving, indicating the different compositions of the surface groups in the initial array and the engraved samples. Considering the high thermal stability of MWCNTs, the prior oxidation of amorphous particles indicates that the oxygen-containing groups are located mainly on these contaminants.

Figure 2d shows the SEM image of a column from Sample D with marked regions (denoted as 1, 2, and 3) that were used to measure the local elemental composition with EDX spectroscopy. There are signals from carbon, silicon, oxygen, and iron, in agreement with the XPS data. The data collected from a side (point 1) show 86.6 at % of C, 10.9 at % of Si, 0.9 at % of Fe, and 1.4 at % of O. A flat region of vertex contains ca. 92.2 at % of C, 0.1 at % of Si, 2.2 at % of Fe, and 5.4 at % of O (point 2). The values for Fe and O are close to those (5.3 and 2.1 at %, respectively) found inside a crater (point 3). Based on these data, we

propose that, air oxygen quickly leaves the reaction zone and interacts with MWCNT walls at elevated temperatures. This process is followed by the emission of CO_2 and equalization of oxygen content through the whole sample. The signal from silicon was absent at point 3. Since the electrons escaped from a depth of about $5 \mu\text{m}$, the EDX spectra probed the composition of the entire laser-affected zone of the nanotube array, while the previously discussed XPS method studied the surface layer of about 3 nm. The lower EDX oxygen concentration indicates stronger oxidation of the outermost nanotubes.

To further analyze the surface composition of the engraved samples, the local Raman spectra were collected from the points indicated in Figure 3a–c. For the initial sample, we compared spectra taken from the top surface (Figure 3, point 1) and a side crack of the array (Figure 3, point 1'). Both spectra have three prominent peaks located at 1351 , 1572 , and 2710 cm^{-1} , which are related to the D, G, and 2D bands, respectively. The G band is a graphite E_{2g} mode, where neighboring atoms vibrate along to the graphitic sheet. The D band is due to a breathing mode of sp^2 carbon rings. The 2D band, arising from the two-phonon process, is associated with the crystallinity of MWCNT walls. The spectra of the initial array acquired from points 1 and 1' show different intensities of the D band (the I_D/I_G value was ca. 0.7 and 0.4, Table 1) and 2D band (the I_{2D}/I_G value was ca. 0.7 and 0.8, Table 1). Hence, the sp^2 networks of MWCNTs located close to the array top were more disordered than in the internal nanotubes. This result agrees with the XPS and NEXAFS data.

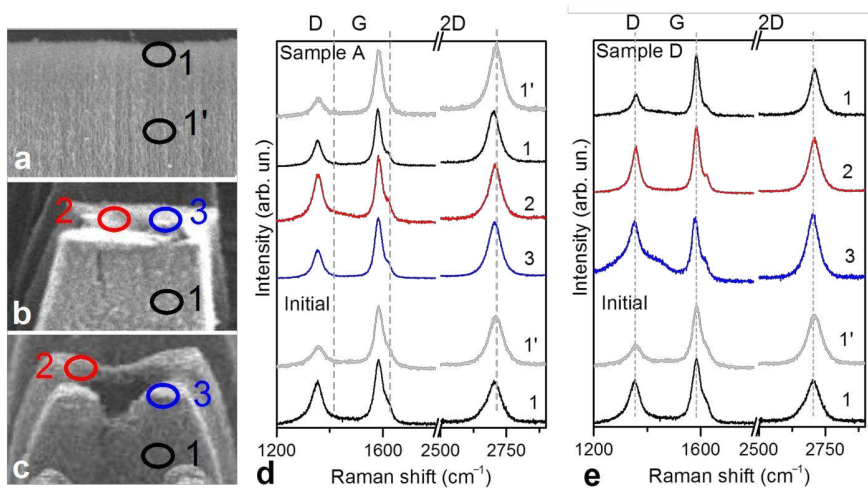


Figure 3. Points used to collect Raman spectra for initial MWCNT array (a), Sample A (b), and Sample D (c). Local Raman spectra of Sample A (d) and Sample D (e) compared with those of the initial array. Spectra are labeled by collection point explained in (a,b,c).

The Raman data for the engraved samples also depend on the collection point (Figure 3d,e). The effect of laser treatment on the defectiveness of the sp^2 carbon network can be estimated from the change of intensities of the D and 2D bands (Table 1). MWCNTs located on the side surface of columns exhibit the comparable (Sample D) or even better (Sample A) crystallinity of the walls than the nanotubes within the initial array. Therefore, when external nanotubes are not directly exposed to the laser beam, they remain unchanged. The exception is craters formed in the centers of columns of Sample D. The

spectrum acquired from this position had an intense and broad D band and enhanced 2D band, contributed by the amorphous constituent and highly crystalline short MWCNTs, respectively [48]. The contribution from silicon substrate in the low-wave-number region (not shown) indicated that the crater was rather deep. The spectrum of Sample A collected at a column side crack had the lowest-intensity D band and the highest-intensity 2D band. This observation may indicate improvement in the internal nanotubes' walls due to the engraving, in agreement with the recent results [20,21,24,25].

Table 1. Ratios of Raman band intensities for the initial array, Sample A, and Sample D determined from the spectra collected at different array points as indicated in Figure 3.

Sample point	Initial Array		Sample A			Sample D			
	1	1'	1	2	3	1'	1	2	3
I_D/I_G	0.66	0.37	0.47	0.66	0.48	0.26	0.36	0.71	0.92
I_{2D}/I_G	0.69	0.81	0.95	0.72	0.95	1.14	0.78	0.82	1.07

The results described above indicate that the CO₂ laser treatment affects the MWCNTs located both on the surface of engraved elements and inside them. This can be explained as follows: absorption of the laser beam results in the oxidation of nanotubes and ablation of carbon clusters [22,34]. White-light emission of heating MWCNTs is observed, followed by the burnout of nanotubes directly exposed to a laser. The nanotubes located at the surface layer of the engraved elements are oxidized at defect sites. This process likely causes the partial burning of the disordered external layers of MWCNTs and amorphous carbon produced during sample synthesis. Moreover, the flow of heat air can cause the straightening of MWCNTs, decreasing their bending [24]. As a result, the sample purity and the crystallinity of nanotubes walls are improved compared with the MWCNTs from the initial array. After irradiating the surface, the ejected material is re-deposited as amorphous nanoparticles on columns and silicon substrate. When the laser moves away, the surface layer cools quickly due to convection by the surrounding gas molecules [31], broadband light emissions, and energy transfer inside the array. Although the CNT–CNT coupling decreases the thermal conductivity of the array [49], when laser power is high enough, inside engraved elements at some distance from the laser pass, the hot zone is formed [27]. Unlike the surface layer, the cooling of this zone is hampered due to its limiting interaction with air molecules and self-absorption of emitted light through heating the MWCNTs. As a result, the nanotubes located there react with oxygen trapped inside the array, further increasing local temperature. This process is supposed to be self-sustained until all oxygen moieties react with carbon. In particular, that could explain the formation of craters in the center of columns obtained using a 38 W laser.

3.2. THz Response of the Arrays

Previous investigations showed that CNTs have attractive intrinsic electromagnetic properties in the THz frequency range [50,51] and as a filler in dielectric matrices [52–54]. In particular, the properties of composites are strongly affected by the ordering of nanotubes [52,53] and surface functionalization [54]. The nano-structured arrays show a morphology-governed response in the optical region [15,16,21]. To test the suitability of the microstructured arrays of CNTs for THz applications, we fabricated two samples composed of engraved strips and columns (Samples 1 and 2) and measured their reflection coefficient in the frequency range of 0.1–1.4 THz. The patterning was performed at a laser power of 15 W to keep the engraved elements' interior intact. Because engraved arrays of MWCNTs are fragile, the samples were uniformly covered by a thin epoxy layer (ca. 70–90 μm), as can be seen from the optical image in Figure 4a. The structural characterization results discussed above reveal strong oxidation of the MWCNTs' surface after the treatment. Despite some deterioration in THz conductivity [54], the oxidized MWCNTs had an advantage over the initial ones due to improved wettability of the nanotube arrays with an epoxy

resin, caused by the direct chemical interaction of MWCNTs with the matrix molecule through different oxygen-containing functional groups [55,56].

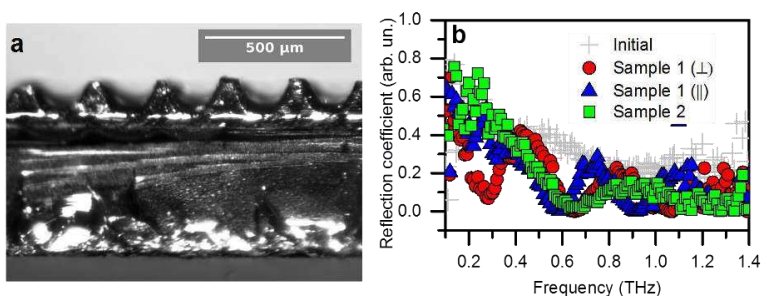


Figure 4. Optical image of Sample 1 (a). Reflection coefficients of Sample 1 and Sample 2 compared with epoxy-coated initial array of CNTs (b). Symbols || and \perp correspond to the parallel and perpendicular orientation of engraved strips of Sample 1 relative to the polarization of the incident wave.

As shown in Figure 4b, the initial epoxy-covered array reflected from 30% to 80% of the incident light power in the frequency range of 0.3–1.4 THz, indicating that the covered array was no longer a perfect absorber. This effect was caused by an interference of waves reflected from the front and back sides of the epoxy layer. For the patterned samples, the portion of reflected radiation decreased to about 1–5% above 1 THz. This indicates an increase in the contribution of absorption in our samples compared with the non-structured epoxy-coated array. The spectra of the engraved samples showed interference oscillations. Because they were absent in the coated initial array, the oscillations arose due to strips and columns of MWCNTs arrays in Samples 1 and 2. Moreover, the response of Sample 1 depended on the strips' orientation relative to the polarization direction of the incident wave. The spectra of the perpendicularly oriented pattern and the columns are alike. This suggests that the polarization-dependent properties can be assigned to the presence of a conduction path along the strips, while the conductivity between neighboring strips or columns behaves in a tunneling manner. A polarization-dependent THz response is essential for bio detectors [57]. Therefore, patterned arrays of CNTs can promote the design of advanced THz devices, which can distinguish polar biomolecules more accurately.

4. Conclusions

In conclusion, we synthesized aligned arrays of MWCNTs and patterned them with strips and columns through CO₂ laser treatment. A comprehensive investigation of morphology and surface state revealed that the engraved elements consisted of aligned MWCNTs with improved crystallinity of their walls due to the oxidation of the outermost disordered layers. Changing the laser power controlled the microstructure of the engraved elements. In particular, the increase in the laser power from 15 to 38 W caused the formation of deep craters on the flat columns' vertexes. The insufficient convection by surrounding gas molecules and self-absorption of incandescent light of heated MWCNTs was the origin of oxidation of the MWCNT array areas, which were not directly exposed by the laser beam. Owing to the improved wettability, the treated surface of MWCNTs robustly bound to epoxy molecules. This allowed the fabrication of lasting materials composed of epoxy-coated patterned MWCNTs arrays, which act as frequency-selective absorption elements in the THz frequency range. The results presented in this work develop a technological basis for THz metasurface production.

Supplementary Materials: The following are available online at <https://www.mdpi.com/article/10.3390/ma14123275/s1>, Figure S1: TEM image of MWCNTs from an array (a). Outer (b) and inner (c) diameter distribution of MWCNTs calculated from (a). HR TEM image of MWCNTs (d).

Author Contributions: Investigation, D.V.G., A.G.K., K.I.B., E.V.S., A.A.M. and G.V.G.; conceptualization, A.V.O., O.V.S. and S.A.M.; supervision, A.V.O., S.A.M. and O.V.S.; data curation, D.V.G. and G.V.G.; validation: O.V.S., A.V.O., L.G.B., P.P.K., D.S.B. and S.A.M.; writing—original draft preparation, O.V.S.; writing—review and editing O.V.S., D.V.G., G.V.G., D.S.B., L.G.B., P.P.K., S.A.M. and A.V.O.; visualization, O.V.S. and D.V.G.; project administration, O.V.S. and S.A.M.; funding acquisition, O.V.S. All authors have read and agreed to the published version of the manuscript.

Funding: The work was supported by RFBF grant number 20-52-00020 and BRFBF grant number F20R-214. P.P.K. was supported by Horizon 2020 IF TURANDOT project 836816 and the Academy of Finland Flagship Programme, Photonics Research and Innovation (PREIN), decision 320166. The authors thank the Helmholtz-Zentrum Berlin für Materialien und Energie for allocation of a beamtime and support within bilateral program “Russian-German Laboratory at BESSY II”. A.A.M. acknowledges BMBF (grant no. 05K19KER).

Institutional Review Board Statement: Not applicable.

Informed Consent Statement: Not applicable.

Data Availability Statement: The data presented in this study are available on request from the corresponding authors.

Conflicts of Interest: The authors declare no conflict of interest.

References

- Lawler, N.B.; Ho, D.; Evans, C.W.; Wallaceb, V.P.; Iyer, K.S. Convergence of terahertz radiation and nanotechnology. *J. Mater. Chem. C* **2020**, *8*, 10942–10955. [\[CrossRef\]](#)
- Rosenau da Costa, M.; Kibis, O.V.; Portnoi, M.E. Carbon nanotubes as a basis for terahertz emitters and detectors. *Microelectronics J.* **2009**, *40*, 776–778. [\[CrossRef\]](#)
- Akyildiz, I.F.; Jornet, J.M. Electromagnetic wireless nanosensor networks. *Nano Commun. Netw.* **2010**, *1*, 3–19. [\[CrossRef\]](#)
- Wang, R.; Xie, L.; Hameed, S.; Wang, C.; Ying, Y. Mechanisms and applications of carbon nanotubes in terahertz devices: A review. *Carbon* **2018**, *132*, 42–58. [\[CrossRef\]](#)
- Batracov, K.G.; Kibis, O.V.; Kuzhir, P.P.; Rosenau da Costa, M.; Portnoi, M.E. Terahertz processes in carbon nanotubes. *J. Nanophotonics* **2010**, *4*, 041665.
- Portnoi, M.E.; Kibis, O.V.; Rosenau da Costa, M. Terahertz applications of carbon nanotubes. *Superlattices Microstruct.* **2008**, *43*, 399–407. [\[CrossRef\]](#)
- Chen, Y.; Zhang, Y.; Hu, Y.; Kang, L.; Zhang, S.; Xie, H.; Liu, D.; Zhao, Q.; Li, Q.; Zhang, J. State of the art of single-walled carbon nanotube synthesis on surfaces. *Adv. Mater.* **2014**, *26*, 5898–5922. [\[CrossRef\]](#)
- Das, D.; Roy, A. Synthesis of diameter controlled multiwall carbon nanotubes by microwave plasma-CVD on low-temperature and chemically processed Fe nanoparticle catalysts. *Appl. Surf. Sci.* **2020**, *515*, 146043. [\[CrossRef\]](#)
- Dini, Y.; Faure-Vincent, J.; Dijon, J. How to overcome the electrical conductivity limitation of carbon nanotube yarns drawn from carbon nanotube arrays. *Carbon* **2019**, *144*, 301–311. [\[CrossRef\]](#)
- Kuramochi, E. Manipulating and trapping light with photonic crystals from fundamental studies to practical applications. *J. Mater. Chem. C* **2016**, *4*, 11032–11049. [\[CrossRef\]](#)
- Corletto, A.; Shapter, J.G. Nanoscale patterning of carbon nanotubes: Techniques, applications, and future. *Adv. Sci.* **2021**, *8*, 2001778. [\[CrossRef\]](#) [\[PubMed\]](#)
- Li, J.; Papadopoulos, C.; Xu, J.M. Highly-ordered carbon nanotube arrays for electronics applications. *Appl. Phys. Lett.* **1999**, *75*, 367–369. [\[CrossRef\]](#)
- Su, J.S.; Lee, J.S. Highly ordered two-dimensional carbon nanotube arrays. *Appl. Phys. Lett.* **1999**, *75*, 2047.
- Teo, K.B.K.; Chhowalla, M.; Amaratunga, G.A.J.; Milne, W.I.; Hasko, D.G.; Pirio, G.; Legagneux, P.; Wyczisk, F.; Pribat, D. Uniform patterned growth of carbon nanotubes without surface carbon. *Appl. Phys. Lett.* **2001**, *79*, 1534–1536. [\[CrossRef\]](#)
- Butler, T.P.; Rashid, I.; Montelongo, Y.; Amaratunga, G.A.J.; Butt, H. Optical bandgap modelling from the structural arrangement of carbon nanotubes. *Nanoscale* **2018**, *10*, 10683–10690. [\[CrossRef\]](#)
- Rajasekharan, R.; Butt, H.; Dai, Q.; Wilkinson, T.D.; Amaratunga, G.A.J. Can nanotubes make a lens array? *Adv. Mater.* **2012**, *24*, OP170–OP173. [\[CrossRef\]](#)
- Elmera, J.W.; Yaglioglu, O.; Schaeffer, R.D.; Kardosb, G.; Derkach, O. Direct patterning of vertically aligned carbon nanotube arrays to 20 μm pitch using focused laser beam micromachining. *Carbon* **2012**, *50*, 4114–4122. [\[CrossRef\]](#)

18. Labunov, V.; Prudnikava, A.; Bushuk, S.; Filatov, S.; Shulitski, B.; Tay, B.K.; Shaman, Y.; Basaev, A. Femtosecond laser modification of an array of vertically aligned carbon nanotubes intercalated with Fe phase nanoparticles. *Nanoscale Res. Lett.* **2013**, *8*, 375. [[CrossRef](#)]
19. Wu, X.; Yin, H.; Li, Q. Ablation and patterning of carbon nanotube film by femtosecond laser irradiation. *Appl. Sci.* **2019**, *9*, 3045. [[CrossRef](#)]
20. Yoon, J.-W.; So, H.-M.; Cho, S.-H.; Chang, W.S. Effect of polarization of ultrafast laser irradiation on carbon nanotube film. *Thin Solid Films* **2013**, *546*, 69–72. [[CrossRef](#)]
21. Choi, S.B.; Byeon, C.C.; Park, D.J.; Jeong, M.S. Polarization-selective alignment of a carbon nanotube film by using femtosecond laser ablation. *J. Korean Phys. Soc.* **2016**, *68*, 210–214. [[CrossRef](#)]
22. Langheinrich, D.; Dörfler, S.; Althues, H.; Kaskel, S.; Lasagni, A. Rapid and scalable method for direct and indirect microstructuring of vertical aligned carbon nanotubes. *Surf. Coat. Technol.* **2012**, *206*, 4808–4813. [[CrossRef](#)]
23. Cheong, F.C.; Lim, K.Y.; Sow, C.H.; Lin, J.; Ong, C.K. Large area patterned arrays of aligned carbon nanotubes via laser trimming. *Nanotechnology* **2003**, *14*, 433–437. [[CrossRef](#)]
24. Gerasimenko, A.Y.; Kitsyuk, E.P.; Kuksin, A.V.; Ryazanov, R.M.; Savitskiy, A.I.; Savelyev, M.S.; Pavlov, A.A. Influence of laser structuring and barium nitrate treatment on morphology and electrophysical characteristics of vertically aligned carbon nanotube arrays. *Diamond Relat. Mater.* **2019**, *96*, 104–111. [[CrossRef](#)]
25. Lasagni, A.; Cross, R.; Graham, S.; Das, S. The fabrication of high aspect ratio carbon nanotube arrays by direct laser interference patterning. *Nanotechnology* **2009**, *20*, 245305. [[CrossRef](#)] [[PubMed](#)]
26. Kichambare, P.D.; Chen, L.C.; Wang, C.T.; Ma, K.J.; Wu, C.T.; Chen, K.H. Laser irradiation of carbon nanotubes. *Mater. Chem. Phys.* **2001**, *72*, 218–222. [[CrossRef](#)]
27. Gbordzoe, S.; Yarmolenko, S.; Kanakaraj, S.; Haase, M.R.; Alvarez, N.T.; Borgemenke, R.; Adusei, P.K.; Shanov, V. Effects of laser cutting on the structural and mechanical properties of carbon nanotube assemblages. *Mater. Sci. Eng. B* **2017**, *223*, 143–152. [[CrossRef](#)]
28. Lim, K.Y.; Sow, C.H.; Lin, J.; Cheong, F.C.; Shen, Z.X.; Thong, J.T.L.; Chin, K.C.; Wee, A.T.S. Laser pruning of carbon nanotubes as a route to static and movable structures. *Adv. Mater.* **2003**, *15*, 300–303. [[CrossRef](#)]
29. Zhang, L.; Li, H.; Yue, K.-T.; Zhang, S.-L.; Wu, X.; Zi, J.; Shi, Z.; Gu, Z. Effects of intense laser irradiation on Raman intensity features of carbon nanotubes. *Phys. Rev. B* **2002**, *65*, 073401. [[CrossRef](#)]
30. Lim, Z.H.; Lee, A.; Zhu, Y.; Lim, K.-Y.; Sow, C.-H. Sustained laser induced incandescence in carbon nanotubes for rapid localized heating. *Appl. Phys. Lett.* **2009**, *94*, 073106. [[CrossRef](#)]
31. Mialichi, J.R.; Brasil, M.J.S.P.; Iikawa, F.; Verissimo, C.; Moshkalev, S.A. Laser irradiation of carbon nanotube films: Effects and heat dissipation probed by Raman spectroscopy. *J. Appl. Phys.* **2013**, *114*, 024904. [[CrossRef](#)]
32. Kumaneck, B.; Janas, D. Thermal conductivity of carbon nanotube networks: A review. *J. Mater. Sci.* **2019**, *54*, 7397–7427. [[CrossRef](#)]
33. Vanab, H.H.; Badurab, K.; Zhang, M. Laser-induced transformation of freestanding carbon nanotubes into graphene nanoribbons. *Nanoscale* **2015**, *5*, 44183–44191.
34. Momma, C.; Chichkov, B.N.; Nolte, S.; Alvensleben, F.; Tiinnermann, A.; Welling, H.; Wellegehausen, B. Short-pulse laser ablation of solid targets. *Opt. Commun.* **1996**, *129*, 134–142. [[CrossRef](#)]
35. Okotrub, A.V.; Bulusheva, L.G.; Kudashov, A.G.; Belavin, V.V.; Komogortsev, S.V. Arrays of carbon nanotubes aligned perpendicular to the substrate surface: Anisotropy of structure and properties. *Nanotechnol. Russia* **2008**, *3*, 191–200. [[CrossRef](#)]
36. Gorokhov, G.V.; Bychanok, D.S.; Kuzhir, P.P.; Gorodetskiy, D.V.; Kurennya, A.G.; Sedelnikova, O.V.; Bulusheva, L.G.; Okotrub, A.V. Creation of metasurface from vertically aligned carbon nanotubes as versatile platform for ultra-light THz components. *Nanotechnology* **2020**, *31*, 255703. [[CrossRef](#)] [[PubMed](#)]
37. Gorodetskiy, D.V.; Kurennya, A.G.; Gusev, A.V.; Baskkova, K.I.; Smirnov, D.A.; Arkhipov, V.E.; Bulusheva, L.G.; Okotrub, A.V. Laser beam patterning of carbon nanotube arrays for the work of electron field emitters in technical vacuum. *Mater. Sci. Eng. B* **2020**, *262*, 114691. [[CrossRef](#)]
38. Gries, W.H. A Universal Predictive Equation for the Inelastic Mean Free Pathlengths of X-ray Photoelectrons and Auger Electrons. *Surf. Interface Anal.* **1996**, *24*, 38–50. [[CrossRef](#)]
39. Barinov, A.; Malcioglu, O.B.; Fabris, S.; Sun, T.; Gregoratti, L.; Dalmiglio, M.; Kiskinova, M. Initial stages of oxidation on graphitic surfaces: Photoemission study and density functional theory calculations. *J. Phys. Chem. C* **2009**, *113*, 9009–9013. [[CrossRef](#)]
40. Fedoseeva, Y.V.; Pozdnyakov, G.A.; Okotrub, A.V.; Kanygin, M.A.; Nastaushev, Y.V.; Vilkov, O.Y.; Bulusheva, L.G. Effect of substrate temperature on the structure of amorphous oxygenated hydrocarbon films grown with a pulsed supersonic methane plasma flow. *Appl. Surf. Sci.* **2016**, *385*, 464–471. [[CrossRef](#)]
41. Zhan, D.; Ni, Z.; Chen, W.; Sun, L.; Luo, Z.; Lai, L.; Yu, T.; Wee, A.T.S.; Shen, Z. Electronic structure of graphite oxide and thermally reduced graphite oxide. *Carbon* **2011**, *49*, 1362–1366. [[CrossRef](#)]
42. Laikhtman, A.; Gouzman, I.; Hoffman, A.; Comtet, G.; Hellner, L.; Dujardin, G. Sensitivity of near-edge x-ray absorption fine structure spectroscopy to ion beam damage in diamond films. *J. Appl. Phys.* **1999**, *86*, 4192. [[CrossRef](#)]
43. Tang, Y.H.; Sham, T.K.; Hu, Y.F.; Lee, C.S.; Lee, S.T. Near-edge X-ray absorption fine structure study of helicity and defects in carbon nanotubes. *Chem. Phys. Lett.* **2002**, *366*, 636–641. [[CrossRef](#)]

44. Wesner, D.; Krummacher, S.; Carr, R.; Sham, T.K.; Strongin, M.; Eberhart, W.; Weng, S.L.; Willaims, G.; Howells, M.; Kampas, F.; et al. Synchrotron-radiation studies of the transition of hydrogenated amorphous carbon to graphitic carbon. *Phys. Rev. B* **1983**, *28*, 2152. [[CrossRef](#)]
45. Gorodetskiy, D.V.; Gusev, A.V.; Kerensya, A.G.; Smirnov, D.A.; Bulusheva, L.G.; Okotrub, A.V. Hydrogen Plasma Treatment of Aligned Multi-Walled Carbon Nanotube Arrays for Improvement of Field Emission Properties. *Materials* **2020**, *13*, 4420. [[CrossRef](#)] [[PubMed](#)]
46. Sedelnikova, O.V.; Gurova, O.A.; Makarova, A.A.; Fedorenko, A.D.; Nikolenko, A.D.; Plyusnin, P.E.; Arenal, R.; Bulusheva, L.G.; Okotrub, A.V. Light-Induced Sulfur Transport inside Single-Walled Carbon Nanotubes. *Nanomaterials* **2020**, *10*, 818. [[CrossRef](#)] [[PubMed](#)]
47. Fedorovskaya, E.O.; Bulusheva, L.G.; Kerensya, A.G.; Asanov, I.P.; Rudina, N.A.; Funtov, K.O.; Lyubutin, I.S.; Okotrub, A.V. Supercapacitor performance of vertically aligned multiwall carbon nanotubes produced by aerosol-assisted CCVD method. *Electrochim. Acta* **2014**, *139*, 165–172. [[CrossRef](#)]
48. di Leo, R.A. Purity assessment of multiwalled carbon nanotubes by Raman spectroscopy. *J. Appl. Phys.* **2007**, *101*, 064307. [[CrossRef](#)]
49. Van, H.H.; Badura, K.; Zhang, M. Laser-induced transformation of freestanding carbon nanotubes into graphene nanoribbons. *J. Mater. Sci.* **2019**, *54*, 7397–7427. [[CrossRef](#)]
50. Shuba, M.V.; Paddubskaya, A.G.; Kuzhir, P.P.; Slepian, G.Y.; Maksimenko, S.A.; Ksenevich, V.K.; Buka, P.; Seliuta, D.; Kasalynas, I.; Macutkevicius, J.; et al. Experimental evidence of localized plasmon resonance in composite materials containing single-wall carbon nanotubes. *Phys. Rev. B* **2012**, *85*, 165435. [[CrossRef](#)]
51. Shuba, M.V.; Yuko, D.I.; Kuzhir, P.P.; Maksimenko, S.A.; Chigir, G.G.; Pyalitski, A.N.; Sedelnikova, O.V.; Okotrub, A.V. Localized plasmon resonance in boron-doped multiwalled carbon nanotubes. *Phys. Rev. B* **2018**, *97*, 295427. [[CrossRef](#)]
52. Okotrub, A.V.; Kubarev, V.V.; Kanygin, M.A.; Sedelnikova, O.V.; Bulusheva, L.G. Transmission of terahertz radiation by anisotropic MWCNT/polystyrene composite films. *Phys. Status Solidi B* **2011**, *248*, 2568–2571. [[CrossRef](#)]
53. Bychanok, D.S.; Shuba, M.V.; Kuzhir, P.P.; Maksimenko, S.A.; Kubarev, V.V.; Kanygin, M.A.; Sedelnikova, O.V.; Bulusheva, L.G.; Okotrub, A.V. Anisotropic electromagnetic properties of polymer composites containing oriented multiwall carbon nanotubes in respect to terahertz polarizer applications. *J. Appl. Phys.* **2013**, *114*, 114304. [[CrossRef](#)]
54. Macutkevicius, J.; Seliuta, D.; Valusis, G.; Adomavicius, R.; Krotkus, A.; Kuzhir, P.; Paddubskaya, A.; Maksimenko, S.; Kuznetsov, V.; Mazov, I.; et al. Multi-walled carbon nanotubes/PMMA composites for THz applications. *Diam. Relat. Mater.* **2012**, *25*, 13–18. [[CrossRef](#)]
55. Yang, K.; Gu, M.; Guo, Y.; Pan, X.; Mu, G. Effects of carbon nanotube functionalization on the mechanical and thermal properties of epoxy composites. *Carbon* **2009**, *47*, 1723–1737. [[CrossRef](#)]
56. Wei, Y.; Hu, X.; Sun, Z.; Wang, P.; Qiu, P.; Liu, W. Influence of graphene oxide with different oxidation levels on the properties of epoxy composites. *Compos. Sci. Technol.* **2018**, *161*, 75–84. [[CrossRef](#)]
57. Matyushkin, Y.; Danilov, S.; Moskotin, M.; Belosevich, V.; Kurova, N.; Rybin, M.; Obraztsova, E.D.; Fedorov, G.; Gorbenko, I.; Kachorovskii, V.; et al. Helicity-Sensitive Plasmonic Terahertz Interferometer. *Nano Lett.* **2020**, *20*, 7296–7303. [[CrossRef](#)]

SANTRAUKA LIETUVIŲ KALBA

Šis darbas yra skirtas eksperimentiniam tyrimui funkcinių medžiagų tinkamų mikrobangiems ir teraherciniams taikymams, įskaitant gamybą ir charakterizavimą kompozitų su nanodariniiais ir dizainą struktūrų su žinomomis elektromagnetinėmis savybėmis. Funkcinės medžiagos vadinamos dirbtinėmis arba inžinerinėmis medžiagomis jeigu juos sukūrtos specialiai tam tikram tikslui spresti [1, 2]. Šių medžiagų savybės konstruojamos ir jų savybės valdomos tam kad jas pritaikyti praktikoje tokiomis sąlygomis, esant kurioms įprastinių arba natūralių medžiagų funkcionalumas nėra patenkinamas.

Prie funkcinių medžiagų galima priskirti kompozitus [3], metamedžiagas [4, 5] ir struktūras su konstruojama paviršiaus morfologija [6, 7] arba cheminė/tūrinė struktūra [8]. Tačiau kalbant apie funkcines medžiagas negalima ignoruoti kompozitų. Kompozitai su mikro arba nanoanglies intarpais (vienasieniai [9] arba daugiasieniai anglies nanovamzdeliai (DANV) [10–13], grafeno nanolakštai (GNL) [14, 15] ir kiti [16–18] yra labia dažnai siulomi elektromagnetiniams taikymams [19, 20].

Anglies nanovamzdeliai, kurios atrado Ijjima ir kiti [21], turi didžiausią santykį ilgis/spindulis tarp visų žinomų anglies nanodalelių. Jų unikalių savybių priežastis yra susieta su kritiniu sulėtejimu paviršinių bangų (taip vadinamais plazmoniniais-polaritonais) sklindančiais išilgai anglies nanovamzdelių ašies [22, 23], taip pat žinoma su “baigtinio ilgio“ efektais (taip vadinamas lokalizuotų plazmonų rezonansas) būdingus mikrometrinio ilgio vienasieniems anglies nanovamzdeliams ir stebimų teraherciniame ir infraraudonajame dažnių diapazone [24–26]. Kitas tipas anglies nanodalelių dažnai taikomas kompozitų inžinerijoje yra GNL (atrasto Geim ir Novosiolov [27]).

Neseniai, hibridiniai kompozitai su GNL ir anglies nanovamzdeliais susilaukė didelio dėmesio dėl galimų sinerginių efektų mechaniniuose, šiluminėse [28, 29] ir elektrinėse savybėse [30, 31]. Fazių išsidėstymas, kompozitų mechaninės, šiluminės ir elektrinės savybės stipriai priklauso nuo jų vidinės struktūros ir nuo gamybos proceso [32].

Kompozitinės medžiagos yra idealiai pritaikomi konstrukciniai elementai dirbtinėms struktūroms su geometriškai priklausoma elektromagnetine veika, tai yra metamedžiagoms [33–35]. Tam tikra eksperimentinė

technika leidžia sudaryti struktūras kelių fazių pagrindu nano- ir mikroskalėje, pavyzdžiui segreguotos struktūros tinklai, šerdis-apvalakas (*angl.* Core-shell struktūros) [36–39], vertikaliai sulygioti masyvai [40, 41], nanostulpeliai ir nanovielos [42, 43] ir kitos.

Vienas iš svarbesnių pritaikymų kompozitų ir funkcinių medžiagų yra plačiajuostis elektromagnetinis ekranavimas. Kompozitai ir metamedžiagos jų pagrindu leidžia suderinti optimalų elektromagnetinį efektyvumą ir puikų elektromagnetines absorbcijos veiką, gerą elastingumą ir dar daugiau [44]. Įvairūs metodai adityvios gamybos (tai yra 3D spausdinimo) yra naudojami metamedžiagų gamybai panaudojus kompozitus. Polimeriniai kompozitai su nanoanglies tarpais yra plačiai taikomi šiuose 3D spausdinimo technologijuose: lydyto nusėdimo modeliavimas (*angl.* fused deposition modeling) [45–48], selektyvi lazerinė sintezė (*angl.* selective laser sintering, SLS), skaitmeninis šviesos apdorojimas (*angl.* digital light processing, DLP) ir daugybė kitų technikų [49–51].

THz antenų [52], šaltinių [53] ir kitų fazės poslinkio [54, 55], dažniui ar poliarizacijai selektyvių elementų [56–58] uždaviniai ir problemos irgi dažnai sprendžiami metamedžiagų inžinerijos metodais [59, 60]. Šalia daugybės rūšių litografijos įvairūs 3D spausdinimo metodai yra kitas perspektyvus būdas sukurti optinius elementus mikrobangų ir teraherciniam dažnių diapazonui yra pateiktas šiame darbe.

Tam kad efektyviai pasiekti elektromagnetines savybes reikalinga tam tikriems taikymams metamedžiagų paradigma [7, 61–63] gali būti pritaikyta anglies nanovamzdelių masyvams derinant vidines jų savybes su tam tikru struktūravimu kuris sąlygoja konstruktyvią interferenciją [34].

Tikslas ir uždaviniai

Šis darbas yra skirtas kūrimui, charakterizavimui ir modeliavimui funkcinių medžiagų mikrobangų ir teraherciniame dažnių diapazone.

Tam kad būtų pasiektas disertacijos tikslas buvo išspręsti tokie uždaviniai:

- Išplėsti užpildų pasiskirstymo charakterizavimą polimeriniuose kompozituose žemiau ir aukščiau perkoliacijos slenksčio panaudojus terahercinę spektroskopiją.
- Pritaikyti 3D spausdinimo technika kūrimui ultralengvų porėtų medžiagų turinčių stiprią absorbciją gigaherciniame ir teraherciniame dažnių diapazonuose.
- Pasiūlyti naują technologiją tinkančia ultralengvų elektromagnetinių elementų kūrimui, panaudojus anglies nanovamzdelių graviravimą ir polimerinį įpregnavimą.

Mokslinis naujumas

1. Terahercinė spektroskopija buvo pritaikyta kaip neardantis metodas užpildo dalelių pasiskirstymui nustatyti polimerinėse kompozituose tiek žemiau, tiek aukščiau perkoliacijos slenksčio.
2. Porėtoms reguliarioms struktūroms sudarytos iš TPU/nanoanglies segreguotų struktūrų selektyvios lazerinės sintezės metodu yra būdinga reikšminga mikrobangų ir terahercinės spinduliuotės absorbcija.
3. Yra pasiūlyta nauja medžiagų inžinerijos technika paremta lazeriniu profiliavimu ir vertikaliai sulygotų anglies nanovamzdelių masyvų polimeriniu impregnnavimu.

Autoriaus indėlis

Teoriniai ir eksperimentiniai elektromagnetinių savybių tyrimai pateikti šiame darbe autorius atliko asmeniškai vadovaujant Dr. J. Macutkevic, su pagalba Prof. Polina Kuzhir ir Dr. Dmitry Bychanok. Bandinių gamyba buvo atlikta pasinaudojus eksperimentinėmis technologijomis Bulgarijos mokslų akademijos Mechanikos instituto, Sofija Bulgarija (trečiasis disertacijos skyrius), Polimerinių medžiagų inžinerijos valstybinės laboratorijos, Polimerų tyrimo instituto, Sichuano universiteto, Chengdu, Kinija ir Polimerų instituto, Kompozitai ir biomedžiagos, Nationalis tyrimo centras, Portici, Italija (ketvirtas disertacijos skyrius), Nikolaev neorganinės chemijos institutas, Novosibirskas, Rusija (penktas disertacijos skyrius).

Matavimai buvo atlikti Vilniaus universiteto Fizikos fakultete, Naelektromagnetizmo laboratorijoje Branduolinių problemų instituto Baltarusijos valstybinio universiteto, Maskvos pedagoginiame universitete, Maskva, Rusija, bei Maskvos Fizikos ir technologijos institute, Dolgoprudnyj, Rusia.

Publikuoti straipsniai buvo visiškai arba dalinai (Bychanok ir kiti, Ronca ir kiti, Sedelnikova ir kiti) parašyti šios disertacijos autoriaus diskutuojant su J. Macutkevic, D. Bychanok, P. Kuzhir, ir kitais bendraautoriais.

Disertacijos struktūra

Ši disertacija yra sudaryta iš penkių skyrių ir išvadų. Pirmame disertacijos skyriuje pateikti viso darbo teoriniai pagrindai. Antrame skyriuje yra paaiškinti eksperimentiniai metodai ir teoriniai modeliai naudojami darbe. Trečias skyrius yra skirtas neardančiai užpildo dalelių pasiskirtymo kontrolėje hibridiniuose nanoanglės kompozituose terahercinės spektroskopijos pagalba. Ketvirtame skyriuje yra paaiškinta porėtų struktūrų pasižyminčių didele terahercines spinduliotės absorbcija teraherciniame dažnių diapazone. Penktame skyriuje yra pristatytas naujas metodas funkcinį medžiagų inžinerijos. Disertacijos išvados pateikti darbo gale.

Disertacijos gynamieji teiginiai

1. Kompozitų su anglies nanodariniiais dielektrinės skvarbos menamosios dalies priklausomybė nuo dažnio turi maksimumą teraherciniame dažnių diapazone, šis maksimumams yra sąlygotas izoliuotų anglies nanodarinių poliarizacijos tiek žemiau, tiek aukščiau perkoliacijos slenksčio.
2. Reguliari porėta medžiaga pagaminta panaudojus selektyvią lazerinę sintezę termoplastinio polyuretano DANV/GNL kompozito pasižymi stipria elektromagnetinių bangų absorbcija dažnių diapazone 12 GHz–1 THz dėl savo hierarchinės porėtos struktūros.
3. Metapaviršiai pagaminti unikalia technika, įskaitant lazerinį graviravimą ir polimerinį įmpregnavimą vertikaliai orientuotų anglies nanovamzdelių pasižymi selektyviomis ir nuo poliarizacijos priklausončiomis dažninėmis savybėmis dėl sąveikos tarp graviruoto masyvo ir polimerinės dangos.

Moksliniai projektai

Tyrimai įtraukti į šį darbą buvo atlikti dalyvaujant šiuose projektuose:

- Horizont 2020 RISE projektas 734164 Grafenas 3D;
- Suomijos Mokslų Akademijos (Flagship programa Fotonikos tyrimai ir inovacijos, *angl.* Photonics Research and Innovation (PREIN), projektų numeriai 320166 ir 334370);
- Nacionalinė Kinijos programa (2017YFE01115000);
- Horizont RISE projektas 823728 DiSeTCom;

S.1. Literatūros apžvalga

Čia pateikti fundamentiniai teoriniai pagrindai. Plokščios bangos sąveika su medžiaga yra trumpai aprašoma. Elektromagnetinio atsako koncepcija žemų ir aukštų dažnių diapazone yra pateikta tam kad teisingai aprašyti eksperimentinius duomenys. Taip pat aprašomas efektyvios medžiagos modelis heterogeninei aplinkai reikalingas kompozitų savybėms aprašyti.

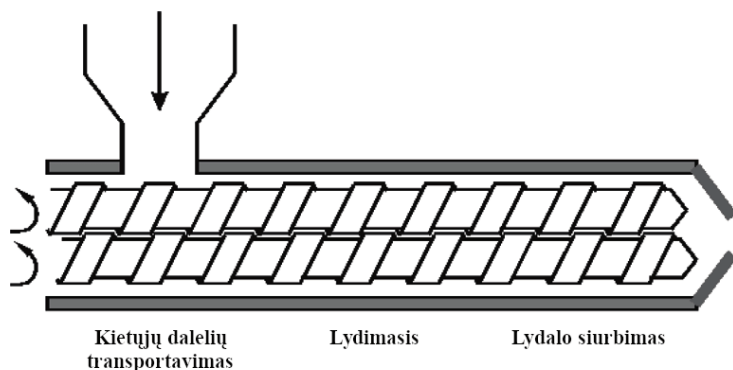
S.2. Eksperimentinės technikos

Eksperimentinis skyrius yra sudarytas iš trijų dalių skirtų medžiagų gamybai, tyrimo metodams ir taikomiems analitinėms modeliams.

S.2.1. Medžiagų gamyba

Nanoanglies ir termoplastinių polimerų kompozitų gamyba

Šiuose tyrimuose buvo naudojama polimerinė matrica Ingeo™ biopolimeras PLA-3D850. Užpildui buvo naudojami: komerciškai pasiekiami pramoniniai GNL, pramoniniai OH funkcionalizuoti DANV. Nanokompozitai buvo pagaminti panaudojus lydimosi ekstruzijos metodą dvigubo varžto ekstruderyje (Pav. 4), kuris sudarytas iš koncentruoto tirpalo pagaminimo ir tolesnio jo praskiedimo.



4 pav.: Dvigubo varžto ekstruderio schema.

Buvo pagaminti kompozitai su vieno tipo užpildu (DANV arba GNL) esant užpildų masinėms koncentracijoms 1.5 %, 3 % ir 6 % ir hibridiniai kompozitai (turintys DANV ir GNL vienu metu) su 3 ir 6 % bendra koncentracija (GNL ir DANV koncentracijos suderintos tam tikromis proporcijomis) polilaktido (PLA) matricoje. Nanokompozitų ploni sluoksniai buvo pagaminti karšto presavimo metodu esant temperatūrai 180 °C ir spaudimui 1 baras. PLA nanokompozitų su nanoanglies tarpais savybės yra pateiktos Lentelėje 1. Kompozitų kristališkumas buvo 30 %.

1 lentelė: Polimerinių kompozitų savybės po karšto presavimo [64, 65].

Parametras	Reikšmė
Stiklėjimo temperatūra T_g , °C	65
Šalto kristalizavimosi temperatūra T_{cc} , °C	87–92
Lydimosi temperatūra T_m , °C	175
Lydimosi kristalizacijos temperatūra T_g , °C	105
Kristališkumas, %	30

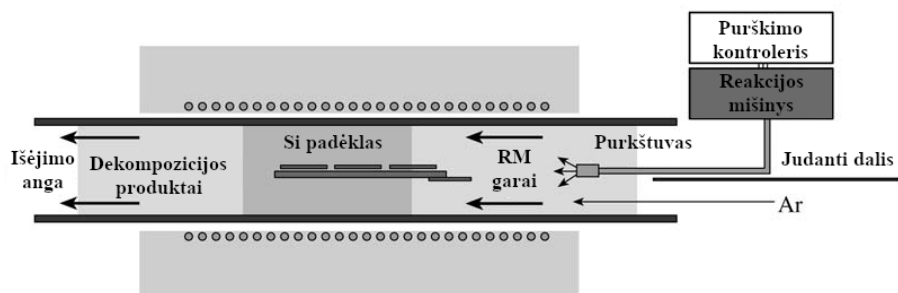
Segreguotos struktūros DANV/GNL/polyuretano pagaminimas SLS 3D spausdinimui

Kompozitai turintys 1 % masinės koncentracijos DANV (NANOCYL 7000, Nanocyl, Sambreville Belgium) ir šių anglies nanovamzdelių ir grafeno (gamintojas The Sixth Element Materials, Changzhou, Kinija) mišiniu esant masių santykiui 70/30 buvo pagaminti panaudojus termoplastinio polyuretano miltelius (Mophene 3D T90A, Nanjing, Kinija).

Užpildų milteliai buvo disperguoti esant šlapiam malimui rutulianiame malūne, paskui disperguoti bevandeniame etanolyje esant ultrasonifikacijai. Termoplastinio polyuretano milteliai buvo pridėti prie užpildo miltelių suspensijos, tokiais kiekiais kad gauti galutinę užpildo masinę koncentraciją būtų 1 % ir vėliau buvo mechaniškai maišomas dvi valandas. Pagamintas mišinys buvo filtruojamas su Buchnerio piltuvečiu esant sumažintam slėgiui ir džiovinamas vakuume esant 70 °C 24 valandas. Palyginimui buvo naudojamas kontrolinis bandinys TPU/DANV kompozito milteliai (Mophene3D T90A, Nanjing, Kinija).

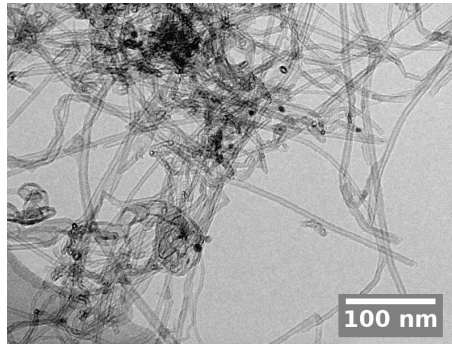
DANV masyvų gamyba

Standartinė eksperimentinė technika, būtent cheminis garų nusodinimas panaudojus aerolinią katalizatorių [40, 41, 66, 67] buvo panaudota vertikaliems anglies nanovamzdelių masyvams auginti. Silicio padėklų rinkinys buvo patalpintas į cheminio reaktoriaus vamzdinę krosnelę (Pav. 5) nuolat prapučiama argonu, esant pūtimo greičiui 18 l/h ir kaitinama 800 °C. Vamzdinės krosnelės įėjimas buvo paliktas visa laiką atviras tam kad palaikyti atmosferos slėgį reaktoriaus viduje. Sintezė buvo atlikta panaudojus 2 % feroceno ($\text{Fe}(\text{C}_5\text{H}_5)_2$) tirpalą toluene ($\text{C}_6\text{H}_5\text{CH}_3$). Rezultate panaudojus 2.5 ml pradinio mišinio buvo pagamintas DANV masivas esant nanovamzdelių aukščiui $\sim 250 \mu\text{m}$.



5 pav.: Cheminio reaktoriaus schema DANV masyvų gamybai garų nusodinimo metodu [40].

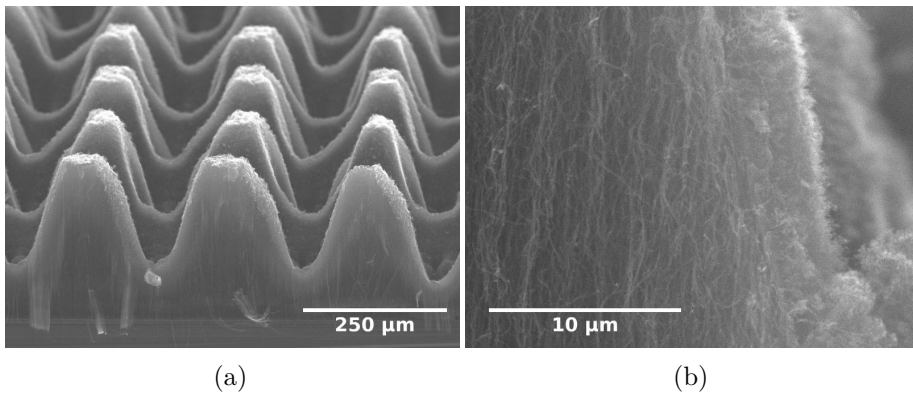
DANV morfologija buvo ištirta prašviečiančios elektronų mikroskopijos (PEM) metodais panaudojus JEOL 2010 mikroskopą. DANV PEM nuotraukos yra parodytos 6 Pav. Vidutinis nanovamzdelių skersmuo yra apie $\sim 6 \text{ nm}$.



6 pav.: PEM nuotraukos anglies nanovamzdelių pagamintų garų nusodinimo metodu.

Vertikaliai orientuotų DANV masyvai buvo transformuoti į periodinius piramidžių masyvus panaudojus lazerinio graviravimo mašiną su skaitmenine kontrole. Grotelių periodas buvo 250 μm .

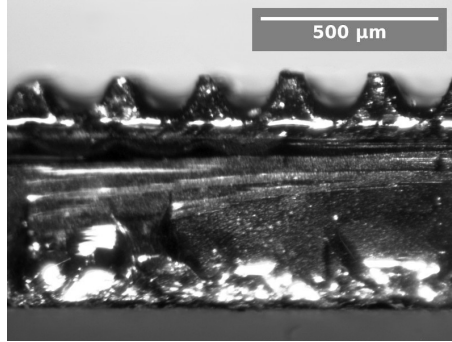
Anglies nanovamzdelių masyvų struktūra buvo tiriama skenuojančiu elektroniniu mikroskopu (SEM) JEOL JSM 6700F. SEM nuotraukos išgraviruotų piramidžių yra pateiktos Pav. 7. Galima pastebėti kad pradinė anglies nanovamzdelių masyvo struktūra po graviravimo procedūros liko nepastebėta.



7 pav.: (a) Periodinis masyvas piramidžių sudarytų iš DANV, (b) anglies nanovamzdelių masyvų struktūra išlikusi nepakitusi.

Po graviravimo anglies nanovamzdelių masyvas buvo padengtas epoksidine derva tam kad išsaugoti trapius anglies nanovamzdelius. Klampi epoksidinė derva (Crystal 76) su specialiu kietikliu buvo lašinama ant graviruoto paviršiaus, o paskui paskirstyta visame paviršiuje esant vaku-

umui. Bendras vaizdas struktūros esant epoksidinės dervos padengimui yra parodytas Pav. 8.



8 pav.: Optinės mikroskopijos nuotrauka graviruoto anglies nanovamzdelių masyvo padengto epoksidinė derva.

Bendras piramidžių aukštis po visų manipuliacijų išmatuotų optiniu mikroskopu buvo $232.9 \pm 11.9 \mu\text{m}$ su $54.9 \pm 6.9 \mu\text{m}$ nenupjautu sluoksniu iš apačios. Maksimalus storis epoksidinės dervos tarpuose tarp piramidžių buvo $77.0 \pm 4.5 \mu\text{m}$.

S.2.2. Modeliavimas

Maksvelo Garneto efektyvios terpės teorijos taikymas kompozitams su anglies nanointarpais

Šiuo atveju kai užpildų koncentracija yra žemesnė negu perkoliacijos slenkstis, tai yra užpildo dalelės nesaveikauja, gali būti pritaikyta Maksvelo Garneto teorija [68, 69]. Šio metodo pagrindinė prielaida kad užpildo dalelės yra elipsinės formos su pusašėmis a, b, c ir poliarizuojamumu

$$\alpha_i(\nu, \sigma) = \frac{4\pi abc}{3} \frac{\varepsilon_m(1 - \frac{i\sigma}{2\pi\nu\varepsilon_0} - \varepsilon_m)}{\varepsilon_m + N_i(1 - \frac{i\sigma}{2\pi\nu\varepsilon_0} - \varepsilon_m)}, \quad (1)$$

kur σ yra elipsoido laidumas, ε_0 yra vakuumo dielektrinė skvarba, N_i yra depolarizacijos faktorius kryptimis $i = a, b, c$ kuris aprašomas formule:

$$N_i = \frac{1}{abc} \int_0^\infty \frac{ds}{(s + i^2)\sqrt{(s + a^2)(s + b^2)(s + c^2)}}. \quad (2)$$

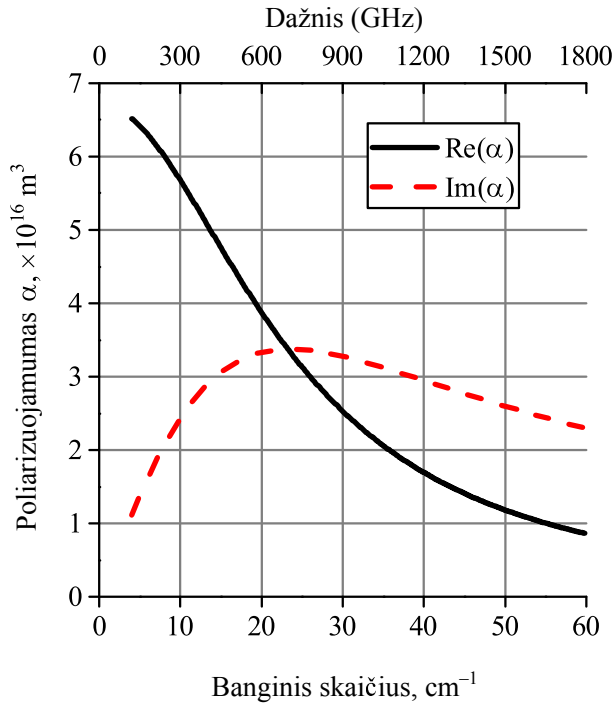
Todėl efektyvi dielektrinė skvarba yra

$$\varepsilon_{eff} = \varepsilon_m + \frac{1/3 \sum_{i=a,b,c} n \alpha_i / V}{1 - 1/3 \sum_{i=a,b,c} \frac{N_i n \alpha_i / V}{\varepsilon_m}}, \quad (3)$$

kur ε_m yra dielektrinės matricos skvarba, n tūrinė užpildų koncentracija.

Yra įmanoma parodyti (pavyzdžiai yra parodyti Pav. 9) kad menama polarizuojamumo dalis apskaičiuota pasinaudojus lygtimi (1) turi maksimumą esant kritiniam dažniui lygtis (4). Todėl menamos dielektrinės skvarbos dalis turi tokį pat maksimumą.

$$\nu_c = \frac{N_i \sigma}{2\pi \varepsilon_0 (\varepsilon_m - N_i \varepsilon_m + N_i)}. \quad (4)$$



9 pav.: Išilginio polarizuojamumo apskaičiuoto ištemptam elipsoidui dažninė dispersija su parametrais $a = b = 5 \mu\text{m}$, $c = 25 \text{ nm}$ (i.e., $\text{AR} = 200$), $\sigma = 10000 \text{ S/m}$, $\varepsilon_m = 2.5 - 0.1i$.

Regulari porėta struktūra aprašoma trigubo minimumo paviršiaus lygtimi

Efektyvus metodas aprašyti trimatę porėtą struktūrą yra sukurti erdvinius regionus apribotus vienam iš trigubam periodiniam pavyršiui (*angl.* tri-periodic minimal surface, TPMS). Šiame tyrime trys porėtos struktūros yra diskutuojamos: Deimantas (Lygtis 5), Giroidas (Lygtis 6), Švarc (Lygtys 7).

$$\text{Deimantas: } \begin{aligned} & \sin x \sin y \sin z + \sin x \cos y \cos z + \\ & + \cos x \sin y \cos z + \cos x \cos y \sin z > C \end{aligned} \quad (5)$$

$$\text{Giroidas: } \sin x \cos y + \sin y \cos z + \sin z \cos x > C \quad (6)$$

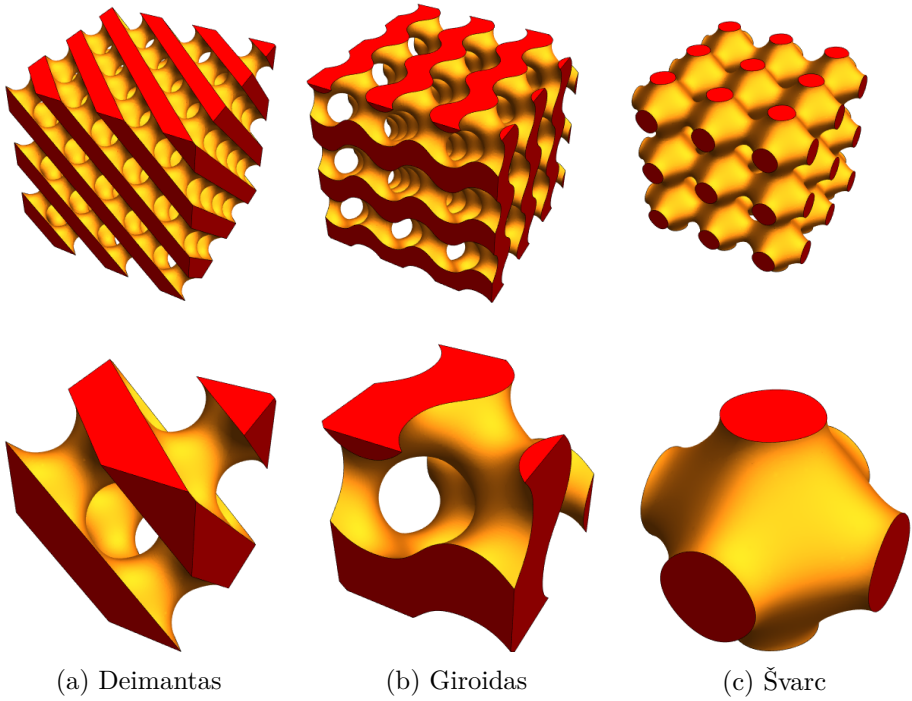
$$\text{Švarc: } \cos x + \cos y + \cos z > C \quad (7)$$

ur C yra poslinkio daugiklis susietas su struktūros porėtumu. Sąryšys tarp porėtumo P ir parametro C yra tiesinis $P = a \cdot C + b$, kur a ir b vertės priklausančios nuo TPMS tipo pateikto Lentelėje 2. Toliau struktūra su tam tikra geometrija ir porėtumu bus žymima AX, kur A yra D, G, ar S ir X porėtumas procentais. Pavyzdžiui, žymėjimas G60 reiškia kūną giroidalinės geometrijos su 60 % porėtumu. Vienetinių narvelių D, G, S paveikslai yra pateikti Pav. 10.

2 lentelė: Proporcingumo koeficientai porėtumo tiesinės priklausomybės nuo poslinkio daugiklio C , esant skirtingiems TPMS geometrijoms [70].

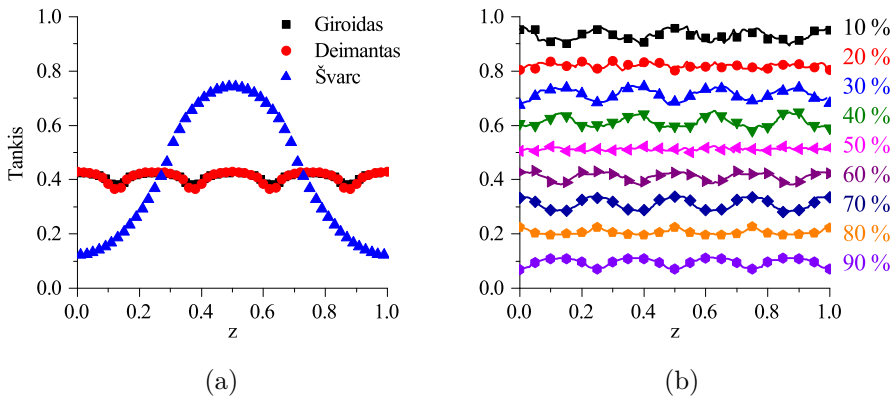
TPMS geometrijos tipas	a	b
Deimantas	41.2	50.8
Giroidas	31.1	51.1
Švarc	27.1	51.7

Kadangi TPMS geometrijos yra užduodamos trigonometrinėmis funkcijomis galima tiketitis kad tankio fluktuacijos keisis pagal harmoninius dėsnius, tai reiškia kad medžiagos tankis, dielektrinė skvarba ir kiti medžiagos parametrai keisis irgi harmoniškai TPMS geometrijos viduje. Tačiau, tai gali būti daugiau ar mažiau svarbu. Kai Švarc geometrijos tankio vertės keičiasi nuo 0.1 iki 0.75, Deimanto ir Giroido geometrijos pasižymi mažesniais tankio fluktuacijomis (Pav. 11a). Dar daugiau kai



10 pav.: 3D periodinės struktūros esant 60 % porėtumui.

porėtumas yra 50 % tankio fluktuacijos išnyksta D ir G geometrijoms (Pav. 11b).

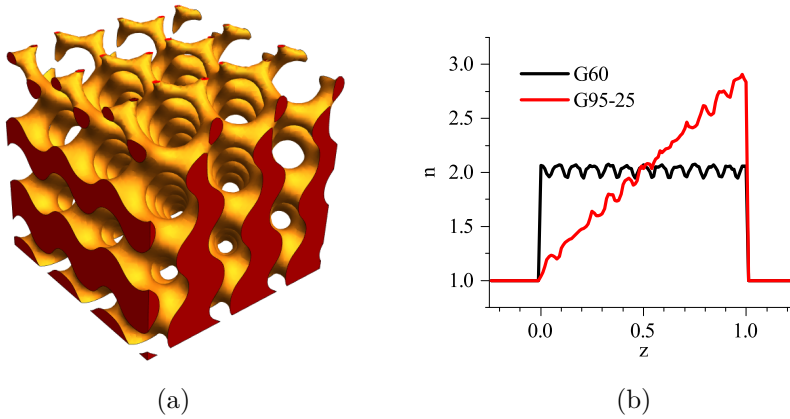


11 pav.: a) tankio fluktuacijos esant vienetingiems gardelės narveliams D, G, S geometrijoms ir 60 % porėtumui, b) tankio fluktuacijos esant vienetingiam gardelės narveliui G geometrijoms ir skirtingam porėtumui.

Efektyvios aplinkos teorijos rėmuose aplinkos parametrai gali būti anizotropiniai. Toliau bus diskutuojamas efektyvus metodas apskaičiuoti elektromagnetinį atsaką struktūros kurios dielektrinė skvarba keičiasi išilgai z ašies. Nagrinėsime trimatę porėta struktūrą aprašyta anksčiau kaip efektyvi terpė su kintamu lūžio rodikliu išilgai z ašies:

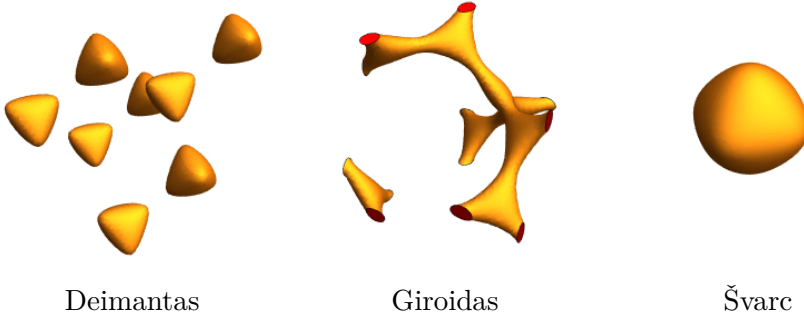
$$\begin{cases} z < 0; & n = n_0, \\ z \in [0, z_0]; & n = n_{bulk}(1 - S) + n_0S, \\ z > z_0; & n = n_0 \end{cases} \quad (8)$$

kur n_0 ir n_{bulk} yra lūžio rodikliai laisvosios erdvės ir tūrinės medžiagos, S yra reliatyvus paviršiaus plotas struktūros skerspjūvio statmeno z ašiai. Akivaizdu, kad reliatyvus paviršiaus plotas yra 2D porėtumo atvaizdas. Nagrinėsime TPMS struktūrą kurios porėtumas tiesiškai kinta išilgai z -ašies (Pav. 12a). Kadangi atspindžio nuostoliai yra proporcingi dvejų fazių lūžio rodiklių santykiui, ši struktūra pasižymi reikšmingomis antireflekcinėmis savybėmis [71]. Pav. 12b yra pavaizduota $n(z)$ priklausomybė giroidui esant pastoviam ir pasiskirstytam erdvėje porėtumui.



12 pav.: G95-25 giroido pagrindo kūnas su porėtumu kintančiu nuo 95 % viršuje iki 25 % kampo apačioje (vidutinis porėtumas 60 %). Efektyvaus lūžio rodiklio priklausomybė nuo z koordinatės G60 ir G95-25 struktūrai.

Galima pastebėti, kad ne visi TPMS išlaiko tolydumą esant dideliame porėtumui, dėl ko tampa neįmanomas praktinis panaudojimas S80, D95 ir kitų labai porėtų struktūrų. Giroido geometrijos struktūros gali būti taikomos esant porėtumui ne didesniau negu 95 % (Pav. 10).



13 pav.: TPMS pagrindu 3D periodinės struktūros esant 95 % porėtumui. Akivaizdu kad tik G95 vienitinis narvelis lieka sujungtas su kitais narveliais, tai yra išlieka tolydus.

Tam kad apskaičiuoti atspindėto (S_{11}) ir praėjusio (S_{21}) signalų per baigtinį bandinį amplitudes panaudosime matricinį metodą [72, 73] skirtą bangų sklidimo modeliavimui per daugiasluoksnę aplinką. Nagrinėsime plokščios bangos sklindančios išilgai z ašies normalią sklaidą tūrinės medžiagos, kurios storis τ ir lūžio rodiklio pasiskirstymas $n(z)$ paviršiuje. Padalinkime visą sluoksnį į N pluokštelių su storiais žymiai mažesniais negu krentančios bangos ilgis. Esant dideliems N galima daryti prielaidą kad lūžio rodiklis yra konstanta kiekvieno sluoksnio viduje. Plokščios bangos sklaida kiekvienam $n(z_t)$ sluoksnyje gali būti aprašytas būdinga matrica ir daugiasluoksnei struktūrai būdinga matrica yra produktas visų sluoksnių atitinkamų matricių. Koeficientai S_{11} ir S_{21} N sluoksnių sistemos laisvoje erdvėje yra:

$$S_{11} = \frac{n_{air} - C/B}{n_{air} + C/B}, \quad (9)$$

$$S_{21} = \frac{2n_{air}}{n_{air} + C/B}, \quad (10)$$

kur

$$\begin{bmatrix} B \\ C \end{bmatrix} = \left\{ \prod_{t=1}^N \begin{bmatrix} \cos(k_t \tau_t) & i \sin(k_t \tau_t) k_0/k_1 \\ i \sin(k_t \tau_t) k_1/k_0 & \cos(k_t \tau_t) \end{bmatrix} \right\} \begin{bmatrix} 1 \\ n_{air} \end{bmatrix}. \quad (11)$$

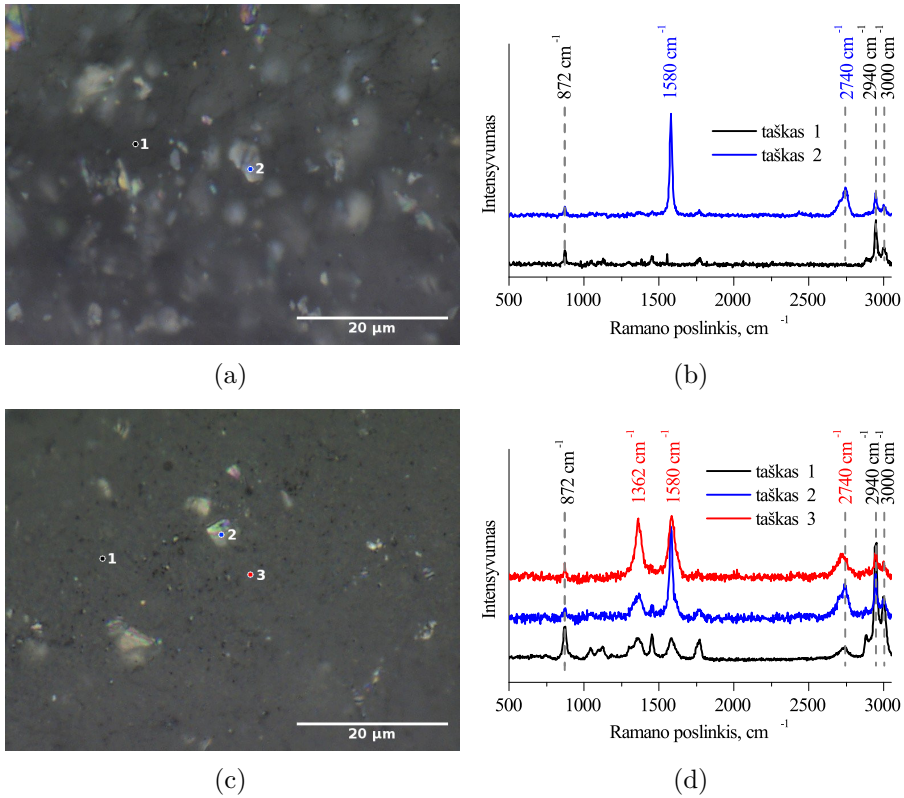
Čia τ_t storis sluoksnio t , $k_t = \frac{2\pi n(z)}{\lambda}$ ir $k_0 = \frac{2\pi n_{air}}{\lambda}$ yra banginiai skaičiai sluoksniuose su lūžio rodikliais $n(z)$ ir n_{air} (tai yra tirta medžiaga ir laisvoji erdve), λ yra bangos ilgis.

S.3. Terahercinė spektroskopija izoliuotų užpildo dalelių kompozite esant koncentracijoms didesniems negu perkoliacijos slenkstis

Kompozitų apibūdinimas

Tirtų kompozitų sistemoje perkoliacijos slenkstis yra tarp 1.5 ir 3 % masinės koncentracijos, tuo tarpu kompozituose su GNL tarpais perkoliacijos slenkstis yra tarp 3 ir 6 % masinės koncentracijos [30]. Todėl tyrimui buvo atrinkti kompozitai tiek žemiau, tiek aukščiau perkoliacijos slenkščio.

Nanodalelių kokybė ir jų pasiskirstymas polimerinėje matricoje buvo ištirtos Ramano spektrometru suderintu su konfokaliniu mikroskopu (Nanofinder High End, Tokyo Instruments, Belarus-Japan). Anglies nanomedžiagų (įskaitant DANV, GNL, grafeną) Ramano spektruose dominuoja trys būdingi pikai esant dažniams $\sim 1360\text{ cm}^{-1}$, $\sim 1580\text{--}1600\text{ cm}^{-1}$ ir $\sim 2600\text{--}2700\text{ cm}^{-1}$ (įprastai vadinamos kaip D, G ir 2D modos atitinkamai, tuo tarpu ryškiausias ypatumas būdingas PLA matricai yra apie 3000 cm^{-1}). Palyginus su Ramano spektrais surinktais įvairiuose taškuose kompozito su 1.5 % GNL leidžia išryškinti GNL nanodalelės, taškai 1 ir 2 Pav. 14b, atitinka sritis be užpildo ir GNL, atitinkamai. Kontrasto skirtumas tarp GNL dalelių ir gryno polimero Pav. 5.14 14a nurodo dalelių pasiskirstymą polimerinėje matricoje.

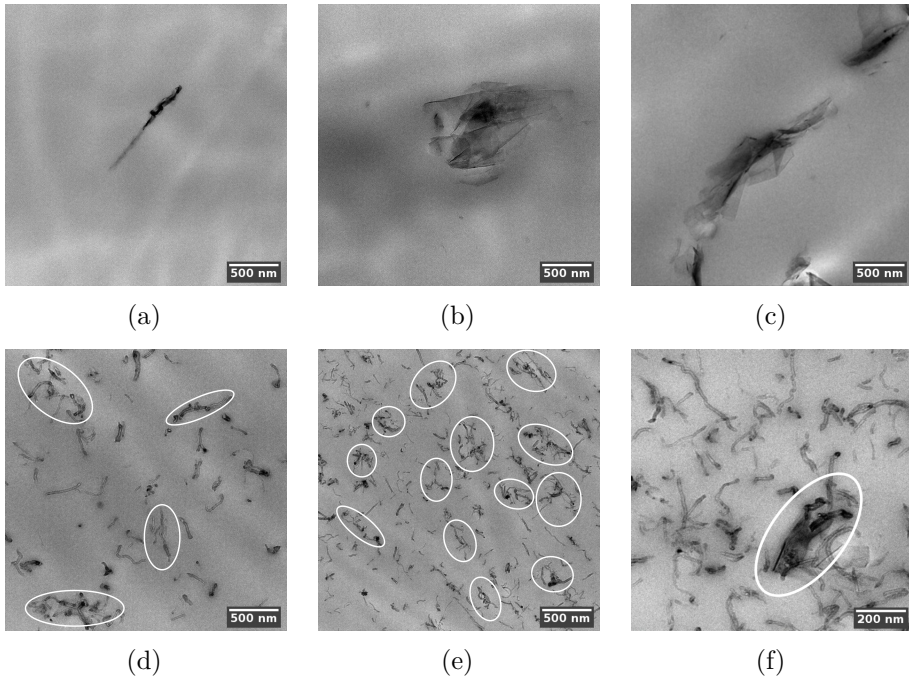


14 pav.: Optinės mikroskopijos nuotrauka (a) ir Ramano spektrai (b) PLA kompozito su 1.5 % GNL. Dėl gryno PLA optinio skaidrumo yra įmanoma pamatyti GNL kompozito paviršiuje. Optinio mikroskopo nuotrauka (c) ir Ramano spektrai (d) PLA kompozito su mišiniu 3 % GNL ir 3 % DANV. Ramano spektras išmatuotas taške 2 turi ypatumus būdingus PLA, GNL ir DANV.

Nagrinėjant Ramano spektrus galima pastebėti (Pav. 14d), kompozituose su dvejų tipų užpildais nanovamzdeliai yra vienodai pasiskirstę polimero matricoje. Tačiau, skirtinguose bandinio taškuose DANV ir PLA santykis įtakoja Ramano spektrus skirtingai (taškai 1 ir 3 Pav. 5.14d). Ramano spektroskopija leidžia atskirti net mažus DANV kiekius GNL dalelių paviršiuje (stebima D moda rodo anglies nanovamzdelius taške 2).

Prašveičianti elektroninė mikroskopija (PEM) nagrinėjamų kompozitų parodo, kad metodas leidžia pagaminti kompozitus su homogeniškai pasiskirsčiusiais dvejų tipų nanodalelėmis. Pav. 15 patvirtina, kad GNL išlaiko savo matmenys po lydimosi ekstruzijos proceso.

PEM nuotraukos kompozitų su vieno arba dvejų skirtingo tipo intarpais rodo, kad visi pagaminti bandiniai turi tam tikrą kiekį elektriškai izoliuotų užpildo dalelių, nors abiejų tipų nanodalelės yra gerai pasiskirstę.

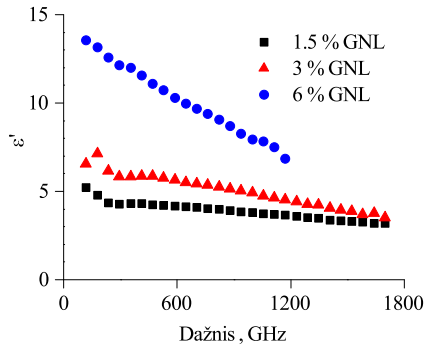


15 pav.: PEM nuotraukos izoliuotų užpildo dalelių PLA kompozituose su 1.5 (a), 3 (b), ir 6 % masinės koncentracijos GNL; elektriškai izoliuotos dalelės ir perkoliaciniai klasteriai (pažymėti ovalais) kompozituose su 1.5 (d) ir 3 % masinės koncentracijos DANV (f). Grafeno nanoplokštelė dalyvaujanti perkoliaciniame kontakte su nanovamzdeliu yra pažymėta ovalu.

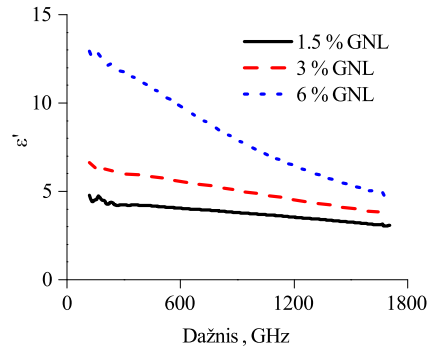
Maksvelo Garneto aproksimaciją kompozitų su GNL intarpais dielektrinės skvarbos

Tirtų bandinių pralaidumas buvo matuotas terahercinė koherentinė spektroskopija. Pralaidumo koeficiento amplitudė ir fazė buvo panaudotos nustatyti kompleksinio elektrinio laidumo ir dielektrinės skvarbos vertėms nustatyti.

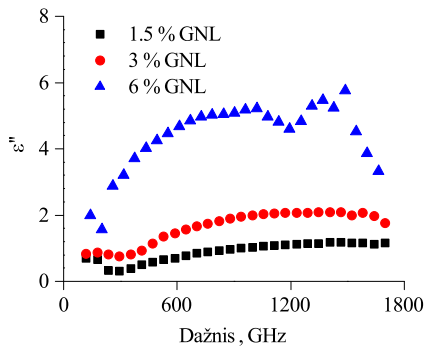
Typinės perkoliacijos slenksčio vertės kompozituose su GNL intarpais yra ne mažesnės negu 3.5 % ir stipriai priklauso nuo GNL geometrinių parametrų, polimero tipo ir dalelių pasiskirstymo kokybės [74, 75]. Atsižvelgus į principus paskelbtus dalyje S.2.2 GNL dalelės aproksimuojamos elipsoidu su $a = b \gg c$ pusašėmis ir tankiu lygiu grafito tankiui (2.2 g/cm^3). Typinis santykis ilgio ir skersmens santykis (AR) grafeno nanoplokštelėms yra apie 100–1000. Kompozitų su 1.5 ir 3 % GNL intarpais (Pav. 16) dielektrinės skvarbos teorinis aprašymas yra patekinamas su parametrais $\sigma = 20000 \text{ S/m}$ ir AR apie 200, kas gerai derinasi su AR GNL dalelių pateiktų Paragrafe S.2.1. Nors aproksimacijos parametrai kompozitams esant koncentracijoms 1.5 ir 3 % yra panašūs, bandinys turintis 6 % užpildo reikalauja kito parametrų rinkinio eksperimentinių duomenų aprašymui. Nors elipsoidų laidumas nekinta, ilgio ir skersmens santykis išauga iki 300.



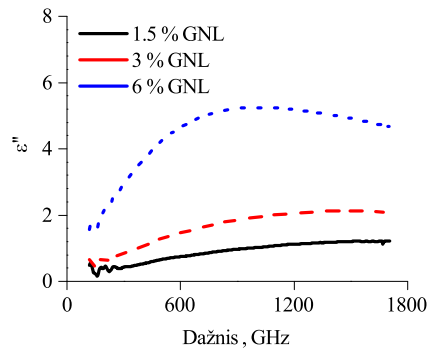
(a)



(b)



(c)



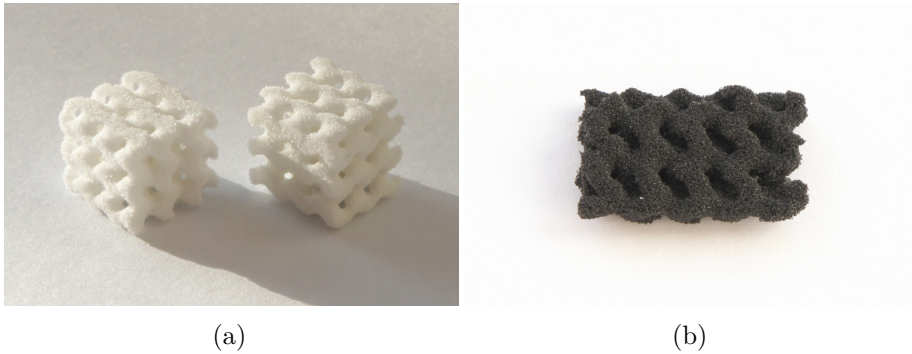
(d)

16 pav.: Kompleksinė dielektrinė skvarba kompozitų turinčių 1.5, 3 ir 6 % masinės koncentracijos GNL (a, c). Maksvelo Garneto aproksimacija eksperimentinių duomenų esant parametrams $\sigma = 20000$ S/m ir $AR \sim 197, 208$ ir 291 , atitinkamai (b, d).

S.4. Trimatės periodinės porėtos struktūros elektromagnetinio slopinimo taikymams.

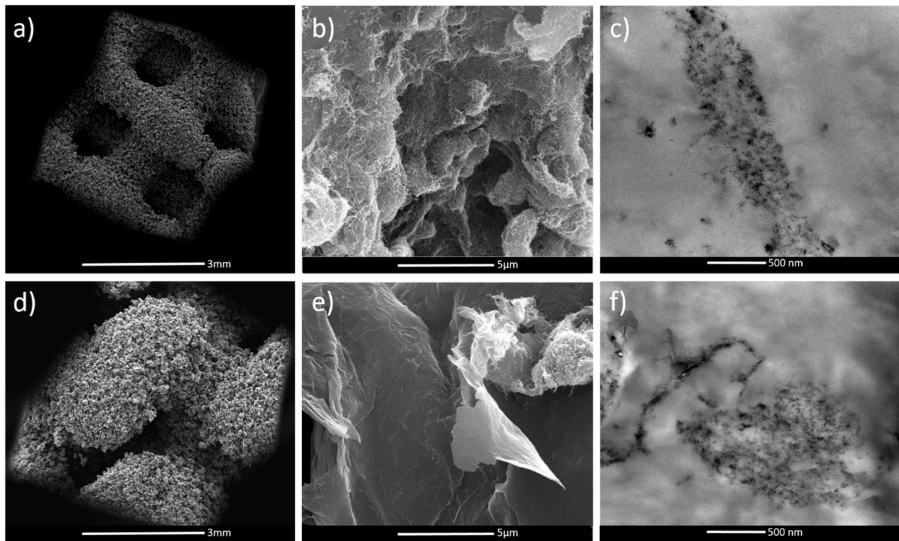
Bandiniai TPMS geometrijos buvo atspausdintos su grynu poliuretanu (TPU) ir TPU/DANV, TPU/DANV-GNL kompozitais esant skirtingam porėtumui: 20 ir 60 %.

Pav. 17 parodyta optinė nuotrauka gryno TPU ir 16×8 mm TPU/DANV-GNL kompozito. Kubas 1 cm^3 tūrio turi $3 \times 3 \times 3$ vienetinių narvelių. Bandiniai su abiejų tipų nanoanglies intarpais pasižymi optimaliu elastiškumu ir mechaniniu stiprumu pakankamu daugkartiniam elektromagnetinių savybių tyrimui.



17 pav.: G60 struktūros atspausdintos iš gryno TPU (a) ir TPU/DANV kompozito (b).

Elektroninės mikroskopijos tyrimai parodo kad TPU/DANV ir TPU/ DANV/GNL suformuoja segreguotas struktūras po atspausdinimo (Pav. 18b, c ir e, f atitinkamai). Skenuojančios elektroninės mikroskopijos tyrimai parodo kad anglies nanodalelių pasiskirstymas TPU paviršiuje prieš sintezę ir po sintezės didžiaja dalimi išlieka toks pats, kas salygoja susiformavimą elektrinio perkoliacinio tinklo. Analizuojant prašviečiamos elektroninės mikroskopijos nuotraukas galima padaryti išvada kad perkoliacinio tinklo siulo storis yra apie 200~500 nm. Plačiajuosčių elektromagnetinių savybių tyrimas buvo atliktas žemų, mikrobangų ir teraherciniame dažnių diapazonuose. Impedansinė spektroskopija buvo atlikta elektrinės perkoliacijos buvimui patikrinti. Mikrobangės savybės G20 ir G60 porėtų struktūrų turinčių DANV ir DANV-GNL buvo ištirtos Ka (12–18 GHz) ir teraherciniame (0.1–1 THz) dažnių diapazonuose. Plokščiai lygiagretus bandiniai 10.6 mm storio buvo patalpinti į bangolaidį ir buvo išmatuoti jų kompleksiniai S_{21} parametrai. Teraherciniame dažnių diapazone savybės buvo ištirtos teraherciniu koherentiniu spektrometru (Ekspla, Vilnius). Bandiniai plokštelės formos (dvejų milimetrų storio) porėtos struktūros ($7 \times 5 \text{ cm}^2$) buvo patalpinti tarp emiterio ir detektorio statmenai krentančiai bangai.

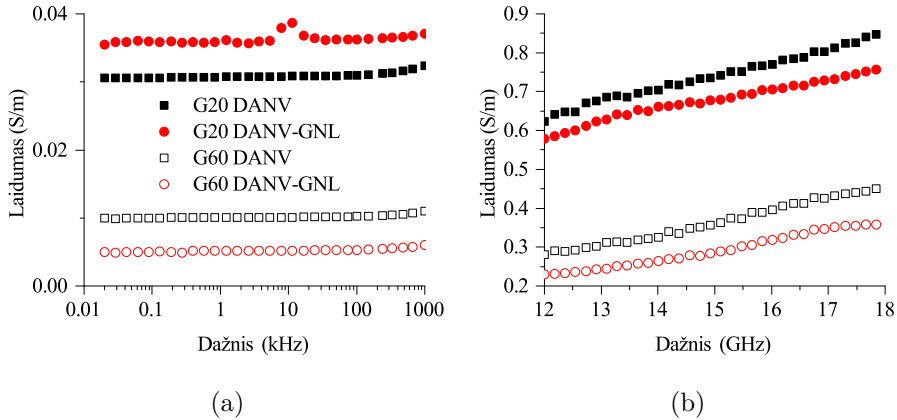


18 pav.: SEM nuotrauka D60 ir G60 struktūrų atspausdintų su TPU/DANV. SEM (b) ir TEM (c) nuotraukos TPU/DANV kompozitų, SEM (e) ir TEM (f) nuotraukos TPU/DANV-GNL atspausdintos G60 struktūros [76].

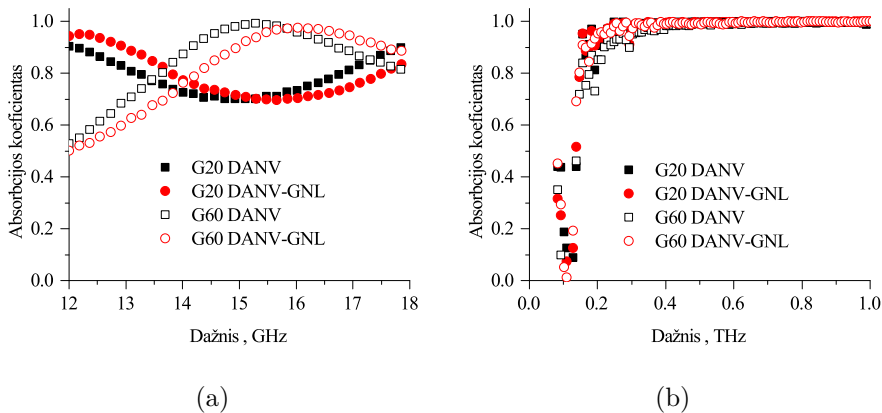
Kompleksinė dielektrinė skvarba ir absorbcijos koeficientai buvo apskaičiuoti panaudojus eksperimentinius duomenys. Efektyvaus elektrinio laidumo plačiajuosčiai spektrai yra parodyti Pav. 19. Visi kompozitai virš perkoliacijos slenksčio pasižymi panašiais elektrinio laidumo spektrais, sudarytais iš dvejų sričių nuo dažnio nepriklausantis plato žemuose dažniuose, susietas su elektriniu laidumu nuostoviam elektriniame lauke, ir nuo dažnio priklausanti dalis, esant aukštesnėms dažniams. Abiems TPU/DANV ir TPU/DANV-GNL struktūroms egzistavimas nuo dažnio nepriklausončio plato laidumo spektruose yra įrodymas elektrinės perkoliacijos buvimo.

Absorbcijos koeficientai buvo išmatuoti mikrobangų ir teraherciniame dažnių diapazonuose, sistema buvo sudaryta iš 10 mm sluoksnio giroidalinės struktūros kuri buvo papildomai patalpinta ant metalinės plokštelės maksimizuojant mikrobangų absorbciją. Pav. 20a yra parodyta yra būdinga interferencija sluoksniuotuose struktūruose. Absorbcijos maksimumai bandinių G60 yra tarp 15 ir 16 GHz bandiniams TPU/DANV ir TPU/DANV-GNL, atitinkamai, tuo tarpu mažiau porėtos struktūros turi minimumus esant šiems dažniams, o maksimumus esant dažniams mažesniems negu 12 GHz arba 18 GHz. Toks elgesis atsklei-

džia struktūros porėtumo įtaką jos efektyviai skvarbai. Kitokia situacija yra stebima teraherciniame dažnių diapazone kur bandiniai be padėklo (tai yra atgalinio veidrodėlio) pasižymi pikia absorbcija esant dažniams aukštesnėms negu 0.3 THz, kai bandinio storis buvo tik 2 mm (Pav. 20b).



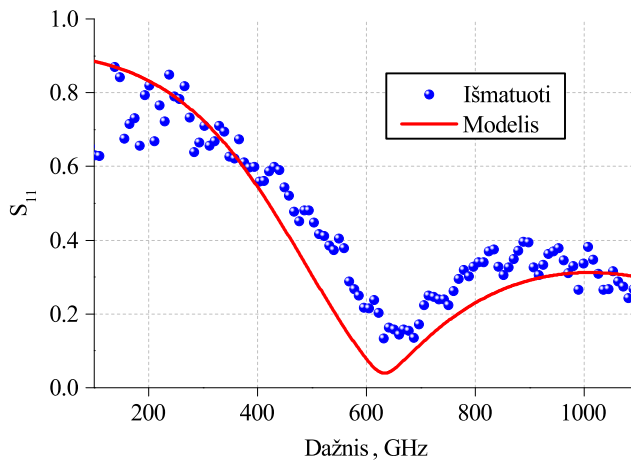
19 pav.: Porėtų struktūrų efektinio elektrinio laidumo spektrai žemų dažnių srityje (a) ir mikrobangų diapazone (b).



20 pav.: (a) Absorbcijos koeficientai 10 mm sluoksnio porėtos struktūros ir metalinio atgalinio veidrodėlio. (b) Absorbcijos koeficientai 2 mm sluoksnio laisvoje erdvėje teraherciniame dažnių diapazone (0.1–1 THz).

S.5. Teraherciniai optiniai elementai vertikaliai orientuotų DANV masyvų pagrindu.

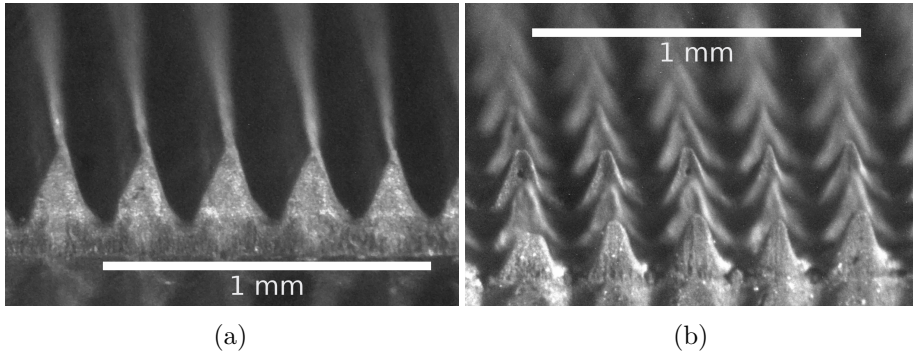
Šis skyrius yra skirtas rezultatams gautiems naujos technologijos pagalba, kuri sudaryta iš DANV masyvų lazerinio profiliavimo ir polimerinio impregnavimo. Atitikimas tarp eksperimentinių rezultatų pateiktų šiame skyriuje ir modeliavimo įrodo kad struktūrų elektromagnetinės savybės teraherciniame dažnių diapazone priklauso nuo polimero ir graviruotų masyvų savybių. Statmenai atspindėto signalo nuo periodinio masyvo piramidžių su $232.9 \pm 11.9 \mu\text{m}$ su $54.9 \pm 6.9 \mu\text{m}$ nemupjauto sluoksnio viršuje (Pav. 7) padengtas epoksidinės dervos sluoksniu $77.0 \pm 4.5 \mu\text{m}$ (Pav. 8) buvo išmatuotas 0.1–1 THz dažnių diapazone. Palyginimas tarp eksperimentiškai išmatuoto signalo atspindėto nuo piramidžių masyvo padengto epoksidinė derva yra pateiktas Pav. 21.



21 pav.: Amplitudė atspindėto signalo S_{11} nuo periodinio anglies nanovamzdelių piramidžių masyvo (piramidės aukštis yra $232.9 \pm 11.9 \mu\text{m}$ ir $54.9 \pm 6.9 \mu\text{m}$ viršutinis sluoksnis uždengtas epoksidinės dervos sluoksniu plonesniu negu $77 \mu\text{m}$). Symboliai atitinka eksperimentinius duomenys, ištisinės linijos modeliavimo rezultatus.

Eksperimentiniai duomenys gerai atitinka modeliavimo rezultatus. Stebimas skirtumas gali būti paaiškintas netiesine priklausomybe epoksidinės dervos srityje arti piramidžių pagrindo. Todėl galima teigti kad pagamintas metapaviršius veikia kaip atspindžiui selektyvus paviršius su didžiausia absorbcija esant $\nu_0 = 700 \text{ GHz}$ dažniui.

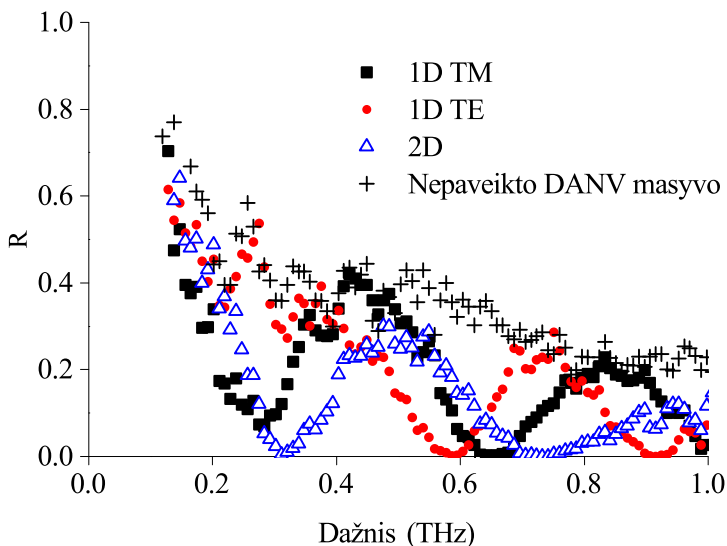
Terahercinė spinduliuotė naudojama koherentiniame spektrometre turi tiesinę poliarizaciją, kas leidžia tyrinėti nagrinėjamų struktūrų savybes priklausančias nuo poliarizacijos. Šiam tikslui buvo sukurtas rinkinys išgraviruotų stulpelių ir juostelių (toliau vadinamas 1D ir 2D grotelėmis) (Pav. 22). Išgraviruotos juostelės buvo vakuume padengtos epoksidinė derva.



22 pav.: Optinės nuotraukos išgraviruotų 1D (a) ir 2D (b) grotelių su 250 μm periodu ir 300 μm bendru aukščiu prieš padengimą epoksidinė dervą.

Matavimo metu 2D grotelės buvo patalpintos statmenai spindulioi, tuo tarpu 1D grotelės buvo orientuotos lygiagrečiai ir ortogonaliai elektrinio lauko vektoriui \vec{E} . Tirtų struktūrų ir anglies nanovamzdelių masyvo (kurio aukštis 300 μm) padengto 70~90 μm epoksidinės dervos sluoksniu yra parodytas Pav. 23. 1D TE kreivė atitinka grotelių orientaciją lygiagrečiai elektrinio lauko vektoriui E tuo tarpu 1D TM reiškia 90° laipsnių kampą tarp grotelių ir elektrinio lauko.

Nepaveiktų DANV masyvų optinio atspindžio koeficientai yra intervale nuo 30 % iki 80 % dažnių diapazone nuo 0.1 iki 1 THz. Šios elektromagnetinės savybės yra rezultatas kombinacijos plokščio DANV masyvo absorbcijos spektro ir interferencijos bangų atspindėtų ribose tarp laisvosios erdvės, epoksidinės dervos ir DANV masyvų. Tuo tarpu graviruotų bandinių atveju atspindėtos bangos dalis mažėja iki 1–5 % arti 1 THz. Tai rodo geresnę absorbciją graviruotų bandinių palyginus su nepaveiktais DANV masyvais padengtais panašiais epoksidinės dervos kiekiais.



23 pav.: Atspindžio spektrai nepaveikto DANV masyvo, 1D ir 2D grotelių su 250 μm periodu.

Abejų tipų 1D ir 2D grotelėms yra stebimos ryškios atspindžio koeficiento osciliacijos, šios osciliacijos nestebimos nepaveiktų masyvų atveju. Šios osciliacijos atsiranda dėl interferencijos tarp atspindėtų bangų nuo polimero paviršiaus ir DANV juostelių ir stripelių masyvų. Dar daugiau 1D bandinių savybės priklauso nuo grotelių orientacijos elektromagnetinės spinduliotės poliarizacijos atžvilgiu. Svarbu kad atspindžio koeficiento spektras 1D grotelių TM orientacijoje yra artimas 2D grotelių atitinkam spektrui. Dėl to savybės priklausančios nuo poliarizacijos gali būti paašškintos laidumo kanalais tarp juostelių, bet laidumas tarp gretimų juostelių arba stripelių atsiranda dėl tuneliavimo. Todėl graviruoti anglies nanovamzdelių masyvai gali būti taikomi teraherciniuose įtaisuose poliniams molekulėms detektuoti.

Išvados

Šis darbas yra skirtas kompozitinių medžiagų inžinerijos metodams. Darbas yra suskirtas į uždavinius: kompozitų struktūros tyrimas terahercinės spektroskopijos metodais, porėtos reguliarios struktūros sukūrimas 3D spausdinimo metodais, naujų medžiagų inžinerijos metodų, paremtų lazerinių profiliavimu ir polimerų impregnavimu, sukūrimas.

Atlėkiant darbą buvo gauti šie rezultatai:

Šis darbas yra skirtas kompozitinių medžiagų inžinerijos metodams. Darbas yra suskirtas į uždavinius: kompozitų struktūros tyrimas terahercinės spektroskopijos metodais, porėtos reguliarios struktūros sukūrimas 3D spausdinimo metodais, naujų medžiagų inžinerijos metodų, paremtų lazerinių profiliavimu ir polimerų impregnavimu, sukūrimas.

Atlėkiant darbą buvo gauti šie rezultatai:

Pirma, buvo atskirtas nanodalelių neįtrauktų į perkoliacinį tinklą indėlis į dielektrinę skvarbą, pasinaudojus terahercine koherentine spektroskopija. Buvo pastebėta smailė kompleksinės dielektrinės skvarbos menamos dalies priklausomybėje nuo dažnio PLA kompozituose užpildytuose GNL, DANV ir jų mišiniais tiek žemiau, tiek aukščiau slenksčio. Buvo pademonstruota, kad terahercinė koherentinė spektroskopija yra jautri priemonė nustatyti užpildo dalelių pasiskirstymą. Pavyzdžiui, atitikimas tarp verčių kompleksinės dielektrinės skvarbos išmatuotų kompozitams su GNL intarpais ir apskaičiuotų pagal Maksvelo Garneto efektyvios aplinkos teoriją nurodo homegenišką pasiskirstymą izoliuotų GNL polimerinėje matricoje. Hybridiniams kompozitams su bendra nanoanglies koncentracija 6 % buvo parodyta kad stiprus pokytis menamosios dielektrinės skvarbos dalies spektrų pokytis yra stebimas kartu su silpnu pokyčiu realiosios dalies atitinkamų spektrų. GNL koncentracijos pokytis lemia menamosios dalies maksimumo dažnio poslinkį, tuo tarpu dielektrinė skvarba lieka praktiškai nepakitusi, kas leidžia valdyti elektromagnetines savybes. Paprastas nanodalelių koncentracijų keitimas leidžia tiksliai keisti menamosios dalies maksimumo poziciją.

Skirtingų nanoanglies užpildų koncentracijų kombinacijos leidžia tiksliai kontroliuoti kompozitų elektromagnetinės savybes, kas kartu su mažesne GNL kaina palyginus su DANV leidžia prognozoti plačias perespektyvas šių medžiagų.

Antra, reguliarios porėtos struktūros buvo pagamintos 3D spausdinimo technika panaudojus TPU ir nanoanglies miltelius. Jų elektromagne-

tinės savybės buvo ištirtos teraherciniame dažnių diapazone. Elektromagnetinės savybės šių struktūrų iš dalies nulemtos jų vidinės morfologijos, tai yra segreguotos struktūros. Parodyta, kad tiek TPU/DANV, tiek TPU/DANV-GNL kompozitai gali būti taikomi absorbojančių struktūrų kūrimui.

Porėtos struktūrų TPMS giroido struktūra pasižymi pastoviu tankiu, tuo tarpu Švarco geometrija sąlygoja reikšmingas tankio fluktuacijas. Tačiau kiekviena iš nagrinėjamų geometrijų gali rasti savo taikymo sritį. Pavyzdžiui, sistema giroido pagrindu su porėtumu kintančiu išilgai z ašies turi geriausias absorbcijos savybes.

Galiausiai, buvo išvystyta koncepcija dažniui selektyvių ir nuo polarizacijos priklausančių reflektorių piramidinių metapaviršių ir grotelių pagrindu. Piramidės aukščio ir dielektrinio sluoksnio skvarbos įtaka visos struktūros elektromagnetinėms savybėms buvo aprašytos teoriškai plačiame dažnių diapazone. Buvo teoriškai pagrįsta galimybė kontroliuoti šių metapaviršių atspindžio savybes.

Metapaviršiai buvo pagaminti lazeriniu graviravimu vertikaliai orientuotų DANV masyvų ir toliau padengti dielektriko sluoksniu. Eksperimentiškai ir teoriškai buvo pademonstruotas šioms struktūroms minimumas atspindžio koeficiento spektruose. Jo vieta dažnio spektre yra nulemta dielektrinio sluoksnio storio, tuo tarpu piramidžių aukštis lemia atspindėto signalo slopinimo greitį.

Pristatytas metapaviršių dizainas yra pirmasis bandymas panaudoti graviruotus DANV masyvus metapaviršių gamybai. Dažniui selektyvus paviršiai, filtrai, lęšiai, slopintuvai ir kiti elementai gali būti gaminomi panaudojus puikias absorbciją ir elektromagnetines savybes graviruotų DANV masyvų užpildytų specifiniu dielektriku.

Šio darbo rezultatai gali būti priskirti prie trečio technologinio parengtumo lygio (angliškai proof of concept) [77]. Menamos dalies maksimumas įskaitant matavimus ir efektyvios modelio taikymą leidžia neardantį detektavimą izoliuotų užpildo dalelių polimero matricio žemiau ir aukščiau perkoliacijos slenksčio. Ekperimentiniai reguliarių struktūrų elektromagnetinių savybių tyrimai kartu su teoriniu modeliavimu sudaro tvirtą laboratoriskai pagrįstą pagrindą ekonomiškai pagrįstoms technologijoms pagaminti ypač lengvus optinius elementus mikrobangų ir teraherciniame dažnių diapazone.

Literatūra

- [1] A. K. Mallik ir kt., “Fabrication of polysaccharide-based materials using ionic liquids and scope for biomedical use”, in *Functional Polysaccharides for Biomedical Applications*, Elsevier, 2019 m., p. 131–171.
- [2] N. Ali ir kt., “Fabrication strategies for functionalized nanomaterials”, in *Nanomaterials: Synthesis, Characterization, Hazards and Safety*, Elsevier, 2021 m., p. 55–95.
- [3] K. K. Chawla, *Composite Materials: Science and Engineering*. Cham: Springer International Publishing, 2019 m.
- [4] C. Caloz, *Electromagnetic metamaterials: transmission line theory and microwave applications: the engineering approach*, bendradarb. su T. Itoh. Hoboken, N.J: John Wiley & Sons, 2006 m., 352 p.
- [5] C. L. Holloway ir kt., “An Overview of the Theory and Applications of Metasurfaces: The Two-Dimensional Equivalents of Metamaterials”, *IEEE Antennas and Propagation Magazine*, t. 54, Nr. 2, p. 10–35, 2012 m. bal. mėn.
- [6] H. Lin ir kt., “Design and fabrication of moth-eye subwavelength structure with a waist on silicon for broadband and wide-angle anti-reflection property”, *Coatings*, t. 8, Nr. 10, p. 360, 2018 m. spal. 9 d.
- [7] V. Popov ir kt., “Designing Metagratings via Local Periodic Approximation: From Microwaves to Infrared”, *Physical Review Applied*, t. 11, Nr. 4, 2019 m. bal. mėn.
- [8] A. Thomas, “Functional materials: From hard to soft porous frameworks”, *Angewandte Chemie International Edition*, t. 49, Nr. 45, p. 8328–8344, 2010 m. lapkr. 2 d.
- [9] S. Paszkiewicz ir kt., “Synergetic effect of single-walled carbon nanotubes (SWCNT) and graphene nanoplatelets (GNP) in electrically conductive PTT-block-PTMO hybrid nanocomposites prepared by in situ polymerization”, *Composites Science and Technology*, t. 118, p. 72–77, 2015 m. spal. mėn.

- [10] F. H. Gojny ir kt., “Surface modified multi-walled carbon nanotubes in CNT/epoxy-composites”, *Chemical Physics Letters*, t. 370, Nr. 5-6, p. 820–824, 2003 m. kov. mèn.
- [11] A. V. Okotrub ir kt., “Transmission of terahertz radiation by anisotropic MWCNT/polystyrene composite films”, *Physica Status Solidi (B)*, t. 248, Nr. 11, p. 2568–2571, 2011 m. lapkr. mèn.
- [12] M. V. Shuba ir kt., “Role of finite-size effects in the microwave and subterahertz electromagnetic response of a multiwall carbon-nanotube-based composite: Theory and interpretation of experiments”, *Physical Review B*, t. 88, Nr. 4, p. 045 436, 2013 m.
- [13] Y. Kato ir kt., “Stretchable electromagnetic-interference shielding materials made of a long single-walled carbon-nanotube-elastomer composite”, *RSC advances*, t. 7, Nr. 18, p. 10 841–10 847, 2017 m.
- [14] S.-E. Lee, O. Choi ir H. T. Hahn, “Microwave properties of graphite nanoplatelet/epoxy composites”, *Journal of Applied Physics*, t. 104, Nr. 3, p. 033 705, 2008 m. rugpj. mèn.
- [15] X. Sun ir kt., “Developing Polymer Composite Materials: Carbon Nanotubes or Graphene?”, *Advanced Materials*, t. 25, Nr. 37, p. 5153–5176, 2013 m. spal. mèn.
- [16] S. Zhu ir G. Xu, “Single-walled carbon nanohorns and their applications”, *Nanoscale*, t. 2, Nr. 12, p. 2538, 2010 m.
- [17] Z. Kang ir S.-T. Lee, “Carbon dots: Advances in nanocarbon applications”, *Nanoscale*, t. 11, Nr. 41, p. 19 214–19 224, 2019 m.
- [18] K. I. Baskakova ir kt., “Modification of structure and conductivity of nanohorns by toluene addition in carbon arc”, *Fullerenes, Nanotubes and Carbon Nanostructures*, t. 28, Nr. 4, p. 342–347, 2020 m. bal. 2 d.
- [19] F. Qin ir C. Brosseau, “A review and analysis of microwave absorption in polymer composites filled with carbonaceous particles”, *Journal of Applied Physics*, t. 111, Nr. 6, p. 061 301, 2012 m. kov. mèn.
- [20] L. Liu, A. Das ir C. M. Megaridis, “Terahertz shielding of carbon nanomaterials and their composites – A review and applications”, *Carbon*, t. 69, p. 1–16, 2014 m. bal. mèn.

- [21] S. Iijima, “Helical microtubules of graphitic carbon”, *Nature*, t. 354, Nr. 6348, p. 56–58, 1991 m. lapkr. mèn.
- [22] G. Y. Slepyan ir kt., “Electrodynamics of carbon nanotubes: Dynamic conductivity, impedance boundary conditions, and surface wave propagation”, *Physical Review B*, t. 60, Nr. 24, p. 17 136, 1999 m.
- [23] J. F. O Hara, R. D. Averitt ir A. J. Taylor, “Terahertz surface plasmon polariton coupling on metallic gratings”, *Optics express*, t. 12, Nr. 25, p. 6397–6402, 2004 m.
- [24] Y. Lan ir kt., “SIMULATION OF CARBON NANOTUBE THz ANTENNA ARRAYS”, *International Journal of Infrared and Millimeter Waves*, t. 27, Nr. 6, p. 871–877, 2007 m. vas. mèn.
- [25] G. Y. Slepyan ir kt., “Terahertz conductivity peak in composite materials containing carbon nanotubes: Theory and interpretation of experiment”, *Physical Review B*, t. 81, Nr. 20, 2010 m. geg. mèn.
- [26] M. V. Shuba ir kt., “Experimental evidence of localized plasmon resonance in composite materials containing single-wall carbon nanotubes”, *Physical Review B*, t. 85, Nr. 16, p. 165 435, 2012 m.
- [27] K. S. Novoselov ir kt., “Electric field effect in atomically thin carbon films”, *Science*, t. 306, Nr. 5696, p. 666–669, 2004 m.
- [28] G. Spinelli ir kt., “Nanocarbon/Poly(Lactic) Acid for 3D Printing: Effect of Fillers Content on Electromagnetic and Thermal Properties”, *Materials*, t. 12, Nr. 15, p. 2369, 2019 m. liep. mèn.
- [29] E. Ivanov ir kt., “PLA/Graphene/MWCNT Composites with Improved Electrical and Thermal Properties Suitable for FDM 3D Printing Applications”, *Applied Sciences*, t. 9, Nr. 6, p. 1209, 2019 m. kov. mèn.
- [30] M. Shuba ir kt., “Frequency and density dependencies of the electromagnetic parameters of carbon nanotube and graphene nanoplatelet based composites in the microwave and terahertz ranges”, *Materials Research Express*, t. 6, Nr. 9, p. 095 050, 2019 m. liep. 3 d., Publisher: IOP Publishing.
- [31] A. Gbaguidi, S. Namilae ir D. Kim, “Synergy effect in hybrid nanocomposites based on carbon nanotubes and graphene nanoplatelets”, *Nanotechnology*, t. 31, Nr. 25, p. 255 704, 2020 m. bal. mèn.

- [32] A. V. Eletskii ir kt., “Electrical characteristics of carbon nanotube-doped composites”, *Physics-Uspekhi*, t. 58, Nr. 3, p. 209–251, 2015 m.
- [33] Y.-J. Chen ir kt., “Porous composites coated with hybrid nano carbon materials perform excellent electromagnetic interference shielding”, *Composites Part B: Engineering*, t. 70, p. 231–237, 2015 m. kov. mèn.
- [34] A. Paddubskaya ir kt., “Tunable Perfect THz Absorber Based on a Stretchable Ultrathin Carbon-Polymer Bilayer”, *Materials*, t. 12, Nr. 1, p. 143, 2019 m. saus. mèn.
- [35] G. Gorokhov ir kt., “Creation of metasurface from vertically aligned carbon nanotubes as versatile platform for ultra-light THz components”, *Nanotechnology*, t. 31, Nr. 25, p. 255 703, 2020 m. bal. 3 d.
- [36] D. Ding ir kt., “Rational design of core-shell co@c microspheres for high-performance microwave absorption”, *Carbon*, t. 111, p. 722–732, 2017 m. saus. mèn.
- [37] K. Wang ir kt., “Iron oxide@graphitic carbon core-shell nanoparticles embedded in ordered mesoporous n-doped carbon matrix as an efficient cathode catalyst for PEMFC”, *Applied Catalysis B: Environmental*, t. 264, p. 118 468, 2020 m. geg. mèn.
- [38] M. Fadeev ir kt., “Iron oxide @ gold nanoparticles: Synthesis, properties and potential use as anode materials for lithium-ion batteries”, *Colloids and Surfaces A: Physicochemical and Engineering Aspects*, t. 603, p. 125 178, 2020 m. spal. mèn.
- [39] M. Zdorovets ir kt., “Phase transformations and changes in the dielectric properties of nanostructured perovskite-like LBZ composites as a result of thermal annealing”, *Ceramics International*, t. 46, Nr. 10, p. 14 460–14 468, 2020 m. liep. mèn.
- [40] A. V. Okotrub ir kt., “Arrays of carbon nanotubes aligned perpendicular to the substrate surface: Anisotropy of structure and properties”, *Nanotechnologies in Russia*, t. 3, Nr. 3-4, p. 191–200, 2008 m.

- [41] C. Castro ir kt., “Dynamics of catalyst particle formation and multi-walled carbon nanotube growth in aerosol-assisted catalytic chemical vapor deposition”, *Carbon*, t. 48, Nr. 13, p. 3807–3816, 2010 m. lapkr. mēn.
- [42] G. A. Wurtz ir kt., “Designed ultrafast optical nonlinearity in a plasmonic nanorod metamaterial enhanced by nonlocality”, *Nature Nanotechnology*, t. 6, Nr. 2, p. 107–111, 2011 m. vas. mēn.
- [43] D. Zagorskiy ir kt., “Formation of nanowires of various types in the process of galvanic deposition of iron group metals into the pores of a track membrane”, *Membranes*, t. 12, Nr. 2, p. 195, 2022 m. vas. 8 d.
- [44] P. Kuzhir ir kt., “Epoxy composites filled with high surface area-carbon fillers: Optimization of electromagnetic shielding, electrical, mechanical, and thermal properties”, *Journal of Applied Physics*, t. 114, Nr. 16, p. 164304, 2013 m. spal. mēn.
- [45] K. Gnanasekaran ir kt., “3D printing of CNT- and graphene-based conductive polymer nanocomposites by fused deposition modeling”, *Applied Materials Today*, t. 9, p. 21–28, 2017 m. gruod. mēn.
- [46] M. Angjellari ir kt., “Beyond the concepts of nanocomposite and 3D printing: PVA and nanodiamonds for layer-by-layer additive manufacturing”, *Materials & Design*, t. 119, p. 12–21, 2017 m. bal. mēn.
- [47] J. Ren ir J. Yin, “3D-printed low-cost dielectric-resonator-based ultra-broadband microwave absorber using carbon-loaded acrylonitrile butadiene styrene polymer”, *Materials*, t. 11, Nr. 7, p. 1249, 2018 m. liep. 20 d.
- [48] X. Lleshi ir kt., “Design and Full Characterization of a 3-D-Printed Hyperbolic Pyramidal Wideband Microwave Absorber”, *IEEE Antennas and Wireless Propagation Letters*, t. 20, Nr. 1, p. 28–32, 2021 m. saus. mēn.
- [49] A. Capasso ir kt., “Ink-jet printing of graphene for flexible electronics: An environmentally-friendly approach”, *Solid State Communications*, t. 224, p. 53–63, 2015 m. gruod. mēn.

- [50] U. Kalsoom, P. N. Nesterenko ir B. Paull, “Recent developments in 3D printable composite materials”, *RSC Advances*, t. 6, Nr. 65, p. 60 355–60 371, 2016 m.
- [51] I. Blanco, “The use of composite materials in 3D printing”, *Journal of Composites Science*, t. 4, Nr. 2, p. 42, 2020 m. bal. 22 d.
- [52] M. Mirzaee, S. Noghianian ir I. Chang, “Low-profile bowtie antenna with 3D printed substrate”, *Microwave and Optical Technology Letters*, t. 59, Nr. 3, p. 706–710, 2017 m. kov. mėn.
- [53] M. A. Yakovleva ir K. G. Batrakov, “Two layer graphene heterostructures for waves slowing down: Operator approach to waveguide problem”, *Journal of the Belarusian State University. Physics*, Nr. 1, p. 73–82, 2020 m. saus. 31 d.
- [54] H.-T. Chen ir kt., “A metamaterial solid-state terahertz phase modulator”, *Nature Photonics*, t. 3, Nr. 3, p. 148–151, 2009 m.
- [55] H.-T. Chen ir kt., “Manipulation of terahertz radiation using metamaterials”, *Laser & Photonics Reviews*, t. 5, Nr. 4, p. 513–533, 2011 m. liep. 1 d.
- [56] L. Deng ir kt., “Manipulating of different-polarized reflected waves with graphene-based plasmonic metasurfaces in terahertz regime”, *Scientific Reports*, t. 7, Nr. 1, p. 10 558, 2017 m. gruod. mėn.
- [57] W. Lai ir kt., “Ultrathin, highly flexible and optically transparent terahertz polarizer based on transparent conducting oxide”, *Journal of Physics D: Applied Physics*, t. 53, Nr. 12, p. 125 109, 2020 m. kov. 18 d.
- [58] Y. Malevich ir kt., “Video-speed graphene modulator arrays for terahertz imaging applications”, *ACS Photonics*, t. 7, Nr. 9, p. 2374–2380, 2020 m. rugs. 16 d.
- [59] N. I. Zheludev, “A roadmap for metamaterials”, *Optics and Photonics News*, t. 22, Nr. 3, p. 30, 2011 m. kov. 1 d.
- [60] R. Wang ir kt., “Graphene based functional devices: A short review”, *Frontiers of Physics*, t. 14, Nr. 1, p. 13 603, 2019 m. vas. mėn.
- [61] S. K. Patel ir kt., “Graphene based tunable grating structure”, *Materials Research Express*, t. 6, Nr. 2, p. 025 602, 2018 m. lapkr. mėn.

- [62] S. K. Patel ir kt., “Graphene-based tunable reflector superstructure grating”, *Applied Physics A*, t. 125, Nr. 8, 2019 m. rugpj. mėn.
- [63] R. Jadeja ir kt., “Numerical investigation of graphene-based efficient and broadband metasurface for terahertz solar absorber”, *Journal of Materials Science*, t. 55, Nr. 8, p. 3462–3469, 2020 m. kov. mėn.
- [64] G. Spinelli ir kt., “Effects of Filament Extrusion, 3D Printing and Hot-Pressing on Electrical and Tensile Properties of Poly(Lactic) Acid Composites Filled with Carbon Nanotubes and Graphene”, *Nanomaterials*, t. 10, Nr. 1, p. 35, 2019 m. gruod. mėn.
- [65] R. Kotsilkova ir kt., “Exploring thermal annealing and graphene-carbon nanotube additives to enhance crystallinity, thermal, electrical and tensile properties of aged poly(lactic) acid-based filament for 3D printing”, *Composites Science and Technology*, t. 181, p. 107712, 2019 m. rugs. mėn.
- [66] A. P. Singh ir kt., “Probing the engineered sandwich network of vertically aligned carbon nanotube-reduced graphene oxide composites for high performance electromagnetic interference shielding applications”, *Carbon*, t. 85, p. 79–88, 2015 m. bal. mėn.
- [67] L. Qiu ir kt., “Remarkably enhanced thermal transport based on a flexible horizontally-aligned carbon nanotube array film”, *Scientific Reports*, t. 6, Nr. 1, p. 21014, 2016 m. rugpj. mėn.
- [68] J. E. Spanier ir I. P. Herman, “Use of hybrid phenomenological and statistical effective-medium theories of dielectric functions to model the infrared reflectance of porous SiC films”, *Physical Review B*, t. 61, Nr. 15, p. 10437–10450, 2000 m. bal. mėn.
- [69] M. S. Sarto ir kt., “Synthesis, Modeling, and Experimental Characterization of Graphite Nanoplatelet-Based Composites for EMC Applications”, *IEEE Transactions on Electromagnetic Compatibility*, t. 54, Nr. 1, p. 17–27, 2012 m. vas. mėn.
- [70] A. Ronca ir kt., “Selective Laser Sintering Fabricated Thermoplastic Polyurethane/Graphene Cellular Structures with Tailorable Properties and High Strain Sensitivity”, *Applied Sciences*, t. 9, Nr. 5, p. 864, 2019 m. vas. mėn.

- [71] D. Meisak ir kt., “Robust design of compact microwave absorbers and waveguide matched loads based on DC-conductive 3D-printable filament”, *Journal of Physics D: Applied Physics*, t. 53, Nr. 30, p. 305301, 2020 m. liep. 22 d.
- [72] M. Born ir E. Wolf, *Principles of optics: electromagnetic theory of propagation, interference and diffraction of light*, 7th expanded ed. Cambridge ; New York: Cambridge University Press, 1999 m.
- [73] H. A. Macleod, *Thin-film optical filters* (Series in optics and optoelectronics), 4th ed. Boca Raton, FL: CRC Press/Taylor & Francis, 2010 m., 782 p., OCLC: ocn176924832.
- [74] O. A. Al-Hartomy ir kt., “Dielectric and Microwave Properties of Graphene Nanoplatelets /Carbon Black Filled Natural Rubber Composites”, *International Journal of Materials and Chemistry*, t. 2, Nr. 3, p. 116–122, 2012 m. rugpj. mēn.
- [75] P. Kopyt ir kt., “Electric Properties of Graphene-Based Conductive Layers from DC Up To Terahertz Range”, *IEEE Transactions on Terahertz Science and Technology*, t. 6, Nr. 3, p. 480–490, 2016 m. geg. mēn.
- [76] G. Rollo ir kt., “On the synergistic effect of multi-walled carbon nanotubes and graphene nanoplatelets to enhance the functional properties of SLS 3D-printed elastomeric structures”, *Polymers*, t. 12, Nr. 8, p. 1841, 2020 m. rugpj. 17 d.
- [77] European Commission, *Technology readiness levels (TRL); Extract from Part 19 - Commission Decision C(2014)4995*, 2014 m.

Trumpos žinios apie disertantą

Vardas Pavarde: Gleb Gorokhov

Išsilavinimas:

- 2010–2015 m. studijavo Baltarusijos valstybiniame universitete ir įgijo fiziko tyrėjo kvalifikaciją;
- 2015–2016 m. studijavo Baltarusijos valstybiniame universitete ir įgijo fizinių-matematinių mokslų magistro kvalifikaciją;
- 2018–2023 m. studijavo Vilniaus universiteto Medžiagų inžinerijos mokslo krypties doktorantūroje.

Kontaktams: glebgorokhov@yandex.ru

Vilniaus universiteto leidykla
Saulėtekio al. 9, III rūmai, LT-10222 Vilnius
El. p. info@leidykla.vu.lt, www.leidykla.vu.lt
bookshop.vu.lt, journals.vu.lt
Tiražas 12 egz.